

Shaofan Li
Bohua Sun

Advances in Soft Matter Mechanics

Shaofan Li
Bohua Sun

Advances in Soft Matter Mechanics

With 134 figures, 42 of them in color



Editors

Prof. Shaofan Li
Department of Civil and Environmental
Engineering
The University of California at Berkeley
Berkeley, CA94720, USA
E-mail: li@ce.berkeley.edu

Prof. Bohua Sun
Centre for Mechanics, Smart Structures
and Microsystems
Cape Peninsula University of Technology
Bellville 7535, Cape Town, South Africa
E-mail: sunb@cput.ac.za

ISBN 978-7-04-031729-9
Higher Education Press, Beijing

ISBN 978-3-642-19372-9 ISBN 978-3-642-19373-6 (eBook)
Springer Heidelberg Dordrecht London New York

Library of Congress Control Number: 2011921307

© Higher Education Press, Beijing and Springer-Verlag Berlin Heidelberg 2012

This work is subject to copyright. All rights are reserved, whether the whole or part of the material is concerned, specifically the rights of translation, reprinting, reuse of illustrations, recitation, broadcasting, reproduction on microfilm or in any other way, and storage in data banks. Duplication of this publication or parts thereof is permitted only under the provisions of the German Copyright Law of September 9, 1965, in its current version, and permission for use must always be obtained from Springer. Violations are liable to prosecution under the German Copyright Law.

The use of general descriptive names, registered names, trademarks, etc. in this publication does not imply, even in the absence of a specific statement, that such names are exempt from the relevant protective laws and regulations and therefore free for general use.

Printed on acid-free paper

Springer is part of Springer Science+Business Media (www.springer.com)

Preface

Since 1990s, soft matter physics has become one of the main focuses in the field of condensed matter physics. Many subjects of soft matter physics have become active research fields, such as colloidal matter, membrane, gel, surfactant, liquid crystals, and polymers etc. Coming into the 21st century, this trend in soft matter research has continued and amplified, because soft matter physics and chemistry are the main connections between life science/biology and nanotechnology/nano-science. As a branch of soft matter physics, soft matter mechanics was a main source of inspiration in the early development of soft matter physics in the last century. Two of the most influential theories in soft matter physics were developed in the field of soft matter mechanics in 1950s and 1960s: (1) the Eriksen–Lislie theory of liquid crystals, and (2) the Biot finite deformation theory of gels. In the recent years, there is a significant resurgence in the research of soft matter mechanics. Comparing to the soft matter research in physics, chemistry, and biology, the contemporary soft matter mechanics research has its own unique character and advantage, because it brings profound insight and interpretation from the viewpoint of mechanics, and it utilizes the powerful computational technology in continuum mechanics, e.g. finite element methods, and other related continuum modeling and simulation methodologies into soft matter modelings and simulations.

In this book, we have selected nine different works from a group of leading young researchers working in the field of soft matter mechanics to be presented here. We have specifically asked the authors to present and introduce their work in a tutorial fashion, so that they will be suitable for readers from other disciplines and the first year graduate students. We believe that this collection of work represents a new trend and a breath of fresh in the soft matter mechanics research.

In Chapter 1, Chen and his colleagues presented their own research and a comprehensive review on both molecular modeling as well as continuum modeling of Deoxyribonucleic acid (DNA). They have not only discussed the DNA modeling at different scales but also discussed statistical modeling and multiscale simulation of mechanical behaviors of DNAs. If you are interested in modeling biomechanical behaviors DNAs, this is a work that you definitely cannot miss. In Chapter 2, Sauer presented his latest work on computational colloidal mechanics, in which a mesoscale coarse grained continuum framework is developed that is capable of solving many problems in colloidal physics and chemistry. In particular, this work presents a special type of atomistic finite element method, which may be useful for solving practical problems in applications of soft matter mechanics and physics, such as contact and adhesion problems at small scales. In Chapter 3, Zeng, Li, and Ren presented their latest work on soft matter modeling of stem cells.

In this work, they have developed a liquid crystal elastomer cell model that can mimic the mechanical behaviors of the cytoskeleton of a cell as well as the cell membranes. In recent developments of stem cell research, there have been many evidences linking the stem cell differentiation mechanism to its ability to sense the extracellular environments. Zeng, Li and Ren's work provide a sophisticated and yet convincing soft matter cell model to explain the mechanotransduction mechanism of the cell. In Chapter 4, Hatami-Marbini and Picu have provided a detailed account on foundation of mechanical modeling of semiflexible bio-polymers. The mechanics of random fiber networks have many important applications in soft matter physics, which includes the study of cellular cytoskeleton and filaments, collagenous connective tissues, battery substrates, and many other bio-polymer systems. In this work, Hatami-Marbini and Picu have mainly focused on non-affine deformation of aggregated polymer chains, their long-range correlations, and associated network elasticity. This is a topic that is seldom discussed in the literature, and authors' lucid exposition on this subject will become a valuable source in literatures. From a different angle on a similar subject, Karpov and Grankin presented their study on the origin of entropic elasticity of polymer chains by using the Monte-Carlo method in Chapter 5. In this work, the authors are trying to elucidate the molecular origin of entropic elasticity of polymer chains through atomistic modeling and statistical simulations. The chapter provides a good case study on the Monte-Carlo simulation of polymer chains, and the results presented here have provided both molecular interpretation and the limitation of the continuum model. Chapter 6 is an overview article by Hong on continuum modeling of stimuli-responsive gels. The author has spent last 7 or 8 years studying mechanical behaviors of stimuli-responsive gels, beginning from his graduate study at Harvard. Mechanics of gels, in particular, stimuli-responsive gels, is an important topic of soft matter mechanics, and the author is one of the leading researchers in this area. This Chapter is a state-of-the-art overview on the subject, and it is worthy of reading for readers who are interested in gels. In Chapter 7, Zamiri and De have documented their recent research of micro-mechanics study on three-dimensional (3D) crystallized protein materials and structures. In nature, proteins are used as the primary building units of biological structures as they are composed of 20 different amino acids in comparison to 4 nucleotides in DNAs. Current research has focused on better understanding and developing approaches to construct 1D, 2D and 3D protein structures and systems such as collagen, keratin, elastin, tubulin, fibroin, enzyme and bio-membranes for a range of applications including regenerative medicine, drug delivery and surface engineering. This Chapter not only presents the authors own research results, but also discussed the latest developments in this research field. In Chapter 8, Li and Gao have presented a research article on micro-mechanics of open-celled foams. Foam is regarded as the simplest example of soft matter. In most of previous studies, research efforts have been focused on liquid-phase foams or foam rheology. In this article, Li and Gao have examined how the microstruc-

ture can affect the mechanical properties of the foams in solid phase, which can be rarely found in the literature. More importantly, such modeling technique can be applied to analysis of foams in more general states. In Chapter 9, Liu and Xia have provided a review on capillary adhesion of micro-beams and plates, which includes some of their own research work in this subject. The capillary adhesive effect of micro-beams and plates is an important subject, which is the theoretical foundation to a crucial issue in marking nanoscale and microscale sensors and nano-electrical and mechanical system (NEMS) as well as micro-electro-mechanical systems (MEMS). In order to help readers to understand this subject, the authors have given us an in-depth discussion and derivation on capillary adhesion theory of micro-beams and micro-plates, which is an excellent tutorial article for the beginners.

The above nine chapters have covered several main types of soft matters, such as polymers and elastomers, membranes, gels, foams, DANs and proteins, etc., but also have discussed the related contact and adhesion theory as well as modeling techniques. By presenting such a unique collection to readers, especially young readers, we wish that the book can promote soft matter mechanics research, application, and education.

Shaofan Li and Bohua Sun
April 1st, 2011

Contents

Chapter 1 Atomistic to Continuum Modeling of DNA Molecules	1
1.1 Introduction	2
1.2 Statistical models for DNAs—polymer elasticity	5
1.2.1 The freely jointed chain (FJC) model	6
1.2.2 The worm-like chain (WLC) model	9
1.2.3 Beyond the entropic regime	10
1.2.4 Long-range electrostatic effects	11
1.3 Atomistic modeling of DNA molecules.....	12
1.3.1 MD basic theory	12
1.3.2 Force fields for nucleic acids	13
1.3.3 Limitations and challenges	14
1.3.4 MD simulation of DNA stretching.....	15
1.4 Continuum DNA models	17
1.4.1 Kirchhoff's elastic Rod model for DNAs	17
1.4.2 Finite element (FE) analysis of DNAs	20
1.4.3 Director field method for modeling of DNA viral packaging	22
1.5 Multiscale homogenization for simulation of DNA molecules	24
1.5.1 Basics of multiscale wavelet projection method	24
1.5.2 First-level homogenization—wavelet-based coarse-grained DNA model	28
1.5.3 Second-level homogenization—hyperelastic beam formulation for DNA	39
1.5.4 Applications	43
1.6 Conclusion.....	48
Appendix: Wavelet and decomposition coefficients for linear spline function	49
References	50
Chapter 2 Computational Contact Formulations for Soft Body Adhesion	55
2.1 Introduction	55
2.2 Continuum contact formulation.....	57

2.3	Finite element formulations	64
2.4	Adhesion examples	72
2.5	Peeling contact	79
2.6	Rough surface contact	83
2.7	Conclusion	87
	References	89
Chapter 3 Soft Matter Modeling of Biological Cells		95
3.1	Introduction	95
3.2	Soft matter modeling of cells	97
3.2.1	The future is soft	97
3.2.2	The reasons to use liquid crystal elastomers to model cell and focal adhesion	98
3.2.3	Elasticity of soft contact/cell adhesion and surface material property sensing	100
3.2.4	Cell and ECM modeling	101
3.3	A nanoscale adhesive contact model	105
3.4	Meshfree Galerkin formulation and the computational algorithm	107
3.5	Numerical simulations	109
3.5.1	Validation of the material models	109
3.5.2	Endothelial cell simulations	110
3.5.3	Stem cell simulations	113
3.6	Discussion and conclusions	114
	References	115
Chapter 4 Modeling the Mechanics of Semiflexible Biopolymer Networks: Non-affine Deformation and Presence of Long-range Correlations		119
4.1	Introduction	119
4.2	Network representation and generation	121
4.3	Affine vs. non-affine deformation	123
4.4	Network microstructure: scaling properties of the fiber density function	127
4.5	Network elasticity: the equivalent continuum and its elastic moduli	131
4.6	Boundary value problems on dense fiber network domains	132
4.6.1	Background: affine and non-affine theories	132
4.6.2	Karhunen – Loeve decomposition	136

4.6.3 Stochastic finite element formulation of 2D problems	137
4.7 Solution of boundary value problems on dense fiber network domains	139
References	141
Chapter 5 Atomic Scale Monte-Carlo Studies of Entropic Elasticity Properties of Polymer Chain Molecules	147
5.1 Introduction	147
5.2 Entropic elasticity of linear polymer molecules	148
5.2.1 Continuum limit	152
5.2.2 Monte–Carlo sampling	154
5.3 Summary	160
References	161
Chapter 6 Continuum Models of Stimuli-responsive Gels	165
6.1 Introduction	165
6.2 Nonequilibrium thermodynamics of neutral gels	166
6.3 A simple material model for neutral gels	171
6.4 Swelling of a spherical gel	174
6.5 Thermodynamics of polyelectrolyte gels	177
6.6 A material model for polyelectrolyte gels	182
6.7 Chemical reactions and pH-sensitive gels	186
6.8 Equilibrium models of polymeric gels	189
6.9 Summary	193
References	194
Chapter 7 Micromechanics of 3D Crystallized Protein Structures	197
7.1 Introduction	197
7.2 3D crystallized protein structures	198
7.3 Thermomechanical properties of protein crystals	199
7.4 A micromechanical model for protein crystals	200
7.5 Application to tetragonal lysozyme as a protein crystal model	202
7.5.1 Elastic deformation in lysozyme crystals	202
7.5.2 Plastic deformation in lysozyme crystals	203
7.5.3 Anisotropic plastic yielding of lysozyme crystals	205

7.5.4 Orientation effect on mechanical behavior of lysozyme crystals	206
References	210
Chapter 8 Micromechanical Modeling of Three-dimensional Open-cell Foams	213
8.1 Introduction	214
8.1.1 Unit cell models	215
8.1.2 Random cell models	217
8.2 Micromechanics model using a tetrakaidecahedral unit cell	218
8.2.1 Formulation	218
8.2.2 Numerical results	232
8.2.3 Summary	235
8.3 Random cell model incorporating cell shape and strut cross-sectional area irregularities	236
8.3.1 Analysis	236
8.3.2 Results and discussion	242
8.3.3 Summary	254
References	256
Chapter 9 Capillary Adhesion of Micro-beams and Plates: A Review	259
9.1 Introduction	259
9.2 Capillary adhesion of micro-beams of infinitesimal deformation	261
9.3 Capillary adhesion of micro-beams of finite deformation	264
9.4 Hierarchical structure of micro-beams induced by capillary force	268
9.5 Capillary adhesion of a plate	270
9.6 Conclusions	273
References	274
Color Plots	277

Contributors

Jiun-Shyan Chen

*Civil & Environmental Engineering Department, University of California,
USA*

Chung-Hao Lee

*Civil & Environmental Engineering Department, University of California,
USA*

Hailong Teng

Livermore Software Technology Company, California, USA

Hankui Wang

Mechanical Engineering Department, Tsinghua University, China

Roger A. Sauer

*Aachen Institute for Advanced Study in Computational Engineering Science
(AICES), RWTH Aachen University, Germany*

Xiaowei Zeng

*Department of Civil and Environmental Engineering, University of California,
USA*

Shaofan Li

*Department of Civil and Environmental Engineering, University of California,
USA*

Bo Ren

*Department of Civil and Environmental Engineering, University of California,
USA*

Hamed Hatami-Marbini

Mechanical Engineering Department, Stanford University, USA

Catalin R. Picu

*Department of Mechanical, Aerospace and Nuclear Engineering, Rensselaer
Polytechnic Institute, USA*

Eduard G. Karpov

Department of Civil & Materials Engineering, University of Illinois, USA

Mykhailo V. Grankin

Department of Civil & Materials Engineering, University of Illinois, USA

Wei Hong

Department of Aerospace Engineering, Iowa State University, USA

Amir Reza Zamiri

Advanced Computational Research Laboratory, Department of Mechanical, Aerospace and Nuclear Engineering, Rensselaer Polytechnic Institute, USA

Suvranu De

Advanced Computational Research Laboratory, Department of Mechanical, Aerospace and Nuclear Engineering, Rensselaer Polytechnic Institute, USA

Ke Li

Department of Mechanical and Industrial Engineering, Southern Illinois University, USA

Xin-Lin Gao

Department of Mechanical Engineering, Texas A&M University, USA

Jianlin Liu

Department of Engineering Mechanics, China University of Petroleum, Qingdao, China

Re Xia

Schoool of Power and Mechanical Engineering, Wuhan University, China

Chapter 1 Atomistic to Continuum Modeling of DNA Molecules

Jiun-Shyan Chen^{1,*}, Chung-Hao Lee¹, Hailong Teng²
and Hankui Wang³

¹*Civil & Environmental Engineering Department, University of California,
Los Angeles (UCLA), Los Angeles, California 90095, USA*

²*Livermore Software Technology Company (LSTC), Livermore, California
94551, USA*

³*Mechanical Engineering Department, Tsinghua University, Beijing,
People's Republic of China*

Abstract: DNA molecules play significant roles in many biological processes. Those biologically important processes involving DNA are accompanied by deformations of the double helix. Thus the mechanics of DNA have created interest in recent years as a result of the possibility of investigating DNA at individual molecule level. In this chapter, we first provide literature review of various mathematical models and computational framework for describing mechanical behavior of DNA molecules at different length scales, including the statistical models, atomistic models, and continuum models. We then introduce the recent advances in multiscale modeling of DNA molecules based on wavelet projection coarse graining approach and its homogenization into a hyperelastic beam. We show that with proper projection of the DNA fine scale potential functions and characterization of elasticity constants based on the coarsened DNA molecules, a continuum model with intrinsic molecular properties can be constructed for effective modeling of fundamental mechanical behavior in DNA molecules.

Keywords: DNA molecules, molecular dynamic simulation, wavelet projection method, hyperelasticity, multiscale method

*Corresponding author, E-mail: jschen@seas.ucla.edu.

1.1 Introduction

The mechanical properties of DNA have very important biological implications. For example, the bending and twisting rigidities of DNA affect how it packs and folds into chromosomes, bends upon interactions with proteins and packs into the confined space within a virus. Many biologically important processes involving DNA are accompanied by deformations of the double helix. Thus the mechanics of DNA have aroused interest in recent years in investigating DNA at individual molecule level. In the past decade, new methods of manipulating single molecules have offered researchers the opportunity to measure directly the forces generated in biochemical reactions and to exert external forces that alter the fate of these reactions.

DNA, or deoxyribonucleic acid, is basically a long relatively rigid polymer that contains coded instructions in the functioning of all known living organisms; it is the basic building block of life. Most DNAs are located in the cell nucleus. Hereditary information stored in DNA is encoded in the chemical language and reproduced in all cells of living organism.

DNA exists in several possible conformations in nature, referred to as A-DNA, B-DNA, and Z-DNA, whereas the most common DNA structure under the conditions found in cells is the B-DNA. A typical B-DNA molecule is a right-handed double helix with about 10.5 base pairs per helical turn, each of which has a pitch of 3.4 nm as shown in Fig. 1.1, consisting of a wide major groove and a narrow minor groove.

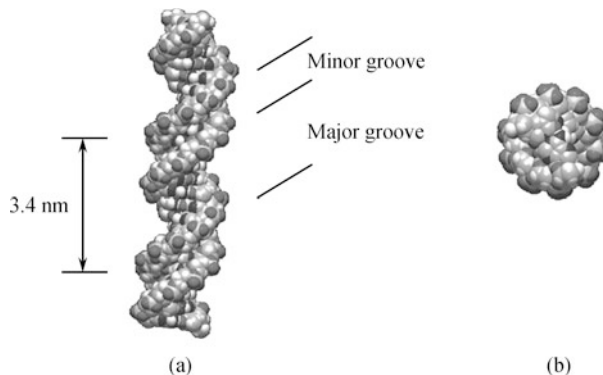


Fig. 1.1 Molecular structure of the double-stranded DNA molecule: (a) side view, (b) top view. (color plot at the end of the book)

The basic monomer units of DNA are called nucleotides. The nucleotide unit consists of a base, a deoxyribose sugar, and a phosphate. There are four types of bases: *adenine* (A), *thymine* (T), *guanine* (G), and *cytosine* (C). Among these four bases, adenine and guanine are purines, which are the larger

two types of bases found in DNA. Cytosine and thymine are pyrimidines. The structures of four bases are shown in Fig. 1.2.

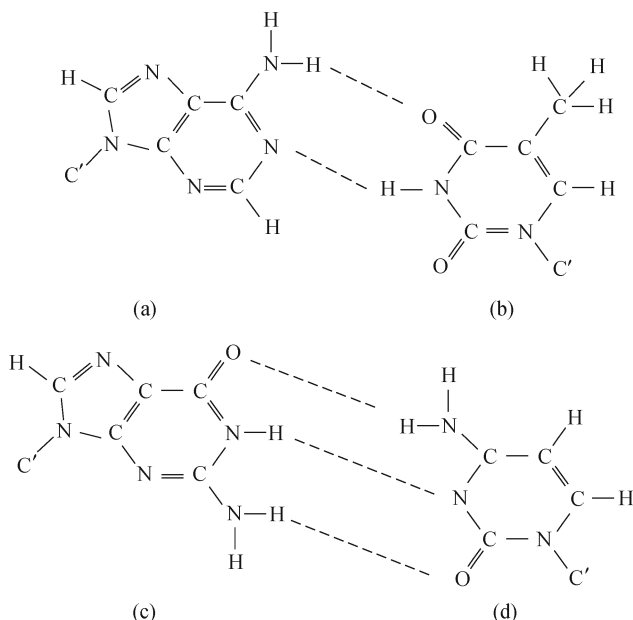


Fig. 1.2 Chemical structures of adenine (a), thymine (b), guanine (c), and cytosine (d).

The deoxyribose sugar of the DNA backbone has five carbon atoms and three oxygen atoms as shown in Fig. 1.3. The hydroxyl groups on the 5' and 3' carbons are linked to the phosphate groups to form the DNA backbone. DNA chains are made by connecting those nucleotides together via chemical bonds.

DNA normally is a double-stranded macromolecule. Double-stranded DNA is simply two chains of single-stranded DNA, positioned so that their bases can interact with each other. Two polynucleotide chains, held together by weak thermodynamic forces, form a DNA molecule as shown in Fig. 1.4. Within the DNA double helix, A forms two hydrogen bonds with T on the opposite strand, and G forms three hydrogen bonds with C on the opposite strand. The base pairs dA – dT and dG – dC have the same length and occupy the same space within a DNA double helix. Therefore the DNA molecule has a uniform diameter.

Many researchers have performed experimental study of the elastic behavior of dsDNA using different mechanical forces, for example, magnetic beads^[1], hydrodynamic drag^[2], glass micro-needles^[3], atomic force microscopy^[4], and optical traps^[5].

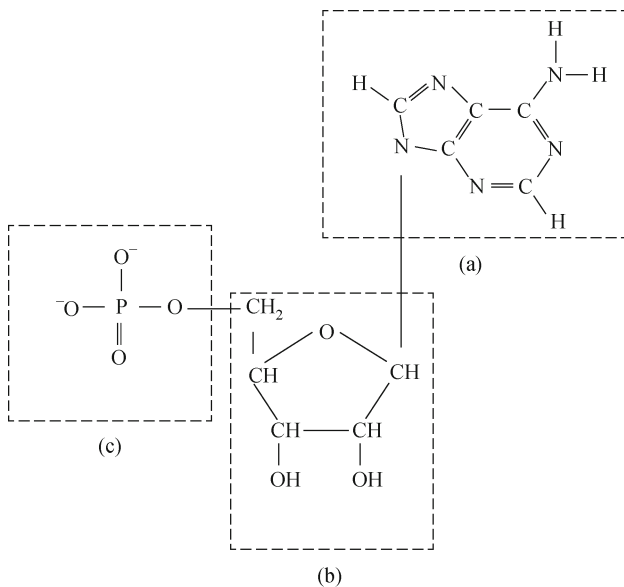


Fig. 1.3 Chemical structures of nucleotide, including (a) nitrogen base (adenine), (b) sugar, and (c) phosphate group.

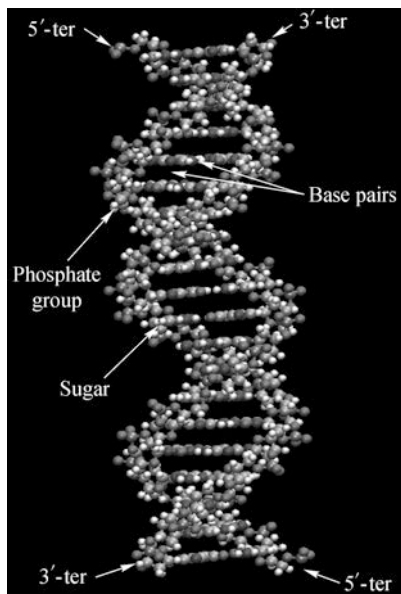


Fig. 1.4 Double helical structure of the dsDNA molecule. (color plot at the end of the book)

In 1992, Smith et al.^[1] chemically attached one end of a single DNA molecule to a glass surface and another end to a magnetic bead. The bead was subjected to magnetic and hydrodynamic forces. By observing the equilibrium positions of the bead, extension versus force curves could be obtained as shown in Fig. 1.7. This early work opened a route for mechanical study on individual molecules, followed by Cluzel et al. ^[3], Smith et al. ^[5], Leger and Chatenay ^[6], and Clausen-Schaumann and Gaub ^[4] with enhanced experimental techniques.

These research groups found that with little force, the molecule could be stretched to its contour length in accordance with predictions from the Worm Like Chain (WLC) model, which will be introduced in Section 1.2.2 and then extended elastically. By a force of around 65 pN, a plateau appeared in the force-extension curve, causing the DNA molecule to increase in length to roughly 1.7 times the normal contour length while roughly maintaining the same force. Beyond this point, further extension led to a rapid increase in force and rupturing of the molecule construction as shown in Fig. 1.5.

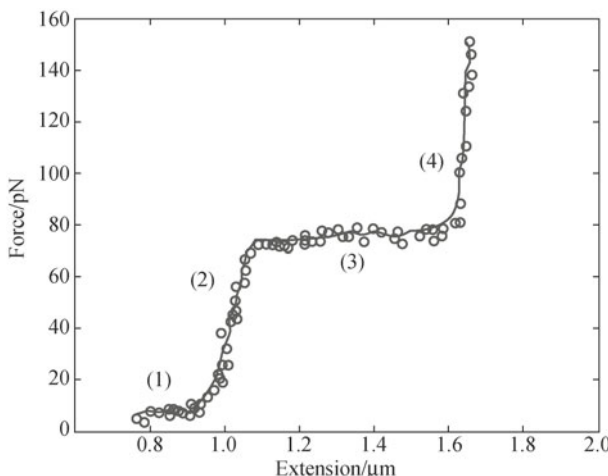


Fig. 1.5 Typical force-extension behavior of the dsDNA molecule (experimental data extracted from [5]): (1) entropic elasticity regime, (2) intrinsic elasticity regime, (3) overstretching transition, and (4) breaking covalent bonds.

1.2 Statistical models for DNAs—polymer elasticity

As discussed in the previous section, under the low-force extension (smaller than 10 pN), the double-stranded DNA (dsDNA) in solution bends and curves as a result of thermal fluctuations. Such fluctuations shorten the end-to-end

distance of the molecule and has the tendency to maximize the disorder (entropy) of the molecule. The fluctuations are purely entropic and can be described by the two simple polymer elasticity models: the freely jointed chain (FJC) model and the worm-like chain (WLC) model. With intermediate and large forces, the WLC model represents DNA behavior much better than the FJC model compared with the experimental measurements. However, modification of these intrinsic elasticity models is needed at the large-force stretching level due to enthalpic effects. In this section, the fundamentals of both the FJC and WLC models are reviewed, followed by the presentation of the extensible WLC model and some modified models accounting for the overstretching transition and long-range electrostatic interactions.

1.2.1 The freely jointed chain (FJC) model

Flory's freely jointed chain (FJC) model^[7] serves as the basis of many single polymer theories. This model treats the polymer as a chain of N statistically independent successive rigid segments, known as Kuhn segments, jointed by perfectly flexible hinges as depicted in Fig. 1.6. Each segment has a fixed length b (also called the Kuhn length), which is a measure of chain stiffness, and its orientation is assumed to be completely uncorrelated in the sense that the polymer segment has no preferred orientation. In the absence of an external force, all configurations have equal energy and the chain displays the characteristics of a random walk. To pull the ends of such a chain away from each other, external forces need to be applied which lead to the reduction of the entropy.

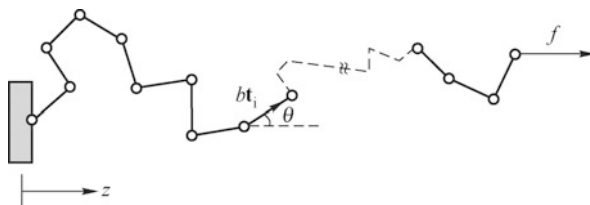


Fig. 1.6 The freely jointed chain consists of identical segments of length b , jointed by perfectly flexible hinges with the external force f applied in the z direction. The polymer configuration is described by the orientation vectors \mathbf{t}_i and angle θ between the i th segment and the applied force direction^[7].

In the FJC model, the probability that the segment is oriented along the angle θ with respect to the applied force is given as^[8]

$$p(\theta) = C \exp \left(-\frac{V}{k_B T} \right) = C \exp \left(\frac{fb \cos \theta}{k_B T} \right) \quad (1.1)$$

where $V = fb \cos \theta$ is the potential energy acquired by a segment aligned along the direction θ with an external force, C is a normalization constant, and k_B and T are the Boltzmann constant (1.381×10^{-23} J/K) and absolute temperature, respectively.

The average angular orientation of the polymer can therefore be expressed by

$$\langle \cos \theta \rangle = \frac{\int_0^\pi p(\theta) \cos \theta 2\pi \sin \theta d\theta}{\int_0^\pi p(\theta) 2\pi \sin \theta d\theta} \quad (1.2)$$

where the bracket denotes the average operation over all the possible orientations. Carrying out the integration leads to an analytical expression describing the entropic elastic behavior

$$\left\langle \frac{l}{L_{\text{contour}}} \right\rangle = \coth \left(\frac{fb}{k_B T} \right) - \frac{k_B T}{fb} \equiv \mathcal{L} \left(\frac{fb}{k_B T} \right) \quad (1.3)$$

where l and $L_{\text{contour}} = Nb$ are the end-to-end distance and the contour length of the polymer, respectively, and \mathcal{L} is the Langevin function.

The above expression can be inverted to yield the following force-extension relation

$$f = \frac{k_B T}{b} \mathcal{L}^{-1} (\langle l/L_{\text{contour}} \rangle) \quad (1.4)$$

where \mathcal{L}^{-1} is the inverse Langevin function. The Langevin and inverse Langevin functions can be approximated by the following series forms:

$$\begin{aligned} \mathcal{L} &\approx \frac{1}{3}x - \frac{1}{45}x^3 + \frac{2}{945}x^5 - \frac{1}{4725}x^7 + \dots \\ \mathcal{L}^{-1} &\approx 3x + \frac{9}{5}x^3 + \frac{297}{175}x^5 + \frac{1539}{875}x^7 + \dots \end{aligned} \quad (1.5)$$

The typical force-extension curve obtained by the FJC model is illustrated in Fig. 1.7. At low-force extension ($l \ll L_{\text{contour}}$), Eq. (1.4) is reduced to the linear Hooke-law behavior by

$$f = \frac{3k_B T}{b} \left\langle \frac{l}{L_{\text{contour}}} \right\rangle = k_{sp} \left\langle \frac{l}{L_{\text{contour}}} \right\rangle \quad (1.6)$$

where $k_{sp} = 3k_B T/b = 3k_B T/2P$ is the effective Hookian spring constant of the polymer for the FJC model, and P is the persistence length of the chain which defines the chain stiffness. The proportionality of the effective spring constant to the absolute temperature only explains that the elastic behavior of this model is purely entropic.

On the other hand, with the high stretching force, Eq. (1.3) yields $\langle l/L_{\text{contour}} \rangle \rightarrow 1$, which means that all the links of the chain are aligned

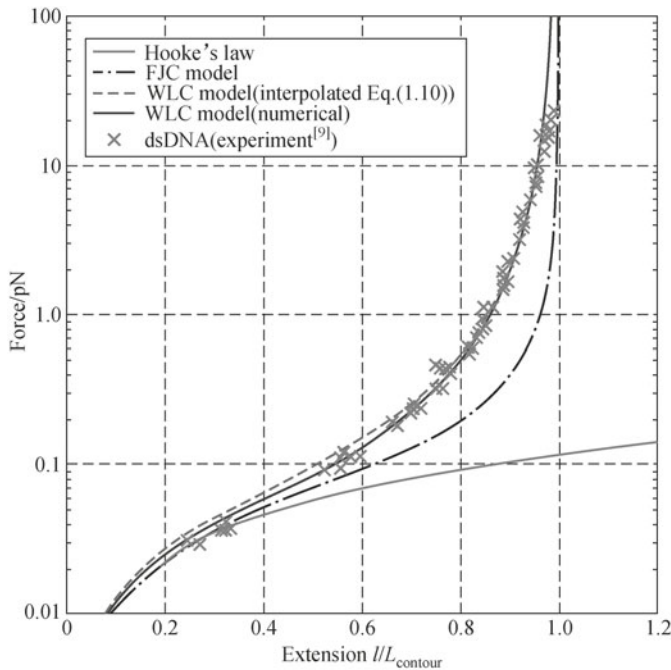


Fig. 1.7 Force versus extension experimental data taken from [1] for λ phage DNA pulled by magnetic beads in 10 mM Na^+ buffer. The data are fit for a WLC model solved numerically (WLC exact, *solid line*), using Eq. (1.10) (WLC interpolated, *dash line*), both assuming the persistence length $P = 53 \text{ nm}$. The FJC curve (*dotted-dash line*) assumes $b = 2P = 106 \text{ nm}$ from Eq. (1.4). The Hooke's law force curve (*solid line with circle*) for the low-force extension is from Eq. (1.6)^[1]. (color plot at the end of the book)

in the same direction as that of the external force. However, the individual segments are slightly extensible in reality while they are inextensible and completely straight in this model. As shown in Fig. 1.8, no thermal fluctuations away from the straight line are allowed and the polymer disorder is

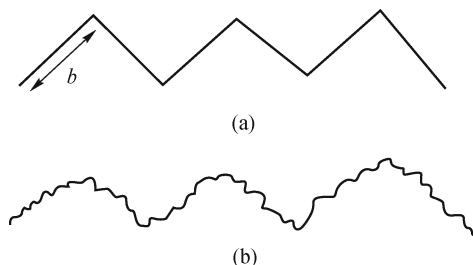


Fig. 1.8 Illustration of the lack description of thermal fluctuation for the FJC model^[10]: (a) idealized freely jointed chain, (b) realistic polymer chain.

restricted at the joints between segments. Therefore, the FJC model can only describe the behavior of dsDNA in the limit of low forces (< 0.1 pN) and is not accurate for DNA molecule with intermediate and large forces.

1.2.2 The worm-like chain (WLC) model

A much more precise description of the elastic behavior of dsDNA with low and intermediate stretching forces is the worm-like chain (WLC) model^[1,11,12] which envisions an isotropic flexible rod that takes bending energy into consideration. This model is also called the Kratky–Porod model^[11] whose configuration can be described by the position vector $\mathbf{r}(S)$ as a function of the relaxed-state contour length S . As shown in Fig. 1.9, the local tangent vector and curvature (\mathbf{t} and \mathbf{k} , respectively) can be defined by

$$\mathbf{t}(S) = \frac{d\mathbf{r}(S)}{dS}, \quad \mathbf{k}(S) = \frac{d\mathbf{t}(S)}{dS} = \frac{d^2\mathbf{r}(S)}{dS^2}. \quad (1.7)$$

Then, by the applied external force f , the energy of the WLC model can be written as follows:

$$\frac{E_{\text{WLC}}}{k_B T} = \frac{P}{2} \int_0^L \left(\frac{dt}{dS} \right)^2 dS - f \int_0^L (\mathbf{t} \cdot \mathbf{z})^2 dS \quad (1.8)$$

where \mathbf{z} is the unit vector in the z direction and P is the persistence length of the chain that is the characteristic length associated with the decay of tangent-tangent correlations with zero stretching force:

$$\langle \mathbf{t}(0) \cdot \mathbf{t}(S) \rangle = \langle \cos \theta(S) \rangle = \exp \left(-\frac{S}{P} \right) \quad (1.9)$$

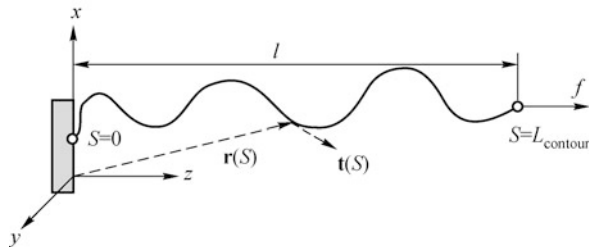


Fig. 1.9 Worm-like chain model as a continuum elastic rod subjected to an external force^[11].

The force-extension relation, which relies on the calculation of the partition function and the free energy of this inextensible WLC model, must be obtained numerically. Although there is no analytical formula equivalent to

Eq. (1.4) for the force-extension curve of a WLC, an interpolation formula was given by Bustamante et al.^[13]:

$$\frac{fP}{k_B T} = x + \frac{1}{4(1-x)^2} - \frac{1}{4} \quad (1.10)$$

where $x = l/L_{\text{contour}}$ defines the end-to-end distance extension. The above interpolation formula approaches to the exact solution as $l \rightarrow 0$ or $l \rightarrow L_{\text{contour}}$, but produces 5%—10% error in-between. Subsequently, an enhanced interpolation formula by Bouchiat et al.^[14] based on Eq. (1.10) with 0.1% error is:

$$\frac{fP}{k_B T} = x + \frac{1}{4(1-x)^2} - \frac{1}{4} + \sum_{i=2}^7 a_i x^i \quad (1.11)$$

with $a_2 = -0.516\ 422\ 8$, $a_3 = -2.737\ 418$, $a_4 = 16.074\ 97$, $a_5 = -38.876\ 07$, $a_6 = 39.499\ 44$, and $a_7 = -14.177\ 18$.

The force versus extension relations of a WLC model by both exact numerical calculation and approximate interpolation formula is shown in Fig. 1.7. As observed from Fig. 1.7, the FJC model works well only at small-force stretching, whereas the WLC model provides a good description of the whole entropic extension in the limit of 10 pN. Beyond this 10 pN entropic limit, the DNA molecule displays a linear stretching behavior due to enthalpic effects. This linear stretching behavior can be described by taking the enthalpic correction into account and will be discussed in Section 1.2.3.

1.2.3 Beyond the entropic regime

Beyond the entropic regime, i.e., from 5 pN to about 50 pN, there is distinct deviation from the WCL model and experimental data as shown in Fig. 1.7. Indeed, the end-to-end distance becomes much longer than its theoretical B-form DNA contour length. Therefore, with these large forces, the DNA molecule undergoes a chemical structure change and the behavior is not purely entropic but intrinsic elasticity. From the experimental observations^[5,15], due to the enthalpic effect, the DNA behaves like an elastic stretchable solid with the stretch modulus K_0 ranging from 500 pN to 1 500 pN which covers the existing experimental measurements^[5,14], and the force-extension relation can be approximated by using the extensible worm-like chain model as given in the following equation^[15,16]:

$$x = 1 - \frac{1}{2} \left(\frac{k_B T}{fP} \right)^{\frac{1}{2}} + \frac{f}{K_0} \quad (1.12)$$

where the stretch modulus of a simple elastic rod with radius a is related to its intrinsic persistence length P_i as follows:

$$P_i = \frac{K_0 a^2}{4kBT}. \quad (1.13)$$

If assuming the dsDNA radius a is 1 nm, an intrinsic persistence length of 60 nm is obtained which is in good agreement with the value determined from the entropic elasticity model^[5].

When the applied external force is larger than 65 pN, the dsDNA molecule undergoes a sudden conformational change from its ordinary B-form to S-form^[5,17]. In this B-to-S overstretching transition, the DNA molecule stretches to about 1.7 times its canonical B-form contour length within a narrow range of forces, indicating a high level of cooperativity. Storm and Nelson^[17] proposed a discrete persistent chain (DPC) model, which borrows the essential ideas from the FJC and WLC models, for describing the large force stretching and overstretching of DNA molecule. This model takes the conformational change transition into consideration by using a two-state Ising model, one state for the B-form DNA and the other for the S-form DNA. The least-squares fit of the Ising-DPC model to the overstretching experimental data exhibits reasonable agreement in the large force stretching and overstretching regions.

1.2.4 Long-range electrostatic effects

Ions play significant roles in the bending rigidity of DNA molecule in many biological processes, for example, DNA replication, RNA transcription, chromosome formation, and viral packaging. From the experimental observation^[18], the lowering of ionic strength increases the measured persistence length, but reduces the stretch modulus K_0 . However, as a WLC type polymer, the increase of the intrinsic persistence length P_i of DNA molecule will increase the effective stretch modulus K_0 as illustrated in Eq. (1.13) which contradicts the experimental measurements. This is one of the major limitations of this elastic rod model for describing the behavior of DNA molecules.

In order to account for the long-range electrostatic interactions due to ionic effects, the following approximation of the screen Debey–Hückel potential^[19,20] can be introduced into the energy expression of the WLC model in Eq. (1.8)

$$\frac{E_{\text{elec-stat}}}{k_B T} = \frac{\nu^2}{\varepsilon_w} \int_0^L ds \int_0^L dS' \frac{\exp(-\kappa|\mathbf{r}(S) - \mathbf{r}(S')|)}{|\mathbf{r}(S) - \mathbf{r}(S')|} \quad (1.14)$$

where $\varepsilon_w = 80$ is the dielectric constant of water, κ is the inverse Debey–Hückel length, and ν is the number of effective electron charges density of DNA. With this modification, the measured persistence length is consistent with the above electrostatic contribution for DNA molecules in monovalent salt (Na^+ , for example). However, with multivalent ions like $\text{MgCl}_2^{[21]}$, the measured persistence lengths are about 25–30 nm which is shorter than the intrinsic persistence length calculated from the WLC model, and this model is no longer appropriate to determining the bending rigidity (persistence length) of the DNA molecules.

In addition to the analytic approaches based on statistical mechanics to investigate the bio-mechanical properties of DNA molecules, computational modeling and simulations provide alternative means to probe the micromanipulation of single DNA molecules, such as overstretching of the DNA induced by external forces, to qualitatively examine the interactions between DNA and proteins, for example, the DNA loop formation due to protein binding in *E. coli*, and to quantitatively study the portal force exerted during the process of DNA being packaged into a virus capsid. The molecular dynamics (MD) method, the continuum modeling approaches, and the multiscale simulation techniques will be introduced in the subsequent sections.

1.3 Atomistic modeling of DNA molecules

One of the important tools in the study of biological molecules is the method of molecular dynamics (MD). Molecular dynamics is a numerical technique for computing the equilibrium and transport characteristics of a many-body atomic system^[22]. It was first introduced by Alder and Wainwright in the late 1950s^[23–25] to study the interactions of hard spheres, and was applied to studying protein in 1970s^[26] and nucleic acids in the mid-1980s^[27]. In molecular dynamics, each atom is treated as a point that carries mass, and a force field is utilized to describe the interactions between atoms. The motions and the time evolution of a set of interacting atoms are obtained by integrating the equations of motion of atoms in time. The thermodynamic statistics are then extracted from the motion of the atoms. The MD method used for the nucleic acids simulation will be introduced in this section.

1.3.1 MD basic theory

The molecular dynamics method is based on the classical Newton's second law, or the equation of motion. These equations may be written in various

ways. The most fundamental form is the Lagrangian equation of motion.

$$\frac{d}{dt} \left(\frac{\partial L}{\partial \dot{q}_k} \right) - \frac{\partial L}{\partial q_k} = 0 \quad (1.15)$$

where q_k are the generalized coordinates, and the Lagrangian function $L = K - V$. $K = \sum \frac{1}{2} m_i \dot{q}_i^2$ is the kinetic energy, and V is the potential to be described in the next section.

If Cartesian coordinates are used, Eq. (1.15) leads to the Newton's law as follows:

$$m_i \ddot{\mathbf{r}}_i = \mathbf{F}_i \quad (1.16)$$

where m_i is the mass of the atoms, \mathbf{r}_i is the position vector of atom i , and \mathbf{F}_i is the force acting on atom i , which is obtained by the gradient of the potential with respect to the atomic position:

$$\mathbf{F}_i = -\nabla_{\mathbf{r}_i} V. \quad (1.17)$$

One of the most popular time integration methods in MD simulations is the velocity Verlet method with second order accuracy and energy conservation:

$$\begin{aligned} \mathbf{r}_i(t + \Delta t) &= \mathbf{r}_i(t) + \mathbf{v}_i(t) \Delta t + \frac{1}{2} \mathbf{a}_i(t) \Delta t^2, \\ \mathbf{v}_i \left(t + \frac{1}{2} \Delta t \right) &= \mathbf{v}_i(t) + \frac{1}{2} \mathbf{a}_i(t) \Delta t, \\ \mathbf{a}_i(t + \Delta t) &= -\frac{1}{m_i} \frac{\partial V(\mathbf{r}_i(t + \Delta t))}{\partial \mathbf{r}_i}, \\ \mathbf{v}_i(t + \Delta t) &= \mathbf{v}_i \left(t + \frac{1}{2} \Delta t \right) + \frac{1}{2} \mathbf{a}_i(t + \Delta t) \Delta t. \end{aligned} \quad (1.18)$$

1.3.2 Force fields for nucleic acids

The force field is the most important part in the MD simulation, which is used to describe the interaction between atoms. Although the force field can be obtained from quantum mechanics calculation^[28], due to its computational intensity, most of the MD simulations are carried out by empirical force fields or by combined quantum and molecular mechanics^[29].

Many empirical force fields have been proposed for the nucleic acid simulations, such as AMBER, CHARMM, BSM, and OPLS. Two of the most widely used force fields for bio-molecules are AMBER, which was developed by Peter Kollman's group at the University of California, San Francisco^[30]

and CHARMM at Harvard University^[31]. With AMBER, AMBER94 and AMBER99 are most suitable for the representation of nucleic acids in long-time simulations^[32].

The potential energy function of AMBER is given as

$$\begin{aligned} V = & \sum_{\text{bonds}} k_b(r_{ij} - r_{\text{eq}})^2 + \sum_{\text{angles}} k_\theta(\theta - \theta_{\text{eq}})^2 \\ & + \sum_{\text{dihedrals}} \sum_n \frac{1}{2} K_n [1 + \cos(n\phi - \gamma)] \\ & + \sum_i \sum_{j>i} 4\varepsilon_{ij} \left[\left(\frac{\sigma_{ij}}{r_{ij}} \right)^{12} - \left(\frac{\sigma_{ij}}{r_{ij}} \right)^6 \right] + \sum_i \sum_{j>i} \frac{q_i q_j}{\epsilon r_{ij}}. \end{aligned} \quad (1.19)$$

The first three terms are used to describe the chemical bond connections and the last two terms are used to describe the non-bonded interactions including the van der Waals interaction and Coulomb interaction. The parameter k_b is the bond stretching constant, k_θ is the bond angle constant, $r_{ij} = |\mathbf{r}_i - \mathbf{r}_j|$ is the distance between atoms i and j , θ is the angle between two adjacent bonds, r_{eq} and θ_{eq} are the bond equilibrium distance and bond equilibrium angle, respectively, ϕ is the torsional angle, γ is the phase angle, K_n is the torsional rotation force constant, and n is the multiplicity. For the van der Waals interaction between atom i and atom j , ε_{ij} is the depth of the van der Waals well, and σ_{ij} is the van der Waals diameter. For the Coulomb interaction, q is the charge of the atom and ϵ is the dielectric constant.

One of the most important advances in the DNA simulations is the approximation of long-range interactions such as the Coulomb force. The potential function of the Coulomb interaction is in inverse proportion to the atomic distance r_{ij} . The traditional cut-off long-range interactions could induce artificial errors, while accurate calculation of all the long-range interactions is extremely time-consuming. Some methods have been introduced to address this issue, such as PPPM^[33] and PME^[34].

1.3.3 Limitations and challenges

The time and size limitations are the most severe restrictions in the applications of MD. Typical MD simulations can be performed on systems containing thousands or millions of atoms and for simulation time ranging from a few picoseconds to hundreds of nanoseconds, too short to follow many important biological processes. A simulation is reliable when the simulation time is much longer than the relaxation time of the quantities of interest. For example, the whole chain relaxation of a single polymer chain may take milliseconds or even seconds, whereas protein folding may take minutes. However, the pres-

ence of significantly fast bond vibrations limits the time step in numerical integration to about one femtosecond. Thus, the corresponding number of time steps required may exceed hundreds of billions! Explicit/implicit^[35] or entirely implicit models^[36] have been proposed with limited success.

Complicated force fields for bio-systems like AMBER^[30], CHARMM^[31], and GROMACS^[37] are often used, which call for more demanding force evaluations. Many alternative strategies and extensions of molecular dynamics, such as coarsegrained simulations, are being explored to study slow conformational changes and activated processes. Moreover, many biologically important processes involve quantum effects such as changes in chemical bonding, the presence of important noncovalent intermediates and tunneling of protons or electrons. Oxygen binding to hemoglobin, catalytic cleavage of the peptide bond by chymotrypsin and the lightinduced charge transfer in the photosynthetic reaction center are well-known examples^[38]. Classical molecular dynamics cannot be used to model such phenomena, because a quantum mechanical description is necessary to capture the chemistry of the species involved.

1.3.4 MD simulation of DNA stretching

In this section, we perform the molecular dynamics simulation of a representative segment of DNA molecule. The MD simulation is carried out using GROMACS (GROningen MAchine for Chemical Simulations)^[37] which is a general purpose serial and parallel molecular dynamics simulation package originally developed in University of Groningen. GROMACS is primarily designed for computational chemistry and molecular simulations of bio-chemical molecules such as nucleic acids, proteins, and lipids, which have many bonded and non-bonded interactions. The time integration algorithm adopted is the velocity Verlet scheme with a time step of 1 fs. The AMBER99 force field developed specifically for biomolecules is employed (see also Eq. (1.19)).

The DNA model is composed of regularly repeating base sequences of poly d(CTCGGCTATTAATAGCCGAG) which contains 1 268 atoms with 20 base pairs, and the initial conformation of the dsDNA molecule is obtained from the PDB (Protein Data Bank) 1C7U file, whereas the protein molecule is removed from the original PDB file for demonstration purpose. After energy minimization of the DNA segment, the DNA molecule is solvated with 2 486 water molecules and neutralized by inserting 43 sodium ions (Na^+) and 5 chloride ions (Cl^-) in the simulation box with dimensions of $6.5 \text{ nm} \times 6.5 \text{ nm} \times 20 \text{ nm}$, which leads to the simulation system of 8 774 atoms in total.

The solvated DNA system is then gradually heated to 310 K and equi-

librated under NVT ensemble for 100 ps. The van der Waals interactions are computed with the cutoff distance of 1.1 nm, and the long-range electrostatic forces are calculated more accurately using Particle Mesh Edward (PME) method^[39]. Stretching of the DNA is achieved by imposing a length restraint between the terminal phosphorus atoms as indicated in Fig. 11a. We first impose a slight length increase on DNA molecule and then perform energy minimization. This allows the DNA to be stretched gradually in equilibrium. At each incremental step, the potential energy surface and the force-extension curve are obtained as shown in Fig. 10a and b, respectively.

This force-extension curve can be divided into three distinct regions. In the region before the force reaches around 65 pN, the behavior is essentially linear. When the molecule is subjected to forces of about 65 pN, a sudden increase in the length to stretch ratio of about 1.7 occurs. This overstretching transition occurs within a narrow range of forces (see the plateau in Fig. 1.10b), suggesting a conformational change of the molecular structure. Further stretching of the DNA yields a significant increase in stiffness.

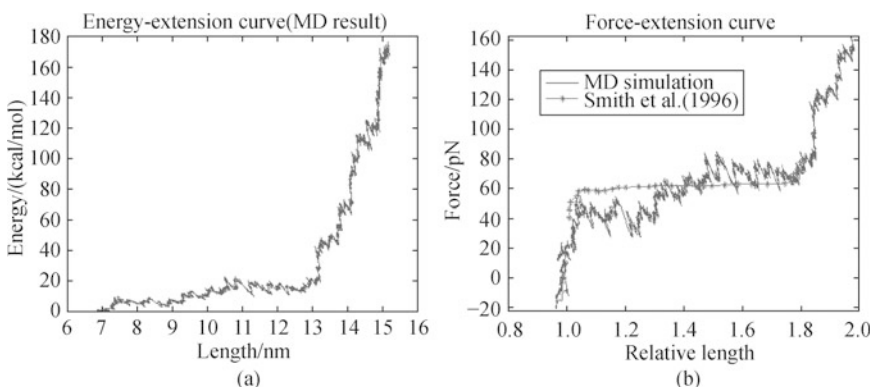


Fig. 1.10 MD simulation results of stretching dsDNA: (a) Energy versus relative length curve, and (b) Force versus relative length curves (MD simulation in blue and experiment by Smith in red cross^[5]).

Figure 1.11 reveals the progressive deformed configurations of the DNA during the stretching process. It shows that during the DNA stretching, the dsDNA is unzipped and leads to significant molecular structural change. A novel ladder form is observed in the simulation which corresponds to the overstretching transition region also depicted in Fig. 1.11 and is consistent with the experimental observations^[3,5].

This example demonstrates the ability of MD simulation in modeling the mechanical and bio-chemical properties of DNAs. Nevertheless, the computational demand becomes unaffordable when applying MD simulation to biologically meaningful molecular systems involving millions of atoms with

simulation time up to milliseconds. In the following sections, we will introduce two types of methods to achieve this goal, the coarse-grained models, continuum models and multiscale simulation methods.

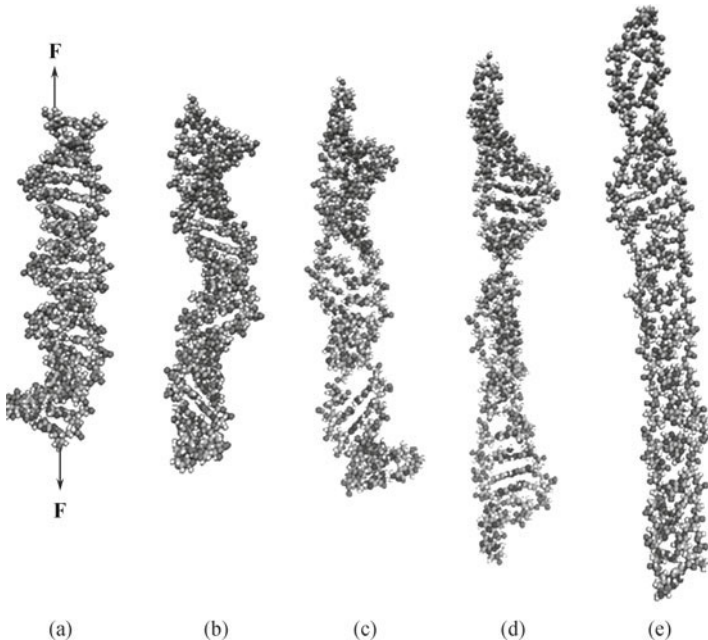


Fig. 1.11 Conformational changes of DNA molecule during the stretching process: (a) initial, (b) 10 ps, (c) 20 ps, (d) 40 ps, (e) 60 ps. (color plot at the end of the book)

1.4 Continuum DNA models

Due to the temporal and spatial constraints of MD for DNA modeling, coarse-grained and continuum models have been proposed to allow the study of events that occur in milliseconds and at the micron level. We first introduce a continuum model in this section, and present multiscale coarse-grained approaches in Section 1.5. In this section, the representation of DNA molecule using an elastic rod model based on the Kirchhoff's theory^[40] is first introduced, followed by the director field approach^[41,42].

1.4.1 Kirchhoff's elastic Rod model for DNAs

A thin rod can be described by a smooth curve C in the three-dimensional

space parameterized by the arc-length parameter S . Let the configuration of a rod be constructed by a continuous family of orthonormal triad $\{\mathbf{e}_i(S)\}$ (\mathbf{e}_1 = normal, \mathbf{e}_2 = binormal, \mathbf{e}_3 = tangent) as depicted in Fig. 1.12, with the origins of the frames located at the line of centroid of the rod Γ_t .

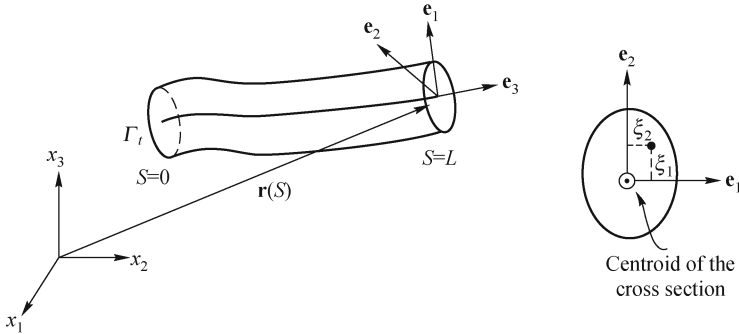


Fig. 1.12 Geometric representation of 3D elastic rod model.

The material point at any location of the cross section (on the \mathbf{e}_1 - \mathbf{e}_2 plane) is defined by means of the triplet $\{\xi_\alpha, S\}$, where S represents the cross section by the parametric coordinate of this material point location, and $\{\xi_\alpha\}$ determines the position vector of the point away from the centroid in a cross section.

Consider the general mapping describing the deformation of the rod as

$$x_i = \varphi_i(\mathbf{X}, t) \quad (i = 1, 2, 3) \quad (1.20)$$

where x_i and X_i are the coordinates of a material point in the deformed and undeformed configurations, respectively, and φ is the deformation mapping function.

Let the centerline of the deformed configuration Γ_t be parameterized by S as

$$I_i : \quad x_i = \varphi_i|_{\xi_\alpha=0} = r_i(S, t) \quad (\alpha = 1, 2). \quad (1.21)$$

The deformation of a material point on the cross section (ξ_1, ξ_2) of the rod can be expressed by

$$x_i = \varphi_i = r_i(S, t) + \xi_\alpha e_{i\alpha}(S, t) \quad (1.22)$$

or in the following vector notation

$$\mathbf{x} = \varphi = \mathbf{r}(S, t) + \xi_1 \mathbf{e}_1(S, t) + \xi_2 \mathbf{e}_2(S, t). \quad (1.23)$$

The partial derivatives of the orthonormal triad $\{\mathbf{e}_i(S)\}$ with respect to the space S and time t are

$$\mathbf{e}'_i(S, t) \equiv \frac{\partial \mathbf{e}_i(S, t)}{\partial S} = \mathbf{k}(S, t) \times \mathbf{e}_i(S, t) = \mathbf{K}(S, t) \cdot \mathbf{e}_i(S, t), \quad (1.24)$$

$$\dot{\mathbf{e}}_i(S, t) \equiv \frac{\partial \mathbf{e}_i(S, t)}{\partial t} = \boldsymbol{\omega}(S, t) \times \mathbf{e}_i(S, t) = \mathbf{W}(S, t) \cdot \mathbf{e}_i(S, t) \quad (1.25)$$

where the strain vector $\mathbf{k}(S, t) = k_i(S, t)\mathbf{e}_i$ contains the centerline curvature components projected onto the triad basis vector in the cross sections $k_1(S, t)$ and $k_2(S, t)$, and the local twist $k_3(S, t)$ of the rod. $\boldsymbol{\omega}(S, t) = \omega_i(S, t)\mathbf{e}_i$ is the angular velocity vector.

The Kirchhoff's thin rod theory assumes that the rod is inextensible and unshearable. Therefore, the tangent to the centerline, $\mathbf{r}'(S, t)$, is always parallel to \mathbf{e}_3 , i.e.,

$$\mathbf{r}' = \frac{\partial \mathbf{r}}{\partial S} = \mathbf{e}_3, \quad |\mathbf{r}'| = 1. \quad (1.26)$$

And the strain vector \mathbf{k} can be related to the derivatives of the rotations $\boldsymbol{\vartheta} = [\theta, \phi, \psi]^T$ by

$$\mathbf{k} - \mathbf{k}^0 = [k_1 - k_1^0, k_2 - k_2^0, \omega - \omega^0]^T = [\theta', \phi', \psi']^T \quad (1.27)$$

where k_1^0, k_2^0 , and ω^0 are the initial curvatures and the initial twist of the rod, respectively.

For an isotropic material with homogeneous circular cross sections, the moment vector can be written as

$$\mathbf{M} = A_1(k_1 - k_1^0)\mathbf{e}_1 + A_2(k_2 - k_2^0)\mathbf{e}_2 + C(\omega - \omega^0)\mathbf{e}_3 \quad (1.28)$$

where $A_1 = EI_1$ and $A_2 = EI_2$ are the bending rigidities along the 1, 2 direction, respectively, $C = GJ$ is the torsional rigidity. E and G are the Young's and shear modulus, respectively, I_1, I_2 , and J are the moment of inertia and the polar moment of inertia, respectively. Equation.(1.28) implies that the strain energy of the elastic rod has the following quadratic form:

$$W^{\text{elastic-Kirchhoff}} = \frac{1}{2} \int_0^L A_1(k_1 - k_1^0)^2 + A_2(k_2 - k_2^0)^2 + C(\omega - \omega^0)^2 dS \quad (1.29)$$

and the work done by the external loading can be expressed by

$$\begin{aligned} W^{\text{ext}} = & \int_0^L \bar{\mathbf{N}} \cdot (\mathbf{r} - \mathbf{R}_0) + \bar{\mathbf{M}} \cdot (\mathbf{k} - \mathbf{k}^0) dS \\ & + \sum_{i=1}^n [\mathbf{T}(S_i) \cdot (\mathbf{k}(S_i) - \mathbf{k}^0) + \mathbf{P}(S_i) \cdot (\mathbf{r}(S_i) - \mathbf{R}_0(S_i))] \end{aligned} \quad (1.30)$$

where \mathbf{R}_0 is the position vector of the centerline of the cross section in the undeformed configuration, \mathbf{k}^0 is the intrinsic strain vector describing the initial geometry of the rod, $\bar{\mathbf{N}}$ and $\bar{\mathbf{M}}$ are distributed force and moment, respectively, $\mathbf{T}(S_i)$ and $\mathbf{P}(S_i)$ are concentrated moment and force, respectively, acting on the cross section S_i . Given appropriate boundary conditions and prescribed

loading conditions, the configuration of the rod in equilibrium can be obtained by minimizing the total potential energy $\Pi = W^{\text{elastic-Kirchhoff}} - W^{\text{ext}}$.

Many researchers have successfully applied the above-mentioned Kirchhoff's thin rod theory to the studies of DNA molecules. For example, Wadati and Tsuru^[43] facilitated a combination of topology and energetics for describing the looped DNA. Westcott et al.^[44] employed the elastic rod model to model DNAs, and included the base sequence effects in each element. Purohit and Nelson^[45] investigated the supercoiling effect on the protein-mediated DNA loops via the elastic rod model, and calculated the DNA contour lengths with three different levels of DNA supercoiling. Balaeff et al.^[18,46,47] used the elastic rod model to examine the DNA loop formation during the interaction with the *lac* repressor protein in *E. coli*. This model has been applied to multiscale studies of protein-DNA complexes^[48]. The self-contact has also been considered in modeling the supercoiled DNA molecule^[49-51].

1.4.2 Finite element (FE) analysis of DNAs

The finite element method was first introduced in the analysis of DNA supercoiling by Yang et al. in 1993^[52] based on the Kirchhoff's rod theory. In their approach, in addition to the strain energy and external work defined in Eqs. (1.29) and (1.30), additional energy $W^{\text{self-contact}}$ due to self-contact constraint in the form of Lagrange multiplier was introduced into the total potential energy as follows:

$$\begin{aligned}\Pi^* &= \Pi - W^{\text{self-contact}} \\ &= W^{\text{elastic-Kirchhoff}} - W^{\text{ext}} - W^{\text{self-contact}}\end{aligned}\quad (1.31)$$

where Π^* is the modified total potential energy considering self-contact effects, and

$$W^{\text{self-contact}} = \int_{S_a}^{S_b} \lambda(S) \cdot [\mathbf{r}(L_d + 2S_b - S) - \mathbf{r}(S) - \mathbf{r}_d(S)] dS \quad (1.32)$$

where S_a and S_b are the arc-lengths at the beginning and the end of one contact segment which defines the contact zone, L_d is the arc-length between two contacting points, $\lambda(S)$ is the Lagrange multiplier, and $\mathbf{r}_d(S)$ is the gap function.

The stationary condition of Eq. (1.32) yields the variational equation:

$$\delta\Pi^* = 0 = \int_0^L A_1(k_1 - k_1^0)\delta k_1 + A_2(k_2 - k_2^0)\delta k_2 + C(\omega - \omega^0)\delta\omega dS$$

$$\begin{aligned}
& - \int_0^L \bar{\mathbf{N}} \cdot \delta \mathbf{r} + \bar{\mathbf{M}} \cdot \delta \mathbf{k} dS - \sum_{i=1}^n [\mathbf{T}(S_i) \cdot \delta \mathbf{k}(S_i) + \mathbf{P}(S_i) \cdot \delta \mathbf{r}(S_i)] \\
& - \int_{S_a}^{S_b} \lambda(S) \cdot [\delta \mathbf{r}(L_d + 2S_b - S) - \delta \mathbf{r}(S)] dS \\
& - \int_{S_a}^{S_b} \delta \lambda(S) \cdot [\mathbf{r}(L_d + 2S_b - S) - \mathbf{r}(S) - \mathbf{r}_d(S)] dS. \tag{1.33}
\end{aligned}$$

Equation.(1.33) is generally nonlinear, so standard linearization with Newton–Raphson method is adopted for solving the incremental unknown displacement/rotation vectors and Lagrange multiplier. Consider the finite element approximations of the trial and test functions as

$$\begin{aligned}
\delta \mathbf{r}^h &= \sum_{I=1}^{NEN} N_I(S) \delta \mathbf{r}_I, \quad \Delta \mathbf{r}^h = \sum_{I=1}^{NEN} N_I(S) \Delta \mathbf{r}_I, \\
\delta \boldsymbol{\vartheta}^h &= \sum_{I=1}^{NEN} \hat{N}_I(S) \delta \boldsymbol{\vartheta}_I, \quad \Delta \boldsymbol{\vartheta}^h = \sum_{I=1}^{NEN} \hat{N}_I(S) \Delta \boldsymbol{\vartheta}_I, \\
\delta \lambda^h &= \sum_{I=1}^{NEL} \Lambda_I(S) \delta \lambda_I, \quad \Delta \lambda^h = \sum_{I=1}^{NEL} \Lambda_I(S) \Delta \lambda_I \tag{1.34}
\end{aligned}$$

where $N_I(S)$, \hat{N}_I , and Λ_I are finite element shape functions associated with node I for the approximations of the displacement vector, rotation vector, and Lagrange multiplier, respectively, NEN and NEL are the number of nodes and Lagrange multiplier nodes in each element, respectively, $\delta \mathbf{r}_I$, $\delta \boldsymbol{\vartheta}_I$, and $\delta \lambda_I$ are admissible variations of displacement, rotation, and Lagrange multiplier at node I , respectively, and $\Delta \mathbf{r}_I$, $\Delta \boldsymbol{\vartheta}_I$ and $\Delta \lambda_I$ are unknown incremental field variables of node I . Noting that the shape functions for the Lagrange multiplier approximation generally differ from those for the displacement/rotation fields, N_I and \hat{N}_I , and they should satisfy the LBB (Ladyshenskaya–Babuška–Brezzi) condition^[53–55].

Yang et al.^[52] used the above-mentioned finite element formulation to investigate the equilibrium configurations of supercoiled DNA, and to examine the effects of base-sequence, anisotropy, and various writhes and twists on the DNA conformations. White et al.^[56,57] studied the DNA loop containing equally spaced or non-uniformly distributed intrinsic curvatures, and examined the effects of salt-dependent stiffness on the DNA conformations. They found that DNA folds very differently depending on the distribution of the curvatures and on the point at which the change in the linking number ΔLk is introduced.

1.4.3 Director field method for modeling of DNA viral packaging

The director field method has been proposed by using the local direction and density^[41] for describing the motion of DNAs. In this section, the director field and its computational framework as well as the application to modeling of DNA packaging in bacterial viruses are presented^[41,42].

In the director field approach, the geometry of the DNA is represented by a vector field $\mathbf{m}(\mathbf{x})$ with the following properties: (a) $|\mathbf{m}(\mathbf{x})|$ gives the DNA-length per unit volume, and (b) $\mathbf{t} = \mathbf{m}(\mathbf{x})/|\mathbf{m}(\mathbf{x})|$ defines the unit vector tangent to DNA (Fig. 1.13). The length of DNA contained within any volume Ω is

$$L(\Omega) = \int_{\Omega} |\mathbf{m}| dV. \quad (1.35)$$

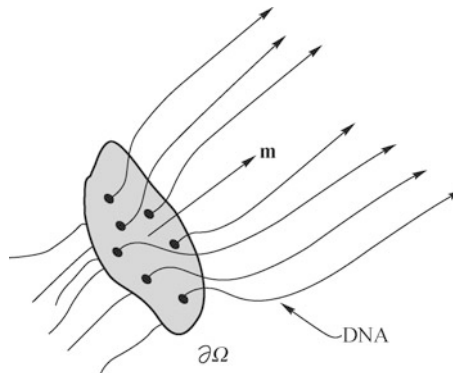


Fig. 1.13 Geometric representation of a DNA by the director field^[41].

For a given surface S with unit normal \mathbf{n} , the number of signed crossings through S (flux) can be expressed by

$$N(S) = \int_S \mathbf{m} \cdot \mathbf{n} dS. \quad (1.36)$$

The crossing is defined as being positive as the DNA pierces S in the direction of \mathbf{n} , and negative otherwise. For any closed surface S , conservation of mass states that

$$\int_S \mathbf{m} \cdot \mathbf{n} dS = 0. \quad (1.37)$$

Consider \mathbf{m} to be differentiable, applying divergence operation of Eq. (1.37) yields

$$\nabla \cdot \mathbf{m} = 0. \quad (1.38)$$

This states that the director field is divergence-free. Further, the Serret-Frenet differential geometry of the local unit tangent \mathbf{t} , the normal vector \mathbf{n} ,

and the binormal vector \mathbf{b} are

$$\mathbf{t}' = \kappa \mathbf{n}, \quad \mathbf{n}' = \tau \mathbf{b} - \kappa \mathbf{t}, \quad \mathbf{b}' = -\tau \mathbf{n} \quad (1.39)$$

where κ and τ are the curvature and torsion, respectively, and a prime denotes the arc-length derivative in the direction of \mathbf{t} , i.e., $f' = \mathbf{t} \cdot \nabla f$. Accordingly, the curvature and torsion are obtained as

$$\kappa^2 = |\mathbf{t}'|^2, \quad (1.40)$$

$$\tau^2 = |\mathbf{n}' + \kappa \mathbf{t}|^2 = |\mathbf{n}'|^2 - \kappa^2 = \frac{\mathbf{t}'' \cdot \mathbf{P}(\mathbf{t}') \cdot \mathbf{t}''}{|\mathbf{t}'|^2} - |\mathbf{t}'|^2 \quad (1.41)$$

where $\mathbf{P}(\mathbf{a}) \equiv \mathbf{I}_3 - \mathbf{a} \otimes \mathbf{a}/|\mathbf{a}|^2$ is the orthogonal projection in the direction of a vector $\mathbf{a} \in \mathbb{R}^3$. From the above, the curvature and torsion of a DNA can be computed in terms of the director field \mathbf{m} .

DNA conformations are energy minimizers where energy due to bending and torsion, electrostatic interactions, and entropic effect is considered. Riemer and Bloomfield^[58] ignored the entropic effect and considered only the strain energy of an inextensible rod and electrostatic interactions as

$$W(\mathbf{m}, \nabla \mathbf{m}, \nabla \nabla \mathbf{m}) = \left(\frac{A}{2} \kappa^2 + \frac{B}{2} \tau^2 \right) |\mathbf{m}| \quad (1.42)$$

where A and B are the bending and torsional stiffnesses, respectively, κ is the local curvature, and τ is the local torsion given in Eq. (1.40). In entropic regime as introduced in Section 1.1, the bending and torsional stiffnesses of DNA are related to the persistence lengths as $A = ak_B T$ and $B = bk_B T$, respectively, where T is the absolute temperature, k_B is Boltzmann's constant, $a \approx 50$ nm is the bend persistence length, and $b \approx 85$ nm is the twist persistence length^[1].

The DNA molecules are highly charged polymers, with one negative charge for every 0.17 nm of its length. According to the experimental work by Parsegian et al. using the osmotic pressure technique^[59,60], the electrostatic energy ϕ per unit volume of hexagonally packed DNA is related to the applied pressure P and helix spacing d as follows:

$$P(d) = \phi_0 e^{-(d-d_0)/c-1}, \quad (1.43)$$

$$e_a(d) = e_0 + \sqrt{3} \int_d^{d_0} P(\xi) \xi d\xi, \quad (1.44)$$

$$\phi(u) = ue_a \left(d = \sqrt{2/\sqrt{3}/u} \right) \quad (1.45)$$

$$= \phi_0 - \mu_0 u + (\mu_0 + \mu_\infty)(u + \sqrt{u_\infty u}) e^{-\sqrt{u_\infty/u}}$$

where $u = |\mathbf{m}| = 2/(\sqrt{3}d^2)$ is the DNA density, $e_a(d)$ is the interaction energy per unit length, $e_0 = -0.8 k_B T \text{ nm}^{-1}$, $\phi_0 = 0.1 k_B T \text{ nm}^{-3}$, $d_0 = 2.8$ nm,

$c = 0.15 \text{ nm}$, $\mu_0 = 1.56 k_B T \text{ nm}^{-1}$, $\mu_\infty = 4.98 \times 10^5 k_B T \text{ nm}^{-1}$, and $u_\infty = 51.3 \text{ nm}^{-2}$ are experimentally measured constants.

Hence, the total free energy of the DNA is expressed as

$$E(\mathbf{m}) = \int_{\Omega} [W(\mathbf{m}, \nabla \mathbf{m}, \nabla \nabla \mathbf{m}) + \phi(|\mathbf{m}|)] dV. \quad (1.46)$$

The constrained minimization problem of DNA packaging in a confined capsid Ω is therefore stated as

$$\inf E(\mathbf{m}) \quad (1.47)$$

$$\text{subject to: } \nabla \cdot \mathbf{m} = 0 \quad \text{in } \Omega, \quad (1.48)$$

$$\mathbf{m} \cdot \mathbf{n} = 0 \quad \text{on } \partial\Omega, \quad (1.49)$$

$$\int_{\Omega} |\mathbf{m}| dV = L \quad (1.50)$$

where \mathbf{n} is the outward unit normal to $\partial\Omega$.

The director field method has been applied to the studies of the conformation of packaged DNA in a confined capsid by Klug et al.^[41,42]. Their numerical results demonstrated good agreement with the experimental measurements^[9], and showed that the inverse spool motif is the lowest energy conformation in all regions of the virus capsid.

1.5 Multiscale homogenization for simulation of DNA molecules

In this section, we introduce the multiscale homogenization techniques for the DNA molecules. A coarse-grained DNA model based on the multiscale wavelet projection method has been proposed by Chen et al.^[61-63]. A continuum description of DNA molecules can be constructed using a coarse-grained DNA within the hyperelastic beam framework as a second-level homogenization.

1.5.1 Basics of multiscale wavelet projection method

Wavelet-based multiscale homogenization has been applied to problems with high heterogenieties^[61,62,64,65] as well as the coarse-grained DNA model^[63]. In this subsection, we present the fundamentals of the wavelet basis functions and the associated decomposition and construction techniques^[63,64,66].

Let us consider the multi-resolution analysis by a sequence of nested subspaces, $\cdots \subset V_{-1} \subset V_0 \subset V_1 \cdots \subset L^2(\mathbb{R})$, where $\bigcup_{j \in \mathbb{Z}} V_j = L^2(\mathbb{R})$ and

$\bigcap_{j \in \mathbb{Z}} V_j = \emptyset$. Each subspace of scale j is spanned by a set of the *scaling functions* $\varphi_{j,k}(x)$

$$V_j = \left\{ \varphi_{j,k}(x) | \varphi_{j,k}(x) = 2^{\frac{j}{2}} \varphi(2^j x - k), k \in \mathbb{Z} \right\} \quad (1.51)$$

where they obey the dilation and translation laws

$$\varphi(x) \in V_j \Leftrightarrow \varphi(2x) \in V_{j+1}, \quad \forall j \in \mathbb{Z} \text{ (dilation)}, \quad (1.52)$$

$$\varphi(x) \in V_0 \Leftrightarrow \varphi(x-n) \in V_0, \quad \forall n \in \mathbb{Z} \text{ (translation)}. \quad (1.53)$$

Then, a mutually orthogonal complement of V_j , a subspace W_j , is defined so that

$$V_{j+1} = V_j \oplus W_j, \quad \forall j \in \mathbb{Z} \quad (1.54)$$

where \oplus is a direct sum. The subspace W_j is spanned by a set of wavelet basis functions $\psi_{j,k}(x)$ as

$$W_j = \left\{ \psi_{j,k}(x) | \psi_{j,k}(x) = 2^{\frac{j}{2}} \psi(2^j x - k), k \in \mathbb{Z} \right\} \quad (1.55)$$

where $\psi(x)$ is the *mother wavelet*, and $\bigoplus_{j \in \mathbb{Z}} W_j = L^2(\mathbb{R})$. The wavelet function $\psi(x)$ is chosen to be orthogonal to the scaling function $\varphi(x)$ with respect to translation. A function $f(x)$ can be approximated by using the scaling functions at scale j as the basis:

$$P_j f = \sum_{k=-\infty}^{\infty} c_k \varphi_{j,k} \quad (1.56)$$

where c_k 's are coefficients and P_j is the operator which projects function $f(x)$ onto the subspace V_j spanned by $\varphi_{j,k}(x)$.

The two-scale relation for the scaling functions can be written as

$$\varphi(x) = \sqrt{2} \sum_{n=-\infty}^{\infty} d_n \varphi(2x - n). \quad (1.57)$$

By imposing the orthogonality conditions between scaling and wavelet functions in the frequency domain by means of Fourier transform, the orthogonal wavelet function can be obtained as follows:

$$\psi(x) = \sqrt{2} \sum_{n=-\infty}^{\infty} (-1)^{n-1} d_{-n-1} \varphi(2x - n) \quad (1.58)$$

where d_n is the wavelet coefficient determined by applying the orthogonality conditions to the scaling functions with respect to the translation parameter,

i.e., $\sum a_n a_{n+2m} = 2\delta_{m0}$ ($n \in \mathbb{Z}$). Note that Eqs. (1.57) and (1.58) are the algorithm for the construction of the scaling and wavelet functions at the coarser scale in terms of the scaling functions at the finer scale. On the other hand, the decomposition relation, which allows the decomposition of the scaling function at the finer scale in terms of the scaling and wavelet functions at the coarser scale, is given as:

$$\varphi(2x - l) = \sum_{k=-\infty}^{\infty} d_{l-2k} \varphi(x - k) + \sum_{k=-\infty}^{\infty} b_{l-2k} \psi(x - k), \quad l \in \mathbb{Z}. \quad (1.59)$$

Orthogonal scaling functions can be constructed by choosing a candidate function $\varphi^*(x)$ so that $\varphi^*(x)$ and its Fourier transform have a reasonable decay and finite support, and $\int \varphi^*(x) dx \neq 0$. Moreover, the candidate function should satisfy the two-scale relation

$$\varphi^*(x) = \sum_n c_n \varphi^*(2x - n), \quad n \in \mathbb{Z}. \quad (1.60)$$

For the linear scaling function candidate, $\varphi^*(x)$ is a hat function with the coefficients c_n 's summarized in Table 1.5 in Appendix, and the corresponding scaling function is called the linear spline function. Figure 1.14 shows the scaling and wavelet functions obtained from the hat candidate function using Eqs. (1.57) and (1.58). The wavelet coefficients d_n and the decomposition coefficients b_n for the linear spline function are shown in Table 1.6 in Appendix.

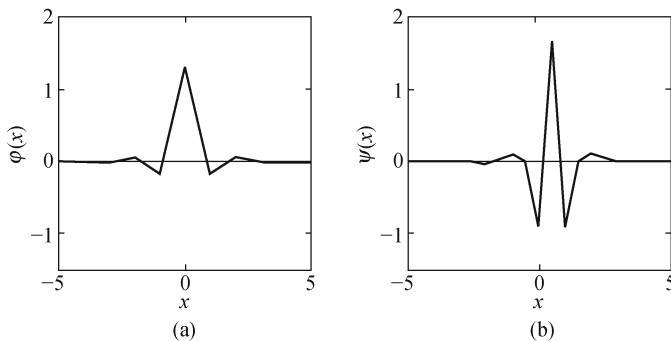


Fig. 1.14 (a) Linear orthogonal scaling function $\varphi(x)$, and (b) corresponding wavelet function $\psi(x)$.

The multiscale wavelet transformation is defined for transforming functions at various scales with the following transformation operator w_j :

$$w_j : V_{j+1} \rightarrow V_j \oplus W_j \quad (1.61)$$

where w_j maps the basis $\{\varphi_{j+1,k}\}$ at scale $j + 1$ onto $\{\varphi_{j,k}\}$ and $\{\psi_{j,k}\}$ at scale j . Then, the projection matrices, \mathbf{P}_j and \mathbf{Q}_j , associated with w_j operator are constructed so that

$$\begin{cases} \mathbf{P}_j : & V_{j+1} \rightarrow V_j, \\ \mathbf{Q}_j : & V_{j+1} \rightarrow W_j. \end{cases} \quad (1.62)$$

These scaling and wavelet functions at different scales are used as the hierarchical basis for wavelet-based multiscale homogenization which are discussed in detail in the next subsection. For scaling and wavelet functions constructed based on the hat candidate function, the discrete forms of projection matrices \mathbf{P}_j and \mathbf{Q}_j are

$$\mathbf{P}_j = \begin{bmatrix} d_{j-2k} & 0 & 0 & \cdots \\ d_{j-2(k+1)} & d_{j+1-2(k+1)} & d_{j+2-2(k+1)} & \cdots \\ \vdots & \vdots & \vdots & \\ 0 & 0 & 0 & \cdots \\ 0 & 0 & 0 & \cdots \\ & 0 & 0 & 0 \\ & 0 & 0 & 0 \\ & \vdots & \vdots & \vdots \\ d_{j+m-2-2(k+n-1)} & d_{j+m-1-2(k+n-1)} & d_{j+m-2(k+n-1)} \\ 0 & 0 & d_{j+m-2(k+n)} \end{bmatrix}, \quad (1.63)$$

$$\mathbf{Q}_j = \begin{bmatrix} b_{j-2k} & 0 & 0 & \cdots \\ b_{j-2(k+1)} & b_{j+1-2(k+1)} & b_{j+2-2(k+1)} & \cdots \\ \vdots & \vdots & \vdots & \\ 0 & 0 & 0 & \cdots \\ 0 & 0 & 0 & \cdots \\ & 0 & 0 & 0 \\ & 0 & 0 & 0 \\ & \vdots & \vdots & \vdots \\ b_{j+m-2-2(k+n-1)} & b_{j+m-1-2(k+n-1)} & b_{j+m-2(k+n-1)} \\ 0 & 0 & b_{j+m-2(k+n)} \end{bmatrix}. \quad (1.64)$$

1.5.2 First-level homogenization — wavelet-based coarse-grained DNA model

The full atomistic simulation is practically unaffordable for biological processes with large and complex systems, such as DNA translocation, DNA replication, DNA-protein interaction, and chromosome formation. In the first-level homogenization^[63], we are aiming at constructing a coarse-grained model for the DNA molecule based on its fine-scale molecular structure and properties. The coarse-grained DNA model will then be used to formulate a hyperelastic beam model for continuum modeling of the DNA (also see Section 1.5.3).

1.5.2.1 Mapping full atomistic model to coarse-grained DNA model

The approach for coarse-graining takes into account the dimension and complexity of the molecular structure of DNA as well as the properties of interest. The coarse-grained procedure^[63] first defines the coarse-grained superatoms (also called beads). Each superatom in the coarse-grained DNA model is assumed to represent a group of atoms. Figure 1.15 illustrates the six building blocks, *four nitrogen bases*, *phosphate group* and *sugar*, for construction of the coarse-grained DNA model.

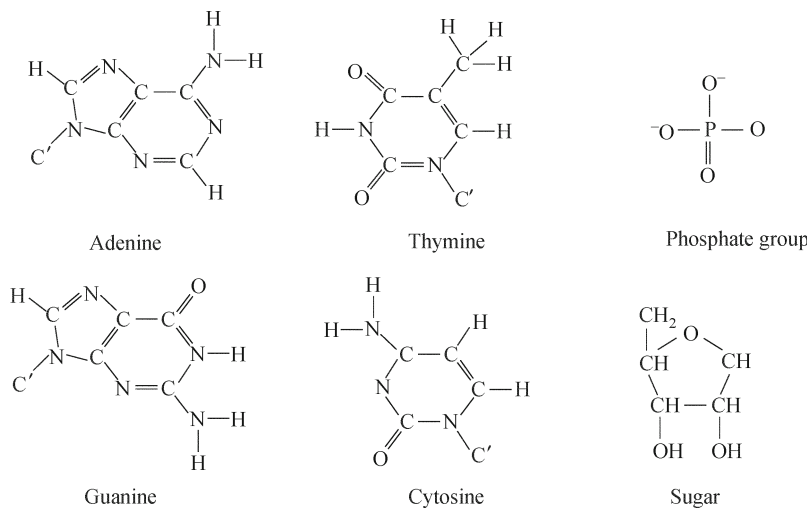


Fig. 1.15 Basic building blocks of ds-DNA.

For the coarse-grained model capable of representing the connectivity of the DNA molecular structure, we choose the center of mass of each building block as the position of the coarse-grained superatom as shown in Fig. 1.16. The essential step is to establish the interaction potential or *force field*

among these superatoms, which is a function of superatom positions \mathbf{r} . The interactions can be expressed in terms of the sum of valence and non-bonded potentials as follows:

$$\bar{U}(\mathbf{r}) = \bar{U}_b(\mathbf{r}) + \bar{U}_{nb}(\mathbf{r}), \quad (1.65)$$

$$\bar{U}_b(\mathbf{r}) = \sum_{\text{bonds}} \bar{k}_b (r_{ij} - \bar{r}_{ij}^{\text{eq}})^2 + \sum_{\text{angles}} \bar{k}_\theta (\theta_{ijk} - \bar{\theta}_{ijk}^{\text{eq}})^2, \quad (1.66)$$

$$\bar{U}_{nb}(\mathbf{r}) = \sum_i \sum_j \left\{ 4\bar{\varepsilon}_{ij} \left[\left(\frac{\bar{\sigma}_{ij}}{r_{ij}} \right)^{12} - \left(\frac{\bar{\sigma}_{ij}}{r_{ij}} \right)^6 \right] + \frac{q_i q_j}{r_{ij}} \right\} \quad (1.67)$$

where \bar{U}_b and \bar{U}_{nb} denotes the effective (coarse-grained) bonded and non-bonded potential functions, respectively, and other parameters with superposed bars are the parameters of coarse-grained potentials. These parameters of the effective force fields for the coarse-grained DNA model are characterized by performing the multiscale wavelet projection onto the fine-scale solutions obtained from the full MD simulation. The details will be illustrated in the following sections. Here, we consider two-body interaction between two connected superatoms and three-body interaction expressed in terms of bending angle between three consecutive connected superatoms for the valence interaction. We also assume the coarse-grained two-body and three-body potential functions to be harmonic. Moreover, the fine-scale atomistic simulation reveals that the probability distributions of torsional angle are almost flat, suggesting that the corresponding forces due to four-body interactions are negligible.

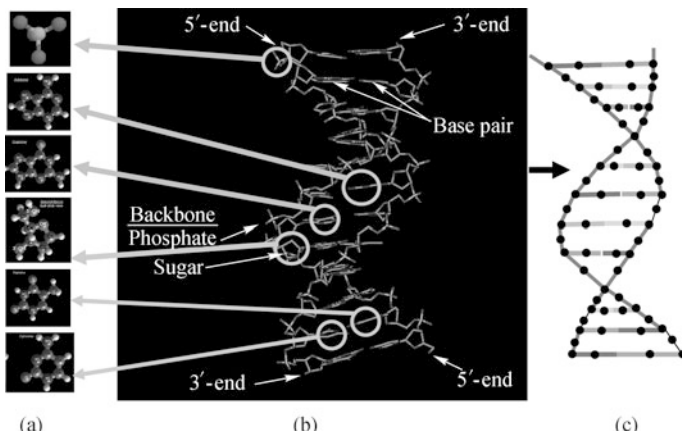


Fig. 1.16 Schematic of mapping full atomistic DNA model to a coarse-grained model: (a) building blocks of DNA molecule, (b) DNA molecular structure, and (c) coarse-grained DNA model. (color plot at the end of the book)

1.5.2.2 Homogenization of potential function from molecular dynamics simulation

The potential functions of the coarse-grained DNA model are constructed in such a way that the coarse-grained molecule is able to represent the same configuration space as the atomistic model. To determine the effective force fields of the coarse-grained model, we first perform a full atomistic simulation of DNA stretching using NVT ensemble, i.e., the number of particles N , the volume of the system V , and the temperature T are kept constant during the MD simulation. The Nose-Hoover method^[67,68] is applied to keep the temperature of the system at 300 K, while the long-range electrostatic interactions are evaluated using Ewald sum technique^[69]. The Leapfrog Verlet algorithm is used for numerical time integration of the equations of motion with time step size of 1 fs.

The positions of the superatoms are defined as the center of mass of each building block as mentioned in the previous section. Then, the time history of relative distance r_{ij} between superatoms is computed based on the trajectory obtained from the full MD simulation. Next, the probability distributions of the distance can be obtained via the histograms of distance between centers of mass in each building block. By the Boltzmann's inversion, the probability distributions of distance functions are used to determine the fine-scale interaction potential $U(d)$ in terms of superatom distance d as follows:

$$P(d) = A \exp\left(\frac{-U(d)}{k_B T}\right) \quad (1.68)$$

where A is the constant to be determined, k_B is Boltzmann's constant, T is the absolute temperature, d is the distance between two bonded superatoms, and U is the fine-scale bond stretching potential. Next, we perform the multiscale wavelet projection (introduced in Section 1.5.1) to homogenize the fine-scale potential function for yielding the effective potential for the coarse-grained model following Eqs. (1.62). As such, we characterize the effective bond constant \bar{k}_b and the effective equilibrium distance \bar{r}_{ij}^{eq} using the effective bond potential. Same procedures, which are summarized in Table 1.1, are used to characterize the parameters of the effective bond angle potential.

However, the effective non-bonded potential is more difficult to determine since the distance distribution functions cannot be directly related to the potential functions due to many-body effects. Fukunaga et al.^[70] proposed the following equation to determine the coarse-grained non-bonded potential as a function of superatom distance for a polymer system:

$$U_{nb}(R) = -k_B T \ln(P(R)) H(R^* - R) - k_B T \ln \left\langle \exp\left(\frac{-U_{nb}^{AA}(R)}{k_B T}\right) \right\rangle_R \quad (1.69)$$

where R is the distance between two superatoms which are not directly

bonded, $H(R^* - R)$ is the Heavside unit step function, R^* is a cutoff distance, which is selected at the position of the first peak of $P(R)$ in this study. The term $U_{nb}^{AA}(R)$ denotes the non-bonded potential energy between one atom in a superatom and all the atoms in another superatom where the distance between the two superatoms is R , and $\langle \cdots \rangle_R$ is an average operator acting on superatoms with distance R .

Table 1.1 Procedure for characterization of effective force fields for the coarse-grained model based on the multiscale wavelet projection method

-
- Step 1 Perform a full MD simulation of stretching DNA in the *NVT* ensemble
 - Step 2 Obtain the probability distributions of distance and angle functions based on the fine-scale simulation results
 - Step 3 Relate probability distributions to the fine-scale interatomic potentials using Eq. (1.68)
 - Step 4 Homogenize the fine-scale potentials using the multiscale wavelet projection method and obtain the effective force fields
 - Step 5 Characterize parameters of effective force field
 - Step 6 Repeat Steps 1–5 for different combinations of bonds, bond angles, and non-bonded pairs
-

It has been shown by Fukunaga et al.^[70] that for polymers, when two segments are located in short distance but are not directly connected, the behavior of the two segments is still strongly correlated as if they are bonded together. Therefore, this part of contribution to the non-bonded potential could be properly described using the similar form as that of the bonded potential as given in the first term on the right-hand side of Eq. (1.65). Note that this term represents the strong repulsive interaction for segments in close distance. On the other hand, at a long distance, due to many-body effects, the potential is described in the second term on the right-hand side of Eq. (1.69), which accounts for the attractive interaction.

We use P, S, A, G, C, and T to represent the superatoms of phosphate group, sugar, adenine, guanine, cytosine, and thymine, respectively. In this study, we consider the DNA molecule in pure G–C sequence with 1 260 atoms in the original full atomistic model, while the coarse-grained DNA model contains only 120 superatoms as depicted in Fig. 1.17. In Sections 1.5.2.3–1.5.2.4, we demonstrate the detail of characterization of the effective bond stretching, effective bond angle, and effective non-bonded potentials as well as the numerical results.

1.5.2.3 Characterization of effective bond stretching potential

The fine-scale atomistic SC–C bond distribution at 300 K and the corresponding fine-scale potential function using $U_b(d) = -k_B T \ln P_b(d)$ are presented in Fig. 1.18a and b, respectively. Figure 1.19 portrays the effective

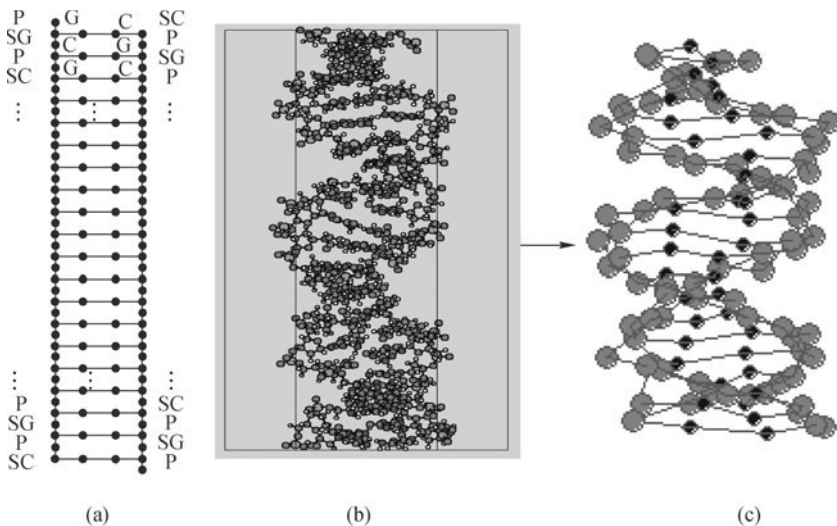


Fig. 1.17 Coarse-graining of DNA molecule: (a) schematic representation of DNA containing pure G – C base pairs, (b) fine-scale atomistic model, and (c) corresponding coarse-grained model. (color plot at the end of the book)

bond potential by performing multiscale wavelet projection of the finest bond potential. First, the fine-scale potential is mapped onto the scaling function space with domain $[0,1]$ and discretized by 2^j grid points. To capture the finest scale potential, the finest grid associated with the finest scale of the solution is set at $j = 7$. Using the wavelet projection operators \mathbf{P}_j and \mathbf{Q}_j defined in Eqs. (1.62)– (1.64), the fine- and coarse-scale components of potential at scale j are extracted. At each scale, fine-scale components which

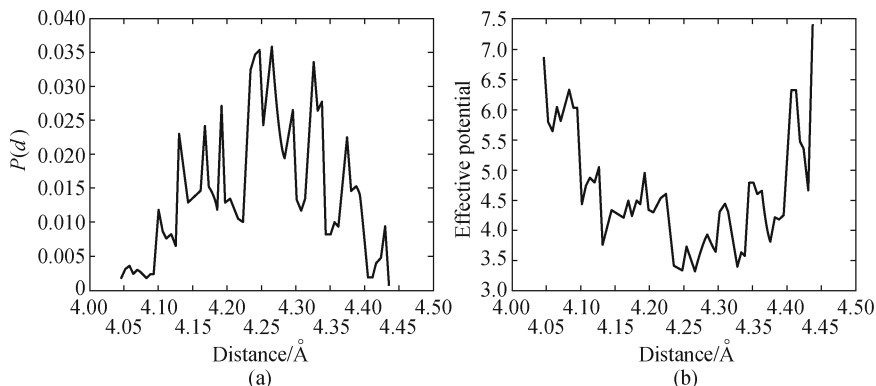


Fig. 1.18 (a) Probability distribution of bond distance for SC–C bond, and (b) fine-scale bond potential obtained from the Boltzmann inversion of the probability distribution function.

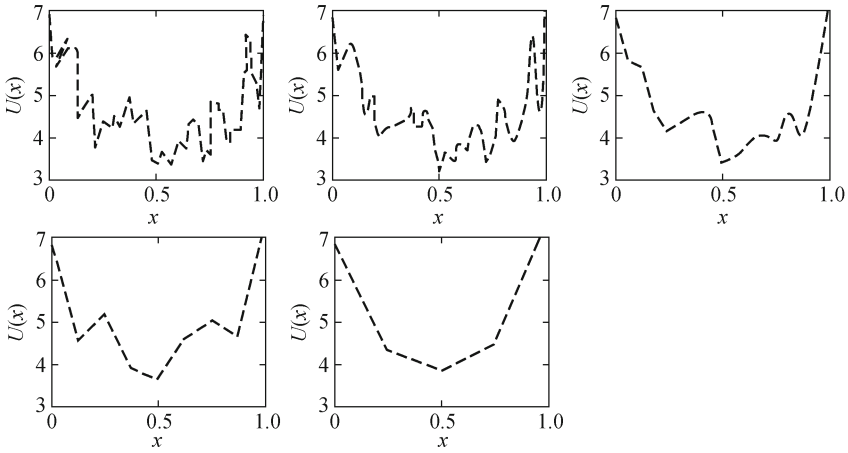


Fig. 1.19 Effective bond potential based on multiscale wavelet projection of fine-scale bond potential function.

represent the high frequency responses are eliminated and only the coarse-scale components are kept. By repeating this projection process from $j = 7$ to $j = 3$, an effective bond potential between the coarse-grained superatoms SC–C is obtained as shown in Fig. 1.19. The effective bond constant and equilibrium distance are determined based on this projected (homogenized) potential function for SC–C bond. The coarse-grained parameters of each bond in the DNA segment obtained from the proposed method are summarized in Table 1.2. It can be seen that the bond constant of the coarse-grained bonds is approximately one order of magnitude lower than the bond constants in the full atomistic model (typically about 400 kcal/mol/Å).

Table 1.2 Parameters of effective bond potential for the coarse-grained model

Bond type	$\bar{r}_{ij}^{\text{eq}}(\text{\AA})$	$\bar{k}_b(\text{kcal/mol}/\text{\AA}^2)$
P–SC	3.98	67.1
P–SC	3.67	66.7
SG–G	4.71	89.7
SC–C	4.17	59.9
G–C	6.40	12.4

The probability distribution computed using coarse-scale model is compared with that of the fine-scale model in Fig. 1.20. We also show the result of a coarse-grained model where the parameters are obtained through a directly curve fitting of the fine-scale effective potential. It is shown that the coarse-grained model obtained from multiscale wavelet project method better represents the gross behavior of the fine-scale atomistic model.

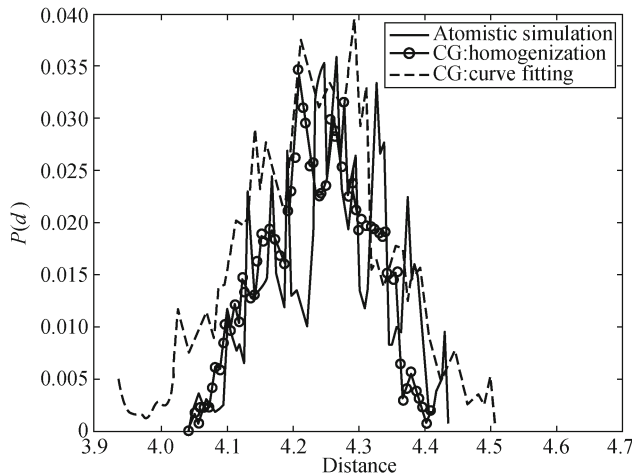


Fig. 1.20 Bond length distribution functions obtained for the DNA molecule with the atomistic and coarse-grained simulations.

1.5.2.4 Characterization of effective bond angle potential

For bond angle potential, eight different bond angle terms need to be parameterized: P–SG–G, G–SG–P, P–SC–C, C–SC–P, SG–G–C, SC–C–G and P–SG–P and P–SC–P. Figure 1.21a shows the atomistic P–SG–G angle distribution at 300 K. The fine-scale potential function of bond angle P–SG–G, obtained from Boltzmann inversion $U_a(\theta) = -k_B T \ln P_a(\theta)$, is presented in Fig. 1.21b. Here $U_a(\theta)$ is the fine-scale potential function of bond angle P–SG–G, and $P_a(\theta)$ is the distribution function for the bond angle P–SG–G.

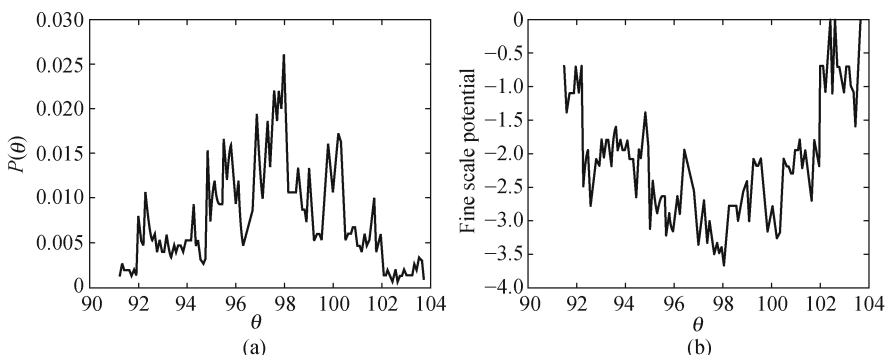


Fig. 1.21 (a) Probability distribution of bond angle for P–SG–G angle, and (b) fine-scale angle potential obtained from the Boltzmann inversion of the probability distribution function.

Figure 1.22 shows the effective bond angle potential for the coarse-grained model based on multiscale wavelet projection method. The fine-scale potential is first projected onto the scaling function space with domain $[0,1]$, and is discretized by 2^j grid points. The grid associated with the finest scale of the solution is set at $j = 7$ to capture finest potential. By performing wavelet projection at the finest scale, fine- and coarse-scale components of potential are extracted using the wavelet projection operators \mathbf{P}_j and \mathbf{Q}_j , and only the coarse-scale component of the potential function is retained. By performing this wavelet projection from scale $j = 7$ to $j = 3$, the effective potential function is obtained as shown in Fig. 1.22. The coarse-grained constant and equilibrium distance are characterized based on this projected potential. The coarse-grained parameters of each angle in the DNA segment obtained from the proposed method are summarized in Table 1.3. It can be seen that the

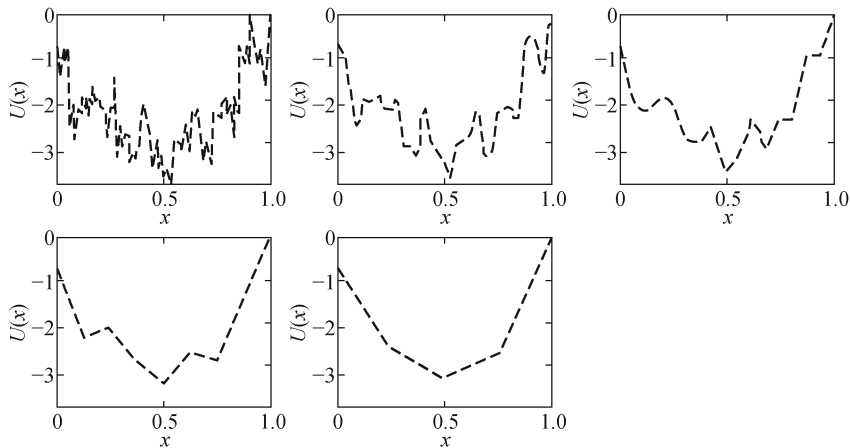


Fig. 1.22 Effective angle potential based on multiscale wavelet projection of fine-scale angle potential function.

Table 1.3 Parameters of effective angle potential for the coarse-grained model

Bond angle type	$\bar{\theta}_{ijk}^{\text{eq}}$ (deg)	\bar{k}_θ (kcal/mol/rad 2)
P–SG–G	91.95	5.87
G–SG–P	120.05	6.48
P–SC–C	96.39	6.04
C–SC–P	127.06	6.00
SG–G–C	156.99	2.96
SC–C–G	144.00	3.33
P–S–P	119.01	4.32
S–P–S	997.82	5.64

bond angle parameters of the coarse-grained potential are approximately one order of magnitude lower than the bond constants in the atomistic model. The lower constant and higher mass of the superatoms yield a significant decrease in the frequency of the bond allowing a larger stable time step in time evolution calculation.

Figure 1.23 compares the bond angle distributions obtained from atomistic and coarse-grained models. It is shown that the coarse-grained model obtained from multiscale wavelet project method adequately represents the gross response of the fine-scale atomistic model.

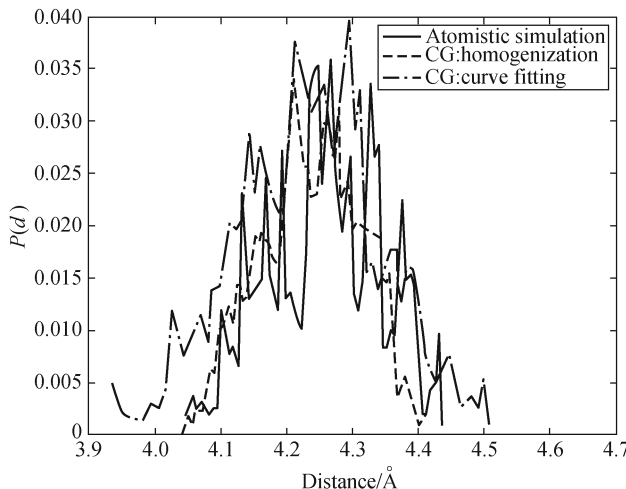


Fig. 1.23 Bond angle distribution functions obtained for the DNA molecule with the atomistic and coarse-grained simulations.

1.5.2.5 Characterization of effective non-bonded potential

The non-bonded potential of the fine-scale follows Eq. (1.69), in which the potentials for the short-range repulsive interaction and long-range attractive interaction are obtained separately. Figure 1.24a shows the short-range radial distribution function of G–C group obtained from the fine-scale atomistic simulation of DNA molecule. The corresponding short-range non-bonded potential, $-k_B T \ln P(R)$ as the first term of Eq. (1.69), is shown in Fig. 1.24b. The long-range non-bonded potential obtained based on the second term of Eq. (1.69) is shown in Fig. 1.24c. By combining the short-range and long-range effects, the effective non-bonded potential based on Eq. (1.69) is given in Fig. 1.24d.

Again the fine-scale potential is first projected onto the scaling function space with domain $[0,1]$, and is discretized by 2^j grid points. The effective non-bonded potential obtained based on multiscale wavelet projection from

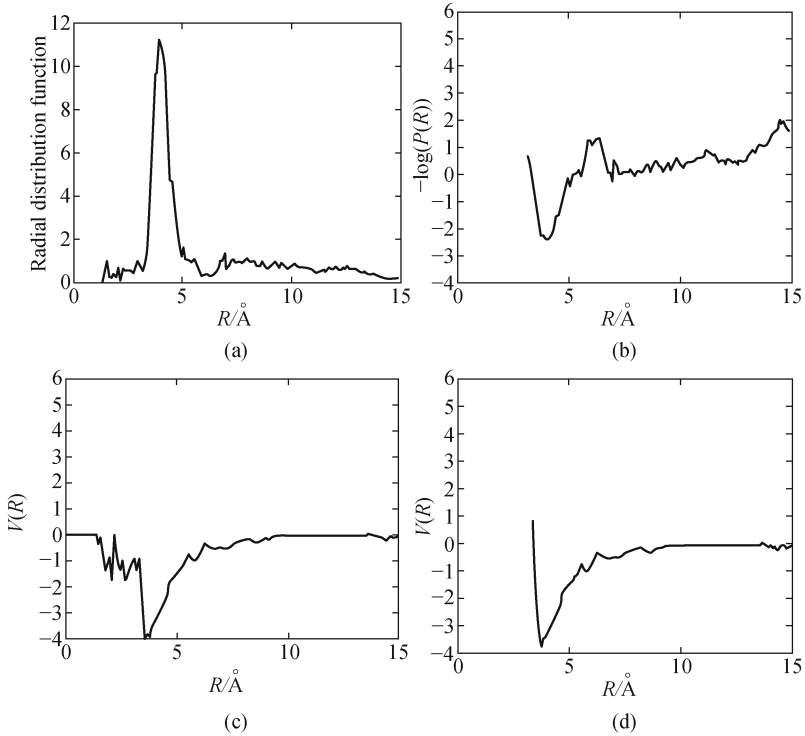


Fig. 1.24 (a) Short-range radial distribution function of G–C group, (b) corresponding short-range fine-scale non-bonded potential by $-k_B T \ln P(R)$, (c) fine-scale long-range non-bonded potential by $-k_B T \ln \langle \exp[-U_{nb}^{AA}(R)/k_B T] \rangle_R$, and (d) fine-scale non-bonded potential of G–C group (combination of short-range and long-range potentials).

scales $j = 6$ to $j = 4$ is shown in Fig. 1.25. The parameters of the non-bonded potential are characterized based on the following 12-6 Lennard–Jones potential

$$\bar{U}_{nb} = 4\bar{\varepsilon} \left[\left(\frac{\bar{\sigma}}{r_{ij}} \right)^{12} - \left(\frac{\bar{\sigma}}{r_{ij}} \right)^6 \right] \quad (1.70)$$

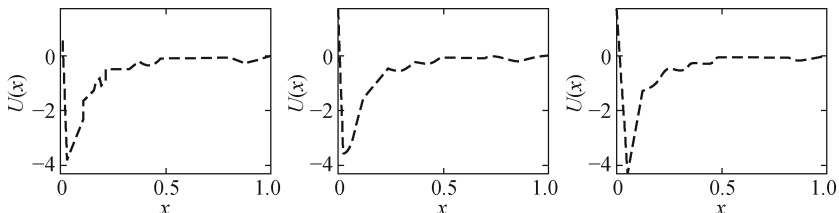


Fig. 1.25 Effective non-bonded potential based on multiscale wavelet projection.

where $\bar{\varepsilon}$ and $\bar{\sigma}$ are the coarse-grained well-depth and van der Waals diameter of the corresponding species, respectively. The characterized coarse-grained parameters of each non-bonded potential in the DNA segment with the form of Eq. (1.70) are summarized in Table 1.4. Figure 1.26 compares the radial distribution functions obtained from atomistic and coarse-grained models. It is shown that the coarse-grained model obtained from wavelet project method properly represents the global behavior of the fine-scale atomistic model.

Table 1.4 Parameters of effective non-bonded potential for the coarse-grained model

Non-bond type	$\bar{\varepsilon}$ (kcal/mol)	$\bar{\sigma}$ (Å)
SS	1.15	5.03
SC	1.09	5.15
SG	2.37	4.32
SP	0.51	3.75
CC	1.59	5.05
CG	1.65	5.10
GG	1.83	5.15
PC	1.52	6.20
PG	1.10	6.50
PP	1.00	6.00

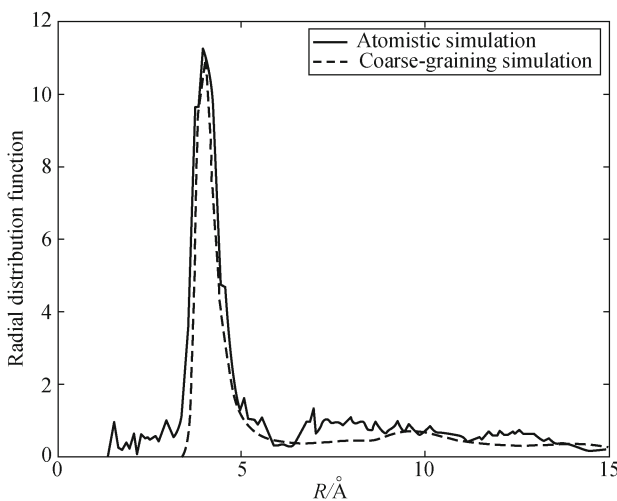


Fig. 1.26 Radial distribution functions of the DNA molecule obtained from the atomistic and coarse-grained simulations.

1.5.3 Second-level homogenization—hyperelastic beam formulation for DNA

The coarse-grained DNA model developed in Section 1.5.2 has the following advantages compared to the full atomistic model: (a) the coarse-grained model contains much less degrees of freedom, (b) the molecular structure of the coarse-grained model is much more regular than the fine-scale model and can be described by simple geometry, and (c) the potential functions are smoother and advantageous for temporal discretization. Therefore, in the second level homogenization, the coarse-grained DNA model is utilized to construct a hyperelastic beam for continuum modeling.

In this level of homogenization, we select each turn of the coarse-grained DNA as a unit cell, which contains about 10–11 base pairs, and adopt the classical Cauchy-Born rule^[71,72] to describe the continuum deformation as,

$$\mathbf{r}^{ij} = \mathbf{F} \cdot \mathbf{r}_0^{ij} \quad (1.71)$$

where \mathbf{r}^{ij} and \mathbf{r}_0^{ij} are bond vectors connecting superatoms i and j in the deformed and undeformed (reference) configurations, respectively, $\mathbf{F}_{ij} = \partial \mathbf{x}_j / \partial X_j$ denotes the deformation gradient of a material point, and X_i and x_i are vector components of the material (undeformed) and spatial (deformed) configurations, respectively.

For the atomistic system, the potential energy stored in the bonds can be expressed as a function of the atomic distance r^{ij} , i.e., $U = U(r^{ij})$. The strain energy density w^c of the material point at the continuum level for a specific DNA unit cell is given as

$$w^c = \frac{\sum U(r^{ij})}{V_0} \quad (1.72)$$

where $V_0 = \pi a^2 h$ is the volume of the representative unit cell in the undeformed configuration. Since the potential functions of a DNA molecule include two-body bond stretching, three-body angle, four-body torsional, and non-bonded interactions, we are seeking for the individual continuum descriptions of those atomistic interactions, i.e., the strain energy density and 2nd Piola-Kirchhoff (PK) stress tensor \mathbf{S} , by means of the deformation gradient \mathbf{F} .

We first derive the continuum description of the two-body bond stretching energy by considering the following harmonic potential function:

$$U^{\text{bond}} = \sum_{\text{bonds}} k_b (r^{ij} - r_0^{ij})^2. \quad (1.73)$$

Considering an arbitrary bond connecting two superatoms i and j in the

undeformed configuration as shown in Fig. 1.27, we have

$$\mathbf{r}_0^{ij} = \mathbf{X}^{(i)} - \mathbf{X}^{(j)}, \quad r_0^{ij} = |\mathbf{X}^{(i)} - \mathbf{X}^{(j)}|, \quad \mathbf{N}^{ij} = \frac{\mathbf{r}_0^{ij}}{r_0^{ij}}. \quad (1.74)$$

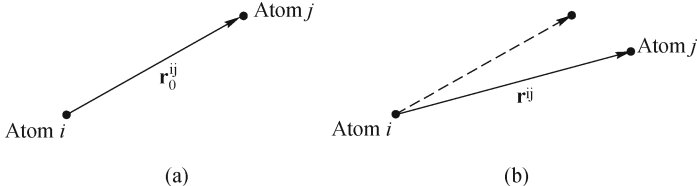


Fig. 1.27 Schematic of orientations of bond vector \mathbf{r}^{ij} in the (a) initial (undeformed) configuration, and (b) current (deformed) configuration.

For simplicity, we omit the superscripts “ i, j ” in the rest of the derivation. Under deformation, the stretch ratio of the bond can be related to the Green–Lagrangian strain tensor \mathbf{E} by the Cauchy–Born rule as follows:

$$\frac{r}{r_0} = \sqrt{\mathbf{N} \cdot \mathbf{C} \cdot \mathbf{N}} = \sqrt{1 + 2\mathbf{N} \cdot \mathbf{E} \cdot \mathbf{N}} \quad (1.75)$$

where $\mathbf{C} = \mathbf{F}^T \mathbf{F} = \mathbf{I} + 2\mathbf{E}$ is the right-Cauchy deformation tensor. Therefore, the strain energy density for the two-body bond stretching potential can be expressed by summing up the atomistic potential energy as follows:

$$w_{\text{bond}}^c = \frac{1}{V_0} U^{\text{bond}} = \frac{1}{V_0} \sum_{\text{bonds}} k_b(r_0)^2 (\sqrt{1 + 2\mathbf{N} \cdot \mathbf{E} \cdot \mathbf{N}})^2. \quad (1.76)$$

It can be seen from Eq. (1.76) that the energy density extracted from the atomistic potential contains the continuum measures such as \mathbf{E} and \mathbf{N} , atomistic potential constant such as k_b , and the atomistic structure information such as r_0 . Equation (1.76) essentially provides a continuum strain energy description with atomistic details involved. We then assume a hyperelasticity material model exists for the DNA molecule, the corresponding stress-strain relationship based on the atomistic potential can be obtained by taking derivative of Eq. (1.76) with respect to the Green-Lagrangian strain tensor \mathbf{E} as

$$\mathbf{S}_{\text{bond}} = \frac{\partial w_{\text{bond}}^c}{\partial \mathbf{E}} = \frac{1}{V_0} \sum_{\text{bonds}} k_b(r_0)^2 \left(1 - \frac{1}{1 + 2\mathbf{N} \cdot \mathbf{E} \cdot \mathbf{N}} \right) \mathbf{M} \quad (1.77)$$

where

$$\mathbf{M} \equiv \begin{bmatrix} N_1^2 & N_1 N_2 & N_1 N_3 \\ N_1 N_2 & N_2^2 & N_2 N_3 \\ N_1 N_3 & N_2 N_3 & N_3^2 \end{bmatrix} \quad (1.78)$$

and N_i is the i th component of the initial bond orientation \mathbf{N} . Similarly, we can obtain the continuum descriptions and stress-strain relations of three-body and four-body potentials based on the atomistic potentials following the same procedures:

3-body potential:

$$w_{\text{angle}}^c = \frac{U^{\text{angle}}}{V_0} = \frac{1}{V_0} \sum_{\text{angles}} k_\theta (\theta_{ijk} - \theta_{ijk}^0)^2, \quad (1.79)$$

$$\mathbf{S}_{\text{angle}} = \frac{\partial w_{\text{angle}}^c}{\partial \mathbf{E}} = \frac{2}{V_0} \sum_{\text{angles}} k_\theta (\theta_{ijk} - \theta_{ijk}^0) \frac{\partial \theta_{ijk}}{\partial \mathbf{E}}. \quad (1.80)$$

4-body potential:

$$w_{\text{dihedral}}^c = \frac{U^{\text{dihedral}}}{V_0} = \frac{1}{V_0} \sum_{\text{dihedrals}} \frac{K_n}{2} (\phi - \phi_0)^2, \quad (1.81)$$

$$\mathbf{S}_{\text{dihedral}} = \frac{\partial w_{\text{dihedral}}^c}{\partial \mathbf{E}} = \frac{1}{V_0} \sum_{\text{dihedrals}} K_n (\phi - \phi_0) \frac{\partial \phi}{\partial \mathbf{E}}. \quad (1.82)$$

The non-bonded interactions are calculated with interatomic potentials by grouping atoms in the same molecule and those in other molecules. The general form of the non-bonded energy of the atomistic system can be written as

$$E_{\text{nb}} = \sum_i \sum_{j > i} V_{\text{nb}}(r_{ij}) \quad (1.83)$$

where V_{nb} is the non-bonded potential, r_{ij} is the distance between superatoms i and j . For DNA molecules, the non-bonded interactions include the van der Waals and Coulomb interactions. They are treated using similar method here. Consider interactions of two unit cells with volume V_0 , with each containing n superatoms. The continuum strain energy density for non-bonded interactions is expressed as^[73]

$$w_{\text{nb}}^c(r) = \left(\frac{n}{V_0}\right)^2 V_{\text{nb}}(r) \equiv \rho_{\text{atom}}^2 V_{\text{nb}}(r) \quad (1.84)$$

where $\rho_{\text{atom}} = n/V_0$ denotes the number density of superatoms per unit cell volume V_0 , and r is the distance between two particles in the deformed configuration. Then, the total energy can be computed by the following integration

$$\Pi^{\text{nb}} = \frac{1}{2} (\rho_{\text{nb}})^2 \int_{\Omega_0} \int_{\Omega_0 - \Omega_X} V_{\text{nb}}(r) d\Omega_0 d\Omega_0 \quad (1.85)$$

where Ω_0 is a sphere of region centered at X with a cutoff radius to exclude the bonded interactions.

Based on the developed continuum hyperelastic material model, we formulate a three-dimensional elastic beam model with contour length L whose internal energy and total energy are given by

$$\Pi^{\text{int}} = \frac{1}{2} \int_0^L \boldsymbol{\kappa}^T \mathbf{D}_b \boldsymbol{\kappa} dS + \frac{1}{2} \int_0^L \boldsymbol{\gamma}^T \mathbf{D}_s \boldsymbol{\gamma} dS + \frac{1}{2} \int_0^L EA\varepsilon^2 dS + \frac{1}{2} \int_0^L GJ\psi^2 dS \quad (1.86)$$

$$\Pi = \Pi^{\text{int}} + \Pi^{\text{nb}} - \Pi^{\text{ext}} \quad (1.87)$$

where $\boldsymbol{\kappa}$ and $\boldsymbol{\gamma}$ are vectors of curvature and strain, respectively, ε is the axial strain, ψ is the twist angle, E and G are the Young's and shear moduli, respectively, A, I and J are the cross-sectional area, moment of inertia, and polar moment of inertia, respectively, Π^{nb} is the non-bonded energy derived previously, Π^{ext} is the external work, and $\mathbf{D}_b = \text{diag}(EI, EI)$ and $\mathbf{D}_s = \text{diag}(GA, GA)$ are bending and shearing stiffnesses, respectively.

The stationary condition of Eq. (1.87) states the equilibrium equation of the 3D beam

$$\delta\Pi = \int_0^L (\mathbf{D}_s \delta\boldsymbol{\kappa} + \mathbf{D}_s \delta\boldsymbol{\gamma} + EA\delta\varepsilon + GJ\delta\psi) dS + \delta\Pi^{\text{nb}} - \delta\Pi^{\text{ext}} = 0. \quad (1.88)$$

The elasticity constants E and G are determined based on the elasticity tensor:

$$\mathbf{C} = \frac{\partial^2 w^c}{\partial \mathbf{E} \partial \mathbf{E}} \quad (1.89)$$

where $w^c = w_{\text{bond}}^c + w_{\text{angle}}^c + w_{\text{dihedral}}^c + w_{\text{nb}}^c$ is the DNA energy density function constructed in Section 1.5.3. By setting $F_{ij} = \delta_{ij}$, the Young's modulus and shear modulus can be extracted from \mathbf{C} .

It is worthy to note that the contribution of the 4-body dihedral angle potential to both shear and Young's moduli is very small, which is only 0.1% of that due to bond stretching potential. We numerically determined the following elasticity constants of pure G–C sequence DNA by summing up the effects due to 2-body bond stretching and 3-body angle potentials:

$$G = 8.7 \times 10^8 \text{ Pa} \quad \text{and} \quad E = 5.1 \times 10^8 \text{ Pa}. \quad (1.90)$$

The above calculated Young's modulus agrees fairly well with the experimental measured quantities, i.e., $E = 0.5 - 0.7 \times 10^8 \text{ Pa}$ ^[74]. However, in the current estimation of the mechanical properties of DNA, we do not consider the solution effect and the sequence-dependent variation, so the presented values could be regarded as the upper bound of the elasticity constants. It is also interesting to note from Eq. (1.90) that the calculated Young's and shear moduli indicate that the corresponding Poisson's ratio is negative, i.e.,

$$\nu = \frac{E - 2G}{2G} \approx -0.7. \quad (1.91)$$

This negative Poisson's ratio was also observed experimentally by Manning^[75] and Baumann^[21], where Poisson's ratios of -0.7 and $-0.4 < \nu < 0$ have been reported. For demonstration purpose, we take 2-body bond stretching potential as an example. Equation.(1.92) gives the expression of the ratio between the shear modulus and the Young's modulus as follows:

$$\frac{G^{\text{bond}}}{E^{\text{bond}}} = \frac{\sum_{\text{bonds}} N_2^2}{\sum_{\text{bonds}} N_3^2}. \quad (1.92)$$

Based on the DNA helical structure, it can be shown that $\sum N_2^2 > \sum N_3^2$, which implies the shear modulus is larger than the Young's modulus, hence resulting in the negative Poisson's ratio. The characterized elasticity constants are also adopted in the three-dimensional beam formulation for the following applications of continuum modeling of DNAs.

1.5.4 Applications

1.5.4.1 Simulations of DNA stretching

For demonstration purpose of the proposed multiscale framework, we first perform a molecular dynamics simulation of a representative segment of DNA molecule with pure G – C sequences as shown in Fig. 1.1. The Verlet velocity time integration algorithm with 1 fs time step size and AMBER force field is used in the MD simulation of stretching DNA molecule. The DNA model is first relaxed to yield its equilibrium position. We then imposed a slightly increased length on the DNA and perform energy minimization accordingly. This allows the DNA to be stretched gradually in equilibrium. A smoothed polynomial function is fit through the total energy curve by least-squares fit as shown in Fig. 1.28a. The corresponding force-extension curve is computed by taking the derivative of the energy polynomial function with respect to a spatial coordinate as illustrated in Fig. 1.28b which is consistent with the single-molecule experiments on DNA under extension^[1,3,5]. Figure 1.29a illustrates the DNA deformed configuration during the stretching process, and the results show that the ds-DNA is unzipped and leads to a significant DNA molecular structural change. This novel ladder form observed in the MD simulation which corresponds to the overstretching transition region in the force-extension curve is consistent with the experimental observation^[3,5].

For simplicity, the solution effect is not considered in the DNA molecular model in the multiscale homogenization. The objective of this work is to construct a coarse-grained model and to formulate the hyperelastic con-

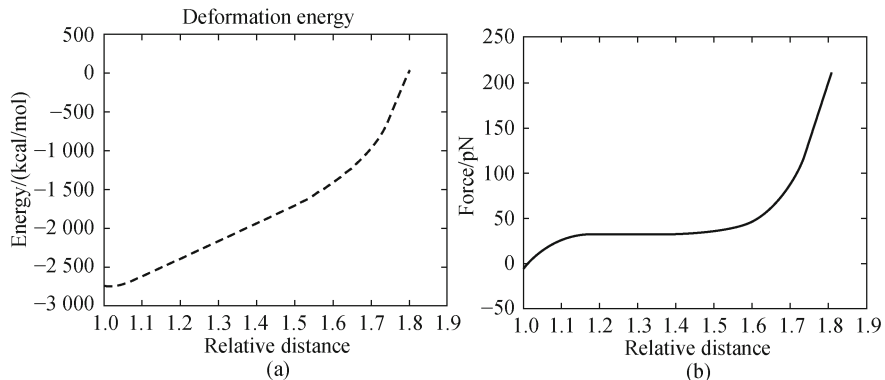


Fig. 1.28 (a) Predicted energy versus extension curve of the full atomistic DNA model, and (b) the corresponding predicted force versus extension curve.

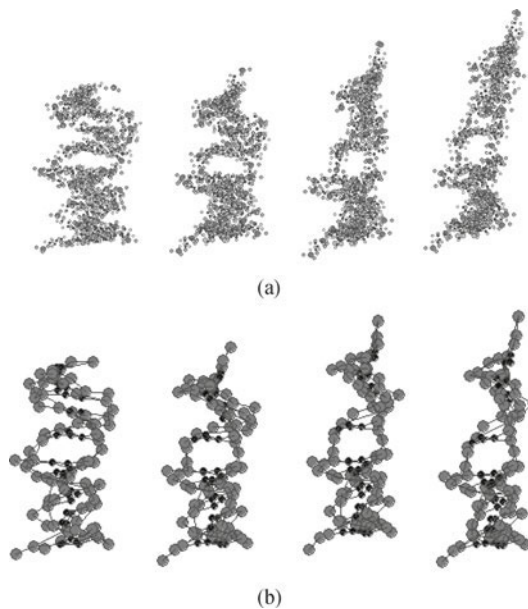


Fig. 1.29 The progressive DNA configurations of (a) full atomistic DNA model, and (b) coarse-grained DNA model. (color plot at the end of the book)

tinuum beam model that can represent the gross response of the fine-scale DNA model. We construct the coarse-grained model following the procedure introduced in Section 1.5.2 as shown in Fig. 1.17c and the corresponding force fields of the coarse-grained DNA model are determined by performing the multiscale wavelet projection. Then, we repeat the stretching process of DNA molecule using the coarse-grained model, and the corresponding energy-extension and force-extension curves and the deformed configurations

are shown in Fig. 1.30a, Fig. 1.30b and Fig. 1.29b, respectively. As we can see from the numerical results, the proposed coarse-grained DNA model is able to predict consistent gross behavior as the full atomistic model, and the homogenized coarse-grained model allows long-time step size and reduces a large number of degrees of freedom leading to the better computational efficiency in three to four orders of magnitude in terms of CPU time.

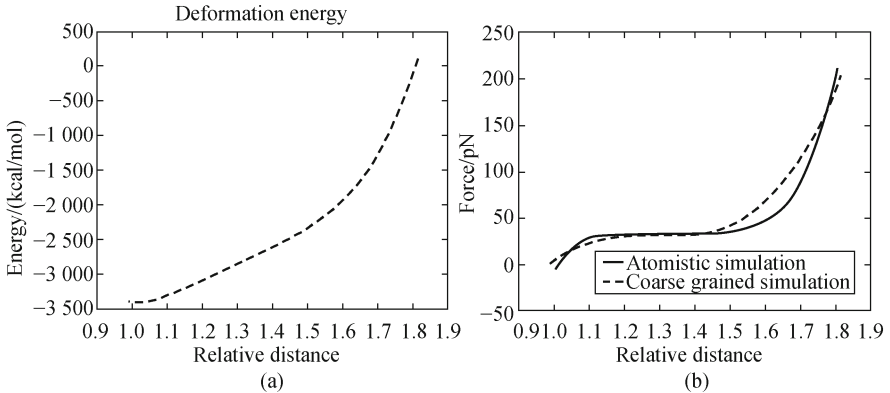


Fig. 1.30 (a) Predicted energy versus extension curve of the coarse-grained DNA model, and (b) the corresponding predicted force versus extension curve.

Next, we model the DNA stretching process by using the proposed continuum beam model through the multiscale two-level homogenization as illustrated in Sections 1.5.2 and 1.5.3. However, we observed from the full atomistic simulation of DNA stretching as shown in Fig. 1.31 that the relative contribution of the 2-body bond stretching energy increases with the increase of DNA extension while the 4-body dihedral angle energy reduces with the DNA further extending. This is due to the molecular structural change from B-DNA to S-DNA in the overstretching transition, and this effect is taken into account by expressing the continuum strain energy function as

$$W = \alpha(s)W^1 + (1 - \alpha(s))W^2 \quad (1.93)$$

where $\alpha(s)$ is a transition function considering the fraction of B-form DNA during the DNA stretching process while $\alpha = 1$ as $s \leq 1.2$ and $\alpha < 1$ as $s > 1.2$. W^1 is the strain energy function derived from the coarse-grained model and W^2 is a phenomenological strain energy function representing the behavior of the S-form DNA and reflecting the rapid strain hardening after transition which is given as follows^[76]:

$$W^2(I_1) = -\frac{G}{2}J_m \ln \left(1 - \frac{I_1 - 3}{J_m} \right) \quad (1.94)$$

where G is the shear modulus, I_1 is the principal invariant of the Green deformation tensor, and $J_m > 0$ is a parameter taking into account the limiting molecule extensibility.

The comparison of force-extension curve between fine-scale simulation and the continuum model is shown in Fig. 1.31. By introducing a transition function from the physical understanding of the DNA stretching process, the continuum model properly captures the behavior of fine scale simulation.

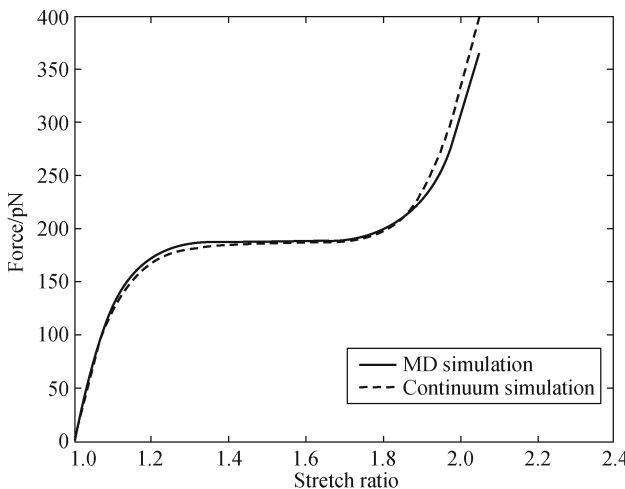


Fig. 1.31 Comparison of force-extension curves between fine-scale simulation and the continuum model.

1.5.4.2 Modeling of DNA loop formation

The loop formation of DNA molecule is one of the important protein-DNA interaction processes in biological systems. We applied the proposed hyperelastic three-dimensional beam to the simulation of the DNA looping associated with a sequence-specific DNA-binding protein—the *lac* repressor (*LacI*), which inhibits the gene coding involved in the metabolism of lactose in bacteria. The *lac* repressor occurs as a tetramer, where the four subunits form a V-shaped molecule as depicted in Fig. 1.32¹. The *lac* repressor protein has three distinct regions: (a) a core domain that binds lactose and other similar molecules, which is divided into *N* and *C* subdomains, (b) a tetramerization domain joining four monomers in an alpha-helix bundle, and (c) a headpiece domain in which two *LacI* proteins bind DNA.

LacI-DNA system in solution contains millions of atoms with time scales spanning from microseconds to milliseconds, and a full atomistic simulation is

¹ 1LBI PDB file for the *lac* repressor is obtained from Protein Data Bank.

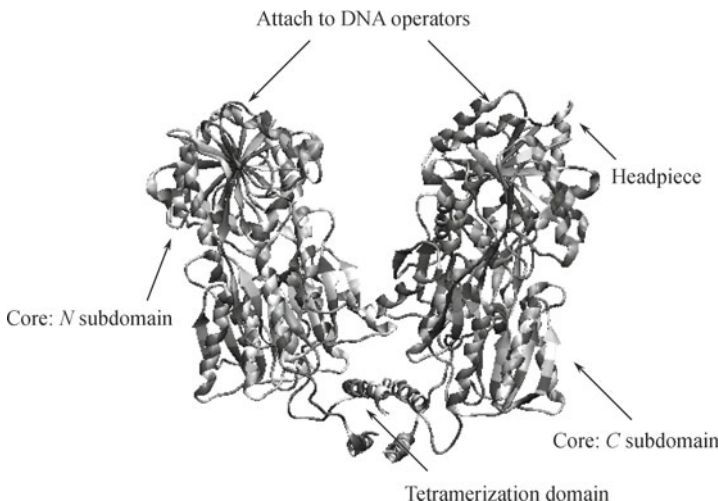


Fig. 1.32 Crystal structure of the *lac* repressor binding DNA. (color plot at the end of the book)

practically unaffordable to investigate the DNA looping behavior. Therefore, the continuum descriptions are preferred to simulate the configuration and free energy of the DNA loop.

In this study, we constructed a three-dimensional hyperelastic beam model of the DNA loop with 76 base pairs long composed of regularly repeating G–C sequences. The elasticity constants are extracted from the multiscale atomistic-continuum model introduced in Section 1.5.4.1, and the DNA loop is modeled by 100 Hughes-Liu beam elements^[77] in DYNA3D^[78]. The *lac* repressor itself is treated as a rigid coupler and the boundary conditions of the beam are obtained from the crystal structure of the *lac* repressor DNA complex^[79]. In the simulation, the two ends of the beam were first moved to their preassumed position as illustrated in Fig. 1.33a, and the two ends were bent to satisfy the above-mentioned boundary conditions. Then, the right end of the beam was rotated around its axial axis to investigate the DNA looping process.

The simulated configurations are shown in Fig. 1.33b which are consistent with Balaeff et al.'s work^[47]. The calculated elastic energy presented in Fig. 1.33c agrees reasonably with the experimentally measured free energy of the DNA loop^[45]. The predicted periodicity of the free energy, which is consistent with the helical periodicity of DNA molecules, can be captured by the continuum beam model. However, since the protein-DNA interaction effect is not considered in the numerical modeling, it results in the deviation of calculated elastic energy from the free energy measured in experiment for short DNA molecules. This will be improved in the future by including the

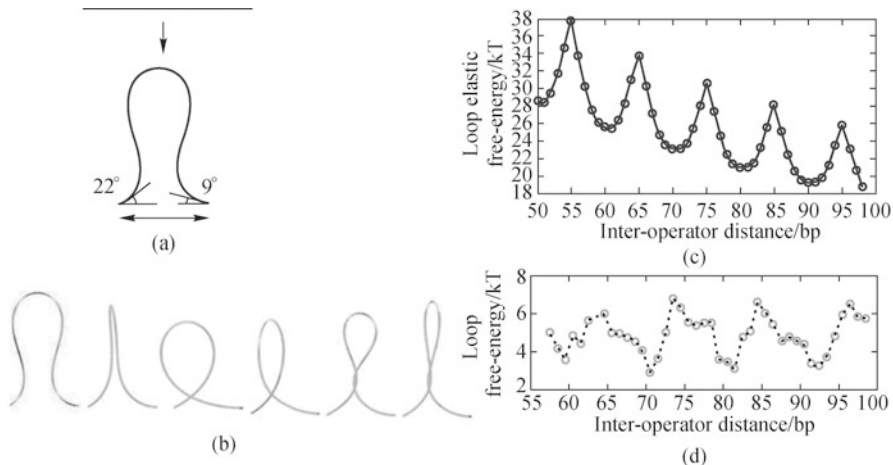


Fig. 1.33 Continuum modeling of DNA loop formation (a) boundary conditions for the continuum beam model, (b) configurations of DNA looping, (c) numerically calculated elastic energy versus DNA length, and (d) experimentally measured loop free-energy versus DNA length.

protein-DNA interactions while treating the *lac* repressor proteins as flexible bodies.

1.6 Conclusion

This chapter presents a state-of-the-art review of mathematical models computational methods, as well as the newly developed multiscale computational approaches, for modeling of DNA molecules. We first reviewed the experimental work on single molecule manipulations of DNAs which reveal the mechanical properties of DNA molecules. The statistical models, such as the FJC and WLC models, were introduced to describe the behavior of DNA molecules in extension, and they are able to capture the force-extension responses in low and intermediate forces. Some modifications were considered to better predict the force-extension responses by taking overstretching transition and electrostatic effects into account. The method of molecular dynamics was presented and numerical results of stretching DNA molecule were presented to demonstrate the effectiveness of MD simulations to investigate the fine-scale behavior of DNA molecules. Due to the time and size limitations of the MD method, continuum approaches, such as the one based on a Kirchhoff theory and the other based on a director field method, were presented. These continuum methods, however, require geometry and material constants that are typically difficult to obtain. A new multiscale multilevel approach was then

introduced. This is based on a multiscale wavelet project method to construct a coarse-grained DNA model, followed by an atomistic continuum homogenization based on a potential equivalence to yield a hyperelastic DNA model with embedded molecular properties. The multiscale DNA model enables systematic characterization of fundamental mechanical properties of DNAs and offers an effective computational framework for modeling DNA molecules.

Acknowledgements

The support of UCLA Dissertation Year Fellowship to the second author is greatly acknowledged.

Appendix: Wavelet and decomposition coefficients for linear spline function

For a linear scaling function candidate, $\varphi^*(x)$ is a hat function with the coefficients c_n 's summarized in the table below:

Table 1.5 Orthogonal expansion coefficients, c_n , for hat candidate function ($c_n = c_{-n}$)

n	c_n
0	1.291 675 492 159 28 E+00
1	- 1.746 632 344 444 64 E-01
2	3.521 011 525 921 82 E-02
3	- 7.874 425 129 503 93 E-03

The wavelet and decomposition coefficients for scale decomposition between scaling function $\varphi(x)$ at scale $j + 1$ and the scaling function $\varphi(x)$ and wavelet function $\psi(x)$ at scale j associated with Eq. (1.59) are given in Table 1.6.

Table 1.6 Wavelet coefficients, ($d_n = d_{-n}$) and decomposition coefficients ($b_n = b_{-n-2}$) for linear spline function

n	d_n	b_n
-1	—	0.817 646 595 961 945
0	8.176 460 570 109 34 E-01	- 0.397 296 919 701 700
1	3.972 970 881 341 91 E-01	- 0.069 101 397 548 309
2	- 6.910 098 674 164 67 E-02	0.051 944 587 049 999
3	- 5.194 534 808 183 84 E-02	0.016 972 531 859 965
4	1.697 104 789 387 06 E-02	- 0.009 987 734 381 633

Continued

<i>n</i>	<i>d_n</i>	<i>b_n</i>
5	9.990 595 444 183 77 E-03	-0.003 888 792 672 210
6	-3.883 262 250 905 55 E-03	0.002 191 236 880 415
7	-2.201 951 238 397 20 E-03	0.000 944 025 366 123
8	9.233 710 054 871 56 E-04	-0.000 473 612 955 027
9	5.116 360 226 930 58 E-04	-0.000 315 829 481 785
10	-2.242 963 267 262 62 E-04	0.000 036 249 000 464

References

- [1] Smith S B, Finzi L, Bustamante C. Direct mechanical measurement of the elasticity of single DNA molecules by using magnetic beads. *Science*, 258: 1122-1126, 1992.
- [2] Perkins T T, Simth D E, Larson R G, et al. Stretching of a single tethered polymer in a uniform-flow. *Science*, 268: 83-87, 1995.
- [3] Cluzel P, Lebrun A, Heller C, et al. DNA: An extensible molecule. *Science*, 271: 792-794, 1996.
- [4] Clausen-Schaumann H, Rief M, Tolksdorf C, et al. Mechanical stability of single DNA molecules. *Biophys J*, 78 (4): 1997-2007, 2000.
- [5] Smith S B, Cui Y, Bustamante C. Overstretching B-DNA: The elastic response of individual double-stranded and single-stranded DNA molecules. *Science*, 271: 795-799, 1996.
- [6] Leger J F, Robert J, Bourdieu L, et al. RecA binding to a single double-stranded DNA molecule: A possible role of DNA conformational fluctuations. *Proc Natl Acad Sci USA*, 95: 12295-12299, 1998.
- [7] Flory P J. Statistical Mechanics of Chain Molecules. Interscience Publishers, New York, 1969.
- [8] Grosberg A Y, Khlokhlov A R. Statistical Physics of Macromolecules. AIP Press, New York, 1994.
- [9] Smith D, Tans S, Smith S, et al. The bacteriophage ϕ 29 portal motor can package DNA against a large internal force. *Nature*, 413: 748-752, 2001.
- [10] Doi M, Edwards S F. The Theory of Polymer Dynamics. Oxford University Press, USA, 1988.
- [11] Kratky O, Porod G. Röntgenuntersuchung gelöster Fadenmoleküle. *Rec Trav Chim Pays-Bas*, 68: 1106-1123, 1949.
- [12] Marko J F, Siggia E D. Stretching DNA. *Macromolecule*, 28: 8759-8770, 1995.
- [13] Bustamante C, Marko J F, Siggia E D, et al. Entropic elasticity of lambda-phage DNA. *Science*, 265: 1599-1600, 1994.
- [14] Bouchiat C, Wang MD, Allemand J F, et al. Estimating the persistence length of a worm-like chain model from force-extension measurements. *Biophys J*, 76: 409-413, 1999.
- [15] Wang M D, Yin H, Landick R, et al. Stretching DNA with optical tweezers. *Biophys J*, 72: 1335-1346, 1997.
- [16] Odijk T. Stiff chains and filaments under tension. *Macromolecules*, 28: 7016-7018, 1995.

- [17] Storm C, Nelson P C. Theory of high-force DNA stretching and over-stretching. *Phys Rev E*, 67: 051906-1-12, 2003.
- [18] Balaeff A, Koudella C R, Mahadevan L. Modelling DNA loops using continuum and statistical mechanics. *Phil Trans R Soc Lond A*, 362: 1355-1371, 2004.
- [19] Odijk T. Polyelectrolytes near the rod limit. *J Polym Sci*, 15: 477-483, 1997.
- [20] Skolnick J, Fixman M. Electrostatic persistence length of a wormlike polyelectrolyte. *Macromolecules*, 10: 944-948, 1977.
- [21] Baumann CG, Smith SB, Bloomfield VA, et al. Ionic effects on the elasticity of single DNA molecules. *Proc Natl Acad Sci USA*, 94: 6185-6190, 1997.
- [22] Allen M P, Tildesly D J. Computer Simulation of Liquids. Clarendon Press, Oxford, 1989.
- [23] Alder B J, Wainwright T E. Phase transition for a hard sphere system. *J Chem Phys*, 27: 1208-1209, 1957.
- [24] Alder B J, Wainwright T E. Studies in molecular dynamics I: General method. *J Chem Phys*, 31: 459-466, 1959.
- [25] Alder B J, Wainwright T E. Studies in molecular dynamics II: Behavior of a small number of elastic spheres. *J Chem Phys*, 33: 1439-1451, 1960.
- [26] Karplus M and McCammon J A. Protein structural fluctuations during a period of 100 ps. *Nature*, 277: 578, 1979.
- [27] Levitt M. Computer-simulation of DNA double-helix dynamics. *Cold Spring Harb Symp Quant Biol*, 47: 251-262, 1982.
- [28] Perez A, Sponer J, Jurecka P, et al. Are the hydrogen bonds of RNA (AU) stronger than those of DNA (AT)? A quantum mechanics study. *Chem*, 11: 5062-5066, 2005.
- [29] Elstner M, Frauenheim T, Suhai S. An approximate DFT method for QM/MM simulations of biological structures and processes. *J Mole Struct Theor*, 632: 29-41, 2003.
- [30] Cornell W D, Cieplak P, Bayly C I, et al. A second generation force field for the simulation of proteins, nucleic acids, and organic molecules. *J Am Chem Soc*, 117: 2309, 1996.
- [31] Brooks B R, Bruccoleri R E, Olafson B D, et al. CHARMM: A program for macromolecular energy, minimization, and dynamics calculations. *J Comput Chem*, 4: 187-217, 1983.
- [32] Perez A, Marchan I, Svozil D, et al. Refinement of the AMBER force field for nucleic acids: Improving the description of alpha/gamma conformers. *Biophys J*, 92: 3817-3829, 2007.
- [33] Beckers JVL, Lowe CP, De Leeuw SW. An iterative PPPM method for simulating Coulombic systems on distributed memory parallel computers. *Mol Simul*, 20: 369-383, 1998.
- [34] Darden T, Perera L, Li LP, et al. New tricks for modelers from the crystallography toolkit: the particle mesh Ewald algorithm and its use in nucleic acid simulations. *Struct Fold Des*, 7: R55-R60, 1999.
- [35] Mazur A K. Accurate DNA dynamics without accurate long-range electrostatics. *J Am Chem Soc*, 120: 10928-10937, 1998.
- [36] Bashford D, Case DA. Generalized born models of macromolecular solvation effects. *Annu Rev Phys Chem*, 51: 129-152, 2000.
- [37] Berendsen HJC, van der Spoel D, van Drunen R. GROMACS: A message-passing parallel molecular dynamics implementation. *Comp Phys Comm*, 91: 43-56, 1995.

- [38] Meller J. Molecular dynamics: encyclopedia of life sciences. John Wiley & Sons, Ltd, 2001.
- [39] Hess B, Kutzner C, van der Spoel D, et al. GROMACS 4: Algorithms for highly efficient load-balanced, and scalable molecular simulation. *J Chem Theory Comput*, 4: 435-447, 2008.
- [40] Love A E H. The Mathematical Theory of Elasticity. Dover, New York, 1944.
- [41] Klug W S, Ortiz M. A director-field model of DNA packaging in viral capsids. *J Mech Phys Solids*, 51: 1815-1847, 2003.
- [42] Klug W S, Feldmann M T, Ortiz M. Three-dimensional director-field predictions of viral DNA packing arrangements. *Comput Mech*, 35: 146-152, 2005.
- [43] Wadati M, Tsuru H. Elastic model of looped DNA. *Physica*, 21D: 213-226, 1986.
- [44] Westcott T P, Tobias I, Olson W K. Elasticity theory and numerical analysis of DNA supercoiling: An application to DNA looping. *J Phys Chem*, 99: 17926-17935, 1995.
- [45] Purohit P K, Nelson P C. Effect of supercoiling on formation of protein-mediated DNA loops. *Phys Rev E*, 74: 061907, 2006.
- [46] Balaeff A, Mahadevan L, Schulten K. Elastic rod model of a DNA loop in the lac operon. *Phys Rev Lett*, 83: 4900-4903, 1999.
- [47] Balaeff A, Mahadevan L, Schulten K. Modeling DNA loops using the theory of elasticity. *Phys Rev E*, 73: 031919, 2006.
- [48] Villa E, Balaeff A, Mahadevan L, et al. Multiscale method for simulating protein-DNA complexes. *Multiscale Model Simul*, 2: 527-553, 2004.
- [49] Starostin E L. Symmetric equilibria of a thin elastic rod with self-contacts. *Phil Trans R Soc Lond A*, 362: 1317-1334, 2004.
- [50] Chamekh M, Mani-Aouadi S, Moakher M. Modeling and numerical treatment of elastic rods with frictionless self-contact. *Comput Mehtods Appl Mech Eng*, 198: 3751-3764, 2009.
- [51] Coleman B D, Swigon D. Theory of self-contact in Kirchhoff rods with applications to supercoiling of knotted and unknotted DNA plasmids. *Phil Trans R Soc Lond A*, 362: 1281-1299, 2004.
- [52] Yang Y, Tobias I, Olson W. Finite element analysis of DNA supercoiling. *J Chem Phys*, 98: 1673-1686, 1993.
- [53] Babuška I. The finite element method with Lagrangian multipliers. *Numer Math*, 20: 179-192, 1973.
- [54] Brezzi F. On the existence uniqueness and approximation of saddle-point problems arising from Lagragian multipliers. *RAIRO Numer Analysis*, 8: 129-151, 1974.
- [55] Ladyshenskaya O A. The Mathematical Theory of Viscous Incompressible Flow. 2nd ed, Gordon and Breach, New York, 1969.
- [56] White J H, Lund R A, Bauer W R. Twist, writhe, and geometry of a DNA loop containing equally spaced coplanar bends. *Biopolymers*, 38: 235-250, 1996.
- [57] White J H, Lund R A, Bauer W R. Effect of salt-dependent stiffness on the conformation of a stressed DNA loop containing initially coplanar bends. *Biopolymers*, 49: 605-619, 1999.
- [58] Riemer S, Bloomfield V. Packaging of DNA in bacteriophage heads—some considerations on energetics. *Biopolymers*, 17: 785-794, 1978.
- [59] Parsegian V A, Rand R P, Fuller N L, et al. Osmotic stress for the direct measurement of intermolecular forces. *Meth Enzymol*, 127: 400-416, 1986.
- [60] Rau D C, Parsegian V A. Direct measurement of temperature-dependent solvation forces between DNA double helices. *Biophys J*, 61: 260-271, 1992.

- [61] Chen J S, Mehraeen S. Multi-scale modelling of heterogeneous materials with fixed and evolving microstructures. *Modelling Simul Mater Eng*, 13: 95-121, 2004.
- [62] Chen J S, Mehraeen S. Variationally consistent multiscale modeling and homogenization of stressed grain growth. *Comput Methods Appl Mech Eng*, 193: 1825-1848, 2004.
- [63] Chen J S, Teng H, Nakano A. Wavelet-based multi-scale coarse graining approach for DNA molecules. *Finite Elem Anal Des*, 43: 346-360, 2007.
- [64] Mehraeen S, Chen J S. Wavelet-based multi-scale projection method in homogenization of heterogeneous media. *Finite Elem Anal Des*, 40: 1665-1679, 2004.
- [65] Mehraeen S, Chen J S. Wavelet Galerkin method in multi-scale homogenization of heterogeneous media. *Int J Numer Meth Eng*, 66: 381-403, 2006.
- [66] Dorobantu M, Engquist B. Wavelet-based numerical homogenization. *J Numer Anal*, 35: 540-559, 1998.
- [67] Nose S. A molecular-dynamics method for simulation in the canonical ensemble. *Mol Phys*, 52: 255-268, 1984.
- [68] Hoover W G. Canonical dynamics-equilibrium phase-space distributions. *Phys Rev A*, 31: 1695-1697, 1985.
- [69] Luty B A, Tironi I G, Vangunsteren W F. Lattice-sum methods for calculating electrostatic interactions in molecular simulations. *J Chem Phys*, 103: 3014-3021, 1995.
- [70] Fukunaga H, Takimoto J, Masao D. A coarse-graining procedure for flexible polymer chains with bonded and nonbonded interactions. *J Chem Phys*, 116: 8183-8190, 2002.
- [71] Ericksen J. The Cauchy-Born hypothesis for crystals. In Phase Transformation and Material Instabilities in Solid by Gurtin M: 61-77, Academic Press, New York, 1984.
- [72] Born M and Huang K. Dynamical Theory of Crystal Lattices. Oxford University Press, New York, 1954.
- [73] Arroyo M, Belytschko T. Finite element methods for the non-linear mechanics of crystalline sheets and nanotubes. *Int J Numer Meth Eng*, 59: 419-456, 2004.
- [74] Gevorkian S G, Khudaverdian E E. Mechanical properties of DNA films. *Biopolymers*, 30: 279-285, 1990.
- [75] Manning G S. Packaged DNA: An elastic model. *Cell Biophy*, 7: 57-89, 1985.
- [76] Gent A N. A new constitutive relation for rubber. *Rubber Chem Technol*, 69: 59-61, 1996.
- [77] Hughes T J R, Liu W K. Nonlinear finite element analysis of shells, part 1: Three-dimensional shells. *Comput Mehtods Appl Mech Eng*, 26: 331-362, 1981.
- [78] Whirley R G, Engelmann B E. DYNA3D: a nonlinear, explicit, three-dimensional finite element code for solid and structural mechanics. (user manual)
- [79] Lewis M, Chang G, Horton N C, et al. Crystal structure of the lactose operon repressor and its complexes with DNA and inducer. *Science*, 271: 1247-1254, 1996.

Chapter 2 Computational Contact Formulations for Soft Body Adhesion

Roger A. Sauer*

*Aachen Institute for Advanced Study in Computational Engineering Science
(AICES), RWTH Aachen University, Templergaben 55, 52056 Aachen,
Germany*

Abstract: This article gives an overview of adhesive contact for soft bodies and focuses on a general computational framework that is suitable for treating a large class of adhesion problems. The contact formulation is based on a non-linear continuum approach that is capable of describing bodies down to length scales of several nanometers. Several finite element formulations are presented, that introduce various approximations in order to increase the computational efficiency. The approaches are illustrated by several examples throughout the text. These include carbon nanotube interaction, adhesion of spheres, nanoindentation, thin film peeling, gecko adhesion and self-cleaning surface mechanisms.

Keywords: adhesion, coarse-graining, computational contact mechanics, finite element method, large deformations, peeling

2.1 Introduction

This article presents an overview of recent progress on the computational modeling of adhesive contact. The demand for computational methods arises since the complexities inherent in adhesive contact problems mostly preclude the use of analytical methods. These complexities include the microstructure, large deformations, nonlinear material behavior and the multiscale and multiphysical nature of many adhesion problems. Computations therefore form an essential part, together with experimental methods, in the study of adhesive contact problems.

The first adhesive contact models that were formulated are the models of Johnson et al.^[1], Derjaguin et al.^[2] and Maugis^[3], which are analytical mod-

*Corresponding author, E-mail: sauer@aices.rwth-aachen.de

els based on the Hertzian contact theory^[4], which in turn is based on linear half-space theory. These models are widely used but have several shortcomings as explained in Section 1.6. With the availability of increasing computational power, accurate computational contact models^[5,6] became available. Recent developments in computational contact mechanics are surface smoothing techniques (see [7, 8, 9] for 2D approaches and [10, 11] for 3D approaches), mortar methods (see [12, 13] for 2D and [14, 15] for 3D approaches), constitutive contact models for friction and adhesion^[16,17], time integration for impact problems^[18], multiscale methods for contact^[19,20], and homogenization methods for contact^[21,22]. Most of the developments in computational contact mechanics are driven by macroscale engineering problem so that formulations for very small length scales have received less attention. At such length scales the approaches of molecular dynamics can be applied to contact problems^[23–25]. But they become quickly inefficient for length scales exceeding several nanometers. Therefore it is advantageous to use coupling methods, that combine atomistic and continuum descriptions, like the “quasi-continuum method”^[26,27], originally formulated for crystalline solids. The quasi-continuum method has been also applied to contact recently^[23]. As an alternative to these coupling methods, one can also coarse-grain the contact behavior at the atomic level into an effective continuum contact formulation. This approach goes back to the analytical integration methods of Bradley^[28] and Hamaker^[29]. These formulations, however, are only valid for rigid bodies, since the contact deformations are not taken into account.¹ These can be taken into account if the framework of molecular coarse-graining is combined with computational contact mechanics^[30]. The model developed there, the so-called “coarse-grained contact model” is used as the basis for the discussion in this article. Two of the major advantages of this model are (a) that it can be used over a wide range of length scales, and (b) that it is particularly suitable for strong adhesion of soft bodies.

The remainder of this paper is structured as follows. Section 2.2 presents the framework of the coarse-grained contact model. Corresponding finite element algorithms are then discussed in Section 2.3. Section 2.4 presents several applications of the contact model. Special attention is placed on peeling contact (Section 2.5) and rough surface contact (Section 2.6). The article concludes with Section 2.7.

¹Taking the deformation into account was already suggested in the thirties by Derjaguin^[31], but it was not achieved until the analytical models of Johnson et al.^[1] and Derjaguin et al.^[2] appeared, as mentioned above.

2.2 Continuum contact formulation

This section presents a theoretical framework for adhesive contact of soft bodies. The formulation is based on the “coarse-grained contact model” introduced by Sauer and Li^[30] and the discussion follows the derivation provided by Sauer^[32] and Sauer and Wriggers^[33]. The key idea is to describe adhesive contact between the bodies by a global interaction potential Π_c , that is based on the local interactions between the individual particles of the neighboring bodies. These local interactions are described by a pair potential ϕ , which, for example, can be taken as the Lennard–Jones potential,

$$\phi(r) := \epsilon \left(\frac{r_0}{r} \right)^{12} - 2\epsilon \left(\frac{r_0}{r} \right)^6. \quad (2.1)$$

Here r denotes the distance of the interacting particles, and ϵ and r_0 are model parameters that describe the strength and range of the interaction. One motivation in using the Lennard–Jones potential is that it is suitable for describing van-der-Waals adhesion. In general, any distance-dependent potential $\phi(r)$ can be used in the following framework.¹ For example, one can also use this framework to construct cohesive zone models.

Figure 2.1a shows the kinematics of two interacting bodies in the framework of nonlinear continuum mechanics. \mathcal{B}_{01} and \mathcal{B}_{02} denote the reference configurations of the two bodies. Their current and deformed configurations are denoted by \mathcal{B}_1 and \mathcal{B}_2 .² The motions mapping two generic material points $\mathbf{X}_1 \in \mathcal{B}_{01}$ and $\mathbf{X}_2 \in \mathcal{B}_{01}$ to the current positions $\mathbf{x}_1 \in \mathcal{B}_1$ and $\mathbf{x}_2 \in \mathcal{B}_2$ are denoted by $\mathbf{x}_1 = \varphi_1(\mathbf{X}_1, t)$ and $\mathbf{x}_2 = \varphi_2(\mathbf{X}_2, t)$. Associated with the two motions are the two deformation gradients $\mathbf{F}_1 = \text{grad } \varphi_1$ and $\mathbf{F}_2 = \text{grad } \varphi_2$, where the gradient operator $\text{grad}(\dots)$ denotes the derivative with respect to the reference configurations \mathcal{B}_{01} and \mathcal{B}_{02} . The two bodies are subjected to the essential and natural boundary conditions

$$\begin{aligned} \varphi_k &= \bar{\varphi}_k, \text{ on } \partial_u \mathcal{B}_k \text{ for } k = 1, 2, \\ \boldsymbol{\sigma}_k \mathbf{n}_k &= \bar{\mathbf{t}}_k, \text{ on } \partial_t \mathcal{B}_k \text{ for } k = 1, 2, \end{aligned} \quad (2.2)$$

where $\bar{\varphi}_k$ and $\bar{\mathbf{t}}_k$ are the values of the prescribed boundary displacement and traction, $\boldsymbol{\sigma}_k$ is the Cauchy stress tensor and \mathbf{n}_k the outward unit normal of $\partial \mathcal{B}_k$. Further, $\partial_u \mathcal{B}_k$ and $\partial_t \mathcal{B}_k$ denote the displacement and traction boundaries in the current configuration which are supposed to satisfy $\partial_u \mathcal{B}_k \cup \partial_t \mathcal{B}_k = \partial \mathcal{B}_k$ and $\partial_u \mathcal{B}_k \cap \partial_t \mathcal{B}_k = \emptyset$. Moreover, we require the initial

¹ $\phi(r)$ must be such that the integration and differentiation appearing in Eqs. (2.11) and (2.15) is well defined.

²The symbol \mathcal{B} is used to denote both the body and the configuration it occupies in \mathbb{R}^3 .

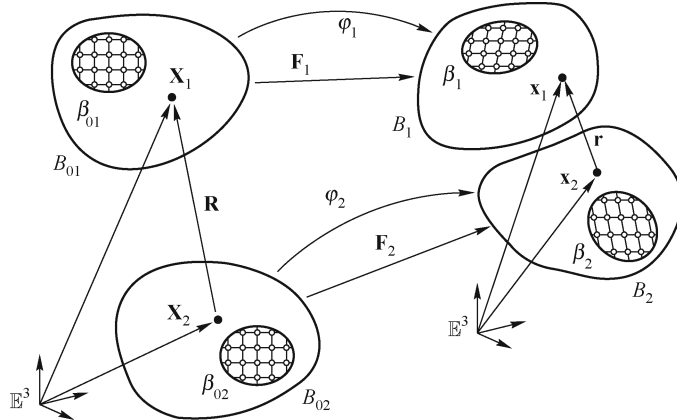


Fig. 2.1 Contact kinematics of two deformable bodies^[30]. The left-hand side shows the undeformed initial configuration; the right-hand side shows the deformed current configuration.

conditions

$$\varphi_k(\mathbf{X}_k, 0) = \varphi_0(\mathbf{X}_k), \quad \dot{\varphi}_k(\mathbf{X}_k, 0) = \mathbf{V}_0(\mathbf{X}_k), \quad \text{in } \mathcal{B}_k, \quad (2.3)$$

where $\dot{\varphi}_k = \frac{\partial}{\partial t} \varphi_k(\mathbf{X}_k, t)$ denotes the material time derivative of φ_k and $\varphi_0(\mathbf{X}_k)$ and $\mathbf{V}_0(\mathbf{X}_k)$ denote the given initial configuration and velocity field of \mathcal{B}_k at $t = 0$.¹ As indicated in Fig. 2.1, the particle densities in the two respective configurations are denoted by β_{0k} (in number of particles per reference volume), and β_k (in number of particles per current volume). The density β_k is related to the mass density by $\rho_k = m_k \beta_k$, where m_k is the mass of the particles in body \mathcal{B}_k . The volume differentials of the spatial configuration, dV_k , and the material configuration, dV_k , are related by

$$dV_k = J_k dV_k, \quad (2.4)$$

where $J_k = \det \mathbf{F}_k$ is the Jacobian determinant of the mapping φ_k . A flux of particles from or into the bodies is not considered. It then follows that the particle and mass densities of the two configurations are in inverse relation to Eq. (2.4), i.e.

$$\beta_k = \beta_{0k} / J_k, \quad \rho_k = \rho_{0k} / J_k, \quad (2.5)$$

and that the total number of particles (and the mass) within a given volume are conserved, i.e. we have

$$\beta_{0k} dV_k = \beta_k dV_k = \text{const.} \quad (2.6)$$

¹The initial configuration of \mathcal{B}_k may or may not coincide with the reference configuration \mathcal{B}_{0k} .

The total potential energy of the two interacting bodies is given by the sum of the internal, external and contact energy, i.e.

$$\Pi = \Pi_{\text{int}} + \Pi_c - \Pi_{\text{ext}}. \quad (2.7)$$

The individual contributions can be defined from the coarse-graining of the corresponding energies of a discrete particulate system^[30]. We thus find the following expressions, which are written in the same form as they usually appear within a continuum mechanical context.

The internal energy of the two bodies is given by

$$\Pi_{\text{int}} = \sum_{k=1}^2 \Pi_{\text{int},k}, \quad \Pi_{\text{int},k} = \int_{\mathcal{B}_{0k}} W_k(\varphi_k) \, dV_k, \quad (2.8)$$

where $W_k(\mathbf{F}_k)$ is the stored energy (per reference volume) of body \mathcal{B}_k that depends on the deformation φ_k . If hyperelastic material behavior of the two bodies is assumed, the first Piola–Kirchhoff stress tensor and the Cauchy stress tensor are given by

$$\mathbf{P}_k = \frac{\partial W_k}{\partial \mathbf{F}_k}, \quad \boldsymbol{\sigma}_k = \frac{1}{J_k} \mathbf{P}_k \mathbf{F}_k^T. \quad (2.9)$$

An example of a suitable material law is the Neo–Hooke model, which is considered for some of the examples discussed in Section 2.4 to 2.6. The internal energy Π_{int} can be complemented by an internal surface energy, expressed analogously as

$$\Pi_{\text{surf}} = \sum_{k=1}^2 \Pi_{\text{surf},k}, \quad \Pi_{\text{surf},k} = \int_{\partial \mathcal{B}_{0k}} U_k(\varphi_k) \, dA_k, \quad (2.10)$$

where $U_k(\varphi_k)$ is the stored surface energy (per reference surface) of body \mathcal{B}_k that depends on the deformation φ_k . Such a framework is suitable to describing membranes and shells^[34] and should also be considered for solids where the surface energy plays an important role.

The contact energy is defined as the total interaction energy between all particle pairs located at positions $\mathbf{x}_1 \in \mathcal{B}_1$ and $\mathbf{x}_2 \in \mathcal{B}_2$. In the continuum limit this is expressed as

$$\Pi_c = \int_{\mathcal{B}_1} \int_{\mathcal{B}_2} \beta_1 \beta_2 \phi(\mathbf{x}_1 - \mathbf{x}_2) \, dv_2 \, dv_1. \quad (2.11)$$

This expression can be easily rewritten as an integration over the reference configurations \mathcal{B}_{0k} due to the relation given in Eq. (2.6).

$\Pi_{\text{ext}} = \Pi_{\text{ext},1} + \Pi_{\text{ext},2}$ is the energy associated with the external loads, i.e. applied surface tractions $\bar{\mathbf{t}}_k$ and body forces $\bar{\mathbf{b}}_k$. We assume $\Pi_{\text{ext},k}$ is

consistent with the variation

$$\delta \Pi_{\text{ext},k} = \int_{\mathcal{B}_k} \delta \boldsymbol{\varphi}_k \cdot \rho_k \bar{\mathbf{b}}_k \, dv_k + \int_{\partial_t \mathcal{B}_k} \delta \boldsymbol{\varphi}_k \cdot \bar{\mathbf{t}}_k \, da_k, \quad (2.12)$$

which expresses the virtual work done by the external loads.

The variation of the other terms lead to the expressions^[32]

$$\delta \Pi_{\text{int},k} = \int_{\mathcal{B}_k} \text{grad}(\delta \boldsymbol{\varphi}_k) : \boldsymbol{\sigma}_k \, dv_k, \quad (2.13)$$

and

$$\delta \Pi_c = \sum_{k=1}^2 \delta \Pi_{c,k}, \quad \delta \Pi_{c,k} = - \int_{\mathcal{B}_k} \delta \boldsymbol{\varphi}_k \cdot \beta_k \mathbf{b}_k \, dv_k, \quad (2.14)$$

where $\text{grad} (\dots)$ denotes the gradient operator w.r.t. the current configuration and \mathbf{b}_k denotes a body force that is defined through the interaction potential ϕ as

$$\mathbf{b}_k(\mathbf{x}_k) := -\frac{\partial \Phi_\ell}{\partial \mathbf{x}_k}, \quad \Phi_\ell := \int_{\mathcal{B}_\ell} \beta_\ell \phi(r) \, dv_\ell. \quad (2.15)$$

Pulling the gradient inside the integral gives the alternative expression

$$\mathbf{b}_k(\mathbf{x}_k) = \int_{\mathcal{B}_\ell} \beta_\ell F(r) \bar{\mathbf{r}}_k \, dv_\ell, \quad (2.16)$$

since

$$\frac{\partial \phi}{\partial \mathbf{x}_k} = -F(r) \bar{\mathbf{r}}_k, \quad (2.17)$$

for $F(r) = -\frac{\partial \phi}{\partial r}$ and

$$\bar{\mathbf{r}}_k := \frac{\mathbf{r}_k}{r_k}, \quad \mathbf{r}_k := \mathbf{x}_k - \mathbf{x}_\ell, \quad r_k := |\mathbf{r}_k|. \quad (2.18)$$

The kinetic energy of the interacting bodies is given by

$$K = \sum_{k=1}^2 K_k, \quad K_k = \frac{1}{2} \int_{\mathcal{B}_k} \rho_k \mathbf{v}_k \cdot \mathbf{v}_k \, dv_k, \quad (2.19)$$

where $\mathbf{v}_k = \dot{\mathbf{x}}_k$ is the velocity field of body \mathcal{B}_k . Given the Lagrangian $L = K - \Pi$, the weak form then follows from Hamilton's variational principle, which states that the action

$$A = \int_{t_1}^{t_2} L \, dt, \quad (2.20)$$

attains its stationary value for the true motion among all kinematically admissible variations within the time interval $\mathcal{T} = \{t_1, t_2\}$ ^[35]. The variation of the action δA of each body \mathcal{B}_k is obtained as

$$\delta A_k = \int_{\mathcal{T}} \int_{\mathcal{B}_k} \rho_k \mathbf{v}_k \cdot \delta \dot{\varphi}_k \, dv_k \, dt - \int_{\mathcal{T}} \delta \Pi_k \, dt, \quad (2.21)$$

where $\delta \Pi_k = \delta \Pi_{\text{int},k} + \delta \Pi_{\text{c},k} - \delta \Pi_{\text{ext},k}$ according to Eqs. (2.7), (2.12), (2.13) and (2.14). By switching the order of integration and by using integration of parts, the first contribution is rewritten as

$$\int_{\mathcal{B}_k} \int_{\mathcal{T}} \rho_k \mathbf{v}_k \cdot \delta \dot{\varphi}_k \, dt \, dv_k = - \int_{\mathcal{B}_k} \int_{\mathcal{T}} \rho_k \dot{\mathbf{v}}_k \cdot \delta \varphi_k \, dt \, dv_k, \quad (2.22)$$

where the variation of the motion $\delta \varphi_k$ is chosen so that it vanishes at $t = t_1$ and $t = t_2$. Following Hamilton's principle the condition $\delta A = 0$ then yields the equation

$$\sum_{k=1}^2 \left[\int_{\mathcal{B}_k} \delta \varphi_k \cdot \rho_k \dot{\mathbf{v}}_k \, dv_k + \int_{\mathcal{B}_k} \text{grad}(\delta \varphi_k) : \boldsymbol{\sigma}_k \, dv_k - \int_{\mathcal{B}_k} \delta \varphi_k \cdot \beta_k \mathbf{b}_k \, dv_k - \delta \Pi_{\text{ext},k} \right] = 0, \quad \forall \delta \varphi_k, \quad (2.23)$$

which is the governing weak form of the contact problem of Fig. 2.1.

Due to the formulation of the contact body forces according to Eq. (2.15), six levels of integration are required in order to evaluate the virtual contact work in Eq. (2.23). While it is straight forward to construct a numerical integration scheme for this^[30], such an approach tends to be very inefficient. This motivates the development of alternative integration methods as discussed by Sauer and Li^[24,30]. The most efficient strategy presented there considers the approximate analytical integration of Eq. (2.15). This approach, which reduces the numerical integration from six levels down to three levels, will be considered in the following. The strategy, outlined in detail by Sauer and Li^[30], consists of two steps:

(1) In order to evaluate the body force \mathbf{b}_k at point $\mathbf{x}_k \in \mathcal{B}_k$, we first project the point perpendicularly onto the neighboring surface $\partial \mathcal{B}_\ell$ ($\ell \neq k$). This gives the surface point $\mathbf{x}_p \in \partial \mathcal{B}_\ell$.¹

(2) Secondly, we approximate the neighboring body \mathcal{B}_ℓ at point \mathbf{x}_p as a flat half-space and integrate field Φ_ℓ , appearing in Eq. (2.15), analytically.

This approach results in an efficient body force formulation which will be denoted in short by "BF" in the remainder of this paper. In [30] a third step is

¹It is important to note that the point $\mathbf{x}_p \in \partial \mathcal{B}_\ell$ depends on point $\mathbf{x}_k \in \mathcal{B}_k$ and is therefore not a material point of \mathcal{B}_ℓ , as the point \mathbf{x}_p , in general, does not follow the motion of \mathcal{B}_ℓ .

taken, which considers projecting the body forces \mathbf{b}_k onto the surface of body \mathcal{B}_k and replaces them by an effective surface traction. This last approach results in an even more efficient surface force formulation, which will be denoted in short by “SF” in the following. The two approaches are illustrated in Fig. 2.2. We note that the closest point projection considered in the first step is a common procedure in computational contact methods^[6]. It depends strongly on the surface where we project onto and it can cause difficulties for non-convex surfaces. In the projection $\mathbf{x}_k \rightarrow \mathbf{x}_p$, we denote the projection distance by r_k and the projection direction by $-\mathbf{n}_p$, which is opposite to the direction of the surface normal \mathbf{n}_p of $\partial\mathcal{B}_\ell$ at \mathbf{x}_p . The approximate half-space integration of Eq. (2.15) according to step 2, which is derived and assessed in [33], yields the simple expression

$$\mathbf{b}_k = \pi\beta_\ell\epsilon r_0^2 \left[\frac{1}{5} \left(\frac{r_0}{r_k} \right)^{10} - \left(\frac{r_0}{r_k} \right)^4 \right] \mathbf{n}_p, \quad (2.24)$$

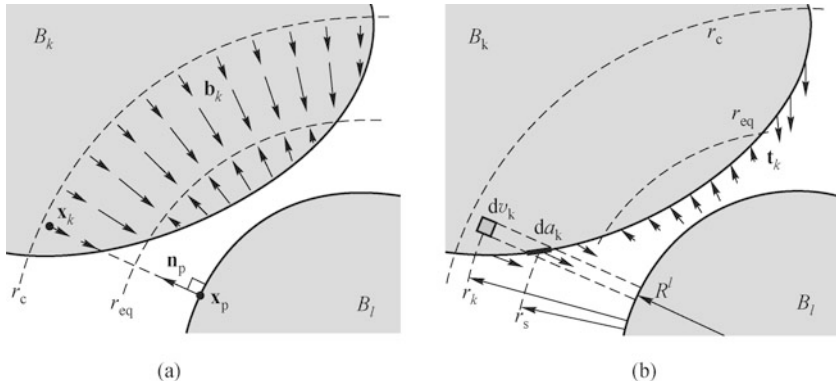


Fig. 2.2 Nanoscale contact-interaction forces according to the body force formulation (a) and the surface force formulation (b)^[33]

for the Lennard–Jones potential (Eq. (2.1)). Here, the density β_ℓ is evaluated at the projection point \mathbf{x}_p . Introducing Hamaker’s constant $A_H = 2\pi^2\beta_{01}\beta_{02}\epsilon r_0^6$ ^[36] we can also write

$$\beta_{0k}\mathbf{b}_k = \frac{A_H}{2\pi r_0^4 J_\ell} \left[\frac{1}{5} \left(\frac{r_0}{r_k} \right)^{10} - \left(\frac{r_0}{r_k} \right)^4 \right] \mathbf{n}_p. \quad (2.25)$$

This expression can be inserted directly into the weak form (Eq. (2.23)). Altogether the BF formulation depends on two parameters, A_H and r_0 , which characterize the strength and range of adhesion.

The SF formulation is obtained by projecting the body force \mathbf{b}_k onto the surface of body \mathcal{B}_k and replacing it by an effective surface traction. The

projection is done parallel to the direction of the body forces in order to keep the balance of angular momentum unaffected. We thus project along $-\mathbf{n}_p$, i.e. in the opposite direction of the surface normal of the neighboring body \mathcal{B}_ℓ at point \mathbf{x}_p . The projection is accomplished by the following integration: According to Fig. 2.2 the volume element dv_k can be expressed by

$$dv_k = c_\ell(r_k) dr_k \cos \alpha_k da_k, \quad (2.26)$$

where da_k denotes the area element obtained from projecting dv_k along $-\mathbf{n}_p$ onto the surface $\partial\mathcal{B}_k$, where c_ℓ is a coefficient that depends on the principle surface curvatures of $\partial\mathcal{B}_\ell^{[33]}$, where r_s denotes the distance between the surfaces of the neighboring bodies, and α_k denotes the inclination of the surface in relation to the direction of projection, that is, we have $\cos \alpha_k = -\mathbf{n}_p \cdot \mathbf{n}_k$. Inserting Eq. (2.26) into the weak form (Eq. (2.23)) we obtain

$$\sum_{k=1}^2 \left[\int_{\mathcal{B}_k} \delta \varphi_k \cdot \rho_k \dot{\mathbf{v}}_k dv_k + \int_{\mathcal{B}_k} \text{grad}(\delta \varphi_k) : \boldsymbol{\sigma}_k dv_k - \int_{\partial_c \mathcal{B}_k} \delta \varphi_k \cdot \mathbf{t}_k \cos \alpha_k da_k - \delta \Pi_{\text{ext},k} \right] = 0, \quad \forall \delta \varphi_k, \quad (2.27)$$

where we have defined the contact traction

$$\mathbf{t}_k := \int_{r_s}^{r_c} c_\ell(r_k) \beta_k \mathbf{b}_k(r_k) dr_k. \quad (2.28)$$

With Eq. (2.28), the body force according to Eq. (2.24) can be easily integrated analytically. Considering the reasonable assumptions $c_\ell \approx 1$ and $\beta_k \approx \text{const}^{[33]}$ one obtains

$$\mathbf{t}_k = \pi \beta_k \beta_\ell \epsilon r_0^3 \left[\frac{1}{45} \left(\frac{r_0}{r_s} \right)^9 - \frac{1}{3} \left(\frac{r_0}{r_s} \right)^3 \right] \mathbf{n}_p. \quad (2.29)$$

In the preceding derivation, the SF formulation is derived as an approximation to the BF formulation. The SF formulation, however, can also be seen as an independent formulation that appears for the case of bodies that only interact via their surfaces^[32].

The contact model governed by Eq. (2.23), or alternatively by Eq. (2.27), is a conservative model, since it is derived from a Lagrangian. In general, dissipative contact models can be formulated by including viscous, i.e. velocity-dependent, damping terms within the internal energy and possibly also within the contact adhesion energy. Dissipation is also introduced if frictional contact is considered. Classical Coulomb-based friction models^[6], however, may be inappropriate for adhesive contact (see Section 2.6). Without considering friction, the contact forces are defined by Eq. (2.24), or alternatively Eq. (2.29), which are normal to the surface of the neighboring body.

2.3 Finite element formulations

This section discusses the 3D finite element formulation of the contact model given in the preceding section. The finite element arrays for the two formulations are derived and the overall contact algorithm is discussed. For general references to non-linear finite element procedures the reader is referred to the monographs of Belytschko et al.^[37] and Wriggers^[38].

The finite element method offers a systematic solution strategy to approximately solve the weak form governing the problem. To facilitate the numerical integration of Eqs. (2.23) and (2.27), the integration domains \mathcal{B}_k and $\partial\mathcal{B}_k$ ($k = 1, 2$) are partitioned into finite volume elements Ω_k^e and surface elements Γ_k^e , that contain a certain number of nodes, denoted by $n_e = n_{ve}$ for Ω_k^e and $n_e = n_{se}$ for Γ_k^e . Within each element ($\mathbf{x}_k \in \Omega_k^e$ or $\mathbf{x}_k \in \Gamma_k^e$), the displacement field \mathbf{u}_k of body \mathcal{B}_k and its variations $\delta\varphi_k$ are approximated by the standard FE interpolation¹

$$\mathbf{u}_k^h(\mathbf{x}_k) = \mathbf{N}_k(\mathbf{x}_k) \mathbf{u}_k^e, \quad \delta\varphi_k^h(\mathbf{x}_k) = \mathbf{N}_k(\mathbf{x}_k) \mathbf{v}_k^e, \quad (2.30)$$

where \mathbf{u}_k^e and \mathbf{v}_k^e are arrays with size $(3n_e \times 1)$ that denote the displacements and variations of the elemental nodes, and

$$\mathbf{N}_k = [N_1 \mathbf{I}, N_2 \mathbf{I}, \dots, N_{n_e} \mathbf{I}] \quad (2.31)$$

is a $(3 \times 3n_e)$ matrix formed by the n_e shape functions N_I ($I = 1, 2, \dots, n_e$) of the element. Inserting approximations (Eq. (2.30)) into the weak forms (Eq. (2.23) and Eq. (2.27)), leads to a discretized weak form which in short can be written as^[32]

$$\mathbf{v}^T [\mathbf{M} \ddot{\mathbf{u}} + \mathbf{f}_{\text{int}} + \mathbf{f}_c - \mathbf{f}_{\text{ext}}] = \mathbf{0}, \quad \forall \mathbf{v} \in \mathcal{V}_h. \quad (2.32)$$

Here the vector $\mathbf{v} \in \mathcal{V}_h$ contains the kinematically admissible virtual displacements of all the finite element nodes and the vectors \mathbf{f}_{int} , \mathbf{f}_c and \mathbf{f}_{ext} denote the internal forces, contact forces and external forces acting on the finite element nodes. These arrays are assembled from the vectors $\mathbf{f}_{\text{int}}^e$, \mathbf{f}_c^e and $\mathbf{f}_{\text{ext}}^e$ that denote the corresponding forces acting on the individual elements and which are listed below. Equation (32) leads to the nonlinear equation

$$\mathbf{f}(\ddot{\mathbf{u}}, \mathbf{u}) := \mathbf{M} \ddot{\mathbf{u}} + \mathbf{f}_{\text{int}} + \mathbf{f}_c - \mathbf{f}_{\text{ext}} = \mathbf{0}, \quad (2.33)$$

where, in general, both \mathbf{f}_{int} and \mathbf{f}_c (and in principle also \mathbf{f}_{ext}) depend nonlinearly on the nodal deformation \mathbf{u} . \mathbf{M} is the mass matrix of the system which,

¹In the following description, \mathbf{u}_k and \mathbf{u}_k^h are used to denote the displacement field and its FE approximation, \mathbf{u}_k^e is used to denote the stacked vector of all nodal displacements of element e , and \mathbf{u} is used to denote the stacked vector of all nodal displacements of the two discretized bodies \mathcal{B}_1^h and \mathcal{B}_2^h . Analogous definitions are used for the reference configuration and the current configuration (characterized by the vector fields \mathbf{X} and \mathbf{x}).

according to Eq. (2.23), is composed of the elemental contributions

$$\mathbf{M}_k^e = \int_{\Omega_k^e} \rho_k \mathbf{N}_k^T \mathbf{N}_k \, dv_k. \quad (2.34)$$

According to Eq. (2.13), which does not consider a velocity dependency, the internal force vector $\mathbf{f}_{\text{int}}^e$ acting on element Ω_k^e can be written as follows^[38]:

$$\mathbf{f}_{\text{int},k}^e = \int_{\Omega_k^e} \mathbf{B}_e^T \boldsymbol{\sigma}_k \, dv_k \quad (2.35)$$

where \mathbf{B}_e is an array with size $(6 \times 3n_e)$ that contains the derivatives of the nodal shape functions N_I .

In the following, four different methods for the evaluation of the contact force \mathbf{f}_c^e are presented. Table 2.1 gives an overview of these methods and lists their main advantages and disadvantages. The first finite element formulation that appears naturally from the body force formulation outlined in Eqs. (2.15) and (2.14) is very simple but inefficient and is therefore denoted as “naive body force FE formulation” (NBF). It is identical to the formulation initially proposed in [30], where it is denoted as “method 1”. According to Eqs. (2.15) and (2.14) it is straightforward to show that the nodal force vector $\mathbf{f}_{c,k}^e$ in $\Omega_k^e \in \mathcal{B}_k$ is given by

$$\mathbf{f}_{c,k}^e = \sum_{\Omega_\ell^e \in \mathcal{B}_\ell^h} \mathbf{f}_{c,\ell}, \quad (2.36)$$

Table 2.1 Comparison of the different contact force evaluation methods in the framework of the finite element method. R_ℓ denotes the minimum curvature radius of the neighboring body^[33]

Formulation	Numerical integration	Advantages	Disadvantages
NBF	Over \mathcal{B}_k and \mathcal{B}_ℓ	Very simple	Very inefficient
NSF	Over $\partial_c \mathcal{B}_k$ and $\partial_c \mathcal{B}_\ell$	Simple	Inefficient
BF	Over \mathcal{B}_k	Efficient	Inaccurate if $R_\ell < 8$ nm
SF	Over $\partial_c \mathcal{B}_k$	Highly efficient & similar to classical contact algorithms	Inaccurate if $R_\ell < 8$ nm and for very strong adhesion

and

$$\mathbf{f}_{c,k}^e = \int_{\Omega_k^e} \int_{\Omega_\ell^e} \mathbf{N}_k^T \beta_k \beta_\ell \frac{\partial \phi}{\partial \mathbf{x}_k} \, dv_\ell \, dv_k, \quad (2.37)$$

where $\partial \phi / \partial \mathbf{x}_k$ is given by Eqs. (2.17) and (2.18). Equation (2.33) is solved iteratively using Newton’s method. Therefore we need to know the tangent matrix \mathbf{k}_c formed by the elemental contributions

$$\mathbf{k}_c^e := \frac{\partial \mathbf{f}_c^e}{\partial \mathbf{u}^e}. \quad (2.38)$$

The force $\mathbf{f}_{c,k}^e$ (Eq. (2.36)) depends on the deformation of the elements $\Omega_k^e \in \mathcal{B}_k$ and $\Omega_\ell^e \in \mathcal{B}_\ell$ ($\ell \neq k$), so that one finds the two tangent contributions

$$\begin{aligned}\mathbf{k}_{c,kk}^e &= \frac{\partial \mathbf{f}_{c,k}^e}{\partial \mathbf{u}_k^e} = \sum_{\Omega_\ell^e \in \mathcal{B}_\ell^h} \mathbf{k}_{c,kk}, \\ \mathbf{k}_{c,k\ell}^e &= \frac{\partial \mathbf{f}_{c,k}^e}{\partial \mathbf{u}_\ell^e} = \mathbf{k}_{c,k\ell},\end{aligned}\quad (2.39)$$

with

$$\begin{aligned}\mathbf{k}_{c,kk} &= \int_{\Omega_k^e} \int_{\Omega_\ell^e} \mathbf{N}_k^T \beta_k \beta_\ell \frac{\partial^2 \phi}{\partial \mathbf{x}_k \partial \mathbf{x}_\ell} \mathbf{N}_k \, dv_\ell \, dv_k, \\ \mathbf{k}_{c,k\ell} &= \int_{\Omega_k^e} \int_{\Omega_\ell^e} \mathbf{N}_k^T \beta_k \beta_\ell \frac{\partial^2 \phi}{\partial \mathbf{x}_k \partial \mathbf{x}_\ell} \mathbf{N}_\ell \, dv_\ell \, dv_k,\end{aligned}\quad (2.40)$$

and

$$\begin{aligned}\frac{\partial^2 \phi}{\partial \mathbf{x}_k \partial \mathbf{x}_\ell} &= \frac{F(r_k)}{r_k} \mathbf{I} + \left[F'(r_k) - \frac{F(r_k)}{r_k} \right] \bar{\mathbf{r}}_k \otimes \bar{\mathbf{r}}_k, \\ \frac{\partial^2 \phi}{\partial \mathbf{x}_k \partial \mathbf{x}_k} &= -\frac{\partial^2 \phi}{\partial \mathbf{x}_k \partial \mathbf{x}_\ell}.\end{aligned}\quad (2.41)$$

In general, this formulation is straightforward to implement, but is very inefficient for practical purposes. Careful attention must be paid to the formulation of symmetry lines^[30]. Similar to this formulation, a “naive surface force FE formulation” (NSF) can be developed. This is based on the analytical integration into the depth of the two bodies which leads to a modification of the interaction potential ϕ . The resulting formulation is analogous to the above NBF formulation, replacing Ω_k^e and Ω_ℓ^e by the surface elements Γ_k^e and Γ_ℓ^e . Details are given in [30, 32], where this formulation is denoted as “method 2”. The NSF formulation is still quite inefficient, especially in 3D.

Therefore it is useful to use the half-space approximation outlined above and replace Eq. (2.15) by Eq. (2.24). This increases efficiency considerably, since numerical integration is only performed over one body. In the resulting finite element body force formulation (BF), the elemental contact force vector acting on the n_{ve} nodes of element Ω_k^e is given by the $(3n_{ve} \times 1)$ vector

$$\mathbf{f}_{c,k}^e = - \int_{\Omega_k^e} \mathbf{N}_k^T \beta_k \mathbf{b}_k \, dv_k = - \int_{\Omega_{0k}^e} \mathbf{N}_k^T \beta_{0k} \mathbf{b}_k \, dV_k, \quad (2.42)$$

which can be evaluated as an integration over either the current or the reference configuration of the element (denoted as Ω_k^e and Ω_{0k}^e). This expression follows directly from Eqs. (2.23), (2.30), (2.31) and (2.32). The tangent as-

sociated with Eq. (2.42) is given by

$$\begin{aligned}\mathbf{k}_{c,kk}^e &= - \int_{\Omega_{0k}^e} \mathbf{N}_k^T \frac{\partial \mathbf{B}_k}{\partial \mathbf{x}_k} \mathbf{N}_k dV_k, \\ \mathbf{k}_{c,k\ell}^e &= - \int_{\Omega_{0k}^e} \mathbf{N}_k^T \frac{\partial \mathbf{B}_k}{\partial \mathbf{x}_p} \frac{\partial \mathbf{x}_p}{\partial \mathbf{u}_\ell^e} dV_k,\end{aligned}\quad (2.43)$$

where we have introduced $\mathbf{B}_k := \beta_{0k} \mathbf{b}_k$. The first matrix, $\mathbf{k}_{c,kk}^e$, has the size $(3n_{ve} \times 3n_{ve})$, where n_{ve} is the number of nodes of element Ω_k^e . The gradient of $\mathbf{B}_k =: B_k \mathbf{n}_p$ is given by^[33]

$$\frac{\partial \mathbf{B}_k}{\partial \mathbf{x}_k} = B'_k \mathbf{n}_p \otimes \frac{\partial r_k}{\partial \mathbf{x}_k} + B_k \frac{\partial \mathbf{n}_p}{\partial \mathbf{x}_k}, \quad (2.44)$$

with $\frac{\partial r_k}{\partial \mathbf{x}_k} = \mathbf{n}_p$ and

$$\frac{\partial \mathbf{n}_p}{\partial \mathbf{x}_k} = \frac{1}{\kappa_1^{-1} + r_k} \mathbf{a}_1^p \otimes \mathbf{a}_1^p + \frac{1}{\kappa_2^{-1} + r_k} \mathbf{a}_2^p \otimes \mathbf{a}_2^p. \quad (2.45)$$

Here κ_1 and κ_2 denote the principal curvatures¹ of the master surface $\partial\mathcal{B}_m$ at the projection point \mathbf{x}_p , and \mathbf{a}_1^p and \mathbf{a}_2^p denote the corresponding tangent vectors at \mathbf{x}_p . The derivative $B'_k = \partial B_k / \partial r_k$ follows readily from Eq. (2.25). The second tangent contribution, $\mathbf{k}_{c,k\ell}^e$, captures the effect of the deformation of surface $\partial\mathcal{B}_\ell$ on $\mathbf{f}_{c,k}^e$ and has the size $(3n_{ve} \times 3n_{se})$, where n_{se} is the number of surface nodes used to interpolate $\partial\mathcal{B}_\ell$ at \mathbf{x}_p . The gradient of \mathbf{B}_k w.r.t., the projection point \mathbf{x}_p can be written as follows:

$$\frac{\partial \mathbf{B}_k}{\partial \mathbf{x}_p} = B'_k \mathbf{n}_p \otimes \frac{\partial r_k}{\partial \mathbf{x}_p} + B_k \frac{\partial \mathbf{n}_p}{\partial \mathbf{x}_p}, \quad (2.46)$$

with $\partial r_k / \partial \mathbf{x}_p = -\mathbf{n}_p$ and

$$\frac{\partial \mathbf{n}_p}{\partial \mathbf{x}_p} = -\frac{1}{r_k} (\mathbf{I} - \mathbf{n}_p \otimes \mathbf{n}_p) \quad (2.47)$$

according to Eq. (2.18). The contribution $\partial \mathbf{x}_p / \partial \mathbf{u}_\ell^e$, appearing in Eq. (2.43), describes how changes of the surface configuration affect the projection point \mathbf{x}_p . It follows from the description of the FE surface and can be computed within the local Newton iteration needed in general to compute \mathbf{x}_p . Further details will be reported in a future publication. If body \mathcal{B}_ℓ is rigid and immobile the tangent contribution $\mathbf{k}_{c,k\ell}^e$ vanishes.

If the body forces are projected onto the surface, according to Fig. 2.2, we obtain the surface force (SF) formulation according to Eqs. (2.27) and

¹Here the curvature is taken to be positive for convex bodies like a sphere.

(2.29). Here, the elemental contact force vector acting on the n_{se} nodes of surface element Γ_k^e is given by the $(3n_{se} \times 1)$ vector

$$\mathbf{f}_{c,k}^e := - \int_{\Gamma_k^e} \mathbf{N}_k^T \mathbf{t}_k \cos \alpha_k dA_k = - \int_{\Gamma_{0k}^e} \mathbf{N}_k^T \mathbf{T}_k \theta_k dA_k, \quad (2.48)$$

where

$$\mathbf{T}_k := J_k \mathbf{t}_k = \pi \beta_{0k} \beta_\ell \epsilon r_0^3 \left[\frac{1}{45} \left(\frac{r_0}{r_s} \right)^9 - \frac{1}{3} \left(\frac{r_0}{r_s} \right)^3 \right] \mathbf{n}_p \quad (2.49)$$

and

$$\theta_k := -\mathbf{n}_p \cdot \mathbf{F}_k^{-T} \bar{\mathbf{N}}_k \quad [33] \quad (2.50)$$

In the equations above \mathbf{N}_k denotes the array of the n_{se} shape function of element Γ_k^e according to Eq. (2.31) while $\bar{\mathbf{N}}_k$ denotes the outward surface normal of Γ_{0k}^e at \mathbf{x}_k . \mathbf{F}_k denotes the deformation gradient at point $\mathbf{x}_k \in \Gamma_k^e$. The vector $\mathbf{f}_{c,k}^e$ can be evaluated as an integration over either the current or the reference configuration of the element (denoted as Γ_k^e and Γ_{0k}^e). In [30] this formulation has been denoted as “method 3”. Considering constant θ_k the tangent matrix of the SF formulation is given by

$$\begin{aligned} \mathbf{k}_{c,kk}^e &= - \int_{\Gamma_{0k}^e} \mathbf{N}_k^T \frac{\partial \mathbf{T}_k}{\partial \mathbf{x}_k} \mathbf{N}_k \theta_k dA_k, \\ \mathbf{k}_{c,k\ell}^e &= - \int_{\Gamma_{0k}^e} \mathbf{N}_k^T \frac{\partial \mathbf{T}_k}{\partial \mathbf{x}_p} \frac{\partial \mathbf{x}_p}{\partial \mathbf{u}_\ell} \theta_k dA_k, \end{aligned} \quad (2.51)$$

where, for $\mathbf{T}_k := T_k(r_k) \mathbf{n}_p$,

$$\begin{aligned} \frac{\partial \mathbf{T}_k}{\partial \mathbf{x}_k} &= T'_k \mathbf{n}_p \otimes \mathbf{n}_p + T_k \frac{\partial \mathbf{n}_p}{\partial \mathbf{x}_k}, \\ \frac{\partial \mathbf{T}_k}{\partial \mathbf{x}_p} &= -T'_k \mathbf{n}_p \otimes \mathbf{n}_p + T_k \frac{\partial \mathbf{n}_p}{\partial \mathbf{x}_p}, \end{aligned} \quad (2.52)$$

analogous to Eqs. (2.43), (2.44) and (2.46). Consider fixed θ_k can actually improve the accuracy of the SF formulation^[33]. If θ_k is kept variable, the additional three tangent contributions

$$\begin{aligned} \mathbf{k}_{c,kk\theta_1}^e &= \int_{\Gamma_{0k}^e} \mathbf{N}_k^T \mathbf{T}_k \otimes \bar{\mathbf{N}}_k \mathbf{F}_k^{-1} \frac{\partial \mathbf{n}_p}{\partial \mathbf{x}_k} \mathbf{N}_k dA_k, \\ \mathbf{k}_{c,kk\theta_2}^e &= \int_{\Gamma_{0k}^e} \mathbf{N}_k^T \mathbf{T}_k \otimes \mathbf{n}_p \frac{\partial \mathbf{F}_k^{-T} \bar{\mathbf{N}}_k}{\partial \mathbf{u}_e} dA_k, \\ \mathbf{k}_{c,k\ell\theta}^e &= - \int_{\Gamma_{0k}^e} \mathbf{N}_k^T \mathbf{T}_k \otimes \bar{\mathbf{N}}_k \mathbf{F}_k^{-1} \frac{\partial \mathbf{n}_p}{\partial \mathbf{x}_p} \mathbf{N}_\ell dA_k, \end{aligned} \quad (2.53)$$

are picked up. Here the first and third contributions are fully specified through Eqs. (2.45) and (2.47). The second contribution, $\mathbf{k}_{c,kk\theta_2}^e$, depends on the

deformation of the volume element Ω_k^e attached behind the surface element Γ_k^e , and therefore has the size $(3n_{se} \times 3n_{ve})$. The matrix

$$\frac{\partial \mathbf{F}_k^{-T} \bar{\mathbf{N}}_k}{\partial \mathbf{u}_e} = \left[\frac{\partial \mathbf{F}_k^{-T} \bar{\mathbf{N}}_k}{\partial \mathbf{u}_1}, \dots, \frac{\partial \mathbf{F}_k^{-T} \bar{\mathbf{N}}_k}{\partial \mathbf{u}_{n_{ve}}} \right] \quad (2.54)$$

consists of the (3×3) blocks

$$\frac{\partial \mathbf{F}_k^{-T} \bar{\mathbf{N}}_k}{\partial \mathbf{u}_I} = (\mathbf{J}_k^{-T} \nabla_{\xi} N_I) \otimes (\mathbf{F}_k^{-T} \bar{\mathbf{N}}_k) \quad (2.55)$$

for $I = 1, \dots, n_{ve}$. Here \mathbf{J}_k denotes the Jacobian of the parametrization of element Ω_k^e . The reader is referred to [33] for a derivation of Eq. (2.55).

Table 2.2 shows the algorithm used to solve the contact problem with the finite element method. The solution algorithm requires four major loops: a loading loop, a Newton iteration loop, a loop over the finite elements and a loop for the numerical quadrature. At the quadrature points of the contact elements we need to determine the projection of these points onto the neighboring surface. This projection is a common task in computational contact mechanics^[32] and may require a second, local Newton iteration. The two elemental loops are needed to assemble the forces \mathbf{f}_{int} and \mathbf{f}_c . We note that for the BF formulation, the vectors \mathbf{f}_c and \mathbf{f}_{int} can, in principle, be evaluated within the same loop, although a higher integration accuracy is usually needed for \mathbf{f}_c . The Newton iteration is used to solve the discretized equilibrium Eq. (2.33). The loading loop is needed to advance the prescribed loading. We further note that no active set strategy is needed in the algorithm. Such a strategy is used to determine if certain contact elements are currently active or not. In the presented approach all contact elements are considered active and no particular distinction is needed, which can result in substantial computational savings. For dynamic problems a time integration scheme, like Newmark's algorithm, has to be considered. The Newmark algorithm leads to a simple modification of the force vector \mathbf{f} and tangent \mathbf{k} ^[38], which can be evaluated at the element level.

The parameter ϵ inside potential ϕ defines the strength of adhesion. For low ϵ the adhesive forces vanish and the resulting contact problem is purely repulsive. For large ϵ , strong adhesive forces appear, which will affect the boundary of the contact area. This is shown in Fig. 2.3, which considers contact between a rigid sphere and a soft substrate^[33]. The figure shows that for strong adhesion a dense mesh refinement is required at the contact boundary. Section 2.5. discusses an enriched finite element method developed to treat such cases efficiently. The strength of adhesion can be characterized by the parameter

$$\gamma_w = \frac{w_0}{W_0}, \quad (2.56)$$

Table 2.2 Solution algorithm for the coarse-grained contact model^[33]

Loading loop: apply load (e.g. prescribed forces, prescribed displacements) in increments; at each load step:

Newton iteration (for obtaining the solution \mathbf{u} to Eq. (2.33))

- Provide starting guess \mathbf{u}_0 , e.g. based on the solution of the previous load step
- Iterate for $i \rightarrow i + 1$ until convergence:

(1) loop over the volume elements Ω_e to compute $\mathbf{f}_{\text{int}}^e$ (Eq. (2.35)) and

$$\mathbf{k}_{\text{int}}^e = \frac{\partial \mathbf{f}_{\text{int}}^e}{\partial \mathbf{u}^e}; \text{ assemble these into the global force and stiffness arrays } \mathbf{f}$$

and \mathbf{k}

(2) NBF: loop over the vol. elements Ω_k^e and Ω_ℓ^e to compute $\mathbf{f}_{c,k}^e$ (Eq. (2.36)) and $\mathbf{k}_{c,kk}^e, \mathbf{k}_{c,k\ell}^e$ (Eq. (2.39)); BF: loop over the volume elements Ω_k^e to compute $\mathbf{f}_{c,k}^e$ (Eq. (2.42)) and $\mathbf{k}_{c,kk}^e, \mathbf{k}_{c,k\ell}^e$ (Eq. (2.43)); SF: loop over the surface elements Γ_k^e to compute $\mathbf{f}_{c,k}^e$ (Eq. (2.48)) and $\mathbf{k}_{c,kk}^e, \mathbf{k}_{c,k\ell}^e$ (Eqs. (2.51) and (2.53)); contributions $\mathbf{f}_{c,k}^e, \mathbf{k}_{c,kk}^e$ and $\mathbf{k}_{c,k\ell}^e$ are computed by numerical quadrature; at each quadrature point \mathbf{x}_k :

- Obtain the projection of \mathbf{x}_k onto the surface of the neighboring body
- BF: evaluate the contact-interaction force according to Eq. (2.25); SF: evaluate the contact-interaction force according to Eq. (2.49)

assemble $\mathbf{f}_{c,k}^e, \mathbf{k}_{c,kk}^e$ and $\mathbf{k}_{c,k\ell}^e$ into \mathbf{f} and \mathbf{k}

(3) Apply boundary conditions

(4) Solve $\mathbf{k} \Delta \mathbf{u} = -\mathbf{f}$ and update $\mathbf{u}_{i+1} = \mathbf{u}_i + \Delta \mathbf{u}$

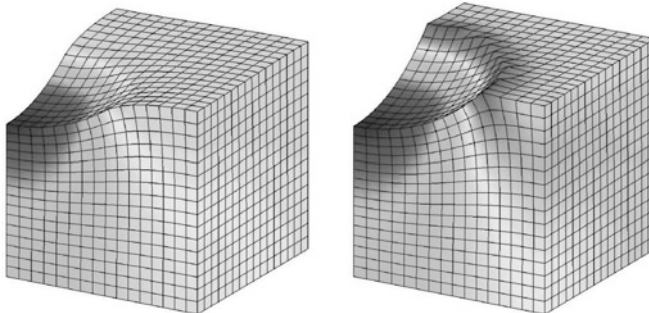


Fig. 2.3 Comparison between weak adhesion ($\gamma_w = 1\,000$, left) and strong adhesion ($\gamma_w = 1$, right)^[33]. Increasing the strength of adhesion has the same relative effect as decreasing the stiffness of the bodies. (color plot at the end of the book)

where W_0 and w_0 denote two energy densities associated with the energy stored in the elastic deformation and in the adhesion. They can be defined

as

$$W_0 = E, \quad w_0 = \frac{A_H}{2\pi^2 r_0^3}, \quad (2.57)$$

where E denotes Young's modulus and A_H denotes Hamaker's constant. According to the definition of Hamaker's constant we can also write $w_0 = \beta_{01}\beta_{02}\epsilon r_0^3$. In the example considered in Figs. 2.3 to 2.5 the adhesion parameter is considered as $\gamma_w = 1\,000$ (weak adhesion) and $\gamma_w = 1$ (strong adhesion).

The computational formulation outlined by the equations in this section converges as Fig. 2.4 shows. This demonstrates the general mesh independence of the contact formulation. The example corresponds to the problem considered in Fig. 2.3. Here the case of strong adhesion is displayed. Figure 2.5 shows the rate of convergence. The rate of convergence is much higher for weak adhesion than for strong adhesion. To capture the deformation and

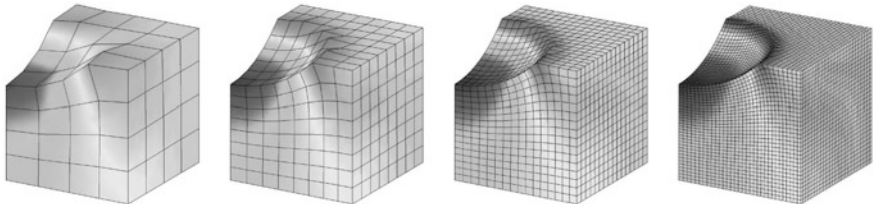


Fig. 2.4 Mesh convergence of the SF formulation (using a mesh with 4^3 , 8^3 , 16^3 and 32^3 finite elements. Contact with a rigid sphere is considered^[33]. (color plot at the end of the book)

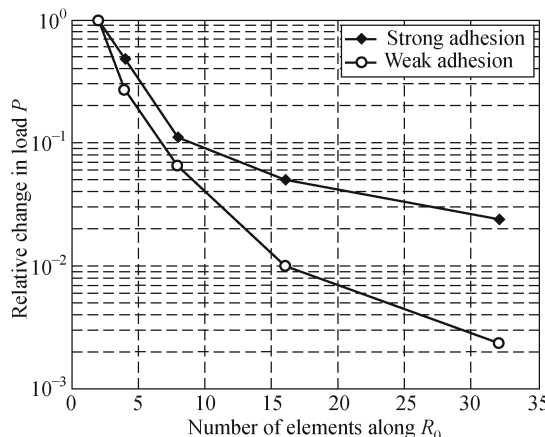


Fig. 2.5 FE convergence rate for contact between a rigid sphere and a soft substrate considering both strong and weak adhesion^[33]. More elements are required to resolve strong adhesion accurately.

stress field of the repulsive contact region at the center of indentation a comparably coarse mesh is adequate. To capture the deformation and stress field of the adhesive contact region at the indentation boundary a comparably fine mesh is required. Therefore, as parameter γ_w decreases (i.e. as the strength of adhesion increases) a larger mesh refinement is required.

The contact forces according to Eqs. (2.24) and (2.49) are always normal to the surface of the neighboring bodies and hence the model is locally frictionless. This is consistent with the observation that atomically smooth surfaces offer only negligible resistance to sliding^[39]. The present contact formulation can still be used to define global friction through dissipative material behavior as is discussed in Section 2.6.

2.4 Adhesion examples

This section presents several numerical examples based on the computational adhesion model outlined in the preceding two sections.

The first example considers the adhesion of (40, 40) carbon nanotubes (CNTs) and is taken from Sauer and Li^[30]. The (40, 40) tube consists of a hexagonal graphene structure with 160 carbon atoms around the circumference. The tube material is modeled linear elastically with Young's modulus $E = 5.0$ TPa, Poisson's ratio $\nu = 0.19$ and wall thickness $t = 0.075$ nm. The non-bonded interaction between distant tube segments is modeled by the Lennard–Jones potential Eq. (2.1) where the parameters are chosen as $r_0 = 0.383$ nm and $\epsilon = 2.39$ meV. Plane strain conditions are considered. Fig. 2.6 shows the undeformed tube, its interaction with a rigid graphite substrate, with neighboring tubes in a bundle and with itself as it collapses (counter-clockwise, starting from the left). All configurations shown are stable and drawn to scale. The tube is modeled by 40 geometrically exact 2-node rod elements^[38]. The black dots in Fig. 2.6 show the FE nodes and not the carbon atoms. Using 40 elements, the atomic density becomes 4 atoms per element corresponding to a reduction in the dofs by about 2.7 compared to a full atomic simulation¹. The results shown in Fig. 2.6 are in agreement with experimental and computational results reported in the literature[40-43].

The second example, that has been published in [17, 44], examines the adhesion of soft spheres. For this case, the JKR^[1] and related models, like the Maugis–Dugdale model^[3], have been formulated. These models are based on linear half-space theory and infinitesimal deformations, which assumes the contact area to be much smaller than the radius of the spheres. For large deformation contact, however, these models cannot be used and one should

¹160 × 2 atomic dofs vs. 40 × 3 nodal FE dofs for plane strain considerations.

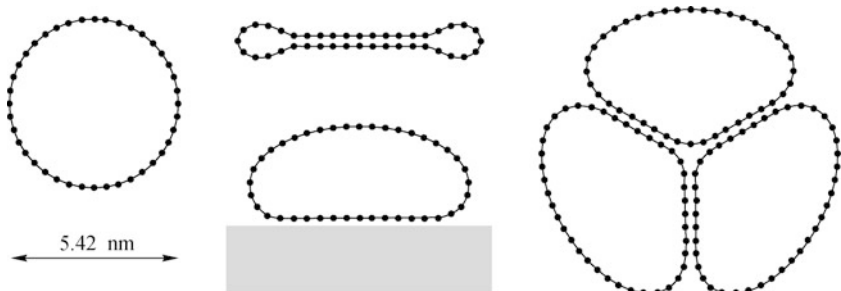


Fig. 2.6 Adhesion of carbon nanotubes^[30].

resort to computational models like the one presented here. Here, contact within a sphere of radius $R_0 = 21$ nm with a flat half-space is considered. In the Maugis model the strength of adhesion is characterized by the parameter $\lambda \in (0, \infty)$. Increasing λ corresponds to increasing adhesion. In fact the limit $\lambda \rightarrow \infty$ reproduces the JKR model as a special case. In the present example the adhesion parameter is chosen as $\lambda = 1.3$. Parameter λ is a model specific parameter that is related but has no explicit correspondence to the physically motivated parameter γ_w . It has been found that the value $\gamma_w = 11.55$ produces a remarkable agreement in the following results.

Figure 2.7 shows the normal contact force P versus the normal contact approach u for the considered problem. For moderate displacements the agreement is excellent. For increasing displacements the two curves diverge since the small deformation assumption used in the Maugis model is no longer valid. For increasing negative displacements, which correspond to separating

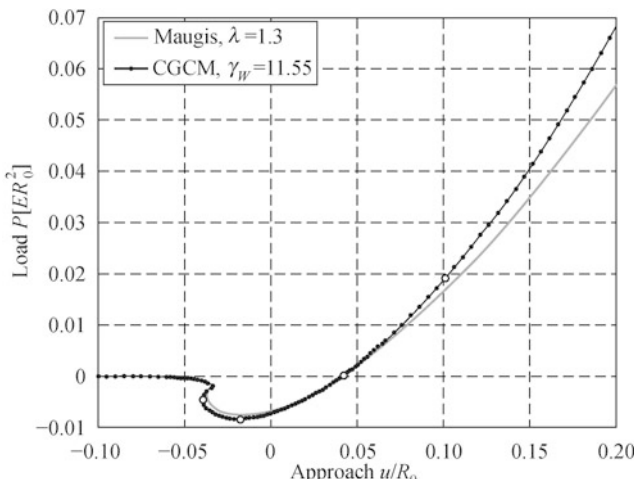


Fig. 2.7 Adhesion of soft spheres: force-displacement curve^[44].

the bodies, the Maugis model loses its applicability since it is not defined there. For the considered parameters a contact instability occurs, which is indicated by the S-shaped section in the force-displacement curve^[30].

To further illustrate the agreement between the two models, the contact pressure between the two bodies is examined in Fig. 2.8. The pressure distribution according to Maugis and the CGC models is shown in the graphs on the right-hand side. The agreement between both models is excellent. The vertical axis displays the radial distance from the center axis measured relative to the sphere radius R_0 . The horizontal axis measures the pressure in multiples of Young's modulus E . Altogether, four cases are shown, which correspond to the four states at $u = -0.0388 R_0$, $u = -0.0176 R_0$, $u = 0.0423 R_0$ and $u = 0.1013 R_0$ that are marked by open circles in Fig. 2.7. According to the Maugis model these correspond to $a = 0.050 R_0$, $a = 0.186 R_0$, $a = 0.329 R_0$ and $a = 0.420 R_0$, where a characterizes the radius of the contact area. The graphs on the left-hand side display the deformation of the contact partners together with the stress field σ_z , which is the stress component in the vertical direction. The stress coloring chosen in the figure ranges from $-0.12 E$ (dark blue) to $0.08 E$ (dark red). Both the stress field, and the pressure distribution show the smooth repulsive compression at the center of contact and the sharp attractive tension at the contact boundary. The agreement between the two models is much better in the repulsive zone than in attractive zone.

The third example considers the computation of the nanoindentation of a thin incompressible rubber film and is taken from Sauer^[44]. A rigid Vickers indenter is considered, which is a four-sided pyramidal indenter with an opening angle of $2 \times 68^\circ$ between opposing faces. The indenter is pressed into a thin film with a considered thickness of $R_0 = 10$ nm. The rubber film is considered perfectly bonded to an underlying rigid substrate. The rubber material is considered nearly incompressible, and is described by the Neo-Hookean material model

$$W(J, \hat{\mathbf{C}}) = U(J) + \frac{\mu}{2}(\hat{I}_1 - 3), \quad (2.58)$$

which is based on a split between the volumetric deformation, described by the determinant of the deformation gradient $J = \det \mathbf{F}$, and the deviatoric deformation, characterized by

$$\hat{I}_1 = \text{tr} \hat{\mathbf{C}}, \quad \hat{\mathbf{C}} = \hat{\mathbf{F}}^T \hat{\mathbf{F}}, \quad \hat{\mathbf{F}} = J^{-\frac{1}{3}} \mathbf{F}. \quad (2.59)$$

The volumetric strain energy is taken as

$$U(J) = \frac{K}{4}(J^2 - 1) - \frac{K}{2} \ln J. \quad (2.60)$$

Parameters K and μ denote the bulk and shear moduli which are related to

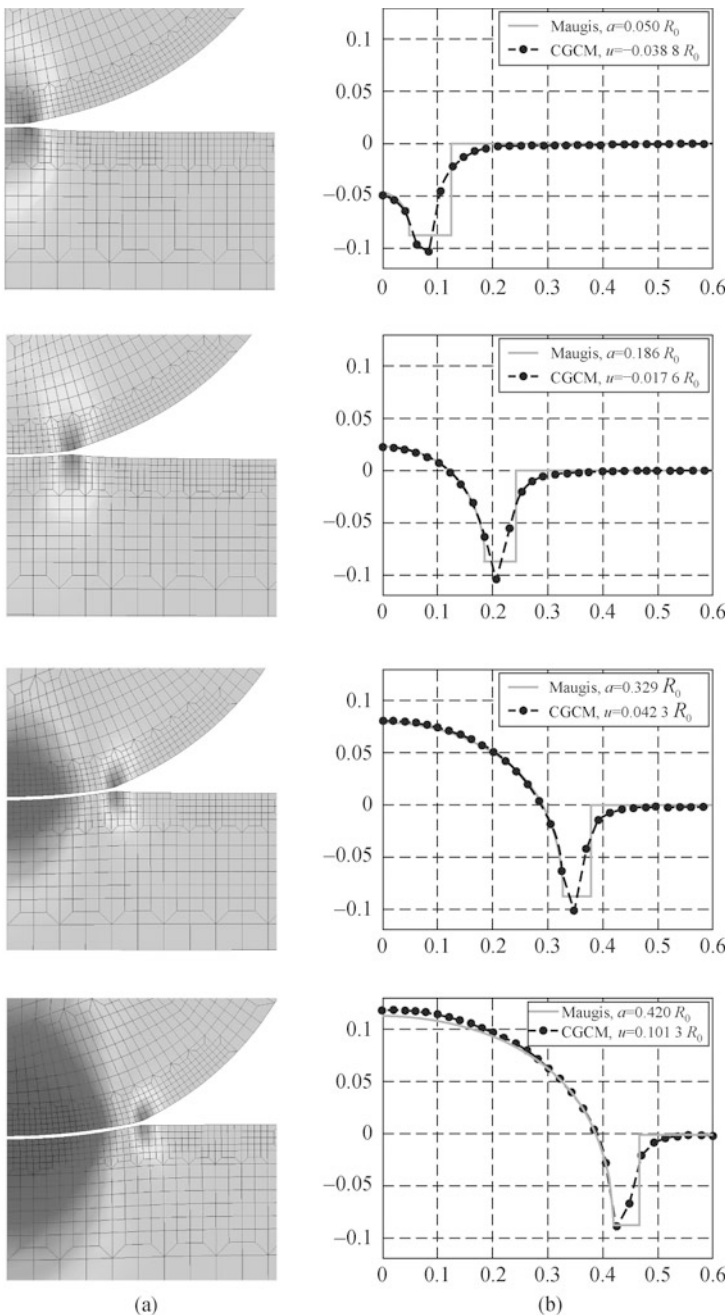


Fig. 2.8 Adhesion of soft spheres: deformation and stress field (a); contact pressure between the two bodies (b)^[44]. The four cases correspond to the four states marked in Fig. 2.7. (color plot at the end of the book)

Young's modulus E and Poisson's ratio ν according to

$$K = \frac{E}{3(1 - 2\nu)}, \quad \mu = \frac{E}{2(1 + \nu)}. \quad (2.61)$$

In the following example Poisson's ratio is chosen as $\nu = 0.499$. E is used for normalization and is thus left unspecified. For the indentation computations a Q1P0 finite element formulation for large deformations is used^[38]. Due to symmetry only one quarter of the contact zone is modeled up to a distance of 30 nm from the indenter tip. Figure 2.9 displays the deformation at $u = 0.5R_0$ for the two cases where the adhesion is very strong (Fig. 2.9a) and very weak (Fig. 2.9b). As observed in Fig. 2.3, strong adhesion leads to large tensile contact forces and surface deformations at the contact boundary, which are not present for weak adhesion. The coloring shown in both figures visualizes the stress field σ_r , which is the stress in the radial direction from the indenter tip. For $\gamma_w = 2.17$, the range of σ_r lies between $-0.55 E$ (blue: compression) and $0.09 E$ (red: tension). Since the tensile stress region is localized in a narrow band at the contact boundary, a high mesh refinement is needed to capture these forces accurately. The adhesion forces lead to the reduction of the resultant contact force: For $\gamma_w = 1\,000$ we have $P = 0.549 ER_0^2$, whereas for $\gamma_w = 2.17$ we only have $P = 0.506 ER_0^2$.

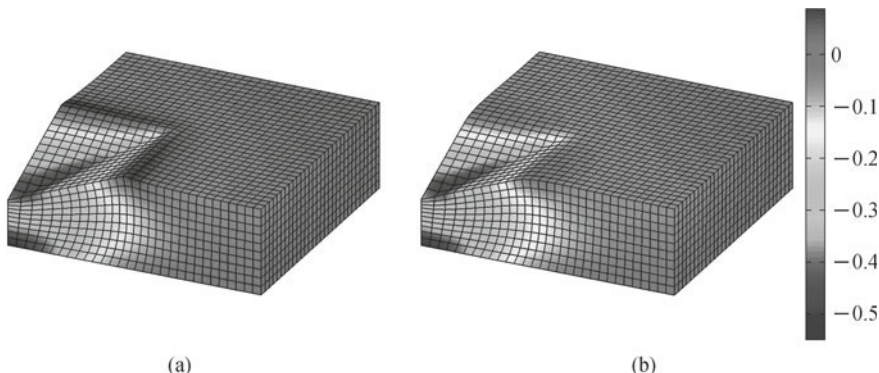


Fig. 2.9 Nanoindentation with strong (a) and weak (b) adhesion^[44]. (color plot at the end of the book)

As a fourth example the dynamic pull-off behavior of an adhering gecko seta is considered^[45]. The seta is a thin, hair-like structure that branches into hundreds of fine tips, the so-called spatulae. The setae are up to 100 μm long and have a cross-sectional diameter of a few micrometers. The spatulae are around 1 μm long and have a cross-sectional diameter of around 100 nm. The adhesion between seta and substrate occurs predominately at the spatula pad, which forms the tip of the spatula and is several hundred

nanometers long and wide, but only a few nanometers thick. The thinness of the pad gives it great flexibility to deform and adapt to the inclination and roughness of the substrate surface. Since the seta dimensions are several orders of magnitude larger than the range of intermolecular adhesion, a hierarchical, three-dimensional multiscale procedure is developed in [20] that spans six orders of magnitude and is able to efficiently simulate the mechanical behavior of a gecko seta during adhesion. The multiscale approach is based on the three distinct modeling levels illustrated in Fig. 2.10. Within the multiscale approach, the coarse-grained contact model is used to model the molecular interaction between the spatula pad and the underlying substrate. The spatula itself is modeled as a thin elastic rod with varying cross-section. At the seta level, a fractal geometry model is constructed that captures the hierarchical branching of the seta. A geometrically exact rod formulation is used to capture the nonlinear kinematics of large deformations^[20]. The constitutive behavior of the seta and spatula is described by a linear elastic isotropic material law with Young's modulus $E = 2 \text{ GPa}$ and Poisson's ratio $\nu = 0.2$. The density is assumed to be $\rho = 1\,000 \text{ kg/m}^3$. The adhesion parameters are chosen as $A_H = 10^{-19} \text{ J}$ and $r_0 = 0.4 \text{ nm}$. Further details of the model, particularly the geometry and the FE rod formulation, are reported by Sauer^[20]. The multiscale seta model described above is used to analyze

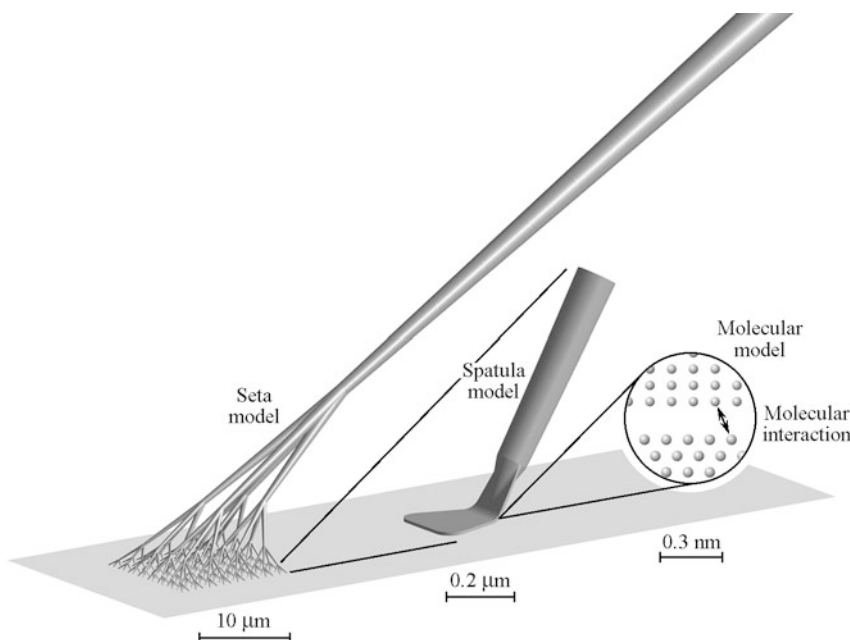


Fig. 2.10 Multiscale model describing the adhesion mechanism of the gecko seta^[20].

the dynamic pull-off behavior of the seta. Therefore, a vertical displacement $u(t)$ is applied to the shaft of the spatula and seta so that the pull-off velocity $v = \dot{u}$ is constant. The rotations and horizontal displacements of the shaft are considered fixed. Figure 2.11 shows the deformation of the spatula and seta and the corresponding force-displacement curves during pull-off. For the considered velocities and model parameters, the maximum pull-off force of a single spatula lies in the range of 8—17 nN, which is in very good agreement with the values observed by Huber et al.^[46] and Sun et al.^[47]. For the clarity of the figure, the entire spatula pull-off curve is only shown for the case $v = 0.1$ m/s, while the other cases are shown only prior to jump-off-contact. The pull-off behavior of the gecko spatula is characterized by peeling, which is discussed in further detail in the following section. The pull-off behavior of the spatula is inserted into the seta model as a contact law for the seta tips. The maximum pull-off force of the seta that is then obtained lies in the range of 0.4—1.4 μ N. These pull-off forces do not agree with the value reported by Autumn et al.^[48]. However the values of Autumn et al. are also inconsistent with the findings of Huber et al.^[46] and Sun et al.^[47]. Newmark's integration algorithm^[38] has been used for the computations.

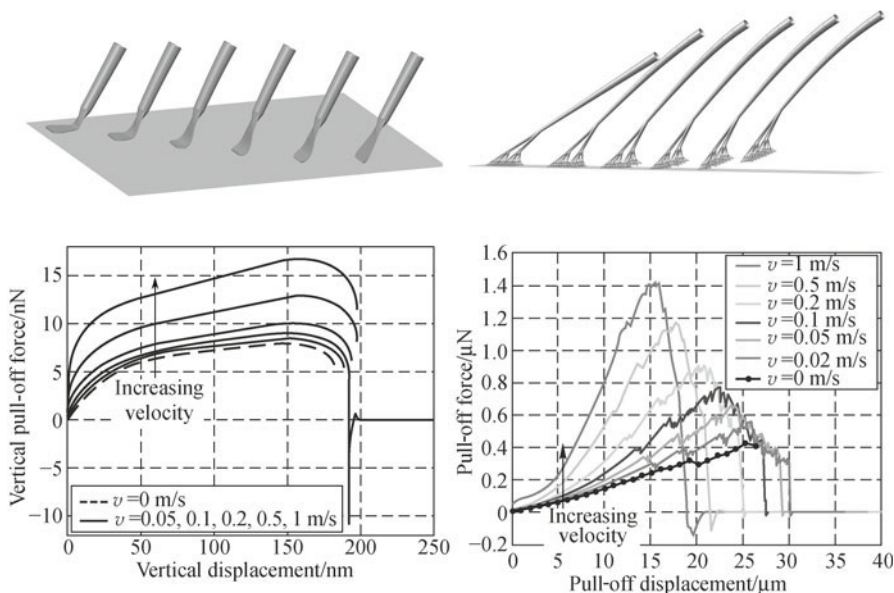


Fig. 2.11 Pull-off computation of a gecko spatula (left) and seta (right); deformation (top) and force-displacement curve (bottom)^[45]. (color plot at the end of the book)

There is a long list of further examples that can be analyzed by the presented contact formulation. These include thin film peeling^[49], MEMS stic-

tion^[50], delamination^[51], atomic force microscopy (AFM), cell adhesion^[52-54], particle adhesion to liquid surfaces^[55], rough surface adhesion^[56], interactions of nanoparticles^[57] and synthetic adhesion mechanisms^[58]. The cases of peeling and rough surfaces are further examined in the following sections.

2.5 Peeling contact

The separation of strongly adhering soft bodies is often characterized by peeling. The understanding of the peeling behavior is therefore central to many important applications in coating, bonding and adhesion technology. Examples include the bonding properties of thin films and the adhesion mechanisms of various insects and lizards. There is also a standardized peeling test used to analyze the properties of adhesives and adherents. For very thin elastic films, where the bending stiffness can be neglected, the peeling behavior can be characterized by the analytical model of Kendall^[49]. But for general applications computational approaches must be used. Adhesive peeling is closely related to cohesive fracture and therefore finite element based cohesive zone models are often considered for peeling computations^[59-62].

A challenge in the computation of peeling problems are the large peeling stresses that can occur in a very narrow zone at the peeling front, as shown in the example of Fig. 2.12. Considered is a strip with length $\ell = 200 L_0$ and height $h = 10 L_0$ adhering to a rigid substrate. The strip is peeled off the substrate by applying a rotation θ incrementally at the right boundary. The strip is modeled by an isotropic, nonlinearly elastic Neo-Hooke material with $E = 2$ GPa and $\nu = 0.2$. Plain strain conditions are considered. Adhesive contact is considered along 75% of the bottom surface (from $x = 0$ to $x = 150 L_0$) using the contact model described above with $r_0 = 0.4$ nm and

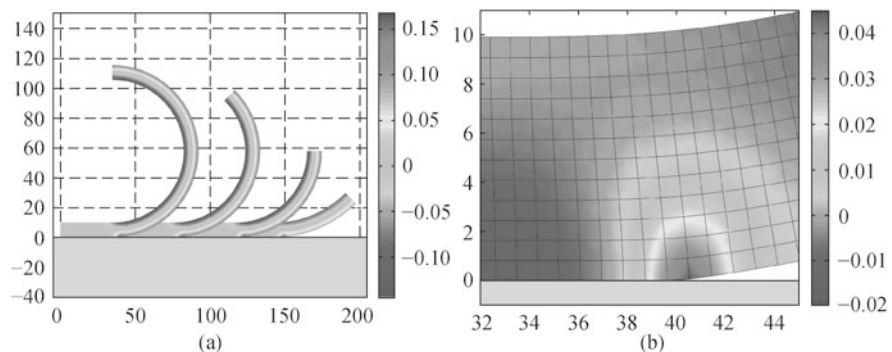


Fig. 2.12 Peeling of an elastic strip by an applied end rotation: deformation of the strip (a); stress at the peeling front (b)^[63]. (color plot at the end of the book)

$A_H = 10^{-19}$ J, which are the values associated with gecko adhesion.

Classical finite element (FE)-based contact formulations often lead to a dilemma: either a highly refined FE description is chosen, which is computationally expensive or a coarse description is used, which is efficient but inaccurate and perhaps even unstable during computations. It therefore becomes desirable to develop improved computational contact formulations for peeling that are both accurate and efficient.

Such a formulation is proposed by Sauer^[63]. The approach is based on a local enrichment of the contact surface so that the contact surface representation is more accurate than the bulk representation. Therefore, a new class of enhanced surface elements for contact is developed. The simplest of these is the so-called Q1C2 element which approximates the contact surface by a quadratic interpolation while the bulk is approximated by a linear interpolation. This is achieved by adding a surface node to the standard 4-node quadrilateral (the Q1 element). The shape functions of the Q1C2 element, expressed in the master configuration ($\Omega_e = (|\xi| \leq 1, |\eta| \leq 1)$), thus are

$$\begin{aligned} N_1 &= \frac{1}{4}(\xi^2 - \xi)(1 - \eta), \\ N_2 &= \frac{1}{4}(\xi^2 + \xi)(1 - \eta), \\ N_3 &= \frac{1}{4}(1 + \xi)(1 + \eta), \\ N_4 &= \frac{1}{4}(1 - \xi)(1 + \eta), \\ N_5 &= \frac{1}{2}(1 - \xi^2)(1 - \eta), \end{aligned} \quad (2.62)$$

so that the displacement is approximated by

$$\mathbf{u}_e^h = \sum_{I=1}^5 N_I \mathbf{u}_I. \quad (2.63)$$

This element is combined with a standard Q1 formulation within the bulk, so that the interpolation is linear in the bulk and quadratic on the surface. In the first element layer a transition zone exists, where the formulation is still quadratic, due to the influence of the surface nodes. Formally this is written as

$$\begin{aligned} \mathbf{u}^h &\in \mathcal{P}^1 \text{ in } \mathcal{B}^h, \\ \mathbf{u}^h &\in \mathcal{P}^2 \text{ on } \partial_c \mathcal{B}^h, \end{aligned} \quad (2.64)$$

where \mathcal{P}^1 denotes the space of continuous, piecewise linear functions (bilinear to be precise) and \mathcal{P}^2 denotes the space of continuous, piecewise quadratic

functions. The enriched 5-node quadrilateral satisfies the compact support condition

$$N_a(\xi_b, \eta_b) = \delta_{ab}, \quad (2.65)$$

at the nodes, and the partition of unity

$$\sum_{I=1}^5 N_I = 1 \quad \forall \xi, \eta. \quad (2.66)$$

Since the element is linear in the bulk and quadratic on the contact surface, it is denoted as Q1C2 in the following. With this notation a standard displacement-based contact formulation is a Q1C1 finite element formulation. Since each node has two dofs, the Q1C2 element has 10 dofs in total.

In principle, the Q1C2 element has the same contact accuracy as a fully quadratic finite element contact description^[64], but is much more efficient. The new elements are initially developed to improve peeling computations but they also show improved behavior for sliding computations. The approach is quite simple, efficient and very effective.

The new enriched contact elements achieve a substantial improvement in peeling computations compared to standard contact formulations. This is shown in Fig. 2.13, which reports the force-displacement curve for the peeling example given in Fig. 2.12. Instead of an oscillatory result the new elements smoothen the forces. Due to the reduction of the oscillations the computation is much more robust. A detailed assessment of the increased accuracy of the new element formulations is discussed by Sauer^[63]. This work also contains a surface enrichment based on Hermite polynomials, the Q1CH element formulation, which constructs an approximation that is continuous (C^0) within the domain \mathcal{B}^h , and continuously differentiable (C^1) on the contact surface $\partial\mathcal{B}^h$, i.e.

$$\begin{aligned} \mathbf{u}^h &\in C^0 \quad \forall \mathbf{x} \in \mathcal{B}^h, \\ \mathbf{u}^h &\in C^1 \quad \forall \mathbf{x} \in \partial_c \mathcal{B}^h. \end{aligned} \quad (2.67)$$

The C1QH formulation gives highly accurate results in peeling and contact sliding computations. An extension of the enrichment strategy to 3D is also shown by Sauer^[63]. For very thin films, the peeling kinematics can also be described accurately by non-linear rod formulations^[65], which provide an efficient alternative to solid formulations.

The enriched contact formulation is suitable to studying the peeling behavior of complex, three-dimensional structures like gecko spatula. The spatulae form the tips of the fine hairs that coat the gecko toes, being responsible for the adhesion mechanism used by the gecko. They transfer the tensile forces between substrate and the gecko toes during adhesion. The spatula consists

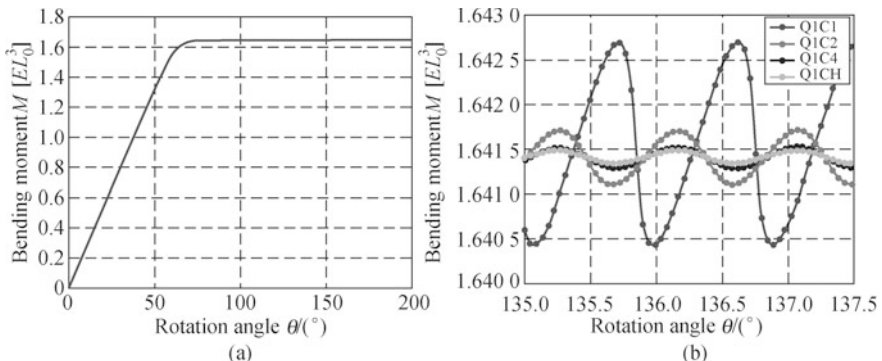


Fig. 2.13 Peeling forces: force-displacement curve (a); oscillation in the force-displacement curve (b)^[63]. (color plot at the end of the book)

of a cylindrical shaft connected to a very thin and flexible pad that can adapt and adhere to the underlying substrate. The entire spatula is about 1 000 nm long (see [20, 66] for further geometrical details). Figure 2.14 shows a finite element computation of a gecko spatula adhering to a flat substrate. The angle between substrate and spatula shaft is considered to be at 60° . Due

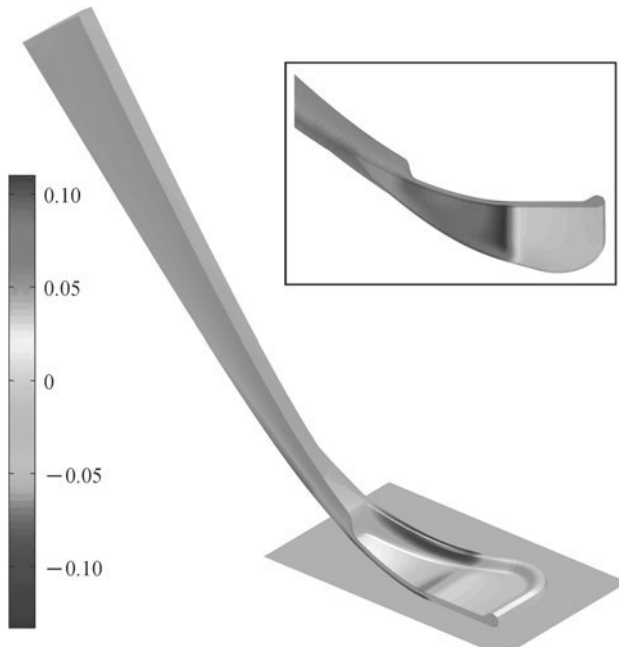


Fig. 2.14 Finite element computation of the peeling of a single gecko spatula^[66]. (color plot at the end of the book)

to symmetry, only half of the spatula is modeled. Around 100 000 elements are used. The contact configuration shown in Fig. 2.14 has a zero net contact force. Large deformations and high stresses occur inside the spatula pad at the boundary of the contact zone. The coloring shows the distribution of the stress $I_1 = \text{tr } \sigma$. The maximum adhesive stress appears at the underside of the pad and has a value of about $0.11E$. The material parameters used for this computation are $E = 2 \text{ GPa}$, $\nu = 0.2$, $A_H = 10^{-19} \text{ J}$ and $r_0 = 0.4 \text{ nm}$, which results in $\gamma_w = 25.3$ according to Eqs. (2.56) and (2.57). Further details of the modeling and simulation of spatula adhesion are discussed by Sauer and Holl^[66].

2.6 Rough surface contact

Real surfaces are not perfectly flat but are characterized by various roughness levels at different length scales, that affect the contact behavior like friction, adhesion, conductivity and wetting^[56,67].

The earliest approaches studying rough surface contact are based on elastic half-space theory and use the analytical solutions of Boussinesq and Hertz^[68]. In order to integrate the effect of multiple contact points, researchers have developed both statistical and deterministic methods:

One of the first studies of rough surface contact is the seminal work of Greenwood and Williamson^{[69]¹}. The Greenwood–Williams (GW) model assumes that the surface roughness follows from a known, e.g. Gaussian, distribution and assumes that all local contacts behave according to Hertzian theory. The GW model has been extended to adhesive contact based on the analytical JKR and DMT contact theories^[70,72]. Recently an extension to adhesion has also appeared by Persson^{[71]²}.

The Greenwood–Williams model does not account for the actual position of local contacts nor does it reflect the fractal nature of rough surfaces. Therefore a second approach, also based on half-space theory, has appeared which considers the integration of the point load solution of Boussinesq over the contact surface. Using a discrete surface representation, a relation between contact displacement and pressure is obtained based on influence coefficients. This approach has also been denoted as the matrix inversion method^[73–77]. Deterministic roughness models together with linear elastic half-space theory have also been applied to frictional contact with adhesion^[78].

The drawback of half-space methods is that they rely on several restricting assumptions. These are: (a) simplified geometry, like that of spheres and half-

¹An earlier study appeared in the 1940s by Zhuravlev^[81].

²This approach was criticized by Borodich^[82].

spaces, (b) small deformation theory and (c) linear material behavior. These assumptions can be suitable for stiff bodies. For soft bodies, on the other hand, large contact deformations can occur, which requires the use of non-linear kinematics, so that the approaches mentioned above cannot be used. Therefore the framework of non-linear continuum mechanics in conjunction with finite element methods offers an ideal framework to study rough surface contact and include the effects of friction and adhesion^[79,80]. For van der Waals adhesion, the continuum contact model outlined in Section 2.2 offers a suitable framework to study rough surface contact. As an example, Fig. 2.15 shows the stress and deformation within a soft elastic block in contact with a rough rigid surface. The surface roughness is described by asperities that

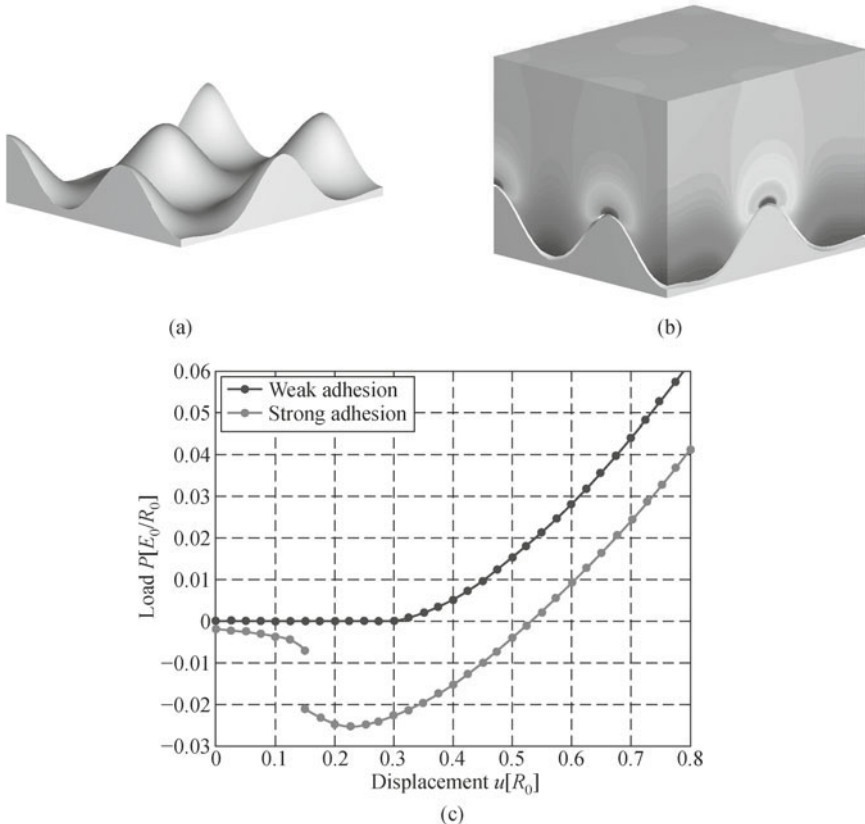


Fig. 2.15 Rough surface contact: surface roughness (a); contact deformation and stress of a soft elastic block pressed onto the surface (b); (c) force-displacement curve considering strong adhesion ($\gamma_w = 2$) in contrast to weak adhesion ($\gamma_w = 1\,000$). Equivalently, this corresponds to comparing a soft block with a stiff block for fixed adhesion strength. The data is normalized by the asperity spacing R_0 and the energy $E_0 = ER_0^2$. (color plot at the end of the book)

follow a Gaussian profile. The block is modeled by a Neo–Hookean material model with initial Young's modulus E , that is left unspecified, and Poisson's ratio $\nu = 0.2$. The coloring shows the distribution of the vertical normal stress component σ_{33} which lies in the range of 0 to $-1.4 E$. The load-displacement curve in Fig. 2.15 shows that the strength of adhesion, which is represented by the parameter γ_w according to Eq. (2.56), has a large effect on the contact forces. A big difference also occurs for the local contact deformation and stress, similarly as observed in Figs. 2.3 and 2.9.

It is known that increased roughness tends to cause an increase of the friction forces and a decrease of the adhesion forces. In many cases, however, the exact nature of these mechanisms is not yet fully understood, especially for soft materials undergoing large contact deformations. Further research is therefore needed to determine the precise effect of surface roughness on adhesion and friction. Classical friction laws, like Coulomb's law, require compressive contact forces in order to provide frictional resistance, and are therefore not applicable to describing friction under adhesive, i.e. tensile, forces as they can be observed in lizard and insect adhesion^[83]. So far, the following origins of friction have been identified:

(1) Atomic friction^[39,84,85], which offers resistance to the sliding of atomically flat surfaces but tends to be very weak compared to roughness-induced friction.

(2) Internal hysteresis within contact bodies with dissipative material behavior. This occurs due to the cyclic loading of bodies in sliding contact and is perceived as friction at the macroscale. Internal hysteresis can be caused by viscosity, plasticity or damage, e.g. wear.

(3) Hysteresis within a contact lubricant. While viscous lubricants tend to reduce friction through reducing the influence of internal hysteresis, they themselves dissipate energy on the other hand.

(4) Hysteresis coming from the adhesion law. This part, however, is sometimes confused with the second contribution. For instance, if the Lennard–Jones potential is used to model adhesion, then there is no hysteresis in the adhesion law. Only the combined effect with the material behavior will result in hysteresis.

Another aspect is the scale transition of contact adhesion and friction. Van der Waals adhesion, for example, has a range of a few nanometers. It therefore has a strong effect on very small bodies that can come into close contact. For large bodies, on the other hand, surface roughness and contaminating surface particles often prevent intimate contact so that the effect of van der Waals adhesion is lost at larger scales. The question thus arises, how to describe the effective contact behavior at a given length scale for given material and roughness parameters of the neighboring bodies. While

the traditional approach has been to use experimental models at increasingly finer length scales, a new emerging paradigm is the use of homogenization or coarse-graining methods that are based on underlying principles, like molecular or even quantum mechanical modeling. For contact, such homogenization strategies have been considered by Luan and Robbins^[23]; Luan et al.^[86]; Sauer and Li^[24,30]; Temizer and Wriggers^[21]; Wriggers and Reinelt^[19]; Yang and Persson^[25]; Temizer and Wriggers^[22]. The basic idea of contact homogenization is outlined in Fig. 2.16. Suppose we are interested in finding the effective contact behavior at the micrometer scale based on the underlying behavior of rough surface contact at the nanometer scale. If we are interested in the behavior of the global problem then it becomes inefficient to model the fine details of the contact zone. Therefore an effective model is sought, which yields the same (or similar) overall contact behavior as the detailed model. In other words, we seek the effective contact potential ϕ^* capable of providing the same effective behavior for smooth contact surfaces as the original potential ϕ (Eq. (2.1)) does for rough surfaces. This can be accomplished by simulating the contact behavior of a representative volume element (RVE) and comparing it to the contact behavior of the effective model. In the case of frictional sliding contact, we may additionally seek an effective friction coefficient μ^* for smooth surfaces which captures the overall sliding behavior of the original rough surface, with coefficient μ , accurately.

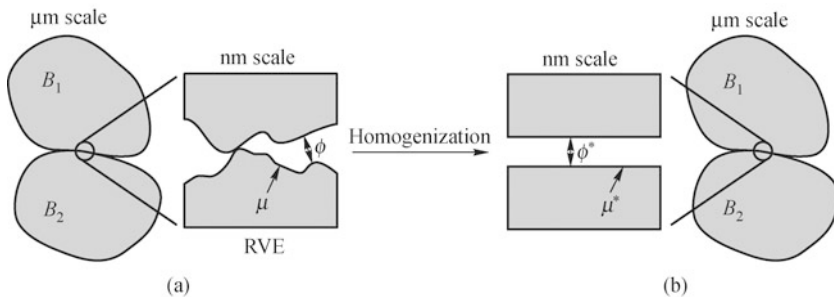


Fig. 2.16 Homogenization of the detailed nanometer scale contact behavior (a) into an effective contact model at the micrometer scale (b).

Rough surfaces also affect the contact behavior of liquids. A prominent example is the self-cleaning mechanism of lotus leaves, which is caused by the complex surface microstructure of the leaves^[87]. Lotus surfaces are hydrophobic, so that water does not coat the surface but rather forms small droplets which roll-off easily, even for a small inclination of the surface. Foreign pollutants clinging to the surface, like dirt or germ particles, adhere to passing water droplets and are thus swept away from the surface. This is possible since the attractive forces between particles and surface are weaker than

those between particles and water. Otherwise the pollutant particles cannot be swept away by water droplets and the surface loses its self-cleaning capability. Figure 2.17 shows a hydrostatic finite element solution of a liquid droplet in contact with a rough surface^[88]. The local contact angle at the three-phase boundary of water, solid and air is considered to be 180° . In this case the droplet sits on top of the asperities instead of wetting the grooves, a state known as the Cassie-Baxter state of wetting. The considered droplet has a volume of 29.45 nL, which corresponds to a spherical diameter of 3.83 mm. The asperity spacing is chosen as 0.383 mm.

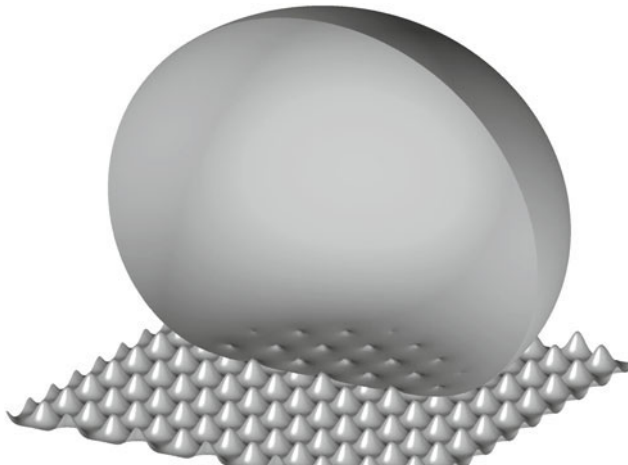


Fig. 2.17 Finite element solution of a liquid droplet in contact with a rough surface. The contact angle at the three-phase boundary is considered to be 180° .

2.7 Conclusion

This article gives an overview of the formulation, implementation, behavior and application of small-scale contact of soft bodies. Due to the high compliance, adhesive forces have a large effect on the contact behavior of soft bodies. Adhesive contact of two bodies can be derived from an interaction potential (see Section 2.2) which provides a very general model framework. The model is expressed in two variants: the body force formulation (BF) and the surface force formulation (SF). The BF formulation is the natural formulation that appears from a long-range, particle-based interaction formulation as the Lennard-Jones potential. The SF formulation is obtained from the projection of these body forces onto the surface, which is useful to increase numerical efficiency. Section 2.3 presents the 3D finite element equations for

both adhesive contact formulations. In both cases two versions are reported: a naive implementation, that is simple, but not efficient and a highly efficient but more complicated implementation that is based on a closest point projection and analytical integration. The contact algorithm used for all methods is then summarized in Table 2.2. Depending on the ratio between the material stiffness and the strength of adhesion, the contact behavior is fundamentally different: for stiff bodies, the effect of adhesion is negligible and only compressive contact forces are observed. For soft bodies, adhesion dominates contact and strong tensile contact forces are observed at the boundary of the contact area. The effect of adhesion is illustrated by several numerical examples in Section 2.4 and Section 2.6. The considered applications include carbon nanotube interaction, adhesion of spheres, nanoindentation, gecko adhesion and self-cleaning surface mechanisms. The separation of adhering soft bodies often leads to a peeling mechanism. These mechanisms can pose a substantial computational challenge, as shown in Section 2.5. Using an enriched surface representation within the peeling zone allows the construction of efficient computational formulations for peeling problems. The contact behavior of soft bodies, like adhesion and friction, is strongly influenced by the surface microstructure. The precise nature of these influences is still an open research topic. A useful tool for determining effective contact models from underlying, fundamental principles, are contact homogenization methods, which are outlined in Section 2.6.

The author is currently working on the extension of some of the contact formulations presented here. Among those are the extension of the enriched contact formulation presented in Section 2.5, the development of efficient integration algorithms for dynamic contact adhesion problems, the formulation of suitable friction laws for adhesive contact and the extension of the contact model for liquid droplets. Further challenges in soft body contact lie in the fields of multifield problems, parameter identification and determination, inverse problems and also the constitutive modeling of the soft materials themselves.

Acknowledgements

The author is grateful to the German Research Foundation (DFG) for supporting this work under project SA1822/5-1 and grant GSC 111.

References

- [1] Johnson K L, Kendall K, Roberts A D. Surface energy and the contact of elastic solids. *Proc. R. Soc. Lond. A*, 324: 301-313, 1971.
- [2] Derjaguin B V, Muller V M, Toporov Y P. Effect of contact deformation on the adhesion of particles. *J. Colloid Interface Sci.*, 53 (2): 314-326, 1975.
- [3] Maugis D. Adhesion of spheres: The jkr-dmt transition using a duddale model. *L. Colloid Interface Sci.*, 150(1): 243-269, 1992.
- [4] Johnson K L. Contact Mechanics. Johns Hopkins, 1985.
- [5] Laursen T A. Computational Contact and Impact Mechanics: Fundamentals of Modeling Interfacial Phenomena in Nonlinear Finite Element Analysis. Springer, 2002.
- [6] Wriggers P. Computational Contact Mechanics. 2nd ed. Springer, 2006.
- [7] Padmanabhan V, Laursen T A. A framework for development of surface smoothing procedures in large deformation frictional contact analysis. *Finite Elem. Anal. Des.*, 37: 173-198, 2001.
- [8] Wriggers P, Krstulovic-Opara L, Korelc J. Smooth C^1 -interpolations for two-dimensional frictional contact problems. *Int. J. Numer. Meth. Engng.*, 51: 1469-1495, 2001.
- [9] Stadler M, Holzapfel G A, Korelc J. C^n continuous modelling of smooth contact surfaces using nurbs and application to 2D problems. *Int. J. Numer. Meth. Engng.*, 57: 2177-2203, 2003.
- [10] Krstulovic-Opara L, Wriggers P, Korelc J. A C^1 -continuous formulation for 3D finite deformation friction contact. *Comp. Mech.*, 29: 27-42, 2002.
- [11] Puso M A, Laursen T A. A 3D contact smoothing method using Gregory patches. *Int. J. Numer. Meth. Engng.*, 54: 1161-1194, 2002.
- [12] Yang B, Laursen T A, Meng X. Two dimensional mortar contact methods for large deformation frictional sliding. *Int. J. Numer. Meth. Engng.*, 62: 1183-1225, 2005.
- [13] Fischer K A, Wriggers P. Mortar based frictional contact formulation for higher order interpolations using the moving friction cone. *Comput. Methods Appl. Mech. Engrg.*, 195: 5020-5036, 2006.
- [14] Puso M A, Laursen T A. A mortar segment-to-segment contact method for large deformation solid mechanics. *Comput. Methods Appl. Mech. Engrg.*, 193: 601-629, 2004.
- [15] Puso M A, Laursen T A. A mortar segment-to-segment frictional contact method for large deformations. *Comput. Methods Appl. Mech. Engrg.*, 193: 4891-4913, 2004.
- [16] Raous M, Cangemi L, Cocu M. A consistent model coupling adhesion, friction, and unilateral contact. *Comput. Methods Appl. Mech. Engrg.*, 177: 383-399, 1999.
- [17] Sauer R A, Li S. An atomic interaction-based continuum model for adhesive contact mechanics. *Finite Elem. Anal. Des.*, 43(5): 384-396, 2007.
- [18] Hesch C, Betsch P. A mortar method for energy-momentum conserving schemes in frictionless dynamic contact problems. *Int. J. Numer. Methods Engng*, doi: 10.1002/nme.2466, 2008.
- [19] Wriggers P, Reinelt J. Multi-scale approach for frictional contact of elastomers on rough rigid surfaces. *Comput. Methods Appl. Mech. Engrg.*. (accepted).
- [20] Sauer R A. Multiscale modeling and simulation of the deformation and adhesion of a single gecko seta. *Comp. Meth. Biomech. Biomed. Engng.*, 12(6): 627-640, 2009.

- [21] Temizer I, Wriggers P. A multiscale contact homogenization technique for the modeling of third bodies in the contact interface. *Comp. Meth. Appl. Mech. Engrg.*, 198: 377-396, 2008.
- [22] Temizer I, Wriggers P. Thermal contact conductance characterization via computational contact homogenization: A finite deformation theory framework. *Int. J. Numer. Meth. Engrg.*, 83: 27-58, 2009.
- [23] Luan B, Robbins M O. Contact of single asperities with varying adhesion: Comparing continuum mechanics to atomistic simulations. *Phys. Rev. E*, 74(2): 026111, 2006.
- [24] Sauer R A, Li S. An atomistically enriched continuum model for nanoscale contact mechanics and its application to contact scaling. *J. Nanosci. Nanotech.*, 8(7): 3757-3773, 2008.
- [25] Yang C, Persson B N J. Molecular dynamics study of contact mechanics: Contact area and interfacial separation from small to full contact. *Phys. Rev. Lett.*, 100(2): 024303, 2008.
- [26] Tadmor E B, Ortiz M, Phillips R. Quasicontinuum analysis of defects in solids. *Phil. Mag. A*, 73(6): 1529-1563, 1996.
- [27] Miller R E, Tadmor E B. The quasicontinuum method: Overview, applications and current directions. *J. Comp.-Aid. Mat. Design*, 9: 203-239, 2002.
- [28] Bradley R S. The cohesive force between solid surfaces and the surface energy of solids. *Phil. Mag.*, 13: 853-862, 1932.
- [29] Hamaker H C. The London-van der Waals attraction between spherical particles. *Physica*, 4(10): 1058-1072, 1937.
- [30] Sauer R A, Li S. A contact mechanics model for quasi-continua. *Int. J. Numer. Meth. Engrg.*, 71(8): 931-962, 2007.
- [31] Derjaguin B V. Untersuchungen über die reibung und adhäsion IV: Theorie des anhaftens kleiner teilchen. *Kolloid Z.*, 69: 155-164, 1934.
- [32] Sauer R A. An atomic interaction based continuum model for computational multiscale contact mechanics. PhD thesis, University of California, Berkeley, USA, 2006.
- [33] Sauer R A, Wriggers P. Formulation and analysis of a 3D finite element implementation for adhesive contact at the nanoscale. *Comput. Methods Appl. Mech. Engrg.*, 198: 3871-3883, 2009.
- [34] Agrawal A, Steigmann D. Modeling protein-mediated morphology in biomembranes. *Biomech. Model. Mechanobiol.*, 8(5): 371-379, 2009.
- [35] Lanczos C. The Variational Principles of Mechanics. Dover edition, 1986.
- [36] Israelachvili J N. Intermolecular and Surface Forces. 2nd ed. Academic Press, 1991.
- [37] Belytschko T, Liu W K, Moran B. Nonlinear Finite Elements for Continua and Structures. Wiley, 2000.
- [38] Wriggers P. Nonlinear Finite Element Methods. Springer, 2008.
- [39] Persson B N J. Sliding friction. *Surf. Sci. Rep.*, 33(3): 83-119, 1999.
- [40] Ruoff S R, Tersoff J, Lorents D C, et al. Radial deformation of carbon nanotubes by van der Waals forces. *Nature*, 364: 514-516, 1993.
- [41] Hertel T, Walkup R E, Avouris P. Deformation of carbon nanotubes by surface van der Waals forces. *Phys. Rev. B*, 58(20): 13870-13873, 1998.
- [42] Pantano A, Parks D M, Boyce M C. Mechanics of deformation of single- and multi-walled carbon nanotubes. *J. Mech. Phys. Solids*, 52: 789-821, 2004.
- [43] Tang T, Jagoda A, Hui C Y, Glassmaker N J. Collapse of single-walled carbon nanotubes. *J. Appl. Phys.*, 97(7): 074310, 2005.

- [44] Sauer R A. A computational contact model for nanoscale rubber adhesion. In Heinrich G, Kaliske M, Lion A and Reese S editors, *Constitutive Models for Rubber VI*. Taylor & Francis Group, 47-52, 2009.
- [45] Sauer R A. A computational model for nanoscale adhesion between deformable solids and its application to gecko adhesion. *J. Adhes. Sci. Technol.*, 24: 1807-1818, 2010.
- [46] Huber G, Mantz H, Spolenak R, et al. Evidence for capillarity contributions to gecko adhesion from single spatula nanomechanical measurements. *Proc. Natl. Acad. Sci. USA*, 102(45): 16293-16296, 2005.
- [47] Sun W, Neuzil P, Kustandi T S, et al. The nature of the gecko lizard adhesive force. *Biophys. J.*, 89(2): L14-L17, 2005.
- [48] Autumn K, Liang Y A, Hsieh S T, et al. Adhesive force of a single gecko foot-hair. *Nature*, 405: 681-684, 2000.
- [49] Kendall K. Thin-film peeling—the elastic term. *J. Phys. D: Appl. Phys.*, 8: 1449-1452, 1975.
- [50] Zhao Y P, Wang L S, Yu T X. Mechanics of adhesion in MEMS: A review. *J. Adhesion Sci. Technol.*, 17(4): 519-546, 2003.
- [51] Lane M. Interface fracture. *Annu. Rev. Mater. Res.*, 33: 29-54, 2003.
- [52] Liu Y, Zhang L, Wang X, et al. Coupling of navier-stokes equations with protein molecular dynamics and its application to hemodynamics. *Int. J. Numer. Methods Fluids*, 46: 1237-1252, 2004.
- [53] McGarry J P, Murphy B P, McHugh P E. Computational mechanics modelling of cell-substrate contact during cyclic substrate deformation. *J. Mech. Phys. Solids*, 53: 2597-2637, 2005.
- [54] Zeng X, Li S. Multiscale modeling and simulation of soft adhesion and contact of stem cells. *J. Mech. Behav. Biomed. Mater.*, doi: 10.1016/j.jmbbm.2010.06.002, 2010.
- [55] Krasovitski B, Marmur A. Particle adhesion to drops. *J. Adhes.*, 81(7-8):869-880, 2005.
- [56] Persson B N J, Albohr O, Tartaglino U, et al. On the nature of surface roughness with application to contact mechanics, sealing, rubber friction and adhesion. *J. Phys. Condens. Matter*, 17(3): R1-R62, 2005.
- [57] Kendall K, Amal R, Jiang X, et al. Effect of adhesion on aggregation in nanoparticle dispersions. *J. Adhes.*, 83: 573-585, 2007.
- [58] Qu L, Dai L, Stone M, et al. Carbon nanotube arrays with strong shear binding-on and easy normal lifting-off. *Science*, 322: 238-242, 2008.
- [59] Wei Y, Hutchinson J W. Interface strength, work of adhesion and plasticity in the peel test. *Int. J. Fracture*, 93: 315-333, 1998.
- [60] Crisfield M A, Alfano G. Adaptive hierarchical enrichment for delamination fracture using a decohesive zone model. *Int. J. Numer. Meth. Engrg.*, 54(9): 1369-1390, 2002.
- [61] Diehl T. On using a penalty-based cohesive-zone finite element approach, part I: Elastic solution benchmarks. *Int. J. Adhesion Adhesives*, 28: 237-255, 2008.
- [62] Lorenzis L D, Zavarise G. Modeling of mixed mode debonding in the peel test applied to superficial reinforcements. *Int. J. Solids Struc.*, 45: 5419-5436, 2008.
- [63] Sauer R A. Enriched contact finite elements for stable peeling computations. *Int. J. Numer. Meth. Engrg.*, (in press)
- [64] Puso M A, Laursen T A, Solberg J. A segment-to-segment mortar contact method for quadratic elements and large deformations. *Comput. Methods Appl. Mech. Engrg.*, 197: 555-566, 2008.

- [65] Sauer R A. The peeling behavior of thin films with finite bending stiffness and the implications on gecko adhesion. *J. Adhes.*. (accepted)
- [66] Sauer R A, Holl M. A 3d finite element analysis of the peeling behavior of a gecko spatula. *Comp. Meth. Biomech. Biomed. Engng.*. (submitted)
- [67] Persson B N J. Contact mechanics for randomly rough surfaces. *Surf. Sci. Rep.*, 61(4): 201-227, 2006.
- [68] Timoshenko S P, Goodier J N. Theory of Elasticity. 3rd ed. McGraw-Hill, 1970.
- [69] Greenwood J A, Williamson J B P. Contact of nominally flat surfaces. *Proc. Roy. Soc. A*, 295(1442): 300-319, 1966.
- [70] Chang W R, Etsion L, Bogy D B. Adhesion model for metallic rough surfaces. *J. Trib.*, 110: 50-56, 1988.
- [71] Persson B N J. Elastoplastic contact between randomly rough surfaces. *Phys. Rev. Lett.*, 87(11): 116101-1, 2001.
- [72] Chowdhury S K R, Ghosh P. Adhesion and adhesional friction at the contact between solids. *Wear*, 174: 9-19, 1994.
- [73] Lai W T, Cheng H S. Computer simulation of elastic rough contacts. *Trib. Trans.*, 28: 172-180, 1985.
- [74] Webster M N, Sayles R S. A numerical model for the elastic frictionless contact of real rough surfaces. *J. Trib.*, 108: 314-320, 1986.
- [75] Ren N, Lee S C. Contact simulation of three-dimensional rough surfaces using moving grid method. *J. Tribol.-T. ASME*, 115(4): 597-601, 1993.
- [76] Tian X, Bhushan B. A numerical three-dimensional model for the contact of rough surface by variational principle. *J. Tribol.-T. ASME*, 118(1): 33-42, 1996.
- [77] Karpenko Y A, Akay A. A numerical model of friction between rough surfaces. *Tribol. Int.*, 34(8): 531-545, 2001.
- [78] Carbone G, Mangialardi L. Adhesion and friction of an elastic half-space in contact with a slightly wavy rigid surface. *J. Mech. Phys. Solids*, 52(6): 1267-1287, 2004.
- [79] Tworzydlo W W, Cecot W, Oden J T, et al. Computational micro- and macroscopic models of contact and friction: Formulation, approach and applications. *Wear*, 220(2): 113-140, 1998.
- [80] Haraldsson A, Wriggers P. A strategy for numerical testing of friction laws with application to contact between soil and concrete. *Comp. Meth. Appl. Mech. Engrg.*, 190: 963-977, 2000.
- [81] Zhuravlev V A. On the question of theoretical justification of the Amontons-Coulomb law for friction of unlubricated surfaces. *Proc. Inst. Mech. Eng. J-J. Eng. Trib.*, 221(J8): 895-898, 2007.
- [82] Borodich F M. Comment on “elastoplastic contact between randomly rough surfaces”. *Phys. Rev. Lett.*, 88(6): 069601, 2002.
- [83] Autumn K, Dittmore A, Santos, D, et al. Frictional adhesion: A new angle on gecko attachment. *J. Exp. Biol.*, 209: 3569-3579, 2006.
- [84] Singer I L. Friction and energy dissipation at the atomic scale: A review. *J. Vac. Sci. Technol. A*, 12(5): 2605-2616, 1994.
- [85] Morita S, Fujisawa S, Sugawara Y. Spatially quantized friction with a lattice periodicity. *Surf. Sci. Rep.*, 23(1): 1-41, 1996.
- [86] Luan B Q, Hyun S, Molinari J F, et al. Multiscale modeling of two-dimensional contacts. *Phys. Rev. E*, 74(4): 046710, 2006.
- [87] Barthlott W, Neinhuis C. Purity of the sacred lotus, or escape from contamination in biological surfaces. *Planta*, 202: 1-8, 1997.

- [88] Sauer R A, Osman M. A computational contact model for liquid droplets. (under preparation).

Chapter 3 Soft Matter Modeling of Biological Cells

Xiaowei Zeng, Shaofan Li* and Bo Ren

Department of Civil and Environmental Engineering, University of California, Berkeley, CA 94720, USA

Abstract: In this work, we review some of our recent work on developments of soft matter models for cells to study the focal adhesion of endothelial cells as well as stem cells, in an attempt to explain mechanical information exchange between the cells and their extracellular environment. Particularly, we model the macroscale endothelial cell as a hyperelastic medium, and the stem cell as a liquid crystal elastomer. A nanoscale adhesive model is introduced to describe the interaction between receptors and ligands. We have developed and implemented a Lagrange type meshfree Galerkin formulation and related computational algorithms for the proposed cell and adhesive contact model. A comparison study with experimental data has been conducted to validate the parameters of the cell model. By using the soft matter cell model, we have simulated the soft adhesive contact process between cells and extracellular substrate. The soft matter cell model presented in this work is a primitive one, but it may have provided a useful approach for more realistic and more accurate modeling of cells, especially stem cells.

Keywords: endothelial cell, focal adhesion, liquid crystal elastomer, multiscale simulations, soft contact, stem cell

3.1 Introduction

A recent advance in cellular and molecular biology is the discovery that the behavior of stem cells depends sensitively on both the rigidity and surface micro-structures of the extracellular environment. For example, Engler et al.^[1] reported that matrix elasticity directs stem cell lineage specification. The ability of the cell to sense the environmental mechanical stimulus and subsequently to mediate its own coordinated responses is called *Mechan-*

*Corresponding author, E-mail: shaofan@berkeley.edu

otransduction. As a process of cellular signal transduction in response to mechanical stimuli, mechanotransduction plays important role in normal physiological processes such as cell motility, angiogenesis, embryonic development, tissue regeneration, and wound healing. However, abnormal mechanotransduction is also responsible for a series of diseases in cardiology, orthopedics, neurology, and oncology. One common channel for force transmission is via focal adhesion. The exact mechanotransduction mechanism of focal adhesion is still unknown, and it is under active investigation. The objectives of current research are: (a) to establish a predictive modeling paradigm that can help us understand biomechanics and biophysics underlying focal adhesion-based mechanotransduction, and (b) to explain and to elucidate protein conformational changes and binding affinity changes in response to external forces, external ligand perturbations, and properties of external environment.

In recent years, we have developed a soft matter coarse-grained model that combines the strength of different modeling methods including nanoscale interatomic potential for adhesive contact and meshfree method of contact mechanics to implement this project. We hope results from this study will give insight into the role of soft elasticity on mechanotransduction of focal adhesion, helping to unravel its molecular mechanisms on diseases, and to assist the design of targeting therapies. Moreover, the study of the contact mechanics of cell adhesion will directly contribute to our knowledge on function, self-assembly, and self-disassembly of focal adhesion, whose molecular mechanism of mechanotransduction is vital to understand many fundamental problems of lifesciences, biology, and medicine, such as the basic cell functions relating to all the issues from cell motility to cell cycle, interaction and relationship between receptors and ligands, cytoskeleton dynamics, and viral binding.

To study the soft contact and focal adhesion of cells may help us design biomimetic models for the extracellular matrix and by analyzing their effect on cell-matrix adhesion, we hope to eventually unravel the basic principles at work at the interface between living cells and their environment. This may pave the way for rational design of scaffolds for tissue engineering and for new strategies in regenerative medicine and cancer therapy. The applications of this research range from dental implants to hip replacements.

Moreover, there are human genetic diseases caused by inability to express a specific adhesion molecule. For example, the leukocytes from leukocyte adhesion deficiency patients fail to adhere to the blood vessel wall during inflammation, which causes patients to exhibit serious infections that can be life threatening. Therefore, the molecular mechanism of focal adhesion plays a very important role in the function of human immune system and curing human genetic diseases.

Furthermore, soft surface properties appear to be important in stem cell lineage specification. Stem cells take their cue from their physical surroundings. To understand the interaction between stem cells and their physical environments, the focal adhesion in particular, will offer potential benefits for the large-scale production of embryonic stem cells.

3.2 Soft matter modeling of cells

3.2.1 The future is soft

Soft matter chemistry, physics, and mechanics have emerged as the frontier multi-disciplinary scientific research, that are concerned with the study of colloidal suspensions, liquid crystals, liquid crystal polymers, and surfactant (soap-like molecules) (Fig. 3.1). The term, soft matter, was coined by the late Professor Pierre-Gilles de Gennes in his visionary 1991 Nobel Physics Prize speech. The behavior of these systems is dominated by one simple fact: they contain mesoscopic structures with sizes between those of a typical small molecule such as water (~ 0.3 nm) and the beaker containing liquid. These mesoscopic structures ranging from 10 nm to 1 μ m can be suspended solid particles or liquid drops, polymer coils formed by linking together tens of thousands of smaller molecular units, or micelles spontaneously formed by soap molecules.

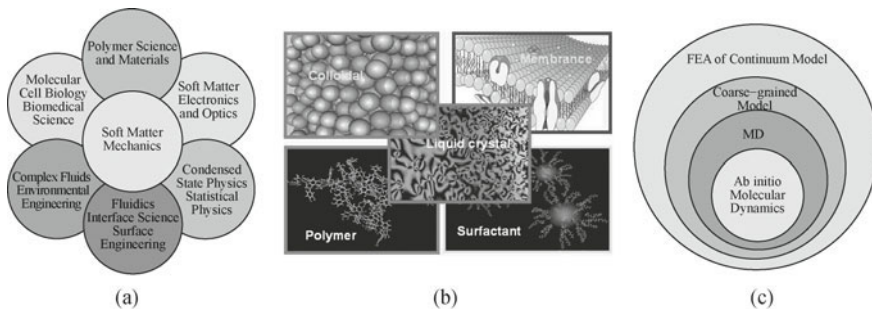


Fig. 3.1 Mechanics of soft matter and its multiscale components. (color plot at the end of the book)

Soft matter displays a range of fascinating properties, with most of them relating to the ability to assemble itself into complex structures. Another important property of some soft elastic materials is that they possess some ‘soft deformation modes’, i.e. some or all of elastic stiffnesses can vanish. It

leads to drastic structure changes or conformation changes, or in other words, the phase transitions.

Soft matter has been studied by chemists, chemical engineers, and biologists for many years. Since 1970s, a group of physicists have joined the research and created a sub-discipline in physics, namely, physics of the soft condensed matter. Due to the emergence of nanoscience and technology, bio-molecular science and technology, and environmental engineering, many nanoscale systems consist of soft matters, such as DNA, RNA, proteins, cells, and tissues, which are either bio-molecule or biopolymer made of bio-molecules, and they are ubiquitous in almost all life forms and organisms.

A common feature of many soft matter systems is their richness in chemical or biological details. Despite of the various forms of these materials, many of their properties have common physiochemical origins. For example, all polymer molecules share some common properties because they are long balls of strings continually wriggling under thermal fluctuations. Almost all soft matter has a large number of internal degrees of freedom, weak interactions between structural elements, and a delicate balance between entropic and enthalpic contributions to the free energy.

Moreover, studying the generic properties of soft matter can give fresh insight into a range of rather broad and fundamental questions that cut across a whole discipline: one example being addressed by this research is the contact mechanics of soft matter and focal adhesion of cells, which is one of the fundamental challenges in today's biology and medicine.

Even though the mechanics of soft matter is still in its infancy today, it has been always an essential part of soft condensed matter physics. Such as an example is the celebrated Ericksen–Leslie theory^[2–5], which is one of the early contributions of soft condensed matter physics. Today, the soft mechanics and its computation have been rising to re-invigorate classical continuum mechanics.

3.2.2 The reasons to use liquid crystal elastomers to model cell and focal adhesion

The first successful coarse-grained modeling of the cell structure should be credited to Helfrich and his co-workers^[6–8]. In 1970s, Helfrich and his co-workers modeled the cell membrane as a liquid crystal, and they carried out calculations to give the correct shape of red blood cells, which was probably the first triumph of soft matter physics. Currently, at spectrin level, the most sophisticated model of cytoskeleton membranes model is proposed by Li et al.^[9] It is based on the worm-like chain (WLC) model^[10,11], which is

essentially an entropic elastomer model without internal microstructure or internal degrees of freedom.

If one combines both the liquid crystal and the entropic elastomer, one will end with a completely new material—*the liquid crystal elastomer!* Liquid crystal elastomers consist of networks of cross-linked polymeric chains, each of which contains rigid rod-like molecules called mesogens^[12,13]. Liquid crystal elastomers combine the elastic properties of rubbers with the order inheritance in nematic liquid crystals. Stretching a monodomain strip of nematic elastomer in a direction transverse to the nematic director results in an energy-free rotation of the director, giving rise to a soft elastic response.

The main reasons that we perceive that this could be a successful model are: (a) Liquid crystal elastomers have soft modes that can be triggered in contact/adhesion through phase transition. This gives a theoretical possibility to capture self-assembly/ self-disassembly of the focal adhesion—a state of liquid gel. (b) The microstructure of myosin in cell cytoskeleton remarkably resembles the microstructure of mesogens in nematic polymers. (c) This is a mathematically elegant and computational tractable model, which is feasible in the current computer and computational technologies.

In Fig. 3.2, we juxtapose the morphology of the myosin in stress fibers and that of the mesogen of nematic polymers. One can see the similarity between them while possessing the same micro-structure in terms of soft elasticity.

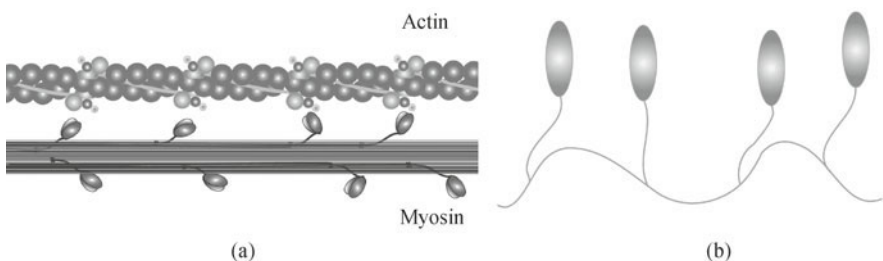


Fig. 3.2 Comparison between (a) myosin-actin in cells and (b) mesogens in liquid crystal elastomers. (color plot at the end of the book)

In fact, the collagen is a long fibrous structural proteins, which is the main constituent of connective tissue and extracellular matrix in animals, and it is the most abundant protein in mammals. Recently, evidences have been discovered that some collagens can be precisely characterized by liquid crystal elastomers. Martin et al.^[14] have shown that type I procollagen, the precursor for mammalian type I collagen fibrils, forms nematic and pre-cholesteric liquid crystals *in vitro* and have argued that this accounts for the assembly of crimped fibrils and other assemblies *in vitro*. Knight et al.^[15] and Knight and Vollrath^[16] have presented evidence that the fibrillar collagens and the

dragline silks of orb web spiders are actual liquid crystal elastomers.

Therefore, we believe that the newly formulated liquid crystal elastomer theory^[17,18] provides the best possible coarse-grained model for both cytoskeleton modeling and the modeling of collagen tissues.

3.2.3 Elasticity of soft contact/cell adhesion and surface material property sensing

Cell contacts are adhesion in nature, involved in one of the most common biological phenomena—the focal adhesion—which is referred to a thin layer of anchorage molecular assemblies of cytoskeleton plasma between the membrane of a cell, e.g. fibroblast and the substratum of extracellular matrix. Focal adhesion may be viewed or modeled as a macromolecular medium that can sense (signaling) the stiffness or rigidity as well as the surface energy density distribution on the extracellular matrix and convert it or transduce it (mechanotransduction) to protein conformation and cell shape and motion as well.

At 2006 Annual Meeting of the American Society for Cell Biology, C. J. Murphy of University of Wisconsin–Madison presented data showing that embryonic stem cells are more likely to keep their *pluripotency*—their ability to become any type of cells—when they are grown on a surface stamped with a pattern of tiny ridges. In the same year, in an issue of *Cell*, a team led by D. E. Discher of the University of Pennsylvania found that stem cells grown on the stiffest matrix became bone precursors. Those grown on the softest surface became nerve cells, and those grown on a medium-stiff substrate assumed the characteristics of muscle cells^[19]. Moreover, experimental studies with soft elastic substrates have shown that fibroblast-like cells spread to larger areas on stiffer substrates, and that they can locomote to stiff or tensed regions in their environment^[1,20], and hence they are controlled by the stiffness of the environment. The rigidity response seems to be coupled with growth inhibition on soft substrates, which distinguishes normal cells from cancer cells.

In the past ten years, several elasticity models of focal adhesion and rigidity sensing have been proposed: (a) the two-spring rigidity sensing model by Schwarz^[21]; (b) thermodynamic self-assemble model by Shemesh et al.^[22]; (c) crosstalk model by Bershadsky et al.^[23]; (d) one-dimensional cluster model by Bickel and Bruinsma^[24]; (e) shear-lag model by Aroush and Wagnet^[25]; (f) force-induced adsorption model by Besser and Safran^[26]; (g) contractility/adhesion cooperation model by Novak et al.^[27]; (h) force regulation model by Bruinsma^[28]; (i) substrate deformation model by Wang^[29].

Most of these models are one-dimensional elasticity models with some biology insights or speculations. The contributors are from different fields: physicists, bio-engineers, material scientists, chemists, and only one mechanician^[29]. Here we briefly introduce the two-spring rigidity sensing model by Schwarz^[21], which is schematically depicted in Fig. 3.3. In this model, a stress fiber connects two sites of focal adhesion. The spring constants K_e and K_i represent extracellular and intercellular stiffnesses, respectively, and k_o is a weak link representing the strength of connecting bonds. A molecular motor can build force inside stress fibers, and it can be shown that the larger the K_e the faster the force will be built up. Therefore, the rigidity can be sensed by a time scale. This model represents the current state and understanding of molecular mechanism of focal adhesion. Even the present authors concede that *a three-dimensional elasticity analysis as well as other feature of cell mechanics should be included*.

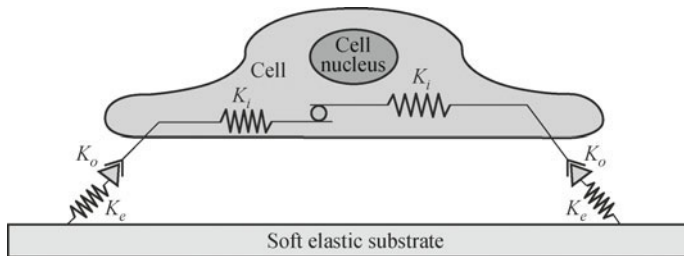


Fig. 3.3 The two-spring rigidity sensing model^[21]. (color plot at the end of the book)

Recently, several general cell contact and focal adhesion models have also been proposed by notables Freund and Lin^[30], Ni and Chiang^[31], and Deshpande et al.^[32]. Continuum models also have been developed recently to predict cell adhesion in the early stage^[33,34] and to simulate cell crawling^[35]. In order to understand the precise bio-mechanical sensing process during cell contact and adhesion and to explain a possible mechanotransduction mechanism of the event, we have developed a multiscale soft matter cell model for simulation of cell contact and adhesion. In a recent paper^[36], the present authors have reported some early results of this study.

3.2.4 Cell and ECM modeling

The main objective of this work is to advance cell modeling and simulation, particularly stem cell modeling and simulation, we systematically build a soft matter cell model by treating stem cells as soft matters. We propose to model

the endothelial cell as hyperelastic materials, which has been used by Caille et al.^[37] to model the endothelia cells. We also propose to use liquid crystal elastomer to model stem cells.

The extra-cellular matrix is modeled as a substrate of hyperelastic block, which has been extensively used as cell models or gel models^[38,39]. An illustration of the cell model is shown in Fig. 3.4. In the following sections, we shall describe both hyperelastic constitutive model and liquid crystal elastomer model used in our cell and extracellular matrix modeling.

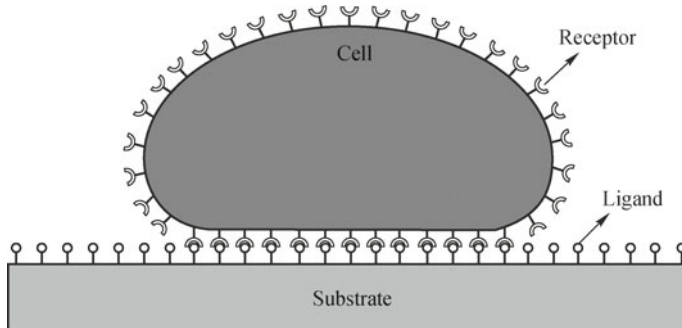


Fig. 3.4 Soft matter cell model and soft adhesive contact model. (color plot at the end of the book)

3.2.4.1 Hyperelastic model

First, we use a hyperelastic constitutive model to represent cell scaffold and cell plasma aggregates, and the cell model is considered to be isotropic and nonlinear, and exhibits elastic response under large strains. There are more than 20 hyperelastic constitutive relations for rubber-like materials, a comparison of different hyperelastic models was found by Marckmann and Verron^[40]. In this research, we adopted the modified Mooney–Rivlin material^[41] to model the cell nucleus and extracellular matrices. The strain energy density function W for the modified Mooney–Rivlin material is given as follows:

$$W = C_1(I_1 - 3I_3^{\frac{1}{3}}) + C_2(I_2 - 3I_3^{\frac{2}{3}}) + \frac{1}{2}\lambda(\ln I_3)^2 \quad (3.1)$$

where C_1, C_2 and λ are material constants and $\mathbf{C} = \mathbf{F}^T \cdot \mathbf{F}$ is the right Cauchy–Green deformation tensor; the three invariants of the right Cauchy–Green tensor are defined as

$$I_1 = \text{tr} \mathbf{C}, \quad (3.2)$$

$$I_2 = \frac{1}{2}[(\text{tr} \mathbf{C})^2 - \text{tr} \mathbf{C}^2], \quad (3.3)$$

$$I_3 = \det \mathbf{C}. \quad (3.4)$$

The corresponding constitutive relations can be expressed in terms of the second Piola–Kirchhoff stress tensor \mathbf{S} , and the invariants of the right Cauchy–Green tensor,

$$\mathbf{S} = 2\{(C_1 + C_2 I_1)\mathbf{I} - C_2 \mathbf{C} - (C_1 I_3^{\frac{1}{3}} + 2C_2 I_3^{\frac{2}{3}} - \lambda \ln I_3) \mathbf{C}^{-1}\}. \quad (3.5)$$

After the second Piola–Kirchhoff stress is obtained, the first Piola–Kirchhoff stress tensor can be immediately computed as $\mathbf{P} = \mathbf{S} \cdot \mathbf{F}^T$, which can then be substituted into the later developed meshfree Galerkin formulation to calculate the internal nodal force.

If the substrate is modeled as a Mooney–Rivlin hyperelastic medium, its elastic stiffness tensor is a fourth order tensor that can be evaluated as follows:

$$\begin{aligned} \mathbb{C} = 4 \frac{\partial^2 W}{\partial \mathbf{C} \partial \mathbf{C}} &= 4C_2 \mathbf{I} \otimes \mathbf{I} + \frac{4}{3}(C_1 I_3^{\frac{1}{3}} + 4C_2 I_3^{\frac{2}{3}} - \lambda) \mathbf{C}^{-1} \otimes \mathbf{C}^{-1} \\ &\quad - 4(C_1 I_3^{\frac{1}{3}} + 2C_2 I_3^{\frac{2}{3}} - \lambda \ln I_3) \mathbf{C}^{-1} \odot \mathbf{C}^{-1} - 4C_2 \mathbb{I}. \end{aligned} \quad (3.6)$$

By making the elastic constants, C_1, C_2 and λ , dependent on spatial coordinates, one can model the substrate with inhomogeneous stiffness.

3.2.4.2 Liquid crystal elastomer model

The main difficulty of applying finite element analysis to a liquid crystal elastomer cell model is that the free-energy density of the model is non-convex, and it is usually a multiwell potential. Since the contact does not allow the system to stay in a uniform equilibrium stress state that is resting entirely in a single well, the domain structures emerge, which is exactly what we would like to capture. The rearrangement of domain structures will lead to soft deformation mode. In fact, we conjecture that the focal adhesion is actually a liquid domain soft mode due to contact and adhesion with the extracellular matrix.

A typical entropic free-energy expression for a liquid crystal elastomer is^[13,42]:

$$\mathcal{F}_{\text{bulk}} = \frac{1}{2} k_B T \text{tr}(\mathcal{L}_0 \cdot \mathbf{F}^T \cdot \mathcal{L}^{-1} \cdot \mathbf{F}) + \frac{1}{2} k_B T \ln \frac{\det \mathcal{L}}{a^3}$$

where k_B is the Boltzmann constant, T is temperature, tr is the trace operator, the scalar a is a material parameter related to the distortion that polymer chains suffer with the establishment of nematic order, \mathcal{L}_0 and \mathcal{L} are polymer's step length tensors at referential configuration and current configuration respectively. They are related to the director field \mathbf{h} as follows:

$$\mathcal{L} = \ell_{\perp} \mathbf{I}^{(2)} + (\ell_{\parallel} - \ell_{\perp}) \mathbf{h} \otimes \mathbf{h}, \quad s = \frac{\ell_{\parallel}}{\ell_{\perp}}$$

and the first Piola–Kirchhoff stress is

$$\mathbf{P} = \frac{\partial \mathcal{F}}{\partial \mathbf{F}}. \quad (3.7)$$

However, this free-energy potential is not convex^[43–45], which poses a serious challenge in the Galerkin weak-form-based computations.

To regularize the free-energy potential, following Fried and Korchagin^[46], we add the Oseen–Zöcher–Frank energy density, a strain gradient term, to the bulk potential

$$\mathcal{F}_{\text{grad}} = J \frac{\kappa(s-1)^2}{2s} |\mathbf{F}^T \nabla \otimes \mathbf{h}|^2 = J \frac{\kappa(s-1)^2}{2s} |\mathbf{F}^T \mathbf{G}|^2$$

where κ is a simplified Oseen–Zöcher–Frank elastic constant, $J = \det \mathbf{F}$ is the determinant of Jacobian, and $\mathbf{G} := \nabla \otimes \mathbf{h}$. Then the total potential energy of the Nematic liquid-crystal elastomer becomes^[46],

$$\begin{aligned} \mathcal{F}_t = & \frac{\mu}{2} \left[|\mathbf{F}|^2 - \frac{s-1}{s} |\mathbf{F}^T \mathbf{h}|^2 + (s-1) |\mathbf{F} \mathbf{h}_0|^2 \right. \\ & \left. - \frac{(s-1)^2}{s} (\mathbf{F}^T \mathbf{h} \cdot \mathbf{h}_0)^2 - 3 \right] + J \frac{\kappa(s-1)^2}{2s} |\mathbf{F}^T \mathbf{G}|^2. \end{aligned} \quad (3.8)$$

The first dynamic equation of motion for the liquid crystal elastomer can be derived from the balance of linear momentum,

$$\rho \frac{\partial^2 \mathbf{u}}{\partial t^2} = -\mathbf{F}^{-T} \nabla p + \text{div} \frac{\partial \mathcal{F}_t}{\partial \mathbf{F}} + \mathbf{B} \quad (3.9)$$

where p is the hydrostatic pressure, div is the divergence operator, and \mathbf{B} is the body force.

Although a few people have derived the hydrodynamic equation for the director field of the liquid crystal elastomers including Anderson et al.^[47] whose derivation is based on the balance of angular momentum, how to establish a thermodynamically correct, general dynamics equation or hydrodynamics equations for the liquid crystal elastomers under finite deformations is still an open problem in soft matter physics research.

Since we are more interested in the evolution of the order parameter, which may correlate with the physical phenomena such as receptor diffusion or myosin head rotatory relaxation, we propose the following Allen–Cahn type of approach^[48]:

$$\frac{D \tilde{\mathbf{h}}}{Dt} = -\mathcal{C} \frac{\delta \mathcal{F}_t}{\delta \mathbf{h}}. \quad (3.10)$$

This approach has solid thermodynamics foundation. Note that the objective rate in Eq. (3.10) should be used for the first order time derivative of director field on the left-hand side of the equation.

3.3 A nanoscale adhesive contact model

Between the cell and its extracellular matrix, there are complex interactions between ligands and receptors. In this research, we do not attempt to model the exact molecular mechanism of cell adhesion or the detailed molecular motions during adhesion. Instead, we are interested in modeling the overall adhesion effect between cells and their substrates. The specific attractive adhesion force may be simulated by a cohesive potential.

In our meshfree simulation, we adopt a cohesive potential given by Seifert^[49]. Roy and Qi^[35] used the same potential to model the interactions between cell and a rigid substrate to study cell crawling.

In our 3D contact simulations, both cell and ECM can be deformable. We treat the cell outer surface as slaves, and we treat the ECM top surface as master surface. The contact algorithm begins with prediction of the slave particles at time step n , the contact-detection algorithm is then used to search all the particles on outer cell surface. The procedures are outlined as follows:

- (i) Discretizing the top surface of the substrate into triangles

In the meshfree computation, the adhesive force between the cell and substrate is calculated based on the following point-interaction algorithm (Fig. 3.5). For contact-detection purpose, we first need to discretize the top surface of the substrate into triangles because each triangle has a unique normal. The distance between a point and a triangle in 3D space can be easily obtained.

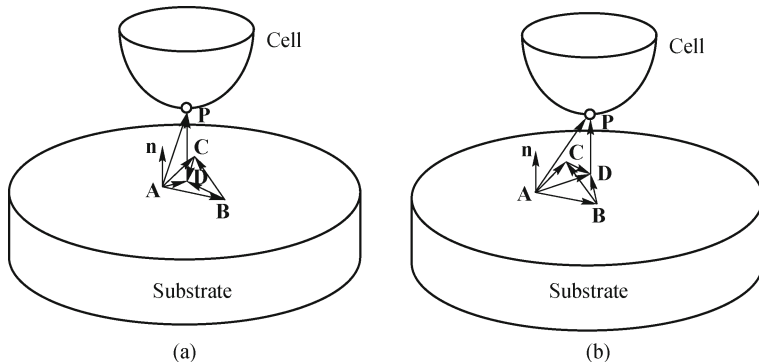


Fig. 3.5 Cell surface particles and corresponding substrate surface element.

- (ii) Searching master triangular surfaces for each slave particle

In meshfree computations, in principle, we need to search all surface triangles on the top surface of the substrate for each slave particle to find the triangle that has the shortest distance to the particle (Fig. 3.5). For example, we have a particle P on the cell surface, and we have a triangle $\triangle ABC$ on

the substrate surface. The normal direction of $\triangle ABC$ is $\mathbf{n} = \mathbf{AB} \times \mathbf{AC}$. The shortest distance between \mathbf{P} and $\triangle ABC$ is $gapn = \|\mathbf{DP}\| = \mathbf{n} \cdot \mathbf{AP}$ with \mathbf{D} the perpendicular intersection point. If the position of \mathbf{D} is in $\triangle ABC$, we find the matching surface triangle for particle \mathbf{P} . If the position of \mathbf{D} is outside $\triangle ABC$, we keep searching until we find the matching surface triangle for the particle \mathbf{P} . Define the area of $\triangle ABD$, $\triangle BCD$, $\triangle CAD$ as:

$$\alpha_A = \frac{1}{2} \|\mathbf{BC} \times \mathbf{BD}\|, \quad (3.11)$$

$$\alpha_B = \frac{1}{2} \|\mathbf{CA} \times \mathbf{CD}\|, \quad (3.12)$$

$$\alpha_C = \frac{1}{2} \|\mathbf{AB} \times \mathbf{AD}\|. \quad (3.13)$$

If $\alpha_A \geq 0$, $\alpha_B \geq 0$, and $\alpha_C \geq 0$, then the position of \mathbf{D} is inside $\triangle ABC$ (Fig. 3.5a), otherwise outside (Fig. 3.5b).

(iii) Calculating the contact force for each slave particle

In this work, the interaction zone between ligands and receptors is modeled as an interactive zone, or gap(<100 nm) that separates the cell from its substrate, and the adhesive force distribution varies according to the magnitude of the gap distribution. In our meshfree simulation, we adopt a adhesive potential given by Seifert^[49]. Roy and Qi^[35] used the same potential to model the interactions between cell and a rigid substrate to study cell crawling.

$$\Phi(r) = \sigma \left[\left(\frac{\varepsilon}{r} \right)^4 - 2 \left(\frac{\varepsilon}{r} \right)^2 \right] \quad (3.14)$$

where σ is the energy depth and $r(r = gapn)$ is the gap length at a specific location. The adhesive force vector can be calculated as follows:

$$\mathbf{F}(r) = -\frac{\partial \Phi}{\partial \mathbf{r}} = \phi'(r) \frac{\mathbf{r}}{r} \quad (3.15)$$

where

$$\phi'(r) = \frac{4\sigma}{\varepsilon} \left\{ \left(\frac{\varepsilon}{r} \right)^5 - \left(\frac{\varepsilon}{r} \right)^3 \right\}. \quad (3.16)$$

Taking the ligand-receptor bond density into consideration, the adhesive force between the cell membrane and the substrate surface can be calculated as follows:

$$\mathbf{f}(r) = N_b \mathbf{F}(r) = N_b \frac{4\sigma}{\varepsilon} \left[\left(\frac{\varepsilon}{r} \right)^5 - \left(\frac{\varepsilon}{r} \right)^3 \right] \frac{\mathbf{r}}{r} \quad (3.17)$$

where N_b is the bond density, we choose $N_b = 500 \mu\text{m}^{-2}$, $\sigma = 0.024 \text{ pN} \cdot \mu\text{m}$ from Roy and Qi (2010) and we choose $\varepsilon = 100 \text{ nm}$.

For the surface particle \mathbf{P} in cell, we can get the adhesive contact force

$$\mathbf{f}^P = \mathbf{f}(r) \quad (3.18)$$

where $\mathbf{f}(r)$ is the force between the surface particle \mathbf{P} and the matching surface triangle element of the substrate (Fig. 3.5).

$$\mathbf{f}(r) = N_b \phi'(r) \frac{\mathbf{r}}{r}, \quad \mathbf{r} = \mathbf{r}^{PD} = \mathbf{r}^P - \mathbf{r}^D, \quad \text{and} \quad r = |\mathbf{r}^{PD}| = gapn. \quad (3.19)$$

(iv) Updating the contact force for master contact particles

Since the substrate is deformable, we should apply the contact force to the master nodal particles to make sure that the total force is balanced. We use shape function to distribute the contact force to the three nodal particles of the corresponding surface triangle element of the substrate as follows:

$$\mathbf{f}^A = -\frac{\alpha_A}{\alpha} \mathbf{f}^P, \quad (3.20)$$

$$\mathbf{f}^B = -\frac{\alpha_B}{\alpha} \mathbf{f}^P, \quad (3.21)$$

$$\mathbf{f}^C = -\frac{\alpha_C}{\alpha} \mathbf{f}^P \quad (3.22)$$

where $\alpha = \alpha_A + \alpha_B + \alpha_C$ is the total area of the triangle element.

(v) Redistribute the contact forces to neighboring particles within the support

The force vectors calculated above are the exact nodal force vectors for each slave particle and corresponding master nodal surface particles. In mesh-free contact approach, one has to redistribute such exact nodal force to its supporting nodal particles. Hence after the force distribution, the contact force at the particle I becomes

$$\bar{\mathbf{f}}_I = \sum_{J=1}^{n_{\text{node}}} N_I(\mathbf{X}_J) \mathbf{f}_J. \quad (3.23)$$

If choosing the finite element interpolation, $N_I(\mathbf{X}_J) = \delta_{IJ}$, we can recover the exact nodal force vector^[50].

3.4 Meshfree Galerkin formulation and the computational algorithm

A total Lagrangian formulation is adopted in the numerical computation. The numerical simulations are conducted by using meshfree methods^[51]. Meshfree method have advantages when solving large deformation problems in contrast to the traditional finite element method. In our meshfree simulation, both the cell and its substrate are discretized by a set of particles, and then they are represented by interpolation functions.

The weak form of the balance of linear momentum under finite strain condition can be expressed as

$$\begin{aligned} & \sum_{i=1}^2 \int_{\Omega_0^{(i)}} \rho_0^{(i)} \ddot{\mathbf{u}}^{(i)} \cdot \delta \mathbf{u}^{(i)} d\Omega^{(i)} + \sum_{i=1}^2 \int_{\Omega_0^{(i)}} \mathbf{P}^{(i)} : \delta \mathbf{F}^{(i)} d\Omega^{(i)} \\ &= \sum_{i=1}^2 \int_{\Omega_0^{(i)}} \rho_0^{(i)} \mathbf{B}^{(i)} \cdot \delta \mathbf{u}^{(i)} d\Omega^{(i)} \\ &+ \sum_{i=1}^2 \int_{\Gamma_t^{(i)}} \bar{\mathbf{T}}^{(i)} \cdot \delta \mathbf{u}^{(i)} dS^{(i)} + \sum_{i=1}^2 \delta \Pi_{AC}^{(i)} \end{aligned} \quad (3.24)$$

where \mathbf{B} is the body force, \mathbf{P} is the first Piola–Kirchhoff stress, $\bar{\mathbf{T}}$ is the prescribed traction on the traction boundary $\Gamma_t^{(i)}$, index $i = 1$ corresponds to cell, and index $i = 2$ corresponds to extracellular matrix substrate. Note that the last term in Eq. (3.24), $\delta \Pi_{AC}^{(i)}$, denotes the virtual work contribution from adhesive contact, which will be discussed in details in the next section.

Following the standard meshfree discretization procedure established by Li and Liu^[51], we can obtain the following discrete equations of motion with the understanding that those equations may be applied to both cell and substrate:

$$\mathbf{M} \ddot{\mathbf{d}} = \mathbf{f}^{\text{ext}} - \mathbf{f}^{\text{int}}(\mathbf{d}) \quad (3.25)$$

where \mathbf{M} is the lumped mass matrix, \mathbf{f}^{int} is the internal force array arising from the current state of stress, \mathbf{f}^{ext} is the external force array including body forces and surface traction and contact forces,

$$\mathbf{M}_{IJ} = \int_{\Omega_0} \rho_0 \mathbf{N}_I \mathbf{N}_J d\Omega, \quad (3.26)$$

$$\mathbf{f}_I^{\text{int}} = \int_{\Omega_0} P_{iJ} \mathbf{N}_{I,J} \mathbf{e}_i d\Omega, \quad (3.27)$$

$$\mathbf{f}_I^{\text{ext}} = \int_{\Omega_0} \rho_0 \mathbf{B}_i \mathbf{N}_I \mathbf{e}_i d\Omega + \int_{\Gamma_t} \bar{\mathbf{T}}_i \mathbf{N}_I \mathbf{e}_i dS + \int_{\Gamma_c} \bar{\mathbf{f}}_i \mathbf{N}_I \mathbf{e}_i dS. \quad (3.28)$$

At time $t_{n+1} = t_n + \Delta t$, the discrete equation of motion can be written as:

$$\mathbf{M} \mathbf{a}_{n+1} = \mathbf{f}_{n+1}^{\text{ext}} - \mathbf{f}_{n+1}^{\text{int}}. \quad (3.29)$$

If the central difference scheme is used in the time integration, we have

$$\mathbf{d}_{n+1} = \mathbf{d}_n + \Delta t \mathbf{v}_n + \frac{1}{2} \Delta t^2 \mathbf{a}_n, \quad (3.30)$$

$$\mathbf{a}_{n+1} = \mathbf{M}^{-1} (\mathbf{f}_{n+1}^{\text{ext}} - \mathbf{f}_{n+1}^{\text{int}}), \quad (3.31)$$

$$\mathbf{v}_{n+1} = \mathbf{v}_n + \frac{1}{2} \Delta t (\mathbf{a}_n + \mathbf{a}_{n+1}) \quad (3.32)$$

where $\mathbf{d}, \mathbf{a}, \mathbf{v}$ denote the nodal displacement, acceleration and velocity arrays, respectively.

3.5 Numerical simulations

We have applied the soft matter cell models together with the multiscale contact-adhesion algorithm to simulating cell-ECM contact and adhesion. To ensure a meaningful simulation, we have first conducted validation test of the proposed cell models. By doing so, we can identify the parameters of the soft matter model. Then we applied the validated material models to simulating contact between a cell and substrates with different stiffnesses.

3.5.1 Validation of the material models

To validate the proposed cell model, we have applied it to simulating cell deformation under compression, and then we compare the simulation result with experiment measurements for endothelial cells^[37]. The constant force is applied at the top and bottom rigid microplates, and the boundary nodes are in contact with the cell surface. The classical contact algorithm is applied in the two contact surfaces. In the simulation, the cell deformation is defined as the relative reduction in height, i.e. $(H_0 - H)/H_0$. We first consider the hyperelastic Mooney–Rivlin cell model, and we fit the force-deformation curve (Fig. 3.6c) to get the material constants for endothelial cell. Then we adjust the material coefficients for nematic liquid crystal elastomer trying to get the best fit as well.

Figure 3.6a and b show the cell shape before and after deformation. The force-deformation curve is plotted in Fig. 3.6c. The applied compressive forces increase non-linearly as a function of the cell height reduction. From the simulation (Fig. 3.6c), one can find that the force required to create the same deformation for endothelia cell is larger than that for stem cells, which

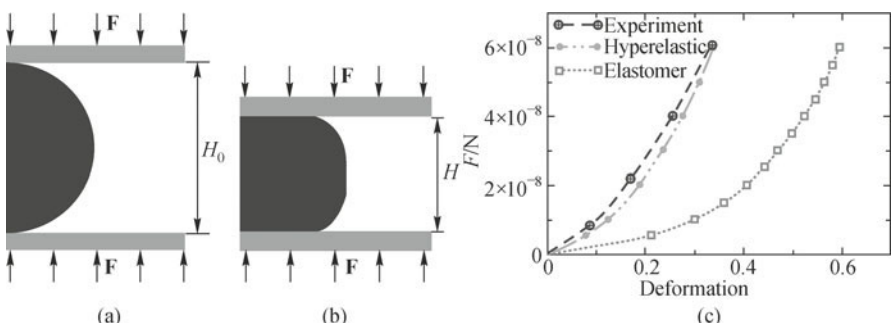


Fig. 3.6 Validation of the cell model: (a) before deformation, (b) after deformation, (c) force-deformation curve. (color plot at the end of the book)

is reasonable considering the fact that the stem cells are undeveloped cells. It can be seen from Fig. 3.6 that our stem cell model is much softer than endothelial cell one, which most likely is true in reality.

3.5.2 Endothelial cell simulations

In this simulation, the endothelial cell is modeled as a spherical ball initially in three-dimensional space, with a diameter of $D = 10 \mu\text{m}$ (Fig. 3.7). The substrate is modeled as a 3D circular plate with a dimension of $(R \times H = 15 \mu\text{m} \times 5 \mu\text{m})$. In our meshfree computation, a total of 4 341 particles are used in discretization of the cell, and 16 640 particles are used to form the meshfree discretization of the substrate. The endothelial cell is modeled as hyperelastic material of the Mooney–Rivlin type. The initial density is $\rho^0 = 1.0 \times 10^3 \text{ kg/m}^3$, and the material constants are $C_1^{\text{Cell}} = 2.126 \times 10^3 \text{ Pa}$, $C_2^{\text{Cell}} = 1.700 \times 10^2 \text{ Pa}$ and $\lambda^{\text{Cell}} = 1.700 \times 10^5 \text{ Pa}$.

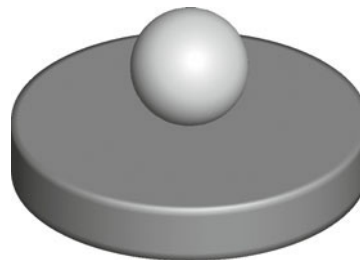


Fig. 3.7 3D Computational model of cell spreading. (color plot at the end of the book)

The substrate is modeled as a Mooney–Rivlin hyperelastic material. Two different substrates with different stiffness are considered. The densities for two substrates are the same as the density for the endothelial cell. The material constants for the soft and stiff substrates are chosen as:

$$\begin{aligned} C_1^{\text{Soft}} &= 6.325 \times 10^4 \text{ Pa}, & C_2^{\text{Soft}} &= 5.06 \times 10^3 \text{ Pa}, & \lambda^{\text{Soft}} &= 5.06 \times 10^6 \text{ Pa}, \\ C_1^{\text{Stiff}} &= 1.265 \times 10^6 \text{ Pa}, & C_2^{\text{Stiff}} &= 1.012 \times 10^5 \text{ Pa}, & \lambda^{\text{Stiff}} &= 1.012 \times 10^8 \text{ Pa}. \end{aligned}$$

The cell is standing still initially and the initial gap between the cell and substrate is set at 200 nm. The bottom surface of the substrate is fixed during the whole simulation. The adhesive force will bring the cell into contact with the substrate, and then the cell will spread under the adhesive contact forces. To expedite the simulation, a big gravitational force is applied.

From this simulation, one may observe the cell spreading over time. In Figs. 3.8 and 3.9, we display the cell shapes and stress contour on two different substrates with different stiffnesses under the same contact conditions at the

same time.

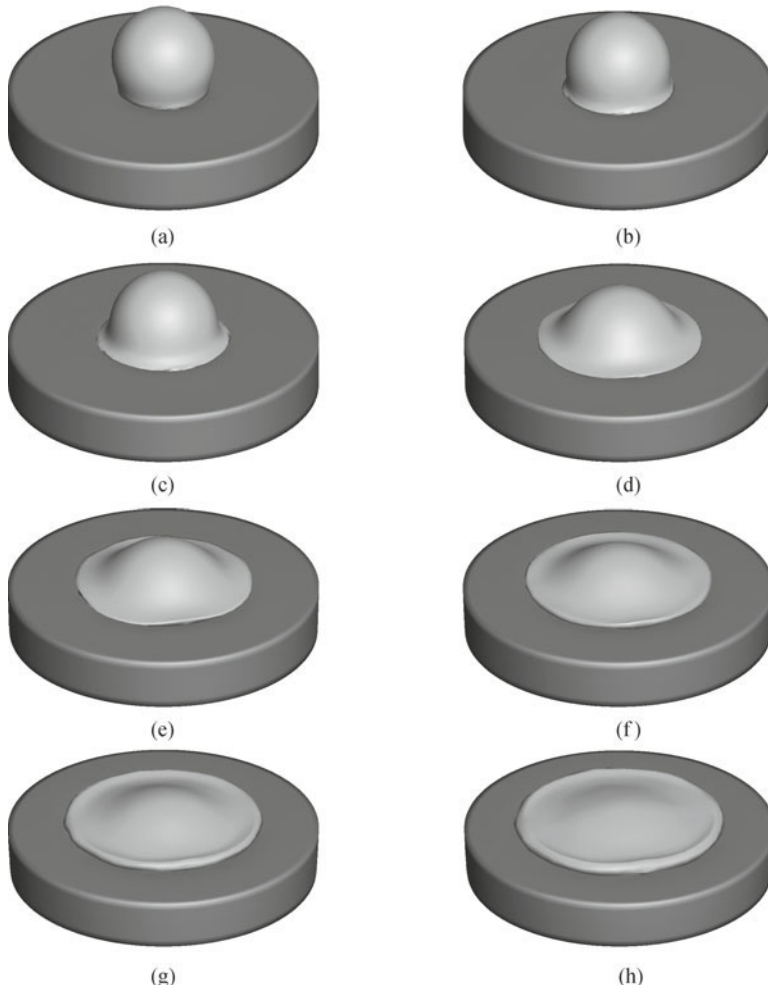


Fig. 3.8 Time sequence of endothelial cell contact with a soft substrate. (color plot at the end of the book)

For comparison, we juxtapose two of the last sequences of cell contact process in Figs. 3.10a and b. One may find that the contact between the cell and stiff substrate generates more spreading than the soft one. As indicated by Winer et al.^[52], many cells show a stiffness-dependent spreading, e.g. the cell exhibits increased spreading and adhesion on stiffer substrates.

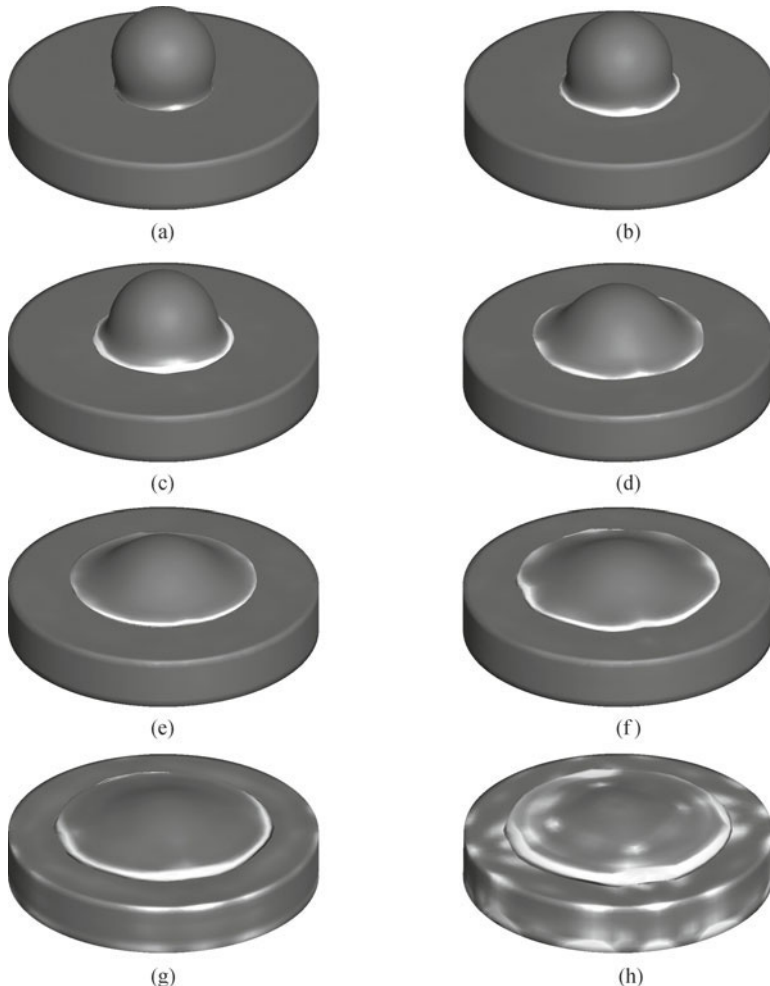


Fig. 3.9 Time sequence of endothelial cell contact with a stiff substrate. (color plot at the end of the book)

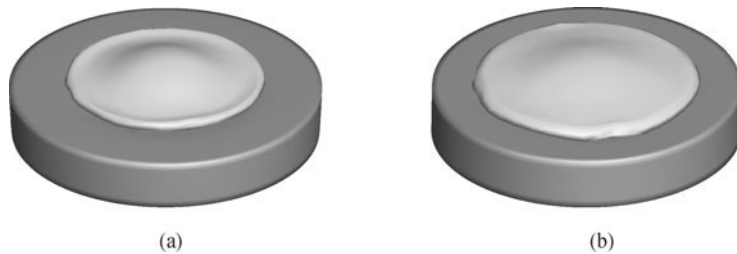
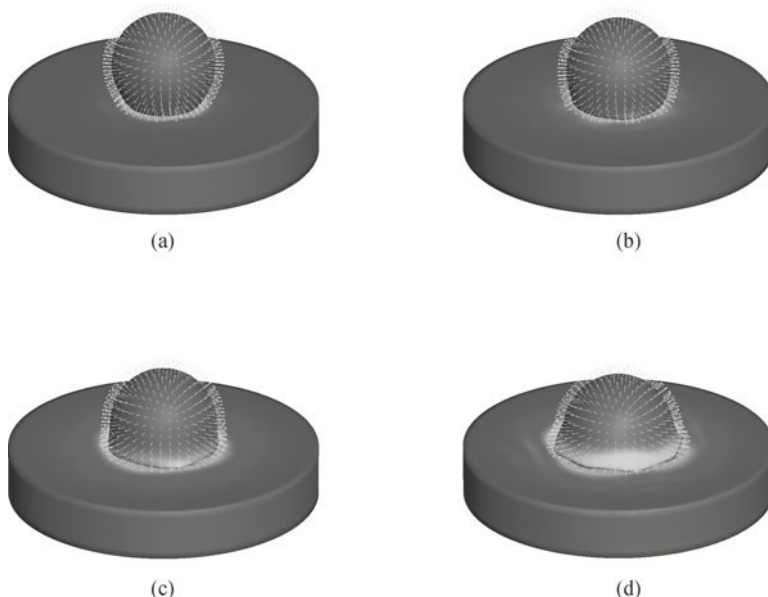


Fig. 3.10 Cell spreading over substrates with different stiffnesses: (a) soft substrate, (b) stiff substrate. (color plot at the end of the book)

3.5.3 Stem cell simulations

For the stem cell simulation, the size and initial condition are exactly the same as the endothelial cell simulation, the only difference is that the stem cell is modeled with liquid crystal elastomers. The material constants for liquid crystal elastomer are chosen as: the shear modulus $\mu = 1.0 \times 10^4 \text{ N/m}^2$, the Frank modulus $\kappa = 1.0 \times 10^{-11} \text{ N}$, the step length anisotropy $s = 2.0$.

Similar results have been obtained for stem cell simulations. In Fig. 3.11, we display a time sequence of a cell contacting the soft substrate. The color contour is the effective stress contour and the white arrow stands for the director field. Comparing to 2D simulations, 3D simulations provide a possible way to capture the cell morphology changes described by Ni and Chiang^[31].



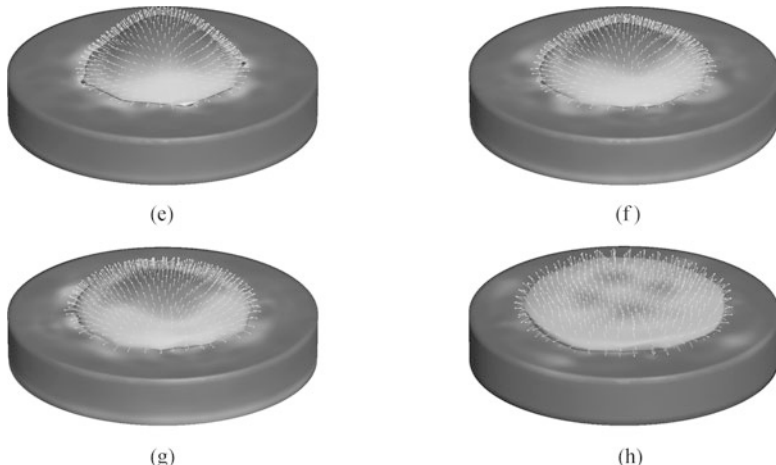


Fig. 3.11 Time sequence of stem cell contact with a soft substrate. (color plot at the end of the book)

3.6 Discussion and conclusions

To develop a fully three-dimensional soft elasticity model capable of explaining cell adhesion, locomotion, and its structure transformation coupled with focal adhesion is a challenge. On the other hand, the soft matter modeling and simulation of cell contact may provide possible explanations on cell mechanotransduction and other issues at the large-scale level.

Our simulation results have shown that: by using the proposed soft matter cell model, when a “cell” is in contact with a substrate, the size of spreading area of the cell also changes or differs depending on the stiffness of extracellular substrate (Fig. 3.10). It should be noted that cell, stem cell in particular, behavior is complex biological phenomenon. The proposed soft matter cell model is only intended to model mechanical behavior of cells at a coarse-grained level, which may not and cannot explain the molecular mechanisms of cell motion, evolution, and proliferation, and it requires in-depth study of every aspect of molecular cell biology including all relevant bio-chemical, bio-physical, as well as bio-mechanical factors and their interactions at different scales.

Developing soft matter models for cells especially stem cells may help us understand bio-mechanical and bio-physical behavior of cells. It is the authors’ opinion that by combining the soft matter cell model with molecular simulation we may be able to achieve qualitative prediction on cell behavior in collaborating with experimental observation. The predictive stem cell model

may give both scientific insight into and clinic guidance on a host of health care problems, such as regenerated medicine and drug design and delivery problems.

Acknowledgements

This research was supported by The A. Richard Newton Research Breakthrough Award from Microsoft Corporation and a grant from National Science Foundation (CMMI No. 0800744). These support is greatly appreciated.

References

- [1] Engler A J, Sen S, Sweeney H L, et al. Matrix elasticity directs stem cell lineage specification. *Cell*, 126, 677-689, 2006.
- [2] Ericksen J L. Equilibrium theory pf liquid crystals. *Advanced in Lquid Crystals*, 2, 233-298, 1976.
- [3] Ericksen J L. On equations of motion for liquid crystals. *Quarterly Journal of Mechanics and Applied Mathematics*, 29, 203-208, 1976.
- [4] Leslie F M. Theory of flow phenomena in liquid crystals. *Advances in Liquid Crystals*, 4, 1-81, 1979.
- [5] Leslie F M. Continuum theory for nematic liquid crystals. *Continuum Mechanics and Thermodynamics*, 4, 167-175, 1992.
- [6] Helfrich W. Elastic properties of lipid bilayer: Theory and possible experiments. *Z. Naturforsch. C*, 28, 693-703, 1973.
- [7] Deuling H J, Helfrich W. Red blood cell shapes as explained on the basis of curvature elasticity. *Biophysics Journal*, 16, 861-868, 1976.
- [8] Deuling H J, Helfrich W. The curvature elasticity of fluid membranes: A catalogue of vesicles shapes. *Journal of Physique (Paris)*, 37, 1335-1345, 1976.
- [9] Li J, Dao M, Lim C T, et al. Spectrin-level modeling of the cytoskeleton and optical tweezers stretching of the erythrocyte. *Biophysics Journal*, 88, 3707-3719, 2005.
- [10] Marko J F, Siggia E D. Statistical mechanics of supercoiled DNA. *Physical Review E*, 52, 2912-2938, 1995.
- [11] Marko J F, Siggia E D. Stretching DNA. *Macromolecule*, 28, 8759-8770, 1995.
- [12] Wang X J, Zhou Q F. Liquid Crystalline Polymers. World Scientific, Singapore, 2004.
- [13] Warner M, Terentjev E M. Liquid Crystal Elastomers. Revised edition. Oxford Science Publications, Oxford, UK, 2007.
- [14] Martin R, Farjanel J, Eichenberger D, et al. Liquid crystalline ordering of procollagen as a determinant of three-dimensional extracellular matrix architecture. *Journal of Molecular Biology*, 301, 11-17, 2000.
- [15] Knight D P, Feng D, Stewart M, et al. Changes in macromolecular organisation in collagen assemblies during secretion in the nidamental gland and formation of the egg capsule wall in the dogfish *Scyliorhinus canicula*. *Phil. Trans. Royal Soc. Lond. B*, 341, 419-436, 1993.

- [16] Knight D P, Vollrath F. Biological liquid crystal elastomers. *Philosophical Transaction of Royal Society of London B*, 357, 155-163, 2002.
- [17] Warner M, Terentjev E M. Nematic elastomers a new state of matter? *Prog. Polym. Sci.*, 21, 853-891, 1996.
- [18] Warner M. New elastic behavior arising from the unusual constitutive relation of nematic solids. *Journal of Mechanics and Physics of Solids*, 47, 1355-1377, 1999.
- [19] Discher D E, Janmey P, Wang Y L. Tissue cells feel and respond to the stiffness of their substrate. *Science*, 310, 1139-1143, 2005.
- [20] Wong J Y, Velasco A, Rajagopalan P, et al. Directed movement of vascular smooth muscle cells on gradient-compliant hydrogels. *Langmuir*, 19, 1908-1913, 2003.
- [21] Schwarz U. Soft matters in cell adhesion: Rigidity sensing on soft elastic substrate. *Soft Matter*, 3, 263-266, 2007.
- [22] Shemesh T, Geiger B, Bershadsky A D, et al. Focal adhesions as mechanosensors: A physical mechanism. *Proceedings of National Academy of Science*, 102, 12383-12388, 2005.
- [23] Bershadsky A, Ran M L, Carramusa L, et al. Cytoskeleton-adhesion crosstalk: Molecular and biophysical aspects. *Life Science Open Day, Weizmann Institute of Science*, 2006.
- [24] Bickel T, Bruinsma R. Focal adhesion: physics of a biological mechano-sensor. arXiv:condmat0306116v1, 2003.
- [25] Aroush D R B, Wagner H D. Shear-stress profile along a cell focal adhesion. *Advanced Materials*, 18, 1537-1540, 2006.
- [26] Besser A, Safran S A. Force-induced adsorption and anisotropic growth of focal adhesion. *Biophysical Journal*, 90, 3469-3484, 2006.
- [27] Novak I L, Slepchenko B M, Mogilner A, et al. Cooperativity between cell contractility and adhesion. *Physical Review Letters*, 93, 268109, 2004.
- [28] Bruinsma R. Theory of force regulation by nascent adhesion sites. *Biophysical Journal*, 89, 87-94, 2005.
- [29] Wang J H C. Substrate deformation determines actin cytoskeleton reorganization: A mathematical modeling and experimental study. *Journal Theoretical Biology*, 202, 33-41, 2000.
- [30] Freund L B, Lin Y. The role of binder mobility in spontaneous adhesive contact and implications for cell adhesion. *Journal of the Mechanics and Physics of Solids*, 52, 2455-2472, 2004.
- [31] Ni Y, Martin Y M C. Cell morphology and migration linked to substrate rigidity. *Soft matter*, 3, 1285-1292, 2007.
- [32] Deshpande V S, Mrksich M, McMeeking R M, et al. A bio-mechanical model for coupling cell contractility with focal adhesion formation. *Journal of the Mechanics and Physics of Solids*, 56, 1484-1510, 2008.
- [33] Liu P, Zhang Y W, Cheng Q H, et al. Simulations of the spreading of a vesicle on a substrate surface mediated by receptor-ligand binding. *Journal of the Mechanics and Physics of Solids*, 55, 1166-1181, 2007.
- [34] Sun L, Cheng Q H, Gao H J, et al. Computational modeling for cell spreading on a substrate mediated by specific interactions, long-range recruiting interactions, and diffusion of binders. *Physical Review E*, 79, 061907, 2009.
- [35] Roy S, Jerry Qi H. A computational biomimetic study of cell crawling. *Biomechanics and Modeling in Mechanobiology*, 9, 573-581, 2010.
- [36] Zeng X, Li S. Multiscale modeling and simulation of soft adhesion and contact of stem cells. *Journal of the Mechanical Behaviors of Biomedical Materials*, 4, 180-189, 2011.

- [37] Caille N, Thoumine O, Tardy Y, et al. Contribution of the nucleus to the mechanical properties of endothelial cells. *Journal of Biomechanics*, 35, 177-187, 2002.
- [38] Sen S, Engler A J, Discher D E. Matrix strains induced by cells: Computing how far cells can feel. *Cellular and Molecular Bioengineering*, 2, 39-48, 2009.
- [39] Fereol S, Fodil R, Laurent V M, et al. Prestress and adhesion site dynamics control cell sensitivity to extracellular stiffness. *Biophysical journal*, 96, 2009-2022, 2009.
- [40] Marckmann G, Verron E. Comparison of hyperelastic models for rubberlike materials. *Rubber Chemistry and Technology*, 79(5), 835-858, 2006.
- [41] Fried I, Johnson A R. A note on elastic energy density functions for largely deformed compressible rubber solids. *Computer Methods in Applied Mechanics and Engineering*, 69, 53-64, 1988.
- [42] Flory P J. Principles of Polymer Chemistry. Cornell University Press, Ithaca, New York, 1953.
- [43] Conti S, DeSimone A, Dolzmann G. Semisoft elasticity and director reorientation in stretched sheets of nematic elastomers. *Physical Review E*, 66, 061710, 2002.
- [44] Conti S, DeSimone A, Dolzmann G. Soft elastic response of stretched sheets of nematic elastomers: A numerical study. *Journal of Mechanics and Physics of Solids*, 50, 1431-1451, 2002.
- [45] DeSimone A. Coarse-grained models of materials with non-convex free-energy two case studies. *Computer Methods in Applied Mechanics and Engineering*, 193, 48-51, 2003.
- [46] Fried E, Korchagin V. Striping of nematic elastomers. *International Journal of Solids and Structures*, 39: 3451-4367, 2002.
- [47] Anderson D R, Carlson D E, Fried E. A continuum-mechanical theory for nematic elastomers, *Journal of Elasticity*, 56: 33-58, 1999.
- [48] Cahn J W, Allen S M. A microscopic theory of domain wall motion and its experimental verification in Fe-Al alloy domain growth kinetics. *Journal of Physics* 38: C7-51, 1977.
- [49] Seifert U. Adhesion of vesicles in two dimensions. *Physical Review A*, 43, 6803-6814, 1991.
- [50] Li S, Qian D, Liu W K, et al. A meshfree contact-detection algorithm. *Computer Methods in Applied Mechanics and Engineering*, 190, 3271-3292, 2001.
- [51] Li S, Kam Liu W. Meshfree Particle Methods. Springer, Berlin, 2004.
- [52] Winer J P, Oake S, Janmey P A. Non-linear elasticity of extracellular matrices enables contractile cells to communicate local position and orientation. *PLoS ONE*, 4(7): e6382, 2009.

Chapter 4 Modeling the Mechanics of Semi-flexible Biopolymer Networks: Non-affine Deformation and Presence of Long-range Correlations

Hamed Hatami-Marbini^{*1} and Catalin R. Picu²

¹*Mechanical Engineering Department, Stanford University, Stanford CA
94305*

²*Department of Mechanical, Aerospace and Nuclear Engineering, Rensselaer Polytechnic Institute, Troy NY 12180*

Abstract: An intertwined network of fibers forms the microstructure of many biological materials and defines their mechanical properties. Depending on the properties of individual fibers, from mechanics point of view, these fibrous materials can be considered to behave as semiflexible networks or flexible networks. While the behavior of flexible networks has been studied thoroughly, the mechanics of semiflexible networks is a less developed subject. In semiflexible networks, the filaments resist the external stresses by storing energy in both bending and axial modes of deformation. Their deformation field is non-affine and has long range correlations within a certain range of scales of observation. Due to the increasing interest in understanding the mechanical and rheological properties of complex systems such as the cell cytoskeleton and connective tissue, a growing interest was manifested in characterizing the mechanics of the semiflexible networks in the recent years. This chapter discusses recent advances in the field of semiflexible random fiber networks, including the quantification of their non-affine deformation and methods for solving boundary value problems on fibrous domains with intrinsic long range correlations.

Keywords: semiflexible fiber networks, non-affinity measure, scaling properties of the network microstructure and mechanics

4.1 Introduction

The mechanics of random fiber networks defines the elasticity and deformation of many biological and non-biological systems such as the cytoskeleton,

^{*}Corresponding author, E-mail: hhatami@stanford.edu.

collagenous connective tissues, battery substrates and paper products among many others. For example, the cytoskeleton is a random network of filamentous proteins: filamentous actin (F-actin), microtubules and intermediate filaments. This network is rendered active by the presence of myosin motor molecules and has a complex role in the mechanics of the cell, the transport of biomolecules within the cytoplasm and in chemo-mechanical transduction and signaling^[1-3]. The cytoskeleton is an out-of-equilibrium network which constantly remodels itself in response to external stimuli using a large number of binding and cross-linking proteins interacting with the cytoskeletal filaments. Fiber networks may also be exploited by several infectious bacteria for self-propulsion^[4,5]. The bacterial pathogen listeria monocytogenes, responsible for more than 2000 annual illnesses and deaths in US, form a filamentous comet tail by taking over the host cell actin machinery. The comet tail is a complex network of cross-linked filaments which are constantly polymerized and depolymerized to generate forces to propel the bacteria within the cytoplasm of the infected cells and into the other neighboring cells. The local elasticity of these media determines to a large extent cellular growth rates. Connective tissues (CTs) such as cartilage and tendon belong to another category of biological fibrous networks. The mechanical functionality of CTs derives directly from the structure and composition of their extracellular matrix (ECM). ECM is a network of insoluble fibrils (e.g., collagen, elastin) and soluble proteoglycan polymers. It is responsible for carrying stresses and maintaining tissue shape while influencing a large number of other biological properties and functions of the tissue. In any connective tissue, the constituents are meticulously arranged inside the extracellular matrix to optimize the function of that specific tissue.

Polymer networks are divided into two broad categories of flexible networks and semiflexible networks. Semiflexible networks are made up of stiff filamentous aggregates that are heavily cross-linked on the scale of their thermal persistence length (the length at which the thermal bending fluctuations become apparent). Therefore, unlike flexible polymers where the energy is stored in the stretching mode of filaments, semiflexible networks store the elastic strain energy in both stretching and bending deformation of the filaments^[6]. This property renders the behavior of semiflexible networks and its relationship to the mechanical properties of its constituents to be more complicated than those of the flexible networks. To provide physical insight into the difference between the mechanics of the flexible and semiflexible networks, it is sufficient to recall that in the flexible networks, segments of a given polymeric chain separated by cross-links behave independently (i.e. the response of a chain segment is not correlated to that of its immediate neighboring segments). However, in semiflexible networks, the long persistence length of the chains imposes correlations on scales larger than that of the average segment length (the distance along the chain between two successive cross-links). For example, the persistence length of F-actin, the main constituent of the cytoskeleton, is on the order of 10 μm , which is compa-

rable to the contour length of the respective molecule/fiber. The persistence length of microtubules is even longer and comparable with the cell size. Generally, the models developed in the literature for flexible networks (mainly for polymeric networks such as rubbers^[7,8]) are not adequate to describe the behavior of semiflexible systems.

This chapter focuses on the elastic behavior of athermal semiflexible networks. The chapter begins with a brief review of the current computational methods and advancements on representing and reconstructing the network topology. Next, the concept of non-affinity and its importance in analyzing the behavior of heterogeneous structures are discussed. The Mikado Model is used to produce computer-generated network architectures and to show that network fiber density is long-range correlated. Moreover, the network elasticity at various length scales is studied to prove the power law scaling property of the network elastic modulus and to show that random fiber networks deform in a manner similar to highly heterogeneous continua with stochastic, long-range correlated distribution of moduli. Finally, a Stochastic Finite Element-based methodology is proposed as an efficient method to solve boundary value problems defined over very large fiber network domains.

4.2 Network representation and generation

The first and essential step in modeling biological fibrous networks is to obtain and reconstruct their true microstructure. Moreover, understanding the fiber network architecture is essential in assessing the effect of various microstructural features in order to manufacture efficient and reliable tissue-engineered constructs. There are various imaging techniques for obtaining network microstructural information. The light level histology technique, magnetic resonance imaging, computed tomography, and optical coherence tomography are among the methods to obtain 3D images of mainly hard, porous tissues such as bone^[9-13]. The structural images of soft tissues can be obtained from confocal microscopy, multiphoton microscopy, electron microscopy and transmission electron microscopy^[14-17]. Estimates of tissue biomechanical properties may be obtained from some of these imaging techniques^[13]. In these techniques, often referred to as elastography, the stiffness of the tissue sample is determined by measuring the tissue strain from variations in optical reflections after and before subjecting the tissue to a uniform pressure. The network microstructure is derived from non-invasive and indirect measurements such as small-angle light scattering and polarimetric imaging where the pattern of scattered laser light transmitted through the sample yields the fiber orientation distribution^[18-20]. These imaging techniques differ from the point of view of resolution, sample size, and their applicability to *in vivo* monitoring.

The network architecture as well as the microstructural features such

as fiber orientation, fiber diameter and their connectivity are extracted from these images. Automated algorithms have been developed to scan the network images and to extract quantitative information on the network morphology such as fiber angle distribution and alignment. These methods are used to extract the network architecture and to assess the effect of various microstructural features in the manufacturing of engineered tissue constructs. Hough transform-based technique, intensity gradient-based approach, direct tracking algorithm, and fast fourier transform-based image analysis are among image analysis methodologies that have been implemented successfully^[21-26]. These algorithms are expensive and their performance depends on the resolution of the images. Complete representation and description of fiber network architecture rely on the capability of these methods to identify network structural details. When the average response of the system is of interest, detailed information on the network geometry is not required and models representing average geometric properties are sufficient. Depending on the microstructural observations, one may develop various computer models for this purpose. For instance, if periodicity and a distinct unit-cell are observed in the real network, models with repeat unit cells such as cellular cubic/hexagonal geometries may be used. The Delaunay triangulation and Voronoi tessellation are among the various algorithms used to represent the structures of cellular networks^[27-31]. Specialized computational techniques such as Metropolis-Hastings importance sampling algorithm are required to represent the details of the microstructure of an actual fibrous structure^[32-34]. Random networks may also be constructed by growing straight fibers from randomly distributed seed points in a domain. In this model, the fiber growth rate is constant and a fiber stops growing when it hits another fiber or a domain boundary^[35]. Another approach to generate random fibrous structures is the Mikado Model which is discussed next.

In the Mikado Model, 2D random fiber networks are generated by randomly placing fibers of length, L_0 , in a square domain of linear dimensions, L . The initial orientation of the fibers is random or selected according to a specified distribution function, in separate models. Rigid connections may or may not be defined at all points where fibers cross. Many dangling ends are produced during fiber deposition; these dangling ends do not contribute to the energy of the system if the fiber excluding volume contribution to stress production is neglected.

In order to fully define the model and investigate the network mechanics, one needs to specify constitutive properties of the individual network fibers in addition to their morphology data (e.g., diameter). For example, there have been many experimental and computational efforts to characterize the mechanical properties of individual cytoskeletal filaments^[36]. In this chapter, the bending and axial stiffness of each fiber are denoted by κ and η , respectively. The system acquires overall rigidity at a critical point defined by a critical fiber density^[40]. This threshold depends on the fiber orientations. The characteristic lengths that may play a role in the mechanics of

fiber networks are the fiber length, L_0 , the mean segment length, l_c (or the fiber number density, N , i.e. the number of fiber centers per unit area) and a parameter with units of length which represents the relative importance of the bending, κ , and stretching, η moduli, $l_b = \sqrt{\kappa/\eta}$. The mean segment length is related directly to the fiber number density, N , as $l_c \sim \pi/2NL_0$, for large N ^[39]. It is known that in the high density limit (large N or small l_c), the network overall response is converging to the affine behavior and the shear modulus scales linearly with the fiber density and approaches the affine prediction^[40,42]. Increasing the bending stiffness κ (large l_b) has a similar effect^[39,42]. In the other limit, when the bending rigidity and/or the fiber number density are low, the non-affinity is important and the shear modulus is smaller than predictions obtained based on the affine approximation.

4.3 Affine vs. non-affine deformation

A material deforms affinely when the strain measured locally is identical to the far field/applied strain. If a spatially homogenous continuum is subjected to a uniform strain field ε_{ij}^0 , the displacement field is affine on all scales of observation and the displacement at all points within the domain is given by $u_i^{\text{aff}}(x_j) = \varepsilon_{ij}^0 x_j$. In inhomogeneous media, the deformation field is given by $u_i(x_j) = \varepsilon_{ij}^0 x_j + \delta u_i(x_j)$ where $\delta u_i(x_j)$ is the local derivation from the affine displacement.

If one assumes that the deformation of the fiber network is affine, a closed-form relation to the overall response of the network (elastic moduli) in terms of fiber properties and orientation can be developed^[37,38]. However, the deformation of random, cross-linked fiber networks is highly non-affine^[39-44]. It is worth mentioning that non-affine deformation has also been evidenced in other disordered systems, such as granular materials and glasses^[45,48,50]. Non-cohesive granular materials consist of discrete macroscopic particles having repulsive forces between them. In fiber networks, non-affine deformation leads to the decrease of effective elastic moduli relative to those expected based on the affine assumption^[35,40,41,44]. In granular packing, non-affine motion of the grains leads to enhanced dissipation and a high loss modulus^[46]. Figure 4.1 shows a network subjected to uniform shear load. Since the network response is non-affine, the deformation field does not follow the deformation of the uniform far-field, i.e. the points on the vertical dash lines in the reference state configuration do not remain on the dash lines after deformation. The energy level of a structure that deforms non-affinely is lower than that of the same structure undergoing affine deformation; therefore, non-affine deformation at the micro- and nano-length scales leads to a more compliant macroscopic response. It is essential to have a measure of non-affinity in order to study the effects of various network geometrical and mechanical parameters (e.g. fiber number density, fiber length, fiber bending / stretching stiffness, far

field loading and fiber initial orientations) on this type of deformation. The next discusses some of the functions proposed for this purpose.

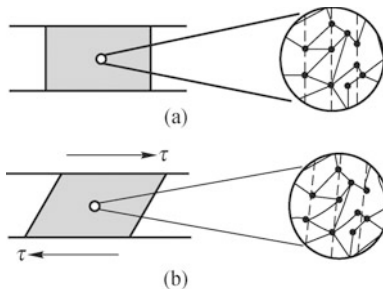


Fig. 4.1 A schematic representation of (a) un-deformed and (b) deformed random fiber networks. The deformation of the network is non-affine since it does not follow the deformation field of the uniform applied far field. If the deformation was affine, network nodes initially located along the vertical dash lines in (a) would remain on the dash lines after deformation in (b)

Various measures have been developed to quantify the non-affinity not only in random networks but in other disordered structures. A detailed study of non-affine behavior and non-affinity correlation functions of the form $\langle \delta u_i(x) \delta u_j(0) \rangle_x$ in random elastic media was performed by DiDonna and Lubensky [6]; $\langle * \rangle_x$ represents the average of the expression $*$ over x . The general aspect of the non-affine response in random discrete systems can be described in terms of a continuum elastic media with a fluctuating elastic modulus tensor with a uniform nonzero average and locally fluctuating local stress tensor with vanishing mean. Langer and Liu^[47] studied the response of foams to small perturbations using three measures of non-affinity, two of which are based on bubble displacements ($\delta \mathbf{u} = \mathbf{u} - \mathbf{u}^{\text{aff}}$, where \mathbf{u} is the actual displacement of a bubble and \mathbf{u}^{aff} is the corresponding affine displacement), while the other one is based on energy. They deform the structure affinely and let it relax from its affine configuration. In the first measure of non-affinity, the shift in the bubble final relaxed positions relative to their initial affine deformation is measured. In the second measure, they compute the difference of a bubble position with respect to the average shift of its neighbors. Finally, the third measure represents the change of the elastic energy between bubbles in their initial affine and final, relaxed configurations. The non-affine displacement, $\delta \mathbf{u}$, was used by Tangut et al.^[48] who studied the deformation of amorphous bodies made from polydisperse Lennard-Jones beads. These are vectorial quantities computed at the site of each discrete entity of the ensemble.

Head et al.^[39] studied non-affinity in networks of semiflexible polymers subjected to shear. They introduced a scalar non-affinity measure based on the infinitesimal change of the angle, θ , made by a vector connecting two

nodes in the structure with one of the global axes, i.e.

$$\delta\theta^2(r) = \langle (\theta - \theta^{\text{aff}})^2 \rangle_r, \quad (4.1)$$

where θ^{aff} denotes the corresponding affine prediction of this angle, r is the distance between the respective two network nodes and represents the scale at which non-affinity is studied. They observed a monotonic power-like decrease in $\delta\theta^2(r)$ as r increases. They used this measure to divide the networks into affine and non-affine. For this purpose they introduced the parameter L/λ , where λ is a length given by $\lambda = l_c(l_c/l_b)^z$ and z is an exponent selected between 0.33 and 0.40. At large L/λ , the non-affinity measure $\delta\theta^2(r)$ appears to reach a plateau at small r/L_0 where this saturation implies that network behavior is approximately affine irrespective of how small the length scale of interest is (does not increase as the length scale of observation decreases). This suggests that the deformation is non-affine for compliant low density networks while it is affine for stiff high density networks. Onck et al.^[41] showed that the degree of non-affinity decreases as the network is subjected to large deformations. They employed a scalar measure defined by

$$\Delta A = \frac{1}{\Delta\gamma} \left\langle \frac{\|\delta \mathbf{u}\|}{\|\mathbf{x}\|} \right\rangle, \quad (4.2)$$

where $\|\cdots\|$ denotes the vector length, \mathbf{x} is the current position vector of a cross link and $\Delta\gamma$ is the applied shear increment. The average is worked out over all network cross-links. They observed that deformation becomes more affine with increasing strain and there exists a transition of bending dominated response at small strain to stretching dominating response at large strains.

Since the behavior of random networks needs to be studied at various length scales, the probing length scale must be incorporated in the non-affinity measure. Most non-affinity measures including those mentioned in the above cannot easily be related to mechanical fields or to a tangible property of the network. Hatami – Marbini and Picu^[43] proposed a probing length-scale-dependent non-affinity measure based on the gradients of the displacement field. The measure provides a unified description of non-affinity in both strains and rotation. This non-affinity measure was used to study the influence of the network characteristic length scales, fiber density and far-field loadings on the degree of non-affinity of the deformation. It is based on the fluctuation of the actual strain/rotation relative to the respective affine quantity (or the far field). The deformation of the system loaded by displacement-imposed boundary conditions is obtained numerically via energy minimization. Once the nodal displacements are obtained, strains are computed at various probing length scales by choosing a triplet of network nodes so that they form approximately an equilateral triangle (Fig. 4.2) The displacement field within the triangle is written in terms of nodal displacements ($\mathbf{u}^i, i = 1..3$) using interpolation functions of the constant-strain triangular element (CST) from

the finite element method:

$$\mathbf{u}(\mathbf{x}) = N_i(\mathbf{x})\mathbf{u}^i, \quad (4.3)$$

where sum over repeated index is implied and $N_i(\mathbf{x})$ are the shape functions of the CST element^[49].

The constant small strain field $\boldsymbol{\epsilon} = (\varepsilon_{11}, \varepsilon_{22}, \varepsilon_{12})$ and the rotation ω_{12} associated with each triplet of nodes can be evaluated from the gradient of the displacements,

$$\begin{aligned}\varepsilon_{ij} &= \frac{1}{2} \left(\frac{\partial u_i}{\partial x_j} + \frac{\partial u_j}{\partial x_i} \right) \quad \text{for } i, j = 1, 2, \\ \omega_{12} &= \frac{1}{2} \left(\frac{\partial u_1}{\partial x_2} - \frac{\partial u_2}{\partial x_1} \right).\end{aligned}\quad (4.4)$$

The resulting gradients are considered to be an average of the underlying fields over the length scale r which is equal to the square root of the area of the respective triangle. For all length scales r , $\langle \boldsymbol{\epsilon} \rangle_r = \boldsymbol{\epsilon}^{\text{aff}}$ where the corresponding affine strain components, $\boldsymbol{\epsilon}^{\text{aff}}$, are the applied far field. The measure of non-affinity is defined as the fluctuation of the actual deformation gradients relative to their affine estimates:

$$\mathbf{H}(r) = (H_1, H_2, H_3, H_4) = \langle (\boldsymbol{\Xi} - \boldsymbol{\Xi}^{\text{aff}})^2 \rangle_r, \quad (4.5)$$

where $\boldsymbol{\Xi} = (\varepsilon_{11} \quad \varepsilon_{22} \quad \varepsilon_{12} \quad \omega_{12})$. The index r denotes the length scale at which \mathbf{H} is evaluated.

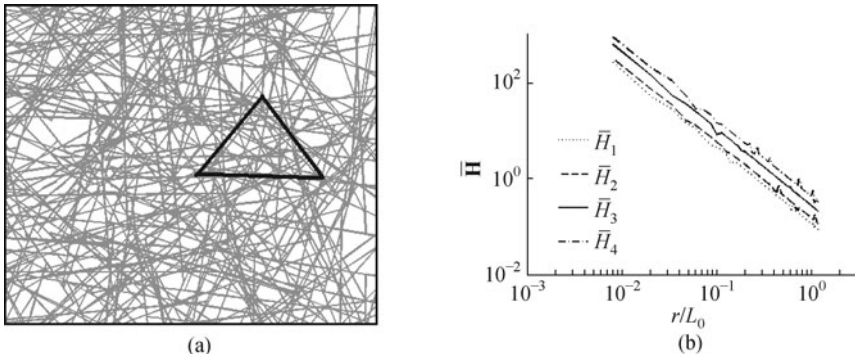


Fig. 4.2 (a) Sample realization of the random fiber network structure along with a representative quasi-equilateral triangle used for probing the strain field, (b) normalized non-affinity measure $\bar{\mathbf{H}}(r) = \mathbf{H}(r)/\varepsilon_0^2$ against the normalized probing length scale, r/L_0 (size of the triangle in (a)) for networks of density $N=200$ fibers per unit area and $l_b/L_0 = 10^{-4}$ subjected to the uniaxial far-field strain $\boldsymbol{\epsilon} = (\varepsilon_0, 0, 0)$ ^[43].

As opposed to the other measures used in the literature, this measure naturally separates the deformation and the rigid body rotation components

of the displacement field. It is independent of the far field loading and is better suited for direct comparison with continuum models in the appropriate limit. Using this non-affinity measure, Hatami–Marbini and Picu^[43,49] preformed a comprehensive study of the non-affine deformation of random fiber networks and studied the effects of network characteristic lengths, type of far-field loadings and initial fiber orientations. They observed that all strains exhibit non-affine fluctuations of comparable magnitudes and the non-affinity in the rotation ω_{12} is similar to that of the strains. This relates to observations of rotatory structures in the non-affine displacements of granular materials^[50]. Based on their results, all components of the non-affinity measure follow a power law scaling with r over the entire range of probed length scales (Fig. 4.2b). In random fiber networks, the scaling exponent does not depend on the far field loading and fiber initial length L_0 .

4.4 Network microstructure: scaling properties of the fiber density function

Structural self-similarity of the network microstructure can be investigated at various length scales using either the box-counting method or density autocorrelation functions. In the box-counting method, the number of squares of size δ required to cover an image is counted and its variation is plotted against δ . If a material has fractal scaling properties, the total number of square N_δ will show a power law variation with the square size δ , i.e.

$$N_\delta \propto \delta^{-D_\delta}, \quad (4.6)$$

where D_δ is the box-counting (fractal) dimension of the structure. The sizes of square elements can be considered as the length scale at which the network microstructure is probed. If the probing length scale δ is larger than the mean fiber segment length l_c , this method fails since the whole 2D domain is tiled and the dimension of the embedding space, i.e. $D_\delta=2$, is recovered. Therefore, the box-counting approach may only be applied to probing the network structure as long as $\delta/l_c < 2.0$ ^[51]. Figure 4.3 shows the number of squares N_δ vs. the mesh size δ in a log-log plot for networks with various fiber number densities. Despite the small range of scales that can be probed by this method, few observations can be made from this plot. At large length scales, $\delta/l_c > 0.5$, the fractal dimension is 1.55 ± 0.05 and at small length scales, $\delta/l_c < 0.5$, it is 1.25 ± 0.05 . The fractal dimension of the network is almost independent of the fiber number density. These fractal dimensions are in agreement with the results reported by Kaye^[52].

Although the above procedure yields valuable information relevant to the hole size distribution in the network, it is not useful when $\delta/l_c > 2$. In order to investigate the structure of the network geometry at larger length scales, the autocorrelation function of the fiber density may be used. The

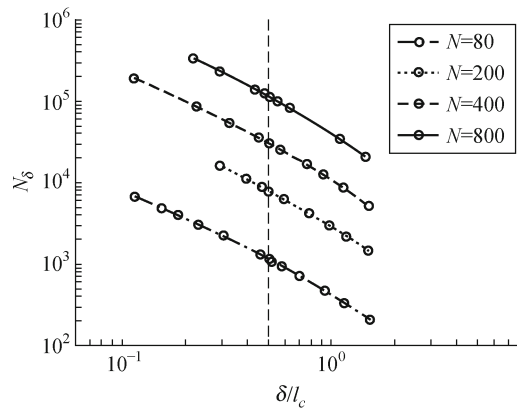


Fig. 4.3 The result of box counting method used to probe the self-similarity of random fiber networks. Results of four different fiber densities are shown. Two distinct scaling regions separated at length scale $\delta/l_c = 0.5$ are observed. The small slope is 1.25 ± 0.05 and the large one is 1.55 ± 0.05 .

autocorrelation function (ACF) is often used to study the stochastic self-similarity of disordered systems. The autocorrelation function $ACF(x, y)$ for a function $f(x, y)$ of mean zero is computed as follows:

$$ACF(x, y) = \int f(x', y') f(x + x', y + y') dx' dy'. \quad (4.7)$$

The result is a 2D function. The radial autocorrelation (a 1D function) can be computed from the result of the integral in Eq. (4.7) by averaging over multiple origins and over all radial lines passing through the current origin. Therefore, the radial autocorrelation function $C(r)$ for the function $f(r, \theta)$ with mean zero is defined as

$$C(r) = \frac{1}{2\pi} \iint f(r', \theta) f(r + r', \theta) dr' d\theta. \quad (4.8)$$

If a function has scaling properties, its radial autocorrelation function decays as a power law with exponent $6-2D_f$ where D_f is the fractal box dimension of the graph of the respective function^[53].

Let function f represent the fiber density, ρ . The fiber density of the network at different probing length scales δ/l_c can be obtained by overlaying the square mesh described above on networks with various fiber number densities N (Fig. 4.4a). The fiber density is measured by computing the total fiber length in each square element. A rough surface of the network fiber density distribution at the length scale specified by the element size/resolution δ is obtained. The discrete form of Eq (4.8) is used to study the fractal properties of this rough surface at various length scales δ . Figure 4.4b shows the normalized ACF of the density distribution, \bar{C}_ρ , of networks with wide variety

of fiber densities probed at various length scales. The normalization is the average of the squared mean densities of fibers over all square elements. It is observed that \overline{C}_ρ varies as a power law function with the probing length scale, i.e. $\overline{C}_\rho(r) \propto r^{-s_\rho}$. The exponent of this function is $s_\rho = 0.88 \pm 0.04$ and is independent of the fiber number density. Therefore, the fractal box dimension of the density surface is $D_\rho = 2.55 \pm 0.02$. The upper cut-off of the power law scaling behavior is approximately $L_0/2$; beyond this limit, the density function becomes uncorrelated.

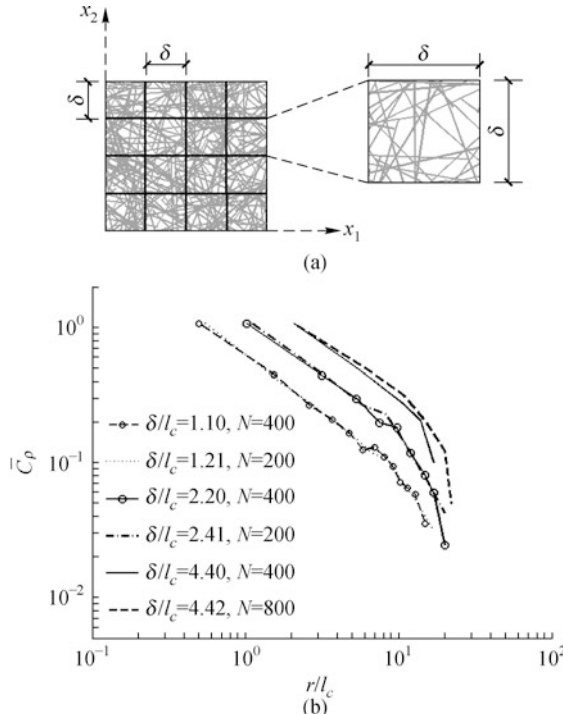


Fig. 4.4 (a) Schematic representation showing a random fiber network along with a regular mesh of characteristic dimension δ . The regular mesh is used exclusively for probing the network. The size of square elements denotes the length scale of observation, (b) the autocorrelation function of the fiber density for networks with various fiber densities probed at different length scales δ/l_c . The power law behavior is independent of the fiber density^[56].

It is also possible to evaluate the probability distribution function (PDF) of fiber densities over all squares of size δ of the probing mesh. Figure 4.5 shows the PDF of the normalized fiber density ($\delta^2 \rho_\delta$) for a random fiber network with $L = 10$ and $N = 150$. It is seen that as the probing length scale, δ/l_c increases, the density function obtained from probing the network at large scales looks more like a random uncorrelated function. Therefore, there exists an upper limit (proportional to L_0) for the fractal scaling of the

network density. This limit is the scale beyond which the network behaves with a very good approximation as a homogeneous continuum.

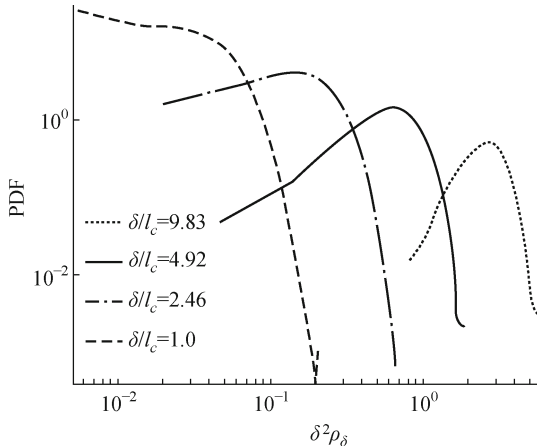


Fig. 4.5 The probability distribution function of normalized densities ($\delta^2 \rho_\delta$) for random fiber networks with $L = 10$ and $N = 150$ probed at various length scales δ/l_c .

It is also useful to perform a multi-fractal analysis using these same data. While perfect fractals are defined by a unique fractal dimension characterizing scaling over the entire range of scales, real materials exhibiting self-similarity often have multi-fractal characteristics, i.e. the fractal dimension changes as the scale of observation is varied. If $\text{PDF}_\delta(\rho)$ denotes the probability distribution function of the fiber density measured at length scale δ , the q -th moment of this distribution is defined as

$$m_\delta^q = \int \rho^q \text{PDF}_\delta(\rho) d\rho. \quad (4.9)$$

If the function $\text{PDF}(x)$ exhibits fractal scaling, one obtains $m_\delta^q \propto \delta^{\beta(q)}$ ^[54], where $\beta(q)$ is a generic function of the moment order. If $\beta(q)$ is not linear in its argument, the respective function has multifractal properties^[55]. The result of multifractal analysis of a network with $N = 400$ is shown in Fig. 4.6. The range of scales considered is $\delta/L_0 \in (2l_c/L_0, 0.5)$, i.e. the range with which scaling is observed in the ACF functions. It is observed that m_δ^q is indeed a power law of δ and $\beta(q)$ has a linear variation with the order q (inset, Fig. 4.6). This indicates that the density function is single-fractal function within this range of scales.

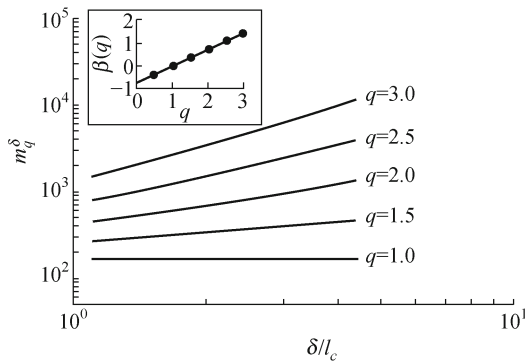


Fig. 4.6 Multifractal analysis of the distribution of densities. The lines represent the scaling of the q -th moment of the density probability distribution function with the probing length scale δ . These are functions of the form $m_\delta^q \propto \delta^{\beta(q)}$, where the power (beta) $\beta(q)$ is linear with q as shown in the inset. This indicates that the density is characterized by a single fractal dimension over the range of scales considered.

4.5 Network elasticity: the equivalent continuum and its elastic moduli

Since the fiber number density is linearly related to the stiffness at high densities^[39], the elastic moduli are expected to have properties similar to those discussed above for the fiber density. In order to test this conjecture and to investigate the elasticity of the network at various length scales, Hatami–Marbini and Piciu^[56] solved the nodal displacements of the network subjected to far-field loading (displacement boundary value problem) by minimizing the potential energy of the entire network. A regular mesh of square elements of size δ was overlaid on the network (Fig. 4.4a). Each square domain was considered separately and the displacements, axial forces and bending moments at the intersection points of fibers with square edges were evaluated. This yields the traction distribution along the perimeter of each square element of size δ from which the average stress state in the respective domain is calculated. Next, using linear finite element shape functions, the displacement field inside each square element is described in terms of the displacements of its corners. The displacements of the corners are unknown; nevertheless, they can be estimated by imposing the condition that predicted displacements of the intersection points on the square element perimeter to be the closest to their actual values. Once the displacement field is known, the strain field distribution and subsequently the average strains within the problem domain are known. The elastic constants in each square domain are evaluated based on the local average stress and strain state. Thus, each square

domain can be replaced by an isotropic homogeneous continuum domain. This fitting can be performed provided that the fiber density in the respective element is sufficiently large so that the elasticity of each element can be assumed to be isotropic and also the total moment acting on each element edge can be neglected; this happens once the probing length scale δ is larger than approximately $2l_c^{[51]}$. Following the above procedure, Hatami–Marbini and Picu^[56] studied the autocorrelation function of Young’s modulus, $C_E(r)$, for networks with various fiber number densities probed at different probing length scales and observed power law scaling, $C_E(r) \propto r^{-s_E}$, with exponent $s_E = 0.92 \pm 0.06$. Therefore, the fractal dimension of the stiffness distribution surface is $D_E = 2.56 \pm 0.03$. This value is in good agreement with D_ρ , confirming the proportionality relation between Young’s modulus and fiber density in this range of parameters.

4.6 Boundary value problems on dense fiber network domains

The power law scaling property of the density function and elastic moduli proves that random fiber networks deform in a manner similar to highly heterogeneous continua with stochastic long-range correlated distribution of moduli. Since scale decoupling does not exist in such structures and within the range of self-similarity, standard information-passing techniques or the usual theoretical tools developed by homogenization theory^[57] cannot be used. This conclusion is essential when addressing big problems such as the deformation of the cytoskeleton consisting of stiff fibers (e.g. microtubules) whose length is comparable with that of the entire cell. Specialized methods such as that developed in [58] are required. In the following, a methodology developed by Hatami–Marbini and Picu^[56] as well as a brief review of other methods used in literature to model the deformation of fiber network are discussed.

4.6.1 Background: affine and non-affine theories

Significant research has been dedicated to describing the macroscopic response of fibrous systems to applied load in terms of their microstructure, i.e. their mechanical (elasticity, plasticity, creep and fatigue behavior of individual fibers) and geometrical (fiber density, fiber length and fiber orientations) properties. Both phenomenological and micromechanics models were used for this purpose. Phenomenological models are based on fitting mathematical equations to sets of experimental data. Although they are usually simple and easy to implement, they provide little insight into the connection between the fitting parameters and the network physical and mechanical properties. Micromechanics models clear-up this ambiguity. Micromechanics models are

divided into two broad categories based on whether they are formulated using the affine or non-affine assumption for the network response.

One of the earliest micromechanics models developed for fibrous materials is due to Cox^[59]. In this model, fibers are assumed to span the entire problem domain and to be loaded only at their ends. Moreover, their bending stiffness is ignored; fiber stores energy only in the stretching mode. The only geometrical parameter is the fiber orientation, which is selected from a specified distribution function. Narter et al.^[37] extended the fiber network theory of Cox to three dimensions (3D) and predicted their elastic moduli in terms of the density and elastic constants of the fibers. In the following, the two-dimensional version of these models is given; the reader is referred to Narter et al.^[37] for the three-dimensional case.

Consider a unit cell of N_v fibers with orientation distribution function $f(\theta)$ subjected to a uniform shear strain γ . The strain in a fiber element with orientation θ is given by

$$\varepsilon(\theta) = \gamma \sin \theta \cos \theta. \quad (4.10)$$

If all fibers obey Hooke's law and have the same axial stiffness μ_f , the total energy Π stored in the fibers can be computed as follows:

$$\Pi = \int_0^\pi \frac{1}{2} N_v f(\theta) A_f \mu_f \gamma^2 \sin^2 \theta \cos^2 d\theta, \quad (4.11)$$

where A_f is the area of the fiber cross-section and N_v is the number of straight fibers of unit length per unit area. If fiber orientations follow a uniform distribution, the corresponding affine modulus, G^{aff} , per unit thickness of fiber network is given by

$$G^{\text{aff}} = \frac{1}{8} N_v A_f \mu_f. \quad (4.12)$$

The above analysis can be extended to consider fiber bending stiffness and transverse deflections. For this purpose, Astrom et al.^[60] estimated the stiffness of random networks consisting of interconnected short fibers using effective medium theory. Furthermore, Wu and Dzenis^[38] derived the effective stiffness of random fiber networks based on the probability distribution function of fiber lengths and orientations. They developed their model for statistically homogenous networks consisting of linear elastic fibers of uniform diameters and lengths. Rigid contacts are considered between fibers and each fiber segment is modeled as a beam element. Besides Euler–Bernoulli beam elements, Timoshenko beam elements and simple rod elements may also be used to model fiber segments depending on their modes of deformation. Similar models have also been developed by considering fiber-fiber bondings as hinged or built-in torsional springs^[61,62]. If the network microstructure is generated by the Mikado model, fiber centers are uncorrelated and the fiber

segment length distribution is Poissonian:

$$f(l) = \frac{1}{l_c} \exp \frac{-l}{l_c} \quad (4.13)$$

where l represents the segment length and $l_c \sim \pi/2NL_0$ (L_0 is the straight fiber length and N is the fiber concentration) is the mean segment length for uniformly distributed fibers. Having the distribution of fiber segments and assuming that the microscopic deformation of a fiber segment complies with the uniform strain of the effective continuum (affine assumption), the network effective moduli are determined from the equivalency of the strain energy stored in the fibers and the energy of the effective continuum domain. If only stretching of fibers is considered, this method yields the effective shear modulus given by Narter, et al.^[37,39],

$$G^{\text{aff}} \sim \frac{\pi}{16} \frac{\mu_f A_f}{L_0} \left(\frac{L_0}{l_c} + 2 \frac{l_c}{L_0} - 3 \right) \sim \frac{\pi}{16} \frac{\mu_f A_f}{l_c}. \quad (4.14)$$

Note $N = N_v L_0$. Although affine models present explicit expressions for the effective stiffness of fiber networks, the significant error in their estimates renders them largely inadequate in most cases^[35]. As discussed above, the mechanics of fiber networks like that of any disordered system is non-affine. In these structures and at scales close to the characteristic length scales of the problem, ordinary homogenization techniques are not applicable due to the absence of a well-defined unit cell. In the following paragraph, some of the previous efforts to consider non-affinity in predicting the network macroscopic behavior are discussed; these models are referred to as network models.

Wilhem and Frey^[40] considered a random network of rigid rods and studied the relation between the shear modulus of the network and the fiber density. They concluded that the network elasticity is dominated by bending deformation. A similar numerical study of semiflexible filaments was conducted by Head, et al.^[39] in which the authors showed that there are two distinct regimes in the behavior of random networks: while networks with large fiber density behave affinely, low density networks deform non-affinely. The strain stiffening of semiflexible random networks at large strain is considered by Onck, et al.^[41]. It is argued that stiffening results from the rearrangement/alignment of fibers, not from the nonlinear response of polymeric filaments themselves. A transition from the bending-dominated response of the system at small strains to the stretching-dominated response at large strains occurs because of the non-affine rearrangement of the fibers during network stretching. Chandran and Barocas^[35] in their study of tissue and tissue equivalents showed that the actual macroscopic stress in random fiber networks is about three fold lower than the stress predicted using the affine deformation assumption. They further concluded that in random networks there is very little correlation between the strain in a fibril and its orientation. Moreover, Barocas and coworkers^[34,63,64] developed an information-passing

multiscale modeling scheme for the network behavior. They assumed that in a large, statistically homogenous fiber network, there exists a representative volume element (RVE) which is structurally typical for the entire sample. The problem is represented at larger scales as a continuum, which is discretized in finite elements. RVEs are used to provide the Cauchy stress at each integration point of the finite element mesh. The mean RVE Cauchy stress is calculated by averaging network fiber forces. The macroscopic balance equations are then solved using this stress to determine the new microscopic deformation field. This process is repeated until the desired degree of convergence is reached. The validity of this methodology hinges on the existence of a representative volume element for the respective network.

In previous sections, it was shown that the deformation of random fiber networks is similar to the deformation of highly heterogeneous continuum domains with stochastic fractal distribution of moduli. In fractal structures, correlations of the deformation field extend to the scale of the entire problem domain. Hence, the structure has no translational symmetry and identifying a representative volume element becomes problematic; in these situations no sub-structuring is possible and the entire boundary value problem has to be solved at once.

A methodology for solving boundary value problems defined on fiber network domains, which takes account of these considerations, was developed by Hatami-Marbini and Picu^[56,65]. This methodolgy is based on the Stochastic Finite Element Method (SFEM) which captures the stochastic nature of the network^[58,66-71]. The fiber network is first mapped to a highly heterogeneous continuum using the method discussed above in connection with the evaluation of the density and Young's modulus ACF. As seen, the map with resolution $\delta < L_0$ exhibits long-range spatial correlations of the moduli. Furthermore, multiple networks with the same global parameters correspond to different continua. The elasticity at a given site in multiple replicas is uncorrelated. In SFEM, the field of elastic constants is generated through a stochastic process having properties similar to those observed for the actual network. This process is written in the form of a Karhunen–Loeve decomposition. This facilitates the representation of spatial correlations. The unknown fields, i.e. the displacements, are represented in terms of chaos polynomials. The variational problem is written in terms of these two expansions in the weak sense (as in FEM formulations) and in the mean (with respect to the stochastic process producing system replicas).

The stochastic finite element formulation for a general mechanics boundary value problem is represented following a brief review of the Karhunen–Loeve decomposition. This general formulation is then used to derive finite element equations for two-dimensional elasticity problems of fiber networks.

4.6.2 Karhunen – Loeve decomposition

Let $f(\mathbf{x}, \xi)$ denote a random process where $\mathbf{x} \in B$ and $\xi \in \Omega$, i.e. $f : B \times \Omega \rightarrow \mathbf{R}$. Here, B denotes a subset of the real space \mathbf{R} and Ω is the probability space. Therefore, the function $f(\mathbf{x}, \xi)$ is a random function with two variables, a probabilistic one ξ and a deterministic spatial one \mathbf{x} . The mean of the random function at any point $\mathbf{x} \in B$ is given by:

$$\langle f(\mathbf{x}, \xi) \rangle_\xi = \bar{f}(\mathbf{x}) = \int_{\Omega} f(\mathbf{x}, \xi) dP(\xi), \quad (4.15)$$

where P is a probability measure defined on the Ω , $\langle * \rangle_\xi$ represents the average of the stochastic function $*$ over ξ and is denoted by a bar over the function, i.e. $\langle * \rangle_\xi = \bar{*}$.

The linear elastic equilibrium and kinematics equations of a boundary value problem with random elastic constants can be written in the most general form as:

$$\mathbf{L}(\mathbf{x}, \xi) \mathbf{u}(\mathbf{x}, \xi) = \mathbf{g}(\mathbf{x}), \quad (4.16)$$

where $\mathbf{x} \in B$, $\mathbf{L}(\mathbf{x}, \xi)$ is a partial differential operator and $\mathbf{u}(\mathbf{x}, \xi)$ is the unknown response of the problem to $\mathbf{g}(\mathbf{x})$ which is a deterministic loading. If the probabilistic information about $\mathbf{L}(\mathbf{x}, \xi)$ is known, the solution of Eq. (4.16) is completely determined by finding the joint probability distribution of $\mathbf{u}(\mathbf{x}, \xi)$ and $\mathbf{L}(\mathbf{x}, \xi)$. Such a complete set of information about the solution is often very difficult to obtain. However, there are few procedures in the literature which provide the modest amount of information about the solution in terms of its moments^[66]. Using Eq. (4.15), Eq. (4.16) can be written as

$$[\bar{\mathbf{L}}(\mathbf{x}) + \mathbf{l}(\mathbf{x}, \xi)] \mathbf{u}(\mathbf{x}, \xi) = \mathbf{g}(\mathbf{x}), \quad (4.17)$$

where $\bar{\mathbf{L}}(\mathbf{x})$ denotes the statistical average of operator $\mathbf{L}(\mathbf{x}, \xi)$ over ξ , i.e.

$$\mathbf{L}(\mathbf{x}, \xi) = \bar{\mathbf{L}}(\mathbf{x}) + \mathbf{l}(\mathbf{x}, \xi). \quad (4.18)$$

The dependence of $\mathbf{l}(\mathbf{x}, \xi)$ on ξ is expressed in terms of a set of random functions $\omega(\xi)$ using the Karhunen – Loeve expansion^[72]. Therefore,

$$\mathbf{l}(\mathbf{x}, \xi) = \sum_i \sqrt{\lambda_i} \omega_i(\xi) \mathbf{a}^{(i)}(\mathbf{x}), \quad (4.19)$$

where $\{\omega_i(\xi)\}$ is a set of orthonormal random variables, $\{\lambda_i\}$ is a set of constants, and $\{\mathbf{a}^{(i)}(\mathbf{x})\}$ is an orthonormal set of deterministic functions. The random variables $\{\omega_i(\xi)\}$ satisfy the following conditions,

$$\begin{aligned} \langle \omega_i(\xi) \rangle_\xi &= 0, \\ \langle \omega_i(\xi) \omega_j(\xi) \rangle_\xi &= \delta_{ij}, \end{aligned} \quad (4.20)$$

where δ_{ij} is the Kronecker delta function. It can be shown that the deterministic functions $\mathbf{a}(\mathbf{x})$ are the solution of the following homogeneous Fredholm integral equation of the second kind,

$$\int_B \text{Cov}(\mathbf{x}, \mathbf{y}) \mathbf{a}(\mathbf{y}) d\mathbf{y} = \lambda \mathbf{a}(\mathbf{x}), \quad (4.21)$$

where

$$\text{Cov}(\mathbf{x}, \mathbf{y}) = \langle l(\mathbf{x}, \xi) l(\mathbf{y}, \xi) \rangle_\xi = \int_\Omega l(\mathbf{x}, \xi) l(\mathbf{y}, \xi) dP(\xi), \quad (4.22)$$

is the covariance function. Since the covariance function is symmetrically and positively definite, its eigenvalues are real. The eigenfunctions are orthogonal and form a complete set, i.e.

$$\int_B \mathbf{a}^{(i)}(\mathbf{y}) \mathbf{a}^{(j)}(\mathbf{y}) d\mathbf{y} = \delta_{ij}. \quad (4.23)$$

It can be shown that the generalized coordinate system defined by these eigenfunctions is optimal in the sense that the mean square error resulting from a finite representation of $l(\mathbf{x}, \xi)$ is minimum^[66]. An alternative statement of the problem is to find the spectral decomposition of the covariance as follows:

$$\text{Cov}(\mathbf{x}, \mathbf{y}) = \sum_i \lambda_i \mathbf{a}^{(i)}(\mathbf{x}) \mathbf{a}^{(i)}(\mathbf{y}). \quad (4.24)$$

Obviously, the constants λ_i are the eigenvalues of the eigenproblem defined by Eq. (4.21).

4.6.3 Stochastic finite element formulation of 2D problems

The explicit form of the governing linear elastic equilibrium and kinematics equations are derived for a two-dimensional static problem with linear elastic constitutive law and infinitesimal deformation. Here only a brief overview of the required steps to obtain the stochastic finite element formulation is given. For a comprehensive overview of the methodology, the reader is referred to Ghanem and Spanos's book^[66]. Let us consider a two-dimensional stochastic domain which is discretized into finite elements. The strain energy V^e stored in each element of area A^e can be expressed as

$$V^e = \frac{1}{2} \int_{A^e} \boldsymbol{\sigma}(\mathbf{x}, \xi)^T \boldsymbol{\epsilon}(\mathbf{x}, \xi) dA^e. \quad (4.25)$$

Here, $\boldsymbol{\sigma}(\mathbf{x}, \xi) = (\sigma_{11}, \sigma_{22}, \sigma_{12})^T$ and $\boldsymbol{\epsilon}(\mathbf{x}, \xi) = (\varepsilon_{11}, \varepsilon_{22}, 2\varepsilon_{12})^T$ are the 2D stress and strain tensors, respectively. For linear elastic materials,

$$\boldsymbol{\sigma}(\mathbf{x}, \xi) = \mathbf{D}^e(\mathbf{x}, \xi) \boldsymbol{\epsilon}(\mathbf{x}, \xi), \quad (4.26)$$

where

$$\mathbf{D}^e(\mathbf{x}, \xi) = \frac{E(\mathbf{x}, \xi)}{1 - \nu^2} \begin{bmatrix} 1 & \nu & 0 \\ \nu & 1 & 0 \\ 0 & 0 & \frac{(1-\nu)}{2} \end{bmatrix}, \quad (4.27)$$

is the matrix of constitutive relation for the 2D plane stress problems with constant Possion's ratio ν and stochastic Young's modulus $E(\mathbf{x}, \xi)$. In general, one can take the Possion's ratio to be a stochastic function, too; however, here ν is assumed to be constant. The strain tensor is related to the displacement field, $\mathbf{u}(\mathbf{x}, \xi)$, through the relation

$$\boldsymbol{\epsilon}(\mathbf{x}, \theta) = \begin{bmatrix} \frac{\partial}{\partial x} & 0 \\ 0 & \frac{\partial}{\partial y} \\ \frac{\partial}{\partial y} & \frac{\partial}{\partial x} \end{bmatrix} \mathbf{u}(\mathbf{x}, \xi) = \mathbf{H}\mathbf{u}(\mathbf{x}, \xi). \quad (4.28)$$

The two-dimensional displacement field is expressed as

$$\mathbf{u}(\mathbf{x}, \xi) = \mathbf{N}(\mathbf{x})\mathbf{d}(\xi), \quad (4.29)$$

where $\mathbf{N}(\mathbf{x})$ is the two-dimensional deterministic finite element shape functions and $\mathbf{d}(\xi)$ are nodal displacements. For simplicity and without loss of generality, consider deterministically distributed loads external forces $\mathbf{T}(\mathbf{x})$. The work performed by the applied forces is then written as

$$W^e = \int_{\Gamma^e} \mathbf{T}(\mathbf{x})\mathbf{u}(\mathbf{x}, \xi)d\Gamma, \quad (4.30)$$

where Γ^e denotes the boundary of element e. Minimizing the potential energy of the system, $\Pi = \sum_e V^e - W^e$ with respect to the nodal displacements yields,

$$\mathbf{K}\mathbf{d} = \mathbf{f}, \quad (4.31)$$

where

$$\begin{aligned} \mathbf{K} &= \sum_e \int_{S^e} \mathbf{B}(\mathbf{x})^T \mathbf{D}(\mathbf{x}, \xi) \mathbf{B}(\mathbf{x}) dS, \\ \mathbf{B}(\mathbf{x}) &= \mathbf{H}\mathbf{N}(\mathbf{x}), \\ \mathbf{f} &= \sum_e \int_{\Gamma^e} \mathbf{N}(\mathbf{x})^T \mathbf{T}(\mathbf{x}) d\Gamma. \end{aligned} \quad (4.32)$$

If the Karhunen–Loeve decomposition of $\mathbf{D}(\mathbf{x}, \xi)$ is written as

$$\mathbf{D}(\mathbf{x}, \xi) = \overline{\mathbf{D}}(\mathbf{x}) + \sum_{i=1} \sqrt{\lambda_i} \omega_i(\xi) \mathbf{a}^{(i)}(\mathbf{x}), \quad (4.33)$$

4.7 Solution of boundary value problems on dense fiber network domains

and is substituted into Eqs. (4.31 — 4.32),

$$\sum_{i=0} \omega_i(\xi) \mathbf{K}^{(i)} \mathbf{d} = \mathbf{f}, \quad (4.34)$$

where

$$\mathbf{K}^{(i)} = \begin{cases} \sum_e \int_{S^e} \sqrt{\lambda_i} \mathbf{B}(\mathbf{x})^T \mathbf{a}^{(i)}(\mathbf{x}) \mathbf{B}(\mathbf{x}) dS, & i \neq 0 \\ \sum_e \int_{S^e} \overline{\mathbf{D}}(\mathbf{x}) \mathbf{B}(\mathbf{x})^T \mathbf{B}(\mathbf{x}) dS, & i = 0 \end{cases} \quad (4.35)$$

and $\omega_0(\xi) = 1$. Rewrite Eq. (4.34) as

$$\left[\mathbf{I} + \sum_{i=1} \omega_i(\xi) \mathbf{Q}^{(i)} \right] \mathbf{d} = \mathbf{g}, \quad (4.36)$$

in which

$$\begin{aligned} \mathbf{Q}^{(i)} &= \mathbf{K}^{(0)^{-1}} \mathbf{K}^{(i)}, \\ \mathbf{g} &= \mathbf{K}^{(0)^{-1}} \mathbf{f}. \end{aligned} \quad (4.37)$$

The random vector of nodal displacements can be expanded as follows:

$$\mathbf{d} = \sum_j \mathbf{c}^{(j)} \Psi_j[\omega(\xi)], \quad (4.38)$$

where $\Psi_j[\omega(\xi)]$ are chaos polynomials. A complete discussion of chaos polynomials is given in [66]. Substituting Eq. (4.38) into Eq. (4.36) and forming the inner product of the result with $\Psi_j[\omega(\xi)]$ yield,

$$\mathbf{c}^{(m)} + \sum_j \sum_i \varsigma_{ijm} \mathbf{Q}^{(i)} \mathbf{c}^{(j)} = \langle \mathbf{g} \Psi_m[\omega(\xi)] \rangle_\xi, \quad (4.39)$$

where

$$\varsigma_{ijm} = \langle \omega_i \Psi_j(\omega) \Psi_m(\omega) \rangle_\xi. \quad (4.40)$$

The solution of Eq. (4.39) with \mathbf{c} as unknowns provides the statistics of the nodal displacements through Eq. (4.40).

4.7 Solution of boundary value problems on dense fiber network domains

Hatami-Marbini and Picu^[56] employed the above procedure to solve mechanics boundary value problems defined on domains of random fiber networks subjected to uniform and non-uniform loadings. For this purpose and in order to find the response of a network at resolution δ/l_c , they considered the network equivalent stochastic continuum problem subjected to the

same boundary conditions. The equivalent continuum is divided into square elements of size δ/l_c with elastic moduli $E(\xi)$ having a power law spatial autocorrelation function. The Karhunen–Loeve expansion of the stiffness matrix $\mathbf{D}(\mathbf{x}, \xi)$ is written and the procedure outlined in the previous section is followed to find the statistics of the deformation field. Note that the stochastic input to the problem is the spatially correlated stiffness tensor. The solution obtained from this approach can be compared with solutions of (a) the equivalent continuum replica averaging and (b) the fiber network replica averaging. In the equivalent continuum replica averaging (referred to as C-Averaging), the classical finite element method is used to solve a large number of realizations of the equivalent continuum, with each being a deterministic problem and the stiffness distribution inside the domain is obtained from sampling the probability distribution function of the stochastic Young's modulus. The fiber network replica averaging (referred to as N-Averaging) is based on solving numerically the deformation of a much fuller realization of random fiber networks subjected to similar boundary conditions. Figure 4.7 shows Hatami–Marbini and Picu's solution of the deformation field for a network subjected to uniform tension, i.e. $p(L, x_2) = p_0$. In this figure, the nodal displacements of the overlaid mesh obtained from stochastic finite elements are compared with those evaluated from replica averaging. $\mathbf{u}[i, j]$ represent the displacements of a node located at $x_1 = (i - 1)\delta$ and $x_2 = (j - 1)\delta$ where $i, j = 1..n + 1$, δ is the size of square elements, $n = L/\delta$ and L is the size of the network square domain. Moreover, $\langle \bar{\mathbf{u}}[i, .] \rangle_{x_2}$ and $\langle \sigma_{\mathbf{u}[i, .]} \rangle_{x_2}$ are

$$\begin{aligned}\langle \bar{\mathbf{u}}[i, .] \rangle_{x_2} &= \frac{1}{n+1} \sum_{j=1}^{n+1} \bar{\mathbf{u}}[i, j], \\ \langle \sigma_{\mathbf{u}[i, .]} \rangle_{x_2} &= \frac{1}{n+1} \sum_{j=1}^{n+1} \sigma_{\mathbf{u}[i, j]},\end{aligned}\quad (4.41)$$

where $\langle \mathbf{u}[i, j] \rangle_\xi \equiv \bar{\mathbf{u}}[i, j]$ and $\sigma_{\mathbf{u}[i, j]}$ denote the mean and standard deviation of nodal displacements, respectively. It is seen that the accuracy of the stochastic finite element solution depends on the order of chaos polynomials and the number of terms in the Kahunen–Loeve expansion where the effect of the latter is more significant. Since they used a limited number of replicas to perform the fiber network replica averaging, it is expected that N-averaging yields an upper limit for the standard deviation. The results are in agreement with those obtained from replica averaging over many deterministic structures. Hatami–Marbini and Picu stated that because traditional homogenization theory approaches are not applicable to problems with long-range correlations, the above approach is a practical alternative for the solution of boundary value defined on dense random fiber networks. This procedure is considerably faster and cheaper than replica averaging especially for large problem domains containing large number of fibers.

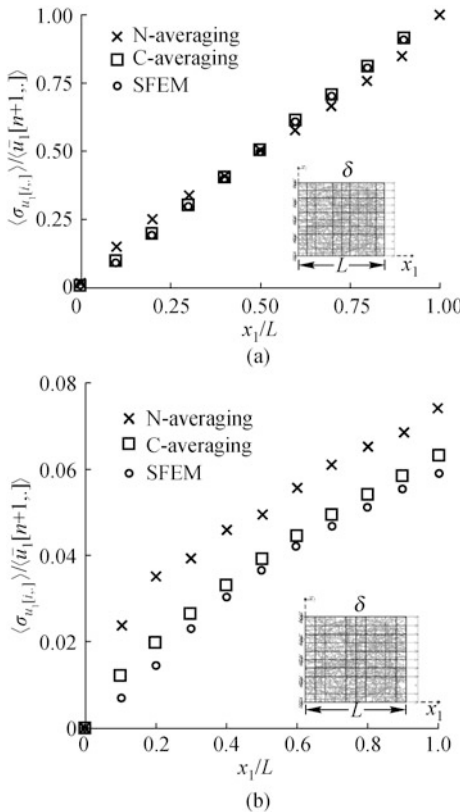


Fig. 4.7 The variation of (a) the normalized average of mean horizontal nodal displacement, and (b) the normalized standard deviation of the horizontal nodal displacement inside the stochastic continuum equivalent to the network pulled with a uniform tension along the edge $x_1/L = 1$. The results obtained from the stochastic finite element method (SFEM) with $M_n = 4$ terms in the Karhunen–Loeve decomposition and $n_p = 2$ terms in the chaos polynomial expansion are shown, along with results from N-and C-averaging (described in text).

References

- [1] Janmey P A. Mechanical properties of cytoskeletal polymers. *Current opinion in cell biology*, 3: 4-11, 1991.
- [2] Mofrad M R K, Kamm R G. Cytoskeletal mechanics: Models and measurements. Cambridge University Press, 2006.
- [3] Hatami-Marbini H, Mofrad M R K. Cytoskeletal mechanics and rheology: A review. In Advances in Cell Mechanics, ed. S. Li and B. Sun, Springer, 2011.
- [4] Dickinson R B, Caro L, Purich D L. Force generation by cytoskeletal filament end-tracking proteins. *Biophysical Journal*, 87: 2838-2854, 2004.

- [5] Shenoy V B, Tambe D T, Prasad A, et al. A kinematic description of the trajectories of Listeria monocytogenes propelled by actin comet tails. *Proceedings of the National Academy of Sciences of the United States*, 104(20): 8229-8234, 2007.
- [6] DiDonna B A, Lubensky T C. Nonaffine correlations in random elastic media. *Physical Review E*, 72(6): 066619, 2005.
- [7] Doi M, Edwards SF. *The Theory of Polymer Dynamics*. Clarendon Press, Oxford, 1988.
- [8] Rubinstein M, Colby RH. *Polymer Physics*. Oxford University Press, 2003.
- [9] Junqueira L C, Carneiro J, Kelley RO. *Basic Histology*. 9th ed. McGraw-Hill, New York, 1998.
- [10] van Rietbergen B, Majumdar S, Pistoia W, et al. Assessment of cancellous bone mechanical properties from micro-FE models based on micro-CT pQCT and MR images. *Technol. Health Care*, 6: 413-420, 1998.
- [11] van Rietbergen B, Muller R, Ulrich D, et al. Tissue stresses and strain in trabeculae of a canine proximal femur can be quantified from computer reconstructions. *J. Biomech.*, 32: 165-173, 1999.
- [12] Hitzenberger C, Gotzinger E, Sticker M, et al. Measurement and imaging of birefringence and optic axis orientation by phase resolved polarization sensitive optical coherence tomography. *Opt. Exp.*, 9: 780-790, 2001.
- [13] Rogowska J, Patel N A, Fujimoto J C, et al. Optical coherence tomographic elastography technique for measuring deformation and strain of atherosclerotic tissues. *Heart*, 90: 556-562, 2004.
- [14] Friedl P, Brocker E. Biological confocal reflection microscopy: Reconstruction of three-dimensional extracellular matrix, cell migration, and matrix reorganization. Hader D ed. *Image Analysis: Methods and Applications*. 2nd ed. CRC Press, Boca Raton, 9-22, 2001.
- [15] Provenzano P P, Vanderby R. Collagen fibril morphology and organization: Implications for force transmission in ligament and tendon. *Matrix Biol.*, 25: 71-84, 2006.
- [16] Liu J, Koenderink G H, Kasza K E, et al. Visualizing the strain field in semiflexible polymer networks: Strain fluctuations and nonlinear rheology of F-actin gels. *Phys. Rev. Lett.*, 98: 198304, 2007.
- [17] D'Amore A, Stella J A, Wagner W R, et al. Characterization of the complete fiber network topology of planar fibrous tissues and scaffolds. *Biomaterials*, 31: 5345-5354, 2010.
- [18] Sacks M S, Smith D B, Hiester E D. A small angle light scattering device for planar connective tissue microstructural analysis. *Annals of Biomedical Engineering*, 25: 678-589, 1997.
- [19] McCally R L, Farrell R A. Structural implications of small-angle light scattering from cornea. *Exp. Eye Res.*, 34: 99-113, 1982.
- [20] Weber A, Cheney M C, Smithwick Q Y I, et al. Polarimetric imaging and blood vessel quantification. *Optics Express*, 12: 5178-5190, 2004.
- [21] Chaudhuri BB, Kundu P, Sarkar N. Detection and gradation of oriented texture. *Pattern Recognition Letter*, 14: 147-153, 1993.
- [22] Gowayed Y, Schreibman D V, Roberts M. Surface inspection of textile composite materials using image analysis techniques. *Journal of Composites Technology and Research*, 18: 3-14, 1996.
- [23] Karlon W J, Covell J W, McCulloch A D, et al. Automated measurement of myofiber disarray in transgenic mice with ventricular expression of ras. *The Anatomical Record*, 252(4): 612-625, 1998.

- [24] Pourdeyhimi B, Ramanathan R, Dent R. Measuring fiber orientation in non-wovens, part II: Direct tracking. *Textile Research Journal*, 66(12): 747-753, 1996.
- [25] Ayres C, Bowlin G L, Henderson S C, et al. Modulation of anisotropy in electrospun tissue-engineering scaffolds: Analysis of fiber alignment by the fast Fourier transform. *Biomaterials*, 27(32): 5524-5534, 2006.
- [26] Ayres C E, Jha B S, Meredith H, et al. Measuring fiber alignment in electrospun scaffolds: A user's guide to the 2D fast Fourier transform approach. *Journal of Biomaterials Science, Polymer Edition*, 19(5): 603-621, 2008.
- [27] Lee D T, Schachter B J. Two algorithms for constructing a Delaunay triangulation. *International Journal of Parallel Programming*, 9: 219-242, 1980.
- [28] Ostoja-Starzewski M, Wang C. Linear elasticity of planar Delaunay networks: Random field characterization of effective moduli. *Acta Mech.* 84: 61-80, 1989.
- [29] Du Q, Faber V, Gunzburger M. Centroidal voronoi tessellations: applications and algorithm. *SIAM Review*, 41: 637-676, 1999.
- [30] Fratzl P. Statistical model of the habit and arrangement of mineral crystals in the collagen of bone. *Journal of Statistical Physics*, 77: 125-143, 1994.
- [31] Hatami-Marbini H, Picu R C. An eigenstrain formulation for the prediction of elastic moduli of defective fiber networks. *European Journal of Mechanics-A/Solids*, 28: 305-316, 2009.
- [32] Metropolis N, Rosenbluth A, Rosenbluth M, et al. Perspective on "equation of state calculations by fast computing machines". *J. Chem. Phys.*, 21: 1087-1092, 1953.
- [33] Hastings W. Monte Carlo sampling methods using Markov chains and their applications. *Biometrika*, 57: 97-109, 1970.
- [34] Sander A, Stein A M, Swickrath M J, et al. Out of Many, One: Modeling Schemes for Biopolymer and Biofibril Networks. Dumitrica T ed. Trends in Computational Nanomechanics: Transcending Length and Time Scales. Springer Netherlands, 557-602, 2010.
- [35] Chandran P L, Barocas V H. Affine versus non-affine fibril kinematics in collagen networks: theoretical studies of network behavior. *J. Biomech. Eng.*, 128: 259-270, 2006.
- [36] Hatami-Marbini H, Mofrad K M R. Cytoskeletal Mechanics and Cellular Mechanotransduction: A Molecular Perspective, in Cellular and Biomolecular Mechanics and Mechanobiology. Gefen A ed. Springer Studies in Mechanobiology, Tissue Engineering and Biomaterials. 2010. (in press)
- [37] Narter M A, Batra S K, Buchanan, D R. Micromechanics of three-dimensional fibrewebs: Constitutive equations. *Proceedings of the Royal Society of London Series A*, 455: 3543-3563, 1999.
- [38] Wu X F, Dzenis Y A. Elasticity of planar fiber networks. *Journal of Applied Physics*, 98(9): 093501, 2005.
- [39] Head D A, Levine A J, MacKintosh F C. Distinct regimes of elastic response and deformation modes of cross-linked cytoskeletal and semiflexible polymer networks. *Physical Review E*, 68(6): 061907, 2003.
- [40] Wilhelm J, Frey E. Elasticity of stiff polymer networks. *Physical Review Letters*, 91(10): 108103, 2003.
- [41] Onck P R, Koeman T, van Dillen T, et al. Alternative explanation of stiffening in cross-linked semiflexible networks. *Physical Review Letters*, 95(17): 178102, 2005.
- [42] Heussinger C, Frey E. Stiff polymers, foams, and fiber networks. *Physical Review Letters*, 96(1): 017802, 2006.

- [43] Hatami-Marbini H, Picu R C. Scaling of nonaffine deformation in random semiflexible fiber networks. *Phys. Rev E*, 77: 062103, 2008.
- [44] Mackintosh F C, Kas J, Jamley P A. Elasticity of semiflexible biopolymer networks. *Physical Review Letters*, 75(24): 4425-4428, 1995.
- [45] Jaeger H M, Nagel S R, Behringer, R P. Granular solids, liquids, and gases. *Reviews of Modern Physics*, 68(4): 1259-1273, 1996.
- [46] Liu A J, Ramaswamy S, Mason T G, et al. Anomalous viscous loss in emulsions. *Phys. Rev. Lett*, 76(16): 3017-3020, 1996.
- [47] Langer S A, Liu A J. Effect of random packing on stress relaxation in foam. *Journal of Physical Chemistry B*, 101(43): 8667-8671, 1997.
- [48] Tanguy A, Wittmer J P, Leonforte F, et al. Continuum limit of amorphous elastic bodies: A finite-size study of low-frequency harmonic vibrations. *Physical Review B*, 66(17): 174205, 2002.
- [49] Hatami-Marbini H, Picu R C. Effect of fiber orientation on the non-affine deformation of random fiber networks. *Acta Mechanica*, 205: 77-84, 2009.
- [50] Leonforte F, Tanguy A, Wittmer J P, et al. Continuum limit of amorphous elastic bodies II: Linear response to a point source force. *Physical Review B*, 70(1): 014203, 2004.
- [51] Hatami-Marbini. Non-affin deformation of fiber networks. PhD thesis, Rensselaer Polytechnic Institute, Troy NY, 2009.
- [52] Kaye B H. A Random Walk through Fractal Dimensions. VCH Publishers, New York, 1989.
- [53] Falconer K. Fractal Geometry: Mathematical Foundations and Applications. John Wiley & Sons, 1990.
- [54] Schertzer D, Lovejoy S. Physical modeling and analysis of rain and clouds by anisotropic scaling multiplicative processes. *Journal of Geophysical Research — Atmospheres*, 92(D8): 9693-9714, 1987.
- [55] Pandey G, Lovejoy S, Schertzer D. Multifractal analysis of daily river flows including extremes for basins of five to two million square kilometres, one day to 75 years. *J. Hydrology*, 208: 62-81, 1998.
- [56] Hatami-Marbini H, Picu R C. Heterogeneous long-range correlated deformation of semiflexible random fiber networks. *Phys. Rev E*, 80: 046703, 2009.
- [57] Nemat-Nasser S, Hori M. Micromechanics: Overall Properties of Heterogeneous Materials. North-Holland, Amsterdam, 1993.
- [58] Soare M A, Picu R C. Boundary value problems defined on stochastic self-similar multiscale geometries. *International Journal for Numerical Methods in Engineering*, 74(4): 668-696, 2008.
- [59] Cox H L. The elasticity and strength of paper and other fibrous materials. *British Journal of Applied Physics*, 3: 72-79, 1952.
- [60] Astrom J A, Makinen J P, Alava M J, et al. Elasticity of Poissonian fiber networks. *Physical Review E*, 61(5): 5550-5556, 2000.
- [61] Wang C W, Berhan L, Sastry A M. Structure, mechanics and failure of stochastic fibrous networks, part I: Microscale considerations. *Journal of Engineering Materials and Technology*, 122(4): 450-459, 2000.
- [62] Wang C W, Sastry A M. Structure, mechanics and failure of stochastic fibrous networks, part II: Network simulations and application. *Journal of Engineering Materials and Technology*, 122(4): 460-468, 2000.
- [63] Stylianopoulos T, Barocas V H. Volume-averaging theory for the study of the mechanics of collagen networks. *Comput. Methods Appl. Mech. Engrg.*, 196: 2981-2990, 2007.

- [64] Luo X, Stylianopoulos T, Barocas VH, et al. Multiscale computation for bioartificial soft tissues with complex geometries. *Engineering with Computers*, 25: 87-95, 2009.
- [65] Picu R C, Hatami-Marbini H. Long-range correlations of elastic fields in semi-flexible fiber networks. *Computational Mechanics*, 46(4): 635-640, 2010.
- [66] Ghanem R G, Spanos P D. Stochastic Finite Elements: A Spectral Approach. Springer-Verlag, New York, 1991.
- [67] Ghanem R. Probabilistic characterization of transport in heterogeneous media. *Computer Methods in Applied Mechanics and Engineering*, 158(3-4): 199-220, 1998.
- [68] Ghanem R, Dham S. Stochastic finite element analysis for multiphase flow in heterogeneous porous media. *Transport in Porous Media*, 32(3): 239-262, 1998.
- [69] Hien T D, Kleiber M. Stochastic finite element modelling in linear transient heat transfer. *Computer Methods in Applied Mechanics and Engineering*, 144(1-2): 111-124, 1997.
- [70] Xiu D B, Karniadakis G E. Modeling uncertainty in flow simulations via generalized polynomial chaos. *Journal of Computational Physics*, 187(1): 137-167, 2003.
- [71] Soare M A, Picu R C. An approach to solving mechanics problems for materials with multiscale self-similar microstructure. *International Journal of Solids and Structures*, 44(24): 7877-7890, 2007.
- [72] Loeve M. Probability Theory. Springer-Verlag, New York, 1977.

Chapter 5 Atomic Scale Monte-Carlo Studies of Entropic Elasticity Properties of Polymer Chain Molecules

Eduard G. Karpov* and Mykhailo V. Grankin

*Department of Civil & Materials Engineering, University of Illinois,
Chicago, IL 60607*

Abstract: This chapter describes atomic scale Monte–Carlo studies of entropic elasticity properties of individual polymer chain molecules. An efficient numerical Monte–Carlo sampling approach is outlined and used to evaluate the entropic contribution to the total elastic force. Specific load-extension curves are obtained numerically for a group of molecules with degenerate potential energy profiles. Results of the atomistic modeling are compared with the limiting continuum model of the same type of polymers. The extent of the linear and nonlinear elastic regimes and dependence on the molecular weight and geometric parameters of the molecules are discussed.

Keywords: entropic elasticity, Monte-Carlo modeling, polymers, statistical properties

5.1 Introduction

Theoretical prediction and validation of mechanical properties of polymer chain molecules, particularly, complex biomolecules^[1-7], proteins and lipids^[8-10], are impeded by the involvement of the entropic elasticity effects^[11-15]. The entropy-driven elastic forces arise from the essential degeneracy of the molecule potential energy function in the configuration space. The entropy dependent term, $-TS$, where T is the system temperature, may notably contribute to the free energy F of a polymer chain and even dominate over the usual interatomic potential energy U , when the chain is subject to an external mechanical loading.

Continuum level empirical approaches to the description of entropic elastic media are currently available^[11-12,16-18]; those utilize the helmholtz free

*Corresponding author, E-mail: ekarpov@uic.edu.

energy thermodynamic potential^[19-22], $F = U - TS$, as a basic physical characteristic of any material system carrying out mechanical work at a constant (nonzero) temperature. However, very few analytical or numerical studies of the entropic elastic properties of *individual* molecules have been conducted, particularly, with an atomistic resolution^[14,23-25]. The entropic elasticity is determined by thermally triggered stochastic transitions between different geometric configurations of the polymer chain occurring continuously in the physical space at the atomic scale. A direct analysis of these geometric conformations for the purpose of establishing a reliable and well parameterized entropy-to-deformation dependence is extremely difficult to the great number of internal degrees of freedom and a high order of degeneracy of the interatomic potential energy function, even for the simplest polymer chains.

This chapter describes a very efficient nondeterministic numerical approach to study entropic elasticity properties of individual polymer chain molecules. the approach is based on a Monte–Carlo^[26-31] random sampling scheme with an atomistic (monomer scale) resolution eligible for the evaluation of entropic contribution to the total elastic force in large polymer chain molecules. Specific load-extension curves^[32-35] are obtained numerically for a group of molecules with degenerate potential energy profiles^[11]. The entropic elastic properties are evaluated by reproducing a numerical probability density function for the configuration entropy of the molecules. Results of the atomistic modeling are compared with the limiting continuum model of the same type of polymers. The extent of linear and nonlinear elastic regimes and dependence on the molecular weight and geometric parameters of the molecules are discussed. The linear regimes for the entropic elastic forces are observed for a wide range of molecular parameters in agreement with a generic continuum scale approach^[11-12]. However, the present atomic scale model shows that the conventional continuum scale linearity of the entropic elasticity is breaking at both very small and large elongations of the individual molecules subject to external loadings, as well as for extreme values of some basic geometric parameters of the molecule. Particularly, the extent of the nonlinear regime is shown to depend on the kink or atomic bond angle, and therefore, the gyration radius of the molecular chain.

5.2 Entropic elasticity of linear polymer molecules

In the presence of significant entropic effects, the elastic response of a physical system at constant temperature subject to external mechanical loading is determined by behavior of the thermodynamic free energy potential of the system associated with such a response^[11-12]. Variance of the free energy

potential defines mechanical work done by the system over external bodies without changing the system temperature. It is convenient to introduce the distance L between two endpoints of a polymer chain molecule loaded with self-equilibrated external forces f (Fig. 5.1). The parameter L can be related to the standard mechanical strain,

$$\varepsilon = \frac{L - L_0}{L_0} \quad (5.1)$$

where L_0 is some relaxed length of the molecule, or the distance between the same endpoints in the absence of external forces. The free energy change then can be written as

$$\partial F = -f \partial L. \quad (5.2)$$

Here, the right-hand side represents an elementary mechanical work of the external forces on the contraction or elongation of the molecule. Then the external force is given by the derivative

$$f = -\left(\frac{\partial F}{\partial L}\right)_{T,a} \quad (5.3)$$

evaluated at a constant temperature T and a constant set $\{a\}$ of any external thermodynamic parameters.

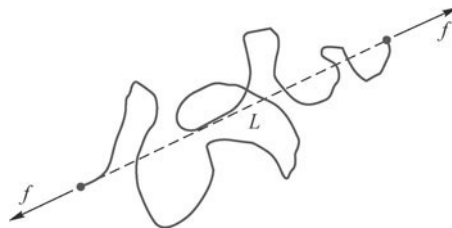


Fig. 5.1 Polymer chain molecule loaded with a pair of self-equilibrated external forces.

Equation (5.3) can be expanded using the standard thermodynamic definition of the Helmholtz free energy potential^[19–22] in terms of the system's internal energy U and entropy S :

$$f = -\frac{\partial F}{\partial L} = -\frac{\partial (U - TS)}{\partial L} = \underbrace{-\frac{\partial U}{\partial L}}_{fu} + T \underbrace{\frac{\partial S}{\partial L}}_{fs}. \quad (5.4)$$

Internal energy change at a constant temperature may only be related to the variance of potential energy of atomic interaction due to bond lengths and bond angles changes. Therefore the first term on the right-hand side of Eq.

(5.4) represents the usual *energetic elastic force* (f_U), while the second term is the *entropic elastic force* (f_S). We note that the entropic elastic force is linear with system temperature for any type of functional dependence of the entropy on the parameter L . This behavior is analogous to the linearity of ideal gas pressure dependence on temperature, which is viewed as an entropic effect in the absence of potential energy interaction between the individual gas molecules^[21-22].

Since the entropic force in Eq. (5.4) is not related to the potential energy, it only depends on the geometrical transformations of the molecule. If such a transformation occurs for a constant potential energy of the molecule, then the resultant change of the configuration entropy represents a pure contribution to the entropic elastic force,

$$\frac{\partial U}{\partial L} = 0 : \quad f = f_S = T \underbrace{\frac{\partial S}{\partial L}}_{f_S}. \quad (5.5)$$

The condition $\partial U / \partial L = 0$ in Eq. (5.5) represents the “ideal rubber” system or model, where entropic forces fully dominate over the energetic elastic forces.

Extension or contraction of the ideal rubber chain is not related to any changes of molecular bond lengths or angles, and should be viewed as a result of mere reorientation of individual blocks (monomers) in the molecule relative to each other. This statement can be clarified using the example shown in Fig. 5.2. Consider first a lower mass molecule, such as C₂H₆ ethane, where the 3-fold symmetric transformation of rotation of the 3H group about the C–C bond is possible. One may anticipate a general form of the relevant rotational potential (Fig. 5.2),

$$U_\varphi = U_0[1 - \cos(3\varphi)] \quad (5.6)$$

where angle φ describes orientation of the two 3H groups relative to each other. The three minima of this potential correspond to three equivalently stable rotational states of the molecule at angles $\varphi = 0^\circ$, 120° and 240° , while the three maxima correspond to the most energetically unfavorable relative orientations of the 3H groups and represent the non-bonding interaction of repulsive character between the hydrogen atoms. For a C₄H₁₀ butane molecule, the rotational potential has different properties (Fig. 5.2 plot). Particularly, rotation about the left or right C–C bond is 3-fold symmetric as in the ethane molecule; however, rotation about the middle C–C bond is characterized by the global minimum at $\varphi = 0^\circ$ and two identical local minima at $\varphi = 120^\circ$ and 240° . These configurations are named the transconformation and gauche states of the molecule, respectively.

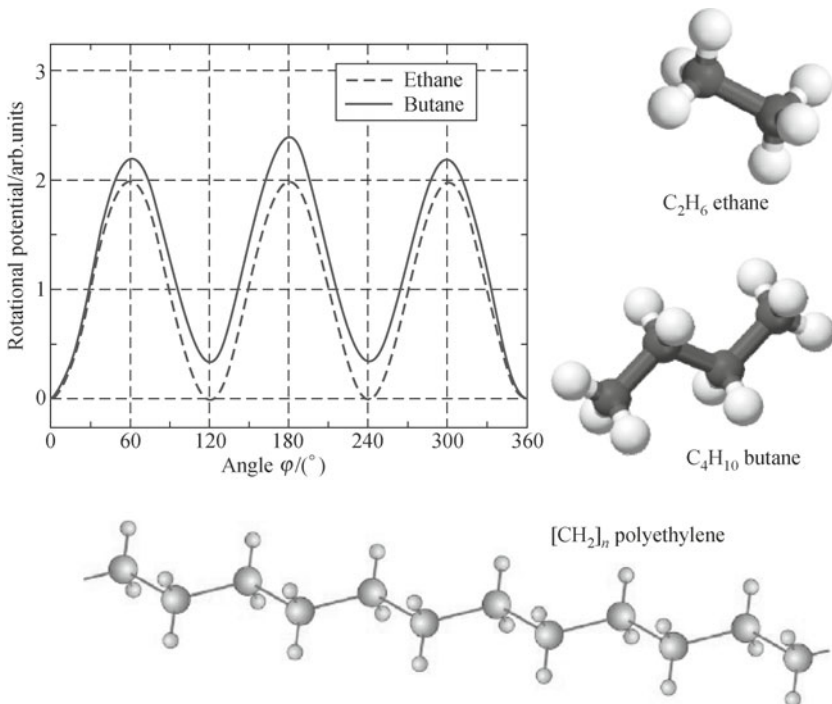


Fig. 5.2 Rotational symmetry of bonding energy potential in hydrocarbon molecules. The plot shows an accurate 3-fold symmetry of the potential for ethane or propane and a quasiperiodicity for butane and higher order molecules, including polyethylene. (color plot at the end of the book)

Similar properties of the rotational potential are also observed in higher order chain molecules, for example, for the relative monomer orientation in $[CH_2]_n$ polyethylene, as well as in more complex organic polymers and biopolymers. Existence of several molecular conformations with identical values of the potential energy in a local repetitive group leads to a very high degeneracy of the total potential energy function of the molecule. Being subject to an external load, such a molecule can respond by changing its configuration and by subsequent entropy decrease, rather than by storing potential energy as a normal elastic body.

Dependence of the molecular entropy onto the separation distance, $S(L)$, can be introduced using the Boltzmann relationship,

$$S(L) = k_B \ln w(L) \quad (5.7)$$

where k_B is the Boltzmann constant, and developing a dependence of the configurational probability density function w on the right-hand side onto the parameter L . Analytical or numerical evaluation of the function $w = w(L)$ is

a key task in studying entropic elastic properties of polymers and other soft matter systems. Indeed, for a given $w(L)$, the entropic force dependence on L can be found using Eqs. (5.7) and (5.5), so that

$$f_S(L) = k_B T \frac{\partial}{\partial L} \ln w(L). \quad (5.8)$$

Section 5.2.1 provides an analytical approach to determine $w(L)$ using a continuum limit approximation for polymer chain molecules, and Section 5.2.2 describes an efficient Monte-Carlo numerical procedure for $w(L)$ evaluation, where an atomic scale resolution is preserved for the molecular structure. Results of the continuum and discrete atomic studies will further be discussed and compared to each other.

5.2.1 Continuum limit

In the limiting case of a very large number of monomers, when the distance between two adjacent monomers is vanishing compared to the total length of the polymer chain, one may assume that the separation distance L between the two loaded endpoints (Fig. 5.1), is essentially a *continuously* distributed quantity. Analytical distribution for L then can be derived by setting the origin of a Cartesian coordinate system at one of the endpoints and analyzing position of the other endpoint in the same system (Fig. 5.1). Since the number of monomers is very large, the free endpoint has no directional preference relative to the origin of the coordinate system. Each of the coordinates of the free endpoint is a random number normally distributed about zero value with some variance a being the same for all three coordinate directions. Thus, position of the free endpoint is of a random Cartesian vector, whose distribution is given by

$$w(\mathbf{r}) = w(x, y, z) = \frac{1}{(2\pi a^2)^{\frac{3}{2}}} e^{-\frac{x^2+y^2+z^2}{2a^2}}. \quad (5.9)$$

The variance a of this distribution depends on the molecule's internal properties, such as the total number of monomers, molecular weight, local bond angles and bond lengths, and potential energy profiles. The distribution (Eq. (5.9)) is spherically symmetric, and therefore it can be simplified using the spherical coordinates (L, θ, φ) , so that

$$x^2 + y^2 + z^2 \rightarrow L^2, \quad d\mathbf{r} = dx dy dz \rightarrow L^2 dL \sin \theta d\theta d\varphi. \quad (5.10)$$

Here L is the earlier introduced distance between two loaded endpoints of the polymer. Using Eq. (5.10), the elementary probability $w(\mathbf{r}) d\mathbf{r}$ can be

written in spherical coordinates as

$$w(\mathbf{r})d\mathbf{r} = \frac{1}{(2\pi a^2)^{\frac{3}{2}}} e^{-\frac{x^2+y^2+z^2}{2a^2}} dx dy dz = \frac{L^2}{(2\pi a^2)^{\frac{3}{2}}} e^{-\frac{L^2}{2a^2}} dL \sin \theta d\theta d\varphi. \quad (5.11)$$

This probability is spatially isotropic, and therefore integration over the spherical coordinate angles leads to mere addition of the 4π factor to give a one-dimensional elementary probability corresponding to the interval of distances from L to $L + dL$:

$$w(L)dL = \frac{4\pi L^2}{(2\pi a^2)^{\frac{3}{2}}} e^{-\frac{L^2}{2a^2}} dL. \quad (5.12)$$

Thus, probability density function for the parameter of distance L between two loaded endpoints of the polymer chain is essentially a spherical normal distribution,

$$w(L) = \sqrt{\frac{2}{\pi}} \frac{L^2}{a^3} e^{-\frac{L^2}{2a^2}}. \quad (5.13)$$

A plot of this distribution is shown in Fig. 5.3, where the most probable and mean values of the distance L are related to the variance a ,

$$L_0 = a\sqrt{2}, \quad \bar{L} = a\sqrt{\frac{8}{\pi}}. \quad (5.14)$$

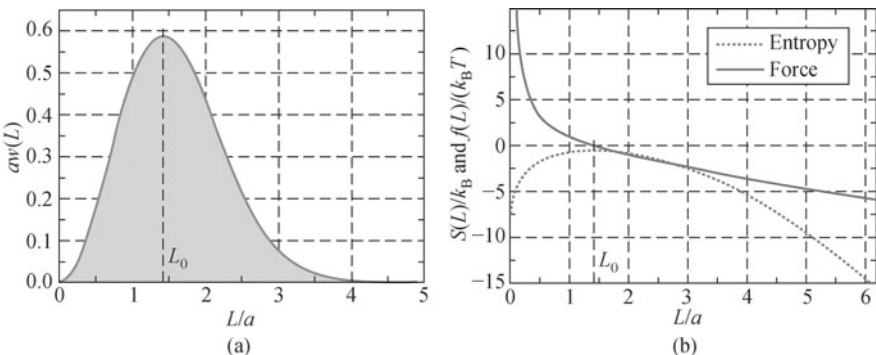


Fig. 5.3 Probability density function for the distance parameter L (a). molecular entropy and entropic elastic force expressed as functions of L (b).

The analytical distribution (Eq. (5.13)) gives the entropy and the entropic force, according to Eqs. (5.7) and (5.8), in the form

$$\begin{aligned} S(L) &= \text{Const} + k_B \left(2 \ln \frac{L}{a} - \frac{L^2}{2a^2} \right), \\ f_S(L) &= T \frac{\partial S}{\partial L} = k_B T \left(\frac{2}{L} - \frac{L}{a^2} \right). \end{aligned} \quad (5.15)$$

As can be seen, the entropic force is linear relative to L , when L is greater than L_0 . The asymptotic slope of the force curve at $L \rightarrow \infty$ in Fig. 5.3 gives the entropic elastic modulus,

$$k = \frac{k_B T}{a^2} = \frac{2k_B T}{L_0^2}. \quad (5.16)$$

Since the entropic elastic force is zero at $L = L_0$ corresponding to a maximum of the molecular entropy, the value L_0 can be referred to as a *relaxed length* of the molecule, which can be used for a standard linear force model of the type $k(L - L_0)$.

5.2.2 Monte–Carlo sampling

Within the continuum assumptions of Section 5.2.1, the variance parameter a for the distribution (Eq. (5.13)) cannot be elucidated, because the internal atomic structure of the polymer is not taken account of. Furthermore, assuming a continuum range for the parameter L implies a possibility for the polymer chain to have critically small local curvature radii that may not be realized for an actual chemical bond structure of the polymer.

Consider a polymer chain model of the type shown in Fig. 5.4, where the vectors **A**, **B** and **C** show spatial orientation of the intra-monomer bonds, such as the C–C bond in the polyethylene molecule of Fig. 5.2. The angle θ between a pair of two adjacent intra-monomer bonds, as well as the bond length, u , are basic characteristics of the chain that determine its entropic elastic properties. Another important parameter is the total number N_e of monomers on the chain under investigation. The two bonds **A** and **B** define a plane so that the next adjacent bond **C** can form an out-of-plane angle φ equal to one of the three possible random values corresponding to the stable energetically favorable confirmations of this local group. Particularly, the triplet of possible random realization of the angle φ could be $\{0^\circ, 120^\circ, 240^\circ\}$ as in the example shown in Fig. 5.2, or another 3-fold symmetric or asymmetric set. These angles define relative rotational orientation of two adjacent monomers on the axis of their chemical bond. For more complex molecules, angle φ may have more than three possible values. Obviously, the total number of possible global configurations of the entire polymer molecule with N_e monomers will be n^{N_e-1} , where n is the dimensionality of the set of angles φ_i being 3 in the above example. If the local rotational potential minima are identical for all three values of φ , then the number 3^{N_e-1} also represents the order of degeneracy of the global molecular potential in the configuration space. In other words, such a molecule can have 3^{N_e-1} different configurations at a constant value of potential energy of the atomic interactions comprising

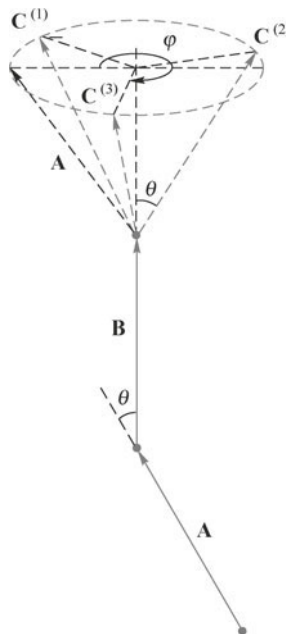


Fig. 5.4 Relative orientation of three intra-monomer bonds (vectors **A**, **B** and **C**) representing a local region of a polymer chain molecule; θ is the principal bonding (kink) angle in the discrete atomic lattice model of the molecule.

this molecule. For example, at $N_e = 1\,000$, the total number of configurations is about 4.4×10^{476} . A direct analysis of such vast numbers of configurations for the elucidation of the $w(L)$ distribution form is generally intractable.

A probabilistic Monte–Carlo sampling approach can be employed to select a sufficiently large number of random molecular configurations N_0 and to build a numerical histogram showing the approximate $w(L)$ distribution. The sampling procedure utilizes probabilities P_i of the realization of each of the angles φ_i in a local group of bonds depicted in Fig. 5.4. These probabilities can be determined as asymptotic (at time $t \rightarrow \infty$) solutions of kinetic balance equations with a matrix of transition probabilities r_{ij} . Values of the coefficients r_{ij} can be determined using the respectable activation energy of the rotational transformations provided by a local potential of the Eq. (5.6). Since the entire approach is quasistatic, only relative probabilities are required rather than the actual dynamic rates, or probabilities per unit time. According to the transition state theory^[36–42], such relative probabilities are proportional to the Boltzmann factors,

$$r_{ij} \sim \exp \left(-\frac{E_{ij}}{k_B T} \right) \quad (5.17)$$

where E_{ij} is the activation energy of the $i \rightarrow j$ transformation. Asymptotic solution of the kinetic equations at $t \rightarrow \infty$ can be found by solving a system of linear equations of the type

$$\begin{aligned} P_1(r_{12} + r_{13}) &= P_2r_{21} + P_3r_{31}, \\ P_2(r_{21} + r_{23}) &= P_1r_{12} + P_3r_{32}, \\ P_1 + P_2 + P_3 &= 1. \end{aligned} \quad (5.18)$$

Here, the last equation represents the fact that the system is always found in one of the three possible states. If there are more than three possible configurations of the local group (Fig. 5.4), the system (Eq. (5.18)) is expanded to a respectable number of the sought probabilities P_i .

On the next step, the probabilities P_i are utilized during the Monte–Carlo sampling procedures to render random global configurations of the polymer molecule. Example configurations are shown in Fig. 5.5, where various bonding angles θ have been utilized. In this and all further numerical examples, the

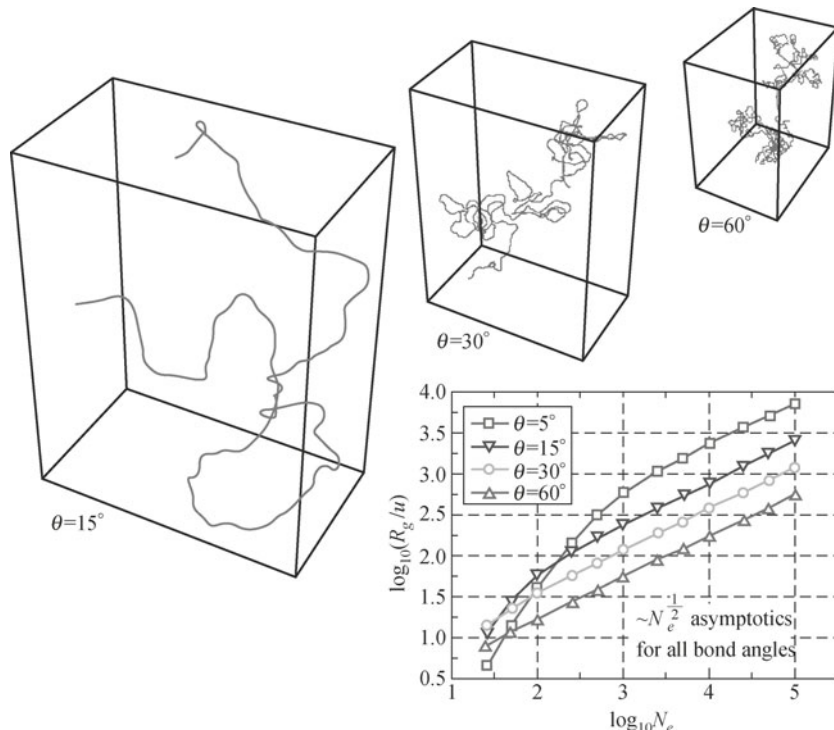


Fig. 5.5 Overall geometry samples for various bond angles θ and constant number N_e of monomers in the molecular chain. The plot shows dependence of the gyration radius of the molecule on N_e . (color plot at the end of the book)

set of local angles φ_i and the respectable set of probabilities P_i are chosen to be $\{0^\circ, 120^\circ, 240^\circ\}$ and $\{1/3, 1/3, 1/3\}$. The three probabilities are selected equally for a more adequate comparison of the discrete numerical model with the continuum limit. Meanwhile, in the analysis of more complex molecules, where a continuum analogy is not sought, a more thorough analysis of the type (Eq. (5.17) and Eq. (5.18)) based on a realistic interatomic potential should be performed. As can be seen from Fig. 5.5, the bonding angles θ has a major influence on the overall geometry of the molecule. Particularly, one may introduce the gyration radius of the molecule,

$$R_g^2 = \frac{1}{2N_e^2} \sum_{i,j} (\mathbf{r}_i - \mathbf{r}_j)^2 \cong \frac{1}{N_e} \sum_{i=1}^N (\mathbf{r}_i - \bar{\mathbf{r}})^2, \quad \bar{\mathbf{r}} = \frac{1}{N_e} \sum_{i=1}^N \mathbf{r}_i \quad (5.19)$$

where \mathbf{r}_i is a position vector of the i th monomer in a global system and $\bar{\mathbf{r}}$ is the centroid of the molecule in the same system. The gyration radius R_g is a basic geometric parameter of the polymer chain, which represents a mean radius of the spherical volume occupied by the molecule characterized by a specific set of local parameters ($\theta, u, \varphi_i, P_i$). Parameter u essentially serves as a geometric scaling parameter, and the value $u = 1$ was employed in the calculations. Therefore, the unit of length for the numerically determined physical parameters plotted in Figs. 5.7 and 5.8 is the actual bond length in a polymer molecule under consideration that is typically several angstroms.

For each specific interval of values of the calculated parameter L , between L_i and $L_i + \Delta L$, the Monte–Carlo sampling procedure will yield a particular number N_i of molecular configurations whose length falls within the range of this interval. Then the approximate value of the distribution function $w(L)$ at $L = L_i$ can be determined as

$$w(L_i) \approx \frac{N_i(L_i, L_i + \Delta L)}{N_0 \Delta L}. \quad (5.20)$$

The accuracy of this approximation is higher for greater total sizes N_0 of the sample set, and for smaller values of the interval ΔL . Examples of this numerical atomic scale distribution are shown in a histogram form in Fig. 5.6 for various bond angles. These numerical histograms are brought to comparison with the analytical distribution (Eq. (5.13)) plotted for the same respectable values L_0 as the numerical distributions. Surprisingly, the shapes of the discrete atomistic and continuous distributions are very different at small bond angles, such as $\theta = 5^\circ - 10^\circ$, while at angles greater than 30° , they are virtually identical.

Since the distribution $w(L)$ ultimately determines the properties of the entropy (Eq. (5.7)) and elastic force (Eq. (5.8)) functions, the atomistic model of Fig. 5.6 demonstrates significant deviations in the physical behavior from

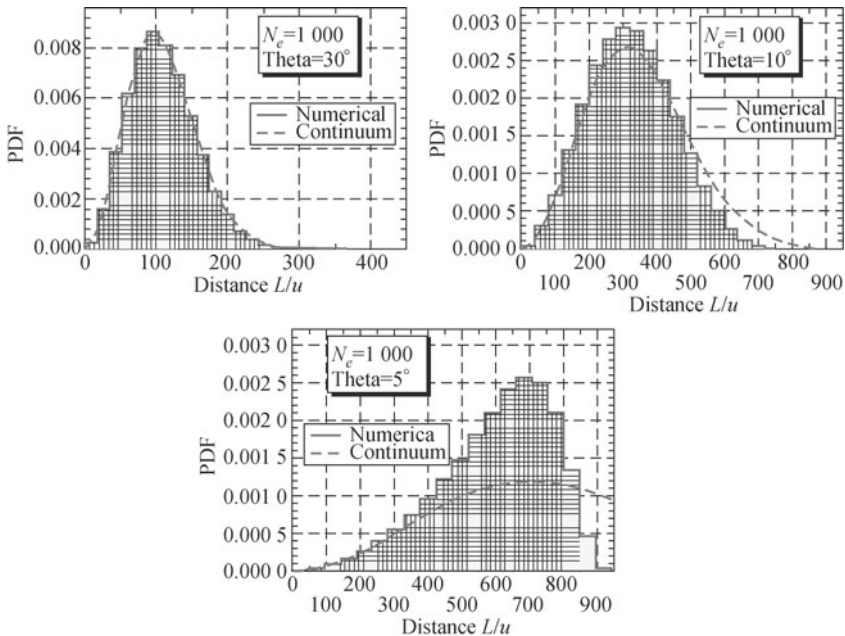


Fig. 5.6 Examples of the numerical distribution (Eq. (5.20)) in comparison with the analytical continuum model distribution (Eq. (5.13)) at various bonding angles θ . (color plot at the end of the book)

the continuum model of Fig. 5.3 for small bonding angles θ . Indeed, calculation of the numerical entropy and entropic elastic force dependence,

$$S(L_i) = k_B \ln w(L_i), \quad f_S(L_i) = k_B T \lim_{\Delta L \rightarrow 0} \frac{\ln w(L_i + \Delta L) - \ln w(L_i)}{\Delta L} \quad (5.21)$$

leads to the results presented in Fig. 5.7 for a polymer chain of 1 000 monomers at various kink angles θ . Here, the total number of sampled molecular configurations, $N_0 = 10^5$. Behavior of the entropic force for the atomistic model is similar to the continuum model of Section 5.2.1 in the range of angles from about 25° to 50° . However, for very small and very large kink angles, the entropic force is nonlinear not only at small L , as in the continuum model of Fig. 5.3, but also at large separation distances L . Furthermore, the entropic force for molecules with low gyration radii (densely packed polymers), i.e. for those with large parameter θ , is linear mostly in the extension or unfolding mode, while for very sparsely packed molecules (with small θ), it is linear mostly in the contraction mode. Increased fluctuations in Fig. 5.7 data for the entropic force at larger L and greater angles θ can be explained by numerical error of calculation of the logarithmic functions at small random arguments.

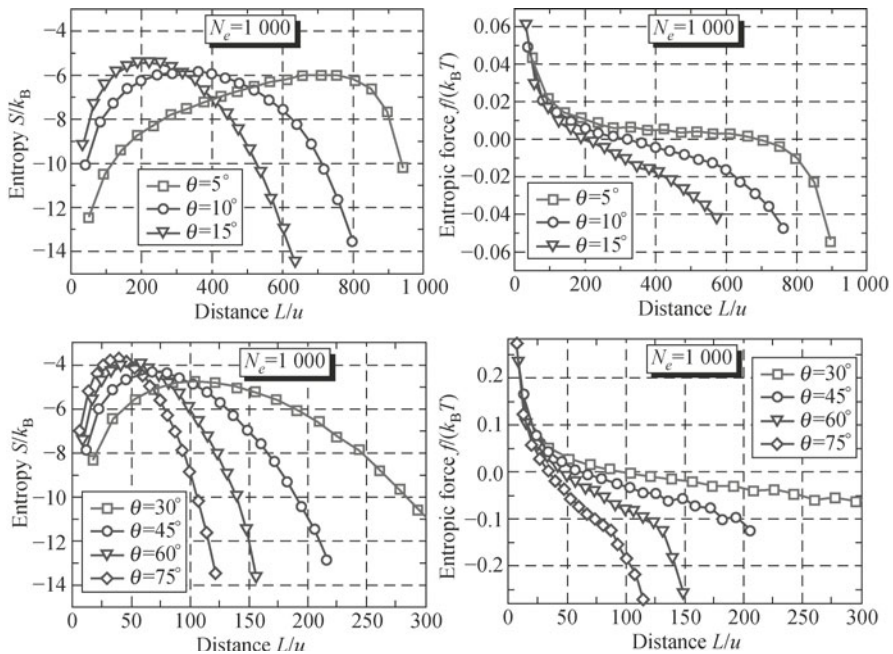
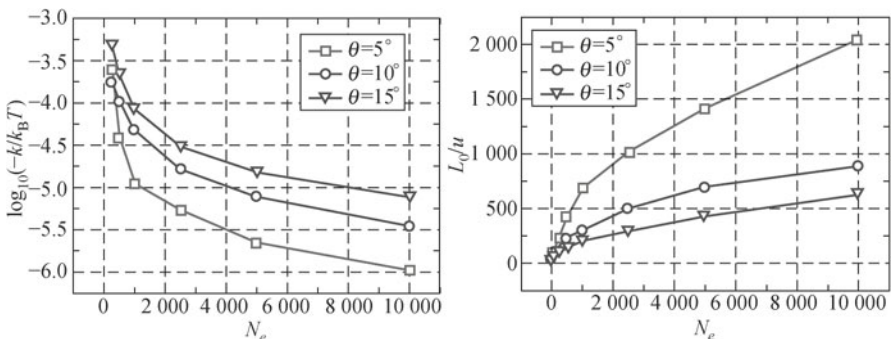


Fig. 5.7 Numerical values of the molecular entropy and entropic elastic force varying with separation distances between two loaded endpoints of the molecule (Fig. 5.1) for small (top) and large (bottom) kink angles θ ; u is the distance between two adjacent monomers or the C–C bond length. (color plot at the end of the book)

Extended linear regimes for the entropic force exist in the sampled polymer chains at all values of θ for moderate elongations of the molecule. Approximate elastic moduli k and relaxed lengths L_0 associated with these linear regimes are plotted in Fig. 5.8 relative to the total number N_e of monomers in the chain. N_e is a basic parameter defining the radius of gyration (Fig. 5.5) and the molecular mass of the polymer. The parameters k and L_0 can be utilized for a standard linear force model of the type $k(L - L_0)$. Similar



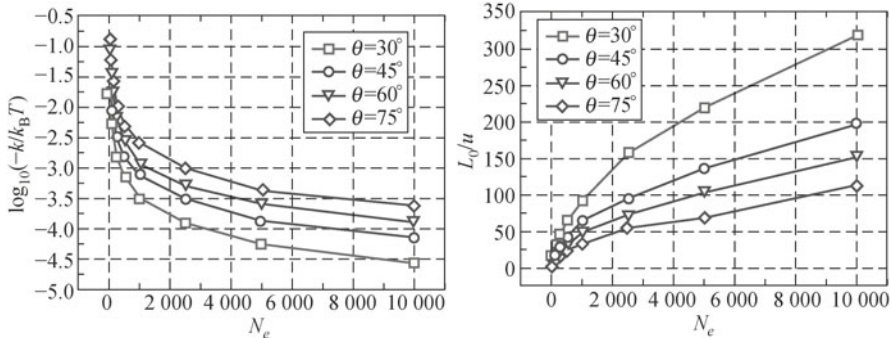


Fig. 5.8 Elastic moduli (left) and relaxed lengths of the endpoint separation (right) for the linear elastic regimes observed in Fig. 5.7. (color plot at the end of the book)

to the gyration radius, the relaxed separation length L_0 grows proportional to $N_e^{\frac{1}{2}}$ at $N_e > 1\,000$. The elastic modulus approaches asymptotically the continuum model value (16) for $N_e \rightarrow \infty$, while significant deviations from Eq. (5.16) can be seen at $N_e < 1\,000$ and for bond angles $\theta \leqslant 15^\circ$.

5.3 Summary

In this chapter, we have discussed a simple and efficient Monte-Carlo sampling approach allowing evaluation of entropic elastic properties of individual polymer chain molecules with an atomistic resolution, where a direct analysis of the n^{N_e-1} molecular configurations at $n \geqslant 3$ and $N_e > 30$ is intractable. Internal atomic scale parameters that determine the global geometric (gyration radius) and entropic elastic properties (linearity, elastic modulus and relaxed length) of the polymer molecule include the intra-monomer bond length u and angle θ , the set of relative rotation angles φ_i of adjacent monomers, and a respectful set of the transition probabilities P_i . These parameters also determine the order of degeneracy of the total potential energy of the molecule in the configuration space.

Results of the numerical studies have been compared with the limiting continuum model of the polymers. A significant divergence with the continuum model behavior is observed at smaller bond angles for all elongations of the molecule. Linearity of the entropic force exists in a wide range of the elongations, however, molecules with low gyration radii (densely packed polymers), i.e. those with large parameter θ , are linear mostly in extension or unfolding, while very sparsely packed molecules are linear mostly in the contraction mode. This logical result, though, cannot be reproduced within

the settings a of continuum model. Furthermore, the nonlinear regimes are observed not only in the contraction, as what has been observed with the continuum approach, but also for high elongations at both very large and very small gyration radii. The latter result cannot be reproduced with the usage of a purely continuum approach.

Acknowledgements

The authors gratefully acknowledge support to this research by the National Science Foundation through CMMI-0900498.

References

- [1] Flyvbjerg H, Julicher F, Ormos P, et al. Physics of Bio-Molecules and Cells. Springer 2002.
- [2] Lauffenburger D A, Linderman J J. Receptors: Models for Binding, Trafficking and Signaling. Oxford University Press, 1993.
- [3] Zuckerman D M. Statistical Physics of Biomolecules: An Introduction. CRC Press, 2010.
- [4] Bhutani S P. Chemistry of Biomolecules. CRC Press, 2010.
- [5] Vries G, Hillen T, Lewis M, et al. A Course in Mathematical Biology. SIAM, 2006.
- [6] Cohen W W. A Computer Scientist's Guide to Cell Biology. Springer, 2007.
- [7] Otto S P, Day T. A. Biologist's Guide to Mathematical Modeling in Ecology and Evolution. Princeton University Press, 2007.
- [8] Alberts B, Johnson A, Lewis J, et al. Molecular Biology of the Cell: Reference Edition. Garland Science, 2007.
- [9] Tamm L K. Protein-Lipid Interactions: From Membrane Domains to Cellular Networks. Wiley-VCH, 2005.
- [10] Whitaker J R, Shahidi F, Munguia A L, et al. Functional Properties of Proteins and Lipids. American Chemical Society, 1998.
- [11] Stroble G. The Physics of Polymers: Concepts for Understanding Their Structures and Behavior. Springer, 2007.
- [12] Eisele U. Introduction to Polymer Physics. Springer, 1990.
- [13] Rocha M S, Mesquita O N. New tools to study biophysical properties of single molecules and single cells. *Anais Da Academia Brasileira De Ciencias*, 79(1), 17-28, 2007.
- [14] Strick T R, Dessinges M N, Charvin G, et al. Stretching of macromolecules and proteins. *Reports on Progress in Physics*, 66, 1-45, 2003.
- [15] Bao G. Mechanics of biomolecules, *Journal of the Mechanics and Physics of Solids*, 50(11), 2237-2274, 2002.
- [16] Humphrey J D. Continuum biomechanics of soft biological tissues. *Proceedings of the Royal Society A*, 459(2029), 3-46, 2003.

- [17] Taylor M, Steigmann D J. Entropic thermoelasticity of thin polymeric films. *Acta Mechanica*, 183, 1-22, 2006.
- [18] Broedersz C P, Storm C, MacKintosh F C. Nonlinear elasticity of composite networks of stiff biopolymers with flexible linkers. *Physical Review Letters*, 101(11), 118103, 2008.
- [19] Landau L D, Lifshitz E M. Statistical Physics. 3rd ed (Course of Theoretical Physics, Volume 5). Butterworth-Heinemann, 1980.
- [20] Terletskii Y P. Statistical Physics. North-Holland Publishing, American Elsevier, 1971.
- [21] Engel T, Reid P. Thermodynamics, Statistical Thermodynamics and Kinetics. 2nd ed. Prentice Hall, 2009.
- [22] Laurendeau N. Statistical Thermodynamics: Fundamentals and Applications. Cambridge University Press, 2005.
- [23] Karplus M, Ichiye T, Petitt B M. Configurational entropy of native proteins. *Biophysics Journal*, 52, 1083-1085, 1987.
- [24] Bustamante C, Marko J F, Siggia E D, et al. Entropic elasticity of lambda-phage DNA. *Science*, 265(5178), 1599-600, 1994.
- [25] Moroz J D, Nelson P. Entropic Elasticity of twist-storing polymers. *Macromolecules*, 31(18), 6333-6347, 1998.
- [26] Gardiner C W. Handbook of Stochastic Methods. Springer, 2004.
- [27] Newman M E J, Barkema G T. Monte-Carlo Methods in Statistical Physics. Clarendon Press, 1999.
- [28] Binder K, Heermann D W. Monte-Carlo Simulation in Statistical Physics: A Introduction. Springer, 2002.
- [29] Landau D P, Binder K A Guide to Monte-Carlo Simulations in Statistical Physics. Cambridge University Press, 2000.
- [30] Rubinstein R Y. Simulation and the Monte-Carlo Method. Wiley, 1981.
- [31] Karpov E G, Chaichenets S, Liu W K, et al. Mechano-kinetic coupling approach for functional materials with dynamic internal structure. *Philosophical Magazine Letters*, 90(7), 471-480, 2010.
- [32] Linke W A, Granzier H L, Kellermayer M. Mechanics of Elastic Biomolecules. Springer, 2003.
- [33] Moore D R, Williams J G, Pavan A. Fracture Mechanics Testing Methods for Polymers, Adhesives and Composites. Elsevier Science, 2001.
- [34] Sun C T, Schapery R A. Time Dependent and Nonlinear Effects in Polymers and Composites. ASTM International, 2000.
- [35] Borsali R, Pecora R. Soft-Matter Characterization. Springer, 2008.
- [36] Wigner E. The transition state method. *Transactions of Faraday Society*, 34, 29-41, 1938.
- [37] Kramers H. Brownian motion in a field of force and the diffusion model. *Physica* 7(4), 284-304, 1940.
- [38] Vineyard G. Frequency factors and isotope effects in solid state rate processes. *Journal of Physics and Chemistry of Solids*, 3(1-2), 121-127, 1957.
- [39] Chandler D. Statistical mechanics of isomerization dynamics in liquids and the transition state approximation. *Journal of Chemical Physics*, 68(6), 2959-2970, 1978.

- [40] Voter A, Doll J. Dynamical corrections to transition state theory for multistate systems: Surface self-diffusion in the rare-event regime. *Journal of Chemical Physics*, 82(1), 80-92, 1985.
- [41] Voth G, Chandler D, Miller W. Rigorous formulation of quantum transition state theory and its dynamical corrections. *Journal of Chemical Physics*, 91(12), 7749-7760, 1989.
- [42] Pollak E, Liao J. A new quantum transition state theory. *Journal of Chemical Physics*, 108(7), 2733-2743, 1998.

Chapter 6 Continuum Models of Stimuli-responsive Gels

Wei Hong*

*Department of Aerospace Engineering, Iowa State University,
Ames, IA 50011, USA*

Abstract: Immersed in a solution of small molecules and ions, a network of long-chain polymers may imbibe the solution and swell, resulting in a polymeric gel. Depending on the molecular structure of the polymers, the amount of swelling can be regulated by moisture, mechanical forces, ionic strength, electric field, pH value, and many other types of stimuli. Starting from the basic principles of non-equilibrium thermodynamics, this chapter formulates a field theory of the coupled large deformation and mass transportation in a neutral polymeric gel. The theory is then extended to study polyelectrolyte gels with charge-carrying networks by accounting for the electromechanical coupling and migration of solute ions. While the theoretical framework is adaptable to various types of material models, some representative ones are described through specific free-energy functions and kinetic laws. A specific material law for pH-sensitive gels—a special type of polyelectrolyte gels—is introduced as an example of incorporating chemical reactions in modeling stimuli-responsive gels. Finally, a simplified theory for the equilibrium but inhomogeneous swelling of a polymeric gel is deduced. The theory and the specific material models are illustrated through several examples.

Keywords: polymer, gel, thermodynamics

6.1 Introduction

Immersed in a liquid, a covalently cross-linked network of long-chain polymers imbibes the small solvent molecules (together with other solutes if present) from the liquid and swells, resulting in a polymeric gel. While the small molecules can readily change their neighbors, the connectivity of the polymer network is usually preserved by the cross-links. As a result, the gel can

*Corresponding author, E-mail: whong@iastate.edu.

swell and shrink repeatedly as the solvent molecules migrate in and out. The volume of a swollen gel is typically many times that of the dry network. Depending on the species of the constituent polymer and solvent, the amount of swelling is affected by mechanical forces, light, salt, pH value, temperature, or electric field^[1,2].

Most biological tissues contain polymeric gels^[3], such as pectin which regulates the water flow in plants in response to changes in ionic concentration^[4], and articular cartilage which maintains low friction in joints^[5]. Synthetic gels are also being developed for diverse applications including tissue engineering^[6], drug delivery^[7], sensors^[8,9], and actuators^[10-12]. In many applications, gels serve as transducers that convert between non-mechanical stimuli (e.g., humidity, temperature, pH value, and ion concentration) and large displacements or appreciable forces. Most of the mechanisms consist of gels swelling against the constraint of hard materials, and the induced stress fields are often inhomogeneous. Therefore, a field theory that couples nonlinear elastic deformation and migration of small molecules is needed to describe those mechanisms as well as other complex swelling phenomena of gels.

The thermodynamics of swelling dates at least back to Gibbs^[13], who formulated an equilibrium theory for the deformation of an elastic solid that absorbs a fluid. When a material-dependent free-energy function is specified, the Gibbs theory leads to a boundary-value problem that governs the fields of deformation and liquid concentration in equilibrium with external loads. For polymeric gels, a free-energy function often used is the Flory–Rehner model^[14], which combines the entropy of stretching the polymer network and the entropy of mixing the polymers with the solvent. The kinetics of swelling also has a long history. The theory developed by Biot^[15] who used Darcy's law to model the motion of a fluid in a porous solid has been widely used to analyze subjects ranging from soil to biological tissues.

In the tradition of Gibbs and Biot, this chapter summarizes the recent developments by Hong and coworkers^[16-18], and formulates a continuum framework in terms of nonequilibrium thermodynamics for the modeling of stimuli-responsive gels. Such an approach, however, leaves the free-energy function and the kinetic law open, both being material-specific. Some simple material laws, which are deduced from theoretical abstraction and idealization, will be presented as examples.

6.2 Nonequilibrium thermodynamics of neutral gels

Since gels are known to be responsive to various types of stimuli due to different mechanisms, it is impossible to build a universal model that covers

all of them. Three types of gels will be selectively studied in this chapter. As the first subject of this chapter, the neutral gels which consist of only one species of polymer chains and one species of solvent molecules, both being electroneutral, will be considered in this section.

The solvent molecules constantly change their neighbors and migrate in and out of the gel freely. In order to trace the deformation of the gel, we will look at the polymer network. Imagine attaching a field of markers to the polymer chains. While the choice of a reference state is more or less arbitrary, here we simply take the dry polymer network under no mechanical load as the reference state, and name each marker by its coordinate \mathbf{X} in the reference state. In the current state at time t , the marker \mathbf{X} moves to a place with coordinate $\mathbf{x}(\mathbf{X}, t)$. We measure both the volume element $dV(\mathbf{X})$ and the area element $\mathbf{N}(\mathbf{X})dA(\mathbf{X})$ of integrals in the reference configuration, where $\mathbf{N}(\mathbf{X})$ is the unit outward-normal vector.

Figure 6.1 illustrates two ways of doing work upon a piece of neutral gel: application of a mechanical force (e.g. by hanging to the polymer network a weight), and attaching to the gel a source of solvent molecules (e.g. by connecting the gel to a reservoir through a pump). Let us first consider the consequence of a field of mechanical forces. In the current state, let $\mathbf{b}(\mathbf{X}, t)dV(\mathbf{X})$ be the force on a volume element and $\mathbf{t}(\mathbf{X}, t)dA(\mathbf{X})$ be that on an area element. When the polymer network deforms by $\delta\mathbf{x}$, the field of forces does work

$$\int \mathbf{b} \cdot \delta\mathbf{x} dV + \int \mathbf{t} \cdot \delta\mathbf{x} dA. \quad (6.1)$$

Similarly, we imagine a field of sources, with chemical potential $\mu(\mathbf{X}, t)$, is connected to the gel. Associated with the number of solvent molecules injected by the sources: $\delta r(\mathbf{X}, t)dV(\mathbf{X})$ in a volume element and $\delta i(\mathbf{X}, t)dA(\mathbf{X})$

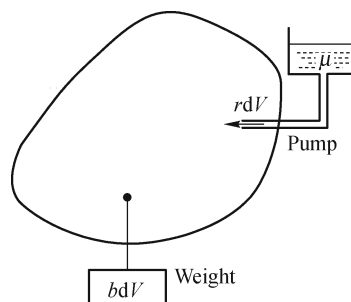


Fig. 6.1 Two ways of doing work on a neutral polymeric gel. Mechanical loads are applied by hanging a field of weights to the network. Chemical loads are applied using a field of pumps to inject solvent molecules into the gel.

on an area element, the field of sources does work

$$\int \mu \delta r dV + \int \mu \delta i dA. \quad (6.2)$$

The sign of δr and δi is so defined that they are positive when molecules migrate into the gel.

In practice, many parts of a gel may not be attached to sources. Instead, the solvent molecules migrate to and from neighboring parts. In line with the theory described here, it is equivalent to imagine that every element of the network is still attached to a source, the chemical potential of which is tuned to a level so that the solvent molecules will neither migrate into nor out of the gel. The imaginary sources provide a way of measuring the local chemical potential near a marker in the gel.

After studying the external loads, we will turn to the energy stored in a gel. Here we will focus on isothermal processes and drop the temperature from the list of state variables. Neglecting the free energy of a surface or interface, we write the Helmholtz free energy of an element of volume in the current state as $W dV$. The Helmholtz free energy of the gel is the integral of the free-energy density W over the volume of the gel. Following a common practice in field theories, we take this approach by assuming that the gel consists of many small volume elements, with each being small enough to be considered to be homogeneous, and the free energy of the gel is just the sum of that of each element.

The free-energy density is a function of a set of the local field variables. The choice of the field variables, together with the functional form of the free-energy density, constitutes a specific material model. For neutral polymeric gel, we take the following two commonly used field variables.

To describe the local stretching state of the polymer network near marker \mathbf{X} , we invoke the deformation gradient

$$\mathbf{F}(\mathbf{X}, t) = \nabla \mathbf{x}. \quad (6.3)$$

Here and throughout the chapter, the spatial differential operator ∇ is taken with respect to the reference configuration.

To account for the mobile species, we define the field of nominal solvent concentration $C(\mathbf{X}, t)$, so that $C dV$ is the number of solvent molecules in a volume element in the current state.

The Helmholtz free-energy density is assumed to be a function of the deformation gradient and the nominal solvent concentration, $W(\mathbf{F}, C)$. Consequently, associated with small changes in the independent variables, the free-energy density changes by

$$\delta W = \frac{\partial W}{\partial \mathbf{F}} : \delta \mathbf{F} + \frac{\partial W}{\partial C} \delta C. \quad (6.4)$$

Following a well-known result in solid mechanics, to rid W of its dependence on rigid-body rotations, we require that W depends on \mathbf{F} only through the product $\mathbf{F}^T \cdot \mathbf{F}$ (i.e. the right Cauchy-Green deformation tensor).

The gel, the pump, the mechanical forces, and the solvent sources form a thermodynamic system. The system is held at a constant temperature by preserving thermal equilibrium with a reservoir of energy. The Helmholtz free energy of the system is the sum of two parts: the change in the free energy of the gel, and the change in the free energy of the mechanical loads or solvent sources, i.e. the negative of the work of Eqs. (6.1) and (6.2). Although the system is in thermal equilibrium with the energy reservoir, it may not be in thermodynamic equilibrium. The principle of thermodynamics dictates that the Helmholtz free energy of the system never increases in a physically possible process:

$$\int \delta W dV - \int \mathbf{b} \cdot \delta \mathbf{x} dV - \int \mathbf{t} \cdot \delta \mathbf{x} dA - \int \mu \delta r dV - \int \mu \delta i dA \leq 0. \quad (6.5)$$

The inequality holds when the process is irreversible, and the equality holds when the system undergoes a reversible process, i.e. the system is in equilibrium.

No chemical reaction takes place in the system, so that the total number of solvent molecules is preserved. Let $\delta \mathbf{I}$ be the nominal flux vector of solvent migration, so that $\delta \mathbf{I} \cdot \mathbf{N} dA$ is the number of molecules passing through the element of area. The conservation of solvent molecules requires that

$$\delta C + \nabla \cdot \delta \mathbf{I} = \delta r \quad (6.6)$$

in the volume, and that

$$\delta \mathbf{I} \cdot \mathbf{N} = -\delta i \quad (6.7)$$

on a surface.

Using Eqs. (6.4), (6.6) and (6.7), we can rewrite Eq. (6.5) as

$$\begin{aligned} & \int (\nabla \cdot \mathbf{P}^T + \mathbf{b}) \cdot \delta \mathbf{x} dV + \int (\mathbf{t} - \mathbf{P} \cdot \mathbf{N}) \cdot \delta \mathbf{x} dA \\ & + \int \left(\frac{\partial W}{\partial C} - \mu \right) \delta C dV - \int \nabla \mu \cdot \delta \mathbf{I} dV \geq 0, \end{aligned} \quad (6.8)$$

where \mathbf{P} is the nominal stress (or the Piola–Kirchhoff stress of the first kind):

$$\mathbf{P} = \frac{\partial W(\mathbf{F}, C)}{\partial \mathbf{F}}. \quad (6.9)$$

All terms on the left-hand side of inequality Eq. (6.8) represent the dissipation of free-energy through distinct processes: the first two are due to

the deformation of the network, the third is due to the injection of solvent molecules, and the fourth due to the migration of solvent molecules.

Let us first consider the process of injection. The imaginary pumps that connect the gel to the sources are added for ease of description, it is safe to assume that they are reversible and dissipate no energy. As a result, the solvent near the pump is always in local equilibrium with the source, namely,

$$\mu = \frac{\partial W}{\partial C}. \quad (6.10)$$

In most cases, a gel does not have any volumetric source of solvent, and the artificially added sources together with Eq. (6.10) serve just as the definition of local chemical potential. The local chemical potential equals that in the imaginary reservoir if no solvent will migrate in or out of the gel when the reservoir is attached.

Admitting Eq. (6.10), to ensure that Eq. (6.9) holds true for any displacement or flux, we require that the integrands of the rest three terms in Eq. (6.8) must be positive-definite for all physically possible processes. One common way to do this is to adopt a kinetic law for each irreversible process. We can correlate the unbalanced body force with the velocity of the polymer network by introducing a viscous-drag-like relation:

$$\nabla \cdot \mathbf{P}^T + \mathbf{b} = \mathbf{f} \cdot \dot{\mathbf{x}} \quad (6.11)$$

in the volume, and

$$\mathbf{t} - \mathbf{P} \cdot \mathbf{N} = \mathbf{f}' \cdot \dot{\mathbf{x}} \quad (6.12)$$

on a surface. An alternative (but not necessarily equivalent) approach to account for the dissipation due to deformation of polymer network would be to introduce viscous stress and correlate it to the velocity gradient, similar to that in finite-deformation viscoelasticity^[19]. For the dissipation due to solvent migration, we can correlate the solvent flux, $\mathbf{J} = \partial \mathbf{I} / \partial t$, to its driving force, the chemical potential gradient, as

$$\mathbf{J} = -\mathbf{M} \cdot \nabla \mu. \quad (6.13)$$

The kinetic tensors \mathbf{f} , \mathbf{f}' , and \mathbf{M} may not be constant in general, but are all positively definite.

By imagining a picture in which all solvent molecules rest still in space, and the polymer network slides through the viscous liquid solvent, Tanaka et al.^[20] derived a simplified model by considering only the network friction through Eq. (6.11) and neglecting the solvent flux. Although the idealized picture may represent the free swelling process of a gel in a still liquid, it deviates from the actual physical process in more general cases. A gel

may deform instantaneously under mechanical loads by carrying the solvent molecules together with the network.

While an actual physical process may involve all types of dissipation, in this chapter we will look at the other extremes and only consider the dissipation due to migration of solvent. Such extremes represent the case when the relative motion of the polymer network to the external solvent is slow, and the pressure gradient through the gel is small, so that the solvent molecules migrate in a process similar to self diffusion, and induce negligible drag on the network. Therefore, the polymer network is in partial mechanical equilibrium, satisfying the equation

$$\nabla \cdot \mathbf{P}^T + \mathbf{b} = \mathbf{0} \quad (6.14)$$

in the bulk, and the boundary condition

$$\mathbf{P} \cdot \mathbf{N} = \mathbf{t} \quad (6.15)$$

on surfaces where a traction \mathbf{t} is prescribed.

The conservation law of solvent molecules, Eqs. (6.7) and (6.8), can also be written in terms of the changing rate of nominal concentration

$$\dot{C} = \dot{r} - \nabla \cdot \mathbf{J}, \quad (6.16)$$

$$\mathbf{J} \cdot \mathbf{N} = -\dot{i}, \quad (6.17)$$

where \dot{r} and \dot{i} are the injection rates of solvent molecules in the bulk and on a surface, respectively.

Equations (6.5), (6.13), (6.14), and (6.16) constitute a closed initial-boundary-value problem. When the material-dependent free-energy function $W(\mathbf{F}, C)$ and mobility tensor \mathbf{M} are determined and proper initial and boundary conditions are prescribed, we can readily evolve the morphology of a neutral polymeric gel by solving the fields $\mathbf{x}(\mathbf{X}, t)$ and $C(\mathbf{X}, t)$.

6.3 A simple material model for neutral gels

When the polymer network absorbs solvent, it swells and increases its volume. The volume change and the solvent concentration are interdependent. The accurate functional relation between $\det \mathbf{F}$ and C may be determined experimentally. Here following a common practice we assume that the individual polymer chains and the individual solvent molecules are incompressible. The relation is then simply expressed as

$$1 + vC = \det \mathbf{F}, \quad (6.18)$$

where v is the volume occupied by one solvent molecule in the gel. The molecular incompressibility condition, Eq. (6.18), can be enforced by adding a term $\int \Pi (1 + vC - \det \mathbf{F}) dV$ to the total free energy of the system, where $\Pi(\mathbf{X}, t)$ is a field of Lagrange multiplier. The field equations (6.13)–(6.17) will maintain the original form if we modify the constitutive relation, Eq. (6.5), to

$$\mathbf{P} = \frac{\partial W(\mathbf{F}, C)}{\partial \mathbf{F}} - \mathbf{F}^{-T} \Pi \det \mathbf{F} \quad \text{and} \quad \mu = \frac{\partial W(\mathbf{F}, C)}{\partial C} + v \Pi. \quad (6.19)$$

The solvent molecules enter or leave the gel freely, but the polymers chains are cross-linked into the network and cannot leave the gel. The situation is analogous to that of a membrane permeable to the solvent but not to the solute. If such a membrane separates a pure solvent from a solution, the solvent will diffuse across the membrane until the solution builds up a counteracting pressure, known as the osmotic pressure. From Eq. (6.19), we can interpret the Lagrange multiplier Π as the osmotic pressure that modifies the ideal behavior of the solvent in the gel.

To illustrate the general procedure and to describe the approximate behavior of polymeric gels, we will adopt a simple form of the free-energy function and kinetic law. The accurate prediction of a specific gel may require additional terms and parameters to fit experimental data, a task that is beyond the scope of this chapter.

The free energy of a neutral gel comes from two molecular processes: stretching the polymer network and mixing the polymers and solvent molecules. A usual treatment is to take the sum of both contributions, and write the energy function in the form^[14]

$$W(\mathbf{F}, C) = W_s(\mathbf{F}) + W_m(C), \quad (6.20)$$

where W_s and W_m are the free energy of stretching and mixing, respectively.

Considering the entropy of polymer chains of Gaussian statistics, we write the free energy of stretching as^{[21]1}

$$W_s(\mathbf{F}) = \frac{1}{2} N k T [\mathbf{F} : \mathbf{F} - 2 \ln(\det \mathbf{F}) - 3], \quad (6.21)$$

where N is the number of polymer chains in the gel per unit reference volume, and kT the temperature in the unit of energy. Other forms of the free energy of stretching are available in the literature [22–24].

¹The coefficient 2 in the second term in the bracket of Eq. (6.21) is a consequence of the stress-free assumption of the dry polymer network in the reference state. If the entropy of cross-linking is accounted for, the coefficient shall be modified to 1, and the reference state is no longer stress-free. The difference in final results, however, is minuscule.

When the long polymers are not cross-linked, they form a liquid solution with the small solvent molecules. Utilizing a lattice model, Flory (1942) and Huggins (1941) obtained the free energy of mixing as follows:¹

$$W_m(C) = -\frac{kT}{v} \left[vC \ln \left(1 + \frac{1}{vC} \right) + \frac{\chi}{1 + vC} \right]. \quad (6.22)$$

The first term inside the bracket comes from the entropy of mixing, and the second from the enthalpy of mixing, characterized by a dimensionless parameter χ . The polymer is more hydrophilic when the value of χ is smaller².

Substituting the specific functional forms in Eqs. (6.20)–(6.22) into Eq. (6.19), we have the equations of state:

$$\mathbf{P} = NkT(\mathbf{F} - \mathbf{F}^{-T}) - \mathbf{F}^{-T}\Pi \det \mathbf{F}, \quad (6.23)$$

$$\mu = kT \left[\ln \frac{vC}{1 + vC} + \frac{1}{1 + vC} + \frac{\chi}{(1 + vC)^2} \right] + v\Pi. \quad (6.24)$$

As a simple example for the kinetic law, we assume the coefficient of diffusion of the solvent molecules, D , to be isotropic and independent of the state. This simplification shall be reasonable for a highly swollen gel, in which the small molecules are the majority component. Let $c(\mathbf{X}, t)$ be the number of solvent molecules per unit volume in the current state, and $\mathbf{j}(\mathbf{X}, t)$ be the corresponding solvent flux crossing per unit area in the current state. The flux relates to the gradient of chemical potential through a well-known equation

$$\mathbf{j} = -\frac{cD}{kT} \nabla_{\mathbf{x}} \mu, \quad (6.25)$$

where the gradient $\nabla_{\mathbf{x}}$ is taken with respect to the coordinates of the markers in the current state, and relates to the gradient in the reference state as $\nabla \mu = \nabla_{\mathbf{x}} \mu \cdot \mathbf{F}$. Utilizing the geometric relations $c = C / \det \mathbf{F}$ and $\mathbf{j} = \mathbf{F} \cdot \mathbf{J} / \det \mathbf{F}$, and comparing Eqs. (6.13) and (6.25), we relate the mobility tensor to the coefficient of diffusion as:

$$\mathbf{M} = \frac{CD}{kT} (\mathbf{F}^T \cdot \mathbf{F})^{-1}. \quad (6.26)$$

Even though the diffusion is isotropic in the current state, under a finite anisotropic deformation, the mobility tensor defined using nominal quantities is anisotropic.

To complete the initial-boundary-value problem, a set of boundary conditions on surface traction (or displacement) and chemical potential (or solvent

¹Some terms independent of \mathbf{F} or C have been removed from Eqs. (6.21) and (6.22) for simplicity.

²To arrive at the functional form of Eq. (6.22), Flory (1942) and Huggins (1941) used a lattice model in which the volume of each segment of polymer chain was the same as that of a solvent molecule, v .

concentration) needs to be prescribed. Due to molecular incompressibility, the changes in volume and solvent concentration are interdependent. As shown in Eqs. (6.23) and (6.24), the constitutive expressions of stress and chemical potential are also related by the Lagrange multiplier Π . As a result, the boundary conditions of surface traction and chemical potential need to be consistent with each other. The functional forms of Eqs. (6.23) and (6.24) imply that the reference of chemical potential (when $\mu = 0$) is taken to be a pressure-free pure solvent. When the gel is immersed in a pressurized solvent, the pressure contribution must appear in both the surface traction and the chemical potential. For example, if the surface of a gel is in contact with a pure solvent under pressure p , the consistent boundary conditions should be $\mathbf{t} = -p\mathbf{n}$ and $\mu = pv$, where \mathbf{n} is the unit normal of the surface element in the current state.

6.4 Swelling of a spherical gel

To illustrate the field theory and material model described in the previous sections, we will look at the swelling process of a spherical gel. Before time zero, the gel is in equilibrium with an unsaturated environment in which the chemical potential of solvent is related to the relative humidity RH as $\mu_0 = kT \ln RH$. The gel is then submerged into a saturated environment with chemical potential $\mu = 0$. The solvent molecules diffuse into the gel, and the gel swells as a consequence.

We will normalize the chemical potential by kT and normalize the stress by kT/v , and denote the corresponding dimensionless fields as $\tilde{\mu}$ and $\tilde{\mathbf{P}}$. A representative volume of a solvent molecule is $v = 10^{-28} \text{ m}^3$. At room temperature, $kT = 4 \times 10^{-21} \text{ J}$ and $kT/v = 40 \text{ MPa}$. The free-energy functions (6.21) and (6.22) introduce two dimensionless material parameters: Nv and χ . The representative values are $Nv = 10^{-4} - 10^{-1}$ and $\chi = 0 - 1.2$. Here in this example, we will take the values $Nv = 10^{-2}$ and $\chi = 0.1$. The theory does not have an intrinsic length scale. The only length scale in the problem is the size of the gel, L . We will normalize time by L^2/D , and denote the dimensionless time with τ . Using the representative value of the coefficient of self diffusion of water at room temperature, $D = 10^{-9} \text{ m}^2/\text{s}$, for a size scale $L \sim 1 \text{ mm}$, we find that the time scale is $L^2/D = 10^3 \text{ s}$.

For simplicity, we assume that the gel swells isotropically, and no instability develops so that both the deformation and the solvent distribution are spherically symmetric. Let L be the radius of the gel and R be the radial coordinate of the markers in the reference state. At time t , the marker R moves to a place $r(R, t)$. We will use $\tilde{r} = r/L$ and $\tilde{R} = R/L$ to represent

the dimensionless coordinates. The radial and circumferential stretches are, respectively,

$$\lambda_r = \frac{\partial \tilde{r}}{\partial \tilde{R}} \quad \text{and} \quad \lambda_\theta = \frac{\tilde{r}}{\tilde{R}}. \quad (6.27)$$

The constitutive equations (6.23) and (6.24) are specialized to

$$\tilde{P}_r = Nv \left(\lambda_r - \frac{1}{\lambda_r} \right) + \left(\lambda_\theta^2 \ln \frac{\lambda_r \lambda_\theta^2 - 1}{\lambda_r \lambda_\theta^2} + \frac{1}{\lambda_r} + \frac{\chi}{\lambda_r^2 \lambda_\theta^2} \right) - \tilde{\mu} \lambda_\theta^2, \quad (6.28)$$

$$\tilde{P}_\theta = Nv \left(\lambda_\theta - \frac{1}{\lambda_\theta} \right) + \left(\lambda_r \lambda_\theta \ln \frac{\lambda_r \lambda_\theta^2 - 1}{\lambda_r \lambda_\theta^2} + \frac{1}{\lambda_\theta} + \frac{\chi}{\lambda_r \lambda_\theta^3} \right) - \tilde{\mu} \lambda_r \lambda_\theta. \quad (6.29)$$

For spherically symmetric case, in the absence of distributed force, the mechanical equilibrium, Eq. (6.14), is specialized to

$$\frac{\partial \tilde{P}_r}{\partial \tilde{R}} + 2 \frac{\tilde{P}_r - \tilde{P}_\theta}{\tilde{R}} = 0. \quad (6.30)$$

Assuming that solvent flux only exists in the radial direction, the solvent conservation, Eq. (6.16), reduces to

$$\frac{\partial}{\partial \tau} (\lambda_r \lambda_\theta^2) = \frac{1}{\tilde{R}^2} \frac{\partial}{\partial \tilde{R}} \left(\tilde{R}^2 \frac{\lambda_r \lambda_\theta^2 - 1}{\lambda_r^2} \frac{\partial \tilde{\mu}}{\partial \tilde{R}} \right). \quad (6.31)$$

The boundary conditions at the surface of the gel, $\tilde{R} = 1$, are given by

$$\tilde{P}_r(1, \tau) = 0 \quad \text{and} \quad \tilde{\mu}(1, \tau) = 0. \quad (6.32)$$

In the center, the natural boundary conditions

$$\tilde{r}(0, \tau) = 0 \quad \text{and} \quad \frac{\partial \tilde{\mu}}{\partial \tilde{R}}(0, \tau) = 0 \quad (6.33)$$

are prescribed by symmetry.

At time zero, the gel is in equilibrium and stress-free. We introduce a set of consistent initial conditions,

$$\tilde{r}(\tilde{R}, 0) = \lambda_0 \tilde{R} \quad \text{and} \quad \tilde{\mu}(\tilde{R}, 0) = Nv \left(\lambda_0 - \frac{1}{\lambda_0} \right) + \ln \frac{\lambda_0^3 - 1}{\lambda_0^3} + \frac{1}{\lambda_0^3} + \frac{\chi}{\lambda_0^6}, \quad (6.34)$$

with the initial swelling ratio $\lambda_0 = 1.05$.

This initial-boundary-value problem is solved numerically with COMSOL Multiphysics 3.5a, and the results are plotted in Fig. 6.2. The profiles of the two main field variables, the normalized radial displacement u_r/L and the dimensionless chemical potential of solvent μ/kT are shown in Fig. 6.2a and b, respectively. Despite the difference in relative time, the evolution of the chemical potential field in the spherical gel is very similar to a regular

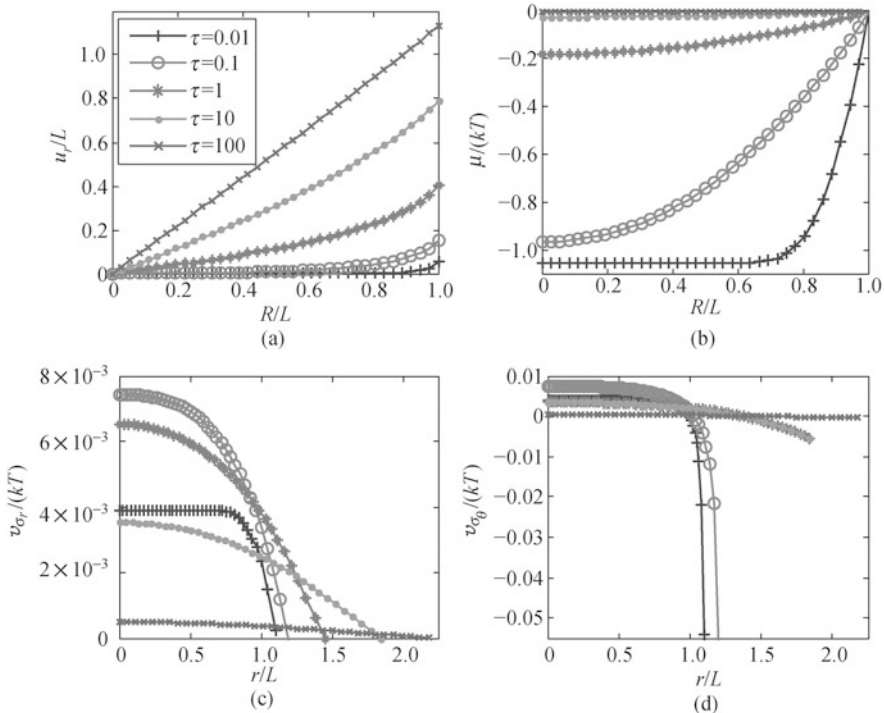


Fig. 6.2 (a) The spatial profiles of normalized radial displacement of a spherical gel at various dimensionless time during swelling, (b) the spatial profiles of normalized chemical potential of solvent, (c) the distribution of normalized true radial stress, plotted in the deformed configuration, (d) the distribution of normalized true hoop stress, plotted in the deformed configuration. (color plot at the end of the book)

concentration-driven diffusion problem. The solvent molecules enter from the surface of the gel, and the front of diffusion gradually propagates to the core.

The swelling and the influx of solvent induce a stress field in the gel. For more explicit comparison, we plot the normalized true stresses $v\sigma_r/(kT)$ and $v\sigma_\theta/(kT)$ as a function of the then-current deformed coordinate r/L , as shown in Fig. 6.2c and d. Shortly after the diffusion process begins, the superficial layer of the gel swells in the radial direction, but the circumferential direction is constrained by the rest of the gels. A high compressive hoop stress thus builds up in the swollen layer, and maximizes at the surface, where it reaches multiples of the initial modulus of the network. Even though the solvent has not yet diffused to the inner part of the gel, the expanding tendency of the swollen layer induces a hydrostatic tension in the unswollen core. Since we have assumed molecular incompressibility in the material model, no deformation takes place in the inner part even with the tension. While the diffusion front propagates inward, the swollen part increases in size and the

stress concentration near the surface gradually relieves, but the hydrostatic tension in the inner part increases. Significant swelling of the whole gel takes place after the diffusion front reaches the center, when both radial and hoop stresses start to decrease.

Unlike a regular concentration-driven diffusion process, the swelling of a spherical gel takes a much longer time to equilibrate. After dimensionless time $\tau \approx 10$, the chemical potential of the solvent molecules has almost reached equilibrium, but a significant level of hydrostatic stress (on the same order of the network stiffness) still resides in the gel. The gradient of the hydrostatic stress would still drive the flux of solvent molecules. The gel continues to swell until dimensionless time $\tau \approx 200—1\,000$. The characteristic swelling time of the gel is determined by the dimensionless stiffness of the polymer network, Nv . For a relatively stiff gel, with Nv close to 1, the swelling will be relatively fast, but the achievable swelling ratio is low. For a relatively compliant gel, the swelling is slower, but the swelling ratio is much higher. The swelling ratios of gels with three stiffness values are plotted as a function of the dimensionless time in Fig. 6.3.

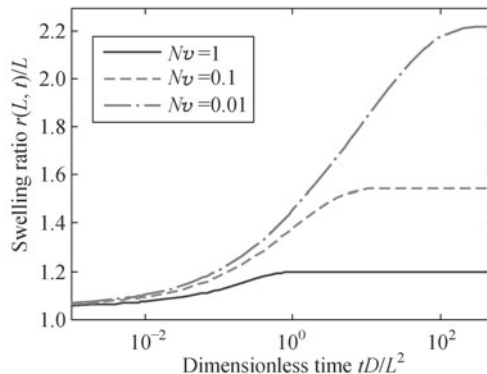


Fig. 6.3 Linear swelling ratio of three gels with different network stiffnesses.

6.5 Thermodynamics of polyelectrolyte gels

Many natural and synthetic macromolecules are polyelectrolytes, long-chain polymers containing ionizable groups. In a solution, the ionizable groups dissociate into fixed charges, which are bonded to the polymer, and mobile ions in the solution, as depicted in Fig. 6.4. The solution consists of solvent molecules of a low molecular weight, as well as ions of two types: co-ions that bear charges of the same sign as the fixed charges, and counterions that

bear charges of the opposite sign. A large number of polyelectrolyte chains can form a three-dimensional network by crosslinks. The network can imbibe liquid solution and swell, resulting in a polyelectrolyte gel. The amount of swelling can be regulated by geometric constraints, mechanical forces, ionic concentrations, and electric fields.

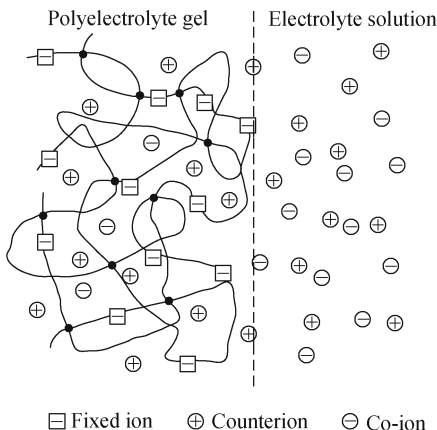


Fig. 6.4 A network of covalently cross-linked polyelectrolyte chains imbibes a solution and swell. The ionizable groups on the polymers dissociate and leave fixed charge on the polymer network. The counterions, co-ions, and solvent molecules (not shown) are mobile and can cross the interface between the gel and the external solution.

In this section, by studying the non-equilibrium thermodynamics of polyelectrolyte gels, we will extend the field theory of neutral gels developed in previous sections to couple electrochemistry and large deformation.

As illustrated in Fig. 6.5, there are three ways for the external agents to do work upon a polyelectrolyte gel. Just as in a neutral gel, the work done by a field of mechanical forces is given by Eq. (6.1). To define the fields of chemical potentials of mobile species, we imagine attaching fields of pumps to the gel. The pumps are connected to idealized reservoirs, and prescribe a time-dependent field of chemical potential $\mu^a(\mathbf{X}, t)$ for mobile species a . Upon injection of δr^a number of particles of species a , the corresponding pump does work $\mu^a \delta r^a$. Accounting for both the pumps connected to the bulk and those connected to the surface, the work done is, similar to Eq. (6.2),

$$\sum_a \int \mu^a \delta r^a dV + \sum_a \int \mu^a \delta i^a dA, \quad (6.35)$$

where the summation is taken over all mobile species, including solvent and

both types of mobile ions.

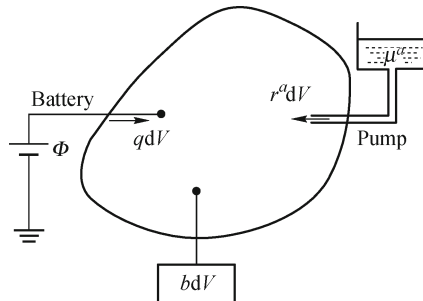


Fig. 6.5 Three ways of doing work on a polyelectrolyte gel. Mechanical loads are applied by hanging a field of weights to the network. Chemical loads are applied using a field of pumps to injecting solvent molecules or solute ions into the gel. Electric loads are applied by connecting a field of batteries to the gel.

The gel is taken to be an ionic conductor, but an electronic insulator. Imagine that every element of the network is attached with an electrode, and that electrodes of neighboring elements are electrically insulated from one another. In the current state, let the electronic charges on electrodes be qdV in a volume element and ωdA on a surface element. The electrodes are then connected to a field of batteries with electric potential $\Phi(\mathbf{X}, t)$. Upon inflow of electronic charges δq and $\delta\omega$ through the electrodes, the field of batteries does work

$$\int \Phi \delta q dV + \int \Phi \delta \omega dA. \quad (6.36)$$

In practice, many parts of the gel are not attached with electrodes and batteries, and are kept in the open-circuit condition. These parts contain no electronic charges, $q = 0$ and $\omega = 0$. Just as the imaginary field of pumps introduced for the definition of chemical potential, the field of imaginary electrodes and batteries here is introduced for definition of the electric potential in a polyelectrolyte gel. When an actual electrode is absent, the electric potential at a material point is defined as the voltage of the imaginary battery needed to keep the electrode charge-free when connected to this point.

Let QdV be the total charge in the current state on a volume element. The total charge includes the contributions from electrons, ions, and fixed charges:

$$Q = q + \sum_b e z^b C^b + e z_0 C_0, \quad (6.37)$$

where e is the elementary charge, C^a is the nominal concentration of species a , and z^a is its valence. The summation is carried over all mobile ions, and the valence and nominal concentration of fixed charges are specifically denoted

as z_0 and C_0 , respectively. Just as in the model of neutral gels, the concentrations of mobile species are assumed to be continuous across any interfaces, so that the total charge on a surface element only includes the electronic contribution, ωdA . Expressed in terms of the nominal fields^[25], the Gauss's law of electrostatics dictates that the nominal electric displacement $\tilde{\mathbf{D}}(\mathbf{X}, t)$ satisfies

$$\nabla \cdot \tilde{\mathbf{D}} = Q \quad (6.38)$$

in the volume, and

$$(\tilde{\mathbf{D}}^+ - \tilde{\mathbf{D}}^-) \cdot \mathbf{N} = \omega \quad (6.39)$$

on an interface between media labeled as $-$ and $+$, with the unit vector \mathbf{N} normal to it in the reference state, pointing towards $+$.

To account for the effect of ions and electric field, we extend the Helmholtz free-energy density of a neutral gel to include its dependence on ion concentrations and nominal electric displacement, $W(\mathbf{F}, \tilde{\mathbf{D}}, C^1, C^2, \dots)$. Consequently, associated with small changes in the independent variables, the free-energy density changes by

$$\delta W = \frac{\partial W}{\partial \mathbf{F}} : \delta \mathbf{F} + \frac{\partial W}{\partial \tilde{\mathbf{D}}} \cdot \delta \tilde{\mathbf{D}} + \sum_a \frac{\partial W}{\partial C^a} \delta C^a. \quad (6.40)$$

The polyelectrolyte gel, together with the weights, the pumps and the batteries, constitutes a thermodynamic system. The change in the Helmholtz free energy of the system is the sum over the parts: the change in the free energy of the gel $\int W dV$, and the changes in the free energy of the weights, pumps, and batteries, i.e. the negative amounts of the work in Eqs. (6.1), (6.35) and (6.36). While the system is assumed to be in thermal equilibrium, it is not necessarily in mechanical, chemical or electrostatic equilibria. In a physically possible process, thermodynamics dictates that the Helmholtz free energy should never increase,

$$\begin{aligned} \int \delta W dV - \int \mathbf{b} \cdot \delta \mathbf{x} dV - \int \mathbf{t} \cdot \delta \mathbf{x} dA - \sum_a \int \mu^a \delta r^a dV \\ - \sum_a \int \mu^a \delta i^a dA - \int \Phi \delta q dV - \int \Phi \delta \omega dA \leq 0, \end{aligned} \quad (6.41)$$

where the equality holds in a reversible process or the system is in equilibrium.

In this section, we still assume that no chemical reaction happens during the process, so that all mobile species are conserved:

$$\dot{C}^a = \dot{r}^a - \nabla \cdot \mathbf{J}^a, \quad (6.42)$$

$$(\mathbf{J}^{a+} - \mathbf{J}^{a-}) \cdot \mathbf{N} = \dot{i}^a, \quad (6.43)$$

where \mathbf{J}^a is the nominal flux of mobile species a , i^a the incoming flux of species a through an interface, and the signs indicate the two media separated by the interface under consideration. Using Eqs. (6.37)–(6.40), (6.42) and (6.43), and applying the divergence theorem, we can rewrite Eq. (6.41) as

$$\begin{aligned} & \int (\nabla \cdot \mathbf{P}^T + \mathbf{b}) \cdot \dot{\mathbf{x}} dV + \int [\mathbf{t} - (\mathbf{P}^+ - \mathbf{P}^-) \cdot \mathbf{N}] \cdot \dot{\mathbf{x}} dA \\ & + \sum_a \int \left(\frac{\partial W}{\partial C^a} + ez^a \Phi - \mu^a \right) \dot{C}^a dV - \sum_a \int \nabla \mu^a \cdot \mathbf{J}^a dV \\ & + \int \left(\frac{\partial W}{\partial \tilde{\mathbf{D}}} - \tilde{\mathbf{E}} \right) \cdot \dot{\tilde{\mathbf{D}}} dV \geq 0, \end{aligned} \quad (6.44)$$

where $\mathbf{P} = \partial W / \partial \mathbf{F}$ is the nominal stress tensor, and $\tilde{\mathbf{E}} = -\nabla \Phi$ is the vector of nominal electric field.

Each integral in Eq. (6.44) accounts for the dissipation of Helmholtz free energy through distinct processes: the first two are due to the deformation of the network, the third is due to the injection of mobile species, the fourth due to the migration of mobile species, and the last due to the polarization of solvent and polymer network. Similar to Section 6.2, we assume the rate of swelling to be limited by the migration of mobile species, and neglect the energy dissipation in all other processes. Consequently, the integrands in all but the fourth term of Eq. (6.44) vanish. The nominal stress \mathbf{P} satisfies the mechanical equilibrium equation

$$\nabla \cdot \mathbf{P}^T + \mathbf{b} = \mathbf{0} \quad (6.45)$$

in the volume, and

$$(\mathbf{P}^+ - \mathbf{P}^-) \cdot \mathbf{N} = \mathbf{t} \quad (6.46)$$

on an interface where the traction \mathbf{t} is prescribed. The local chemical potential of species a is related to the concentration and the electric potential as follows:

$$\mu^a = ez^a \Phi + \frac{\partial W(\mathbf{F}, \tilde{\mathbf{D}}, C^1, C^2, \dots)}{\partial C^a}. \quad (6.47)$$

The local electrostatic equilibrium is achieved, so that

$$\tilde{\mathbf{E}} = \frac{\partial W(\mathbf{F}, \tilde{\mathbf{D}}, C^1, C^2, \dots)}{\partial \tilde{\mathbf{D}}}. \quad (6.48)$$

Once the above condition of partial equilibrium is satisfied, only the fourth integral in Eq. (6.44), and the inequality reduces to

$$-\sum_a \mathbf{J}^a \cdot \nabla \mu^a \geq 0. \quad (6.49)$$

A common way to enforce this inequality is to assume the fluxes of mobile species to be linear in the gradients of chemical potentials:

$$\mathbf{J}^a = - \sum_b \mathbf{M}^{ab} \cdot \nabla \mu^a, \quad (6.50)$$

with a positive-definite matrix $\{\mathbf{M}^{ab}\}$ of the linear transformation. In general, the migration flux of a mobile species depends not only on the gradient of its own chemical potential, but also on that of other mobile species. For example, the migration of solvent molecules in a polyelectrolyte gel may carry along a number of mobile ions.

6.6 A material model for polyelectrolyte gels

A large number of models exist in the literature, describing the liquid mixture of uncrosslinked polymers and solvent molecules. On the other hand, there also exist a large number of models that describe the elasticity of crosslinked polymers. In many gels, the density of crosslinks is so low that to a good approximation, the effect of crosslinks on mixing may be neglected, and one can simply write the free energy of a gel as the sum of the free energy of the network and that of the solution. The Flory–Rehner approach described in Section 6.3 has been extended to polyelectrolyte gels^[26–29]. In this section, we further extend this approach by adding a term due to electric polarization. Specifically, we write the free-energy density of the gel as a sum

$$W = W_s + W_m + W_i + W_p, \quad (6.51)$$

where W_s , W_m , W_i and W_p are the contributions from stretching the polymer network, mixing the polymers and the solution, mixing the solvent and the ions, and polarizing the dielectric polymers and the solvent in the gel.

Similar to a neutral polymeric gel, the volume expansion of a gel is dependent on the concentrations of solvent and mobile ions. Assuming that individual molecules or ions of mobile species are incompressible with volume v^a , we can write the relation as $1 + \sum_a v^a C^a = \det \mathbf{F}$. This incompressibility constraint is enforced by adding the term,

$$\left(1 + \sum_a v^a C^a - \det \mathbf{F} \right) \Pi, \quad (6.52)$$

to the free-energy function Eq. (6.51), where Π is a field of Lagrange multiplier.

The functional form of the energy of stretching, W_s , is identical to Eq. (6.21) in Section 6.3:

$$W_s = \frac{1}{2} NkT [\mathbf{F} : \mathbf{F} - 2 \ln(\det \mathbf{F}) - 3]. \quad (6.53)$$

To estimate the energy of mixing, we take two steps. We first take the mobile ions and solvent molecules to be indistinguishable, and consider the free energy of mixing the polymer chains and the solution. In this section, we only consider a dilute solution with negligible volume fractions of ions, so that W_m has a form identical to Eq. (6.22):

$$W_m = -\frac{kT}{v^s} \left[v^s C^s \ln \left(1 + \frac{1}{v^s C^s} \right) + \frac{\chi}{1 + v^s C^s} \right], \quad (6.54)$$

where C^s is the nominal concentration of solvent molecules in the gel, and v^s is the volume occupied by one solvent molecule which is assumed to be the same as that occupied by a monomer¹.

As a second step, we differentiate between the solute and solvent in the solution. Considering solely the entropy of mixing, the free energy of mixing the ions with solvent is given by

$$W_i = kT \sum_a C^a \left(\ln \frac{C^a}{\sum_b C^b} - \ln \varsigma_0^a - 1 \right). \quad (6.55)$$

To understand this expression, one may think of a liquid solution with no polymer network. Eq. (6.55) is similar to the free energy of an ideal solution. Let ς_0^a be the reference mole fraction of species a , at which the chemical potential of the species is set to be zero. In this context, the choice of the reference mole fraction is arbitrary, and the references of different species need not be the same. When the mole fraction changes to ς^a , the chemical potential is $kT \ln \varsigma^a$. In a gel, we still assume that the ions and the solvent form an ideal solution independent of the polymer network, but the mole fraction is now $\varsigma^a = C^a / \sum C^b$. Under the dilute-solution assumption, the solvent concentration is much higher than the ion concentrations, thus Eq. (6.55) can be approximately rewritten as

$$W_i \approx kT \sum_{b \neq s} C^b \left(\ln \frac{C^b}{C^s} - \ln \varsigma_0^b - 1 \right), \quad (6.56)$$

where the summation is taken over all mobile ions but not solvent molecules.

¹Such an approach neglects the energy of mixing polymer chains with solute ions, and may not be valid if the ion concentration is relatively high or the ions are reactive to polymer chains.

Now let us turn to the energy of electric polarization. In the absence of free electrons, the polyelectrolyte gel is an ionic conductor but an electronic insulator. If we only consider the mixture of pure solvent and the polymer network, excluding all mobile charges, the medium is a dielectric. Here we assume its dielectric property to be ideal and linear, namely, having physically decoupled deformation and polarization with electric permittivity ε independent of the deformation state and history^[30]. Such a material has electric polarization energy per unit volume in the current state $\mathbf{D} \cdot \mathbf{D}/2\varepsilon$, where \mathbf{D} is the true electric displacement and is related to its nominal counterpart as $\mathbf{D} = \mathbf{F} \cdot \tilde{\mathbf{D}} / \det \mathbf{F}$ ^[31]. In terms of nominal fields, the free energy of polarization per unit reference volume is

$$W_p = \frac{1}{2\varepsilon} \frac{\tilde{\mathbf{D}} \cdot \mathbf{F}^T \cdot \mathbf{F} \cdot \tilde{\mathbf{D}}}{\det \mathbf{F}}. \quad (6.57)$$

The permittivity of the mixture, in general, can be a function of the solvent concentration, due to the difference in the dielectric properties between the solvent and the polymer network. However, often the major part of the gel is occupied by solvent molecules, $v^s C^s \gg 1$, and one may be able to use the permittivity of the solvent as that of the gel, independent of the composition.

We now have constructed a specific free-energy function. Applying this free-energy function to the equations of partial equilibrium in Section 6.5, we obtain the specific constitutive equations for stress

$$\mathbf{P} = NkT(\mathbf{F} - \mathbf{F}^{-T}) + \frac{\mathbf{F} \cdot \tilde{\mathbf{D}} \otimes \tilde{\mathbf{D}} - \tilde{\mathbf{D}} \cdot \mathbf{F}^T \cdot \mathbf{F} \cdot \tilde{\mathbf{D}} \mathbf{F}^{-T}}{\varepsilon \det \mathbf{F}} - \mathbf{F}^{-T} \Pi \det \mathbf{F}, \quad (6.58)$$

chemical potential of solvent

$$\mu^s = kT \left[\ln \frac{v^s C^s}{1 + v^s C^s} + \frac{1}{1 + v^s C^s} + \frac{\chi}{(1 + v^s C^s)^2} - \sum_{b \neq s} \frac{C^b}{C^s} \right] + v^s \Pi, \quad (6.59)$$

chemical potential of each species of mobile ions

$$\mu^b = ez^b \Phi + kT \ln \frac{C^b}{C^s \zeta_0^b} + v^b \Pi, \quad (6.60)$$

and the nominal electric field

$$\tilde{\mathbf{E}} = \frac{\mathbf{F}^T \cdot \mathbf{F} \cdot \tilde{\mathbf{D}}}{\varepsilon \det \mathbf{F}}. \quad (6.61)$$

Using the geometric relations between the true fields and the nominal fields^[31], we can rewrite Eq. (6.58) in terms of the true stress σ :

$$\sigma = \frac{NkT}{\det \mathbf{F}} (\mathbf{F}^T \cdot \mathbf{F} - \mathbf{I}) + \frac{1}{\varepsilon} (\mathbf{D} \otimes \mathbf{D} - \mathbf{D} \cdot \mathbf{D} \mathbf{I}) - \Pi \mathbf{I}. \quad (6.62)$$

where \mathbf{I} is second-rank identity tensor. Similarly, we can recover the familiar relation between the true electric field \mathbf{E} and the true electric displacement \mathbf{D} :

$$\varepsilon \mathbf{E} = \mathbf{D}. \quad (6.63)$$

The second term on the right-hand side of Eq. (6.62) is often referred to as the Maxwell stress. It is merely a consequence of the specific material model, and may not be directly applicable to general materials. For example, the form of this term will be different if the dependence of the permittivity on the composition of the gel needs to be accounted for. On the other hand, the electrostatic contribution to the stress, as measured by the dimensionless parameter $\varepsilon E^2/kT$, is very small in the bulk of an aqueous ionic solution, except in the thin electric double layers near electrodes or interfaces. Therefore, this term is often neglected in models of polyelectrolyte gels^[32-34].

If we still use the simple kinetic model for neutral gels, by assuming an isotropic and state-independent diffusion coefficient D^a for each mobile species, we will obtain the mobility tensors in the form:

$$\mathbf{M}^a = \frac{C^a D^a}{kT} (\mathbf{F}^T \cdot \mathbf{F})^{-1}. \quad (6.64)$$

We also assume that the diffusion fluxes of different species are independent of each other, so that $\mathbf{M}^{ab} = \mathbf{0}$ when $a \neq b$. In terms of the true fields, the kinetic equation for the diffusion flux of mobile species a is given by

$$\mathbf{j}^a = -\frac{c^a D^a}{kT} \nabla_{\mathbf{x}} \mu^a, \quad (6.65)$$

where c^a is the true concentration, i.e. the number of a particles per unit current volume, and $\nabla_{\mathbf{x}}$ is the gradient operator in the current configuration. Eq. (6.65) is applicable to the diffusion fluxes of both solvent molecules and mobile ions.

Applying Eq. (6.60) to Eq. (6.65) and then to the conservation of species, Eq. (6.42), we arrive at the evolution equation for the true concentration of mobile ions:

$$\dot{c}^b = \frac{D^b}{kT} \nabla_{\mathbf{x}} \cdot \left(e c^b z^b \nabla_{\mathbf{x}} \Phi + \nabla_{\mathbf{x}} c^b + \frac{c^b}{c^s} \nabla_{\mathbf{x}} C^s + v^b c^b \nabla_{\mathbf{x}} \Pi \right) + r^a. \quad (6.66)$$

In the dilute limit, since the ion concentrations are much lower than the solvent concentration, $c^b \ll c^s$, and the volume fraction of ions is negligible, $v^b c^b \ll 1$, the third and fourth terms in the parentheses of Eq. (6.66) may be ignored. In the absence of volumetric source, Eq. (6.66) further reduces to the Nernst – Planck equation

$$\dot{c}^b \approx \frac{D^b}{kT} \nabla_{\mathbf{x}} \cdot (e c^b z^b \nabla_{\mathbf{x}} \Phi + \nabla_{\mathbf{x}} c^b), \quad (6.67)$$

which has been widely used in models of polyelectrolyte gels^[33,34]. However, the functional form of Eq. (6.66) or (6.67) is only the consequence of the specific free-energy function and kinetic law described in this section, and requires the dilute-solution assumption. Care must be taken when generalizing these equations to gels with different free-energy functions or dealing scenarios with relatively high ion concentrations.

6.7 Chemical reactions and pH-sensitive gels

In previous sections, we have neglected any chemical reaction in a gel, so that the total number of particles is conserved for each mobile species, and the nominal concentration of fixed charges is constant. Here we will use a type of pH-sensitive gel as an example to illustrate the general procedure of modeling chemical reactions in polymeric gels. Figure 6.6 illustrates the model system: a network of covalently cross-linked polymers bearing acidic groups AH. When the network imbibes the solvent, some of the acidic groups on the network dissociate into hydrogen ions H⁺ mobile in the solvent, and conjugate base A⁻ attached on the network. Once dissociated, each network-attached conjugate base A⁻ gives rise to a fixed charge. The dissociation reaction is reversible:



A change in the local concentration of hydrogen ions may affect the balance of the reaction, thus the concentration of fixed charges. The pH-sensitive gel can be regarded as a special type of polyelectrolyte gel that has variable concentration of fixed charges.

For simplicity, we consider a solution that only contains three types of ions: the hydrogel ion H⁺, the co-ion, and the counterion. We assume that the co-ion and the counterion have valences 1 and -1, respectively, and they do not participate in any chemical reaction. Let C^{H+}, C⁺ and C⁻ be the nominal concentrations of the three species, and C^{A-} be the nominal concentration of conjugate bases A⁻, i.e. the fixed-charge concentration. The total charge per unit reference volume of the gel, Eq. (6.37), is now specialized to

$$Q = q + e(C^{H+} + C^+ - C^- - C^{A-}). \quad (6.69)$$

As a special type of polyelectrolyte gel, the pH-sensitive gel satisfies all field equations in Section 6.5, except the conservation law of hydrogen ions. Accounting for the H⁺ generation in reaction Eq. (6.68), we can rewrite the conservation law, Eq. (6.42), as

$$\dot{C}^{H+} = \dot{C}^{A-} + r^{H+} - \nabla \cdot \mathbf{J}^{H+}. \quad (6.70)$$

During reaction, the sum of the number of the associated acidic groups AH and that of the fixed charges A^- is conserved:

$$C^{AH} + C^{A^-} = C_0, \quad (6.71)$$

where C_0 is the number of acidic groups on the network per unit volume in the reference state. Since the co-ions and counterions do not participate in any chemical reaction, their concentrations still follow the conservation law in Eq. (6.42).

Subject to the reversible chemical reaction, Eq. (6.68), the state of a volume element of pH-sensitive gel depends not only on the concentrations of mobile species, but also on the fixed-charge concentration C^{A^-} , which is an indicator of the level of dissociation. We stipulate that the Helmholtz free energy of the gel per unit volume in the reference state is

$$W = W(\mathbf{F}, \tilde{\mathbf{D}}, C^s, C^{H+}, C^+, C^-, C^{A^-}). \quad (6.72)$$

Substituting Eqs. (6.69) — (6.72) into the thermodynamic inequality, Eq. (6.41), and applying the divergence theorem, we obtain that

$$\begin{aligned} & \int (\nabla \cdot \mathbf{P}^T + \mathbf{b}) \cdot \dot{\mathbf{x}} dV + \int [\mathbf{t} - (\mathbf{P}^+ - \mathbf{P}^-) \cdot \mathbf{N}] \cdot \dot{\mathbf{x}} dA \\ & + \sum_a \int \left(\frac{\partial W}{\partial C^a} + ez^a \Phi - \mu^a \right) \dot{C}^a dV - \sum_a \int \nabla \mu^a \cdot \mathbf{J}^a dV. \quad (6.73) \\ & + \int \left(\frac{\partial W}{\partial \tilde{\mathbf{D}}} - \tilde{\mathbf{E}} \right) \cdot \dot{\tilde{\mathbf{D}}} dV + \int \left(\frac{\partial W}{\partial C^{A^-}} - e\Phi + \mu^{H+} \right) \dot{C}^{A^-} dV \geq 0. \end{aligned}$$

Similar to Eq. (6.44), the summations are taken over all mobile species, including the solvent molecules and all mobile ions. The only difference between Eq. (6.73) and Eq. (6.44) lies on the last term, which is associated with the change in the fixed-charge density. If we still assume the kinetic process to be diffusion-limited, and insist that all terms except the fourth vanish, Eq. (6.73) will give rise to the equation,

$$\frac{\partial W}{\partial C^{A^-}} = e\Phi - \mu^{H+} = -\frac{\partial W}{\partial C^{H+}}, \quad (6.74)$$

in addition to all equations of partial equilibrium in Section 6.5, Eqs. (6.45) — (6.48). Eq. (6.74) physically represents the local equilibrium of the chemical reaction, indicating that the chemical reaction is much faster than the diffusion process of mobile species, and the energy dissipation involved in the reaction is negligible. With the addition of Eq. (6.74), the concentration field of the fixed-charge density, $C^{A^-}(\mathbf{X}, t)$, can be determined together with other fields.

Now we will introduce a specific free-energy function for the pH-sensitive polyelectrolyte gel. Starting from Eq. (6.51), we account for the contribution of the dissociation reaction by adding a term, W_d , to the free-energy function:

$$W = W_s + W_m + W_i + W_p + W_d. \quad (6.75)$$

Following Marcombe et al. (2010), we model the dissociation of the acidic groups in analogy with the model of regular solution. The Helmholtz free energy due to dissociation is taken to be

$$W_d = kT \left(C^{A^-} \ln \frac{C^{A^-}}{C_0} + C^{AH} \ln \frac{C^{AH}}{C_0} \right) + \gamma C^{A^-}. \quad (6.76)$$

This expression consists of both the entropy of dissociation and the enthalpy of dissociation, where γ is the increase in the enthalpy when an acidic group dissociates. Note that C^{AH} is not among the independent variables of the free-energy function Eq. (6.72). Using Eq. (6.71), however, we can express it in terms of the fixed-charge concentration, $C^{AH} = C_0 - C^{A^-}$.

Substituting Eqs. (6.75) and (6.76) into Eq. (6.74), we arrive at the local equilibrium condition for the fixed-charge concentration:

$$kT \ln \frac{C^{A^-}}{C_0 - C^{A^-}} + \gamma = -kT \ln \frac{C^{H^+}}{C^s \varsigma_0^{H^+}} - v^{H^+} \Pi. \quad (6.77)$$

Neglecting the excessive volume of hydrogen ion v^{H^+} , we can further write Eq. (6.77) into a more familiar form

$$\frac{\varsigma^{A^-} \varsigma^{H^+}}{\varsigma^{AH}} = \varsigma_0^{H^+} \exp \left(-\frac{\gamma}{kT} \right), \quad (6.78)$$

where ς^{A^-} , ς^{H^+} , and ς^{AH} are the molar fractions of the corresponding species (e.g. $\varsigma^{H^+} = C^{H^+}/C^s$). The right-hand side of Eq. (6.78) is related to a commonly used concept, the *equilibrium constant* K_c , as $K_c = \varsigma_0^{H^+}/v^s \exp(-\gamma/kT)$. It can be seen that when the contribution of a chemical reactions needs to be accounted for, the choice of the reference for the chemical potential of a reactant is no longer arbitrary. Here for Eq. (6.78) to be valid, the reference concentration $\varsigma_0^{H^+}/v^s$ must equal the equilibrium constant K_c at the high-temperature limit ($1/T \rightarrow 0$).

The model of a pH-sensitive gel considered in this section assumes that the co-ions and counterions do not participate in any chemical reaction. As a result, the functional form of the chemical potentials and kinetic relations remain the same as the nonreactive model described in Sections 6.6, Eqs. (6.60) and (6.67). The results may not be used in systems containing reactive co-ions or counterions, e.g. when the gel is immersed in a basis in which the

association between hydrogen ions and hydroxide ions needs to be accounted for. Nevertheless, the general approach of modeling chemical reactions inside a gel may still be applicable to those systems by modifying the corresponding conservation laws. The detailed description on more complex models, however, is beyond the scope of this chapter.

6.8 Equilibrium models of polymeric gels

Due to mathematical complexity, the dynamic models described in the previous sections may only be solved numerically. For example, on numerical implementations, one may refer to the related scientific papers by Nemat-Nasser and Li^[35], De et al.^[33], Baek and Srinivasa^[29], Dolbow et al.^[36], Li et al.^[34], Swaminathan et al.^[37], and many others. A detailed numerical model usually assumes or implies a combination of the free-energy function and kinetic laws. Many numerical models utilize at least partly the simple material models shown in Sections 6.3, 6.6, and 6.7, and many use special material models that represent the behavior of specific materials. Some models are written in the reference configuration, and some others are represented in the current configuration or even in an Euler description. Nevertheless, all models at least agree with the general rules of nonequilibrium thermodynamics as shown in Sections 6.2 and 6.5.

In this section, we will focus on the behavior of a polymeric gel in a long-term limit, namely, the state in which the gel is in thermodynamic equilibrium with mechanical, electrical, and chemical loads. In the absence of electromechanical load or geometric constraint, a homogeneous and isotropic polymer network equilibrates with a liquid solution by a homogeneous and isotropic deformation, which is often referred to as *free swelling*. Such free swelling, however, rarely occurs in practice. Inhomogeneous but equilibrium states occur, for example, when the network itself is modulated^[38-40], or the network is subject to a load or constraint^[41,42]. The swelling of a gel is sometimes modeled by prescribing a constant volumetric strain. This practice is erroneous when swelling is anisotropic or inhomogeneous. Since a swollen gel is highly compressible, the volumetric strain (or the swelling ratio) depends on the local stress state and in general can be inhomogeneous. As will be shown, the volumetric strain should not be prescribed, but rather solved as a part of the boundary-value problem.

In a thermodynamic equilibrium state, the total free energy of the system is minimized, so that the equal sign in Eq. (6.8) for a neutral gel (or Eq. (6.44) for a polyelectrolyte gel) should hold, and all integrands must vanish. Consequently, the chemical potential μ^a of each mobile species, such as the

solvent and the mobile ions in the case of polyelectrolyte, is homogeneous throughout the gel and in the external solution. For a polyelectrolyte gel, we will neglect the electric field inside the gel and assume electroneutrality to further simplify the equilibrium field theory. As an ionic conductor, the major part of a gel or the external solution is nearly neutral, except the region near the interface between dissimilar materials, such as the gel-solution interface. In equilibrium, an electric double layer of a thickness scaled with the Debye length forms on the interface^[18]. The electric field in a double layer decays exponentially and vanishes deep inside the gel or the solution. In many applications, the Debye length is much smaller than other lengths of interest. Therefore, in this section, we will neglect the effect of the electric double layer, and assume the gel to be electroneutral. Under such an assumption, the electric potential Φ inside the gel is homogeneous, but may still be different from that in the solution or in another gel of dissimilar property.

Now let us construct another free-energy function \hat{W} through a Legendre transformation:

$$\hat{W} = W(\mathbf{F}, C^1, C^2, \dots) - \sum_a (\mu^a - ez^a \Phi) C^a. \quad (6.79)$$

Once a functional form of W is specified, Eq. (6.47) becomes a set of algebraic equations, and we can express the concentration of one mobile species C^a in terms of the deformation gradient \mathbf{F} and the chemical potential of all mobile species in the external solution μ^a . Consequently, Eq. (6.79) defines \hat{W} as a function of the deformation gradient and the chemical potential of mobile species, $\hat{W}(\mathbf{F}, \mu^1, \mu^2, \dots)$. Substituting Eq. (6.79) into (6.41) and considering the electroneutrality, we have, in equilibrium:

$$\int \delta \hat{W} dV = \int \mathbf{b} \cdot \delta \mathbf{x} dV + \int \mathbf{t} \cdot \delta \mathbf{x} dA. \quad (6.80)$$

With the aid of the new free-energy function, Eq. (6.80) takes the same form as the equilibrium condition for a hyperelastic solid. Once the material-dependent function $\hat{W}(\mathbf{F}, \mu^1, \mu^2, \dots)$ is specified, we can readily implement a finite-element method for the gel just like a regular hyperelastic solid. As noted above, the equilibrium chemical potentials of mobile species inside the gel are homogeneous and are equal to those in the external solution, μ^a . Indeed, the chemical potentials play a role analogous to that of temperature in an equilibrium thermal expansion problem. The equilibrium condition for a neutral gel is identical to Eq. (6.80), only that one mobile species, the solvent, is present.

Some finite-element software, such as SIMULIA Abaqus and COMSOL Multiphysics, allows users to program special free-energy functions while utilizing the existing computational platform for hyperelastic materials.

Here as an example, we will construct an equilibrium model based on the specific free-energy function for the pH-sensitive gel described in Section 6.7. In the absence of electric field, subject to the Legendre transform Eq. (6.79), the free-energy function prescribed by Eqs. (6.53), (6.54), (6.56), (6.75), and (6.76) gives rise to

$$\begin{aligned}\hat{W} = NkT \left(\frac{1}{2} \mathbf{F} : \mathbf{F} - \ln J - 1 \right) + \frac{kT}{v^s} \left[(J-1) \ln \frac{J-1}{J} - \frac{\chi}{J} \right] \\ - \frac{\mu^s}{kT} (J-1) - kT(C^+ + C^- + C^{H+}) \\ + kT \left[C^{A-} \ln \frac{C^{A-}}{C_0} + (C_0 - C^{A-}) \ln \frac{C_0 - C^{A-}}{C_0} \right] + \gamma C^{A-},\end{aligned}\quad (6.81)$$

where $J = \det \mathbf{F}$. The concentration of dissociated fixed charges C^{A-} is related to that of hydrogen ions by Eq. (6.77) or (6.78), or more explicitly

$$C^{A-} = C_0 \left[1 + \frac{K_C}{C^{H+}} (J-1) \right]^{-1}. \quad (6.82)$$

The concentrations of mobile ions are related to their chemical potentials by Eq. (6.60), and when the excessive volume of ions is neglected,

$$C^\pm = (J-1) \frac{\varsigma_0^\pm}{v^s} \exp \left(\mp \frac{e\Phi}{kT} \right), \quad C^{H+} = (J-1) \frac{\varsigma_0^{H+}}{v^s} \exp \left(- \frac{e\Phi}{kT} \right). \quad (6.83)$$

Here, the molar fractions of ions in the external solution, ς_0^\pm and ς_0^{H+} , are taken to be the references for the corresponding chemical potentials, i.e. the chemical potentials of ions are set to be 0 in the grounded external solution. The equilibrium electric potential in the gel, Φ , is uniform but unknown. One may cancel Φ from Eq. (6.83) and arrive at the following Donnan equations:

$$\frac{C^+}{\varsigma_0^+} = \frac{C^{H+}}{\varsigma_0^{H+}}, \quad \frac{C^-}{\varsigma_0^-} = \left(\frac{C^{H+}}{\varsigma_0^{H+}} \right)^{-1}. \quad (6.84)$$

For solvent molecules, on the other hand, the chemical potential in the external solution is given by

$$\mu^s = - \frac{kT}{J-1} 2(\varsigma_0^+ + \varsigma_0^{H+}). \quad (6.85)$$

In agreement with the chemical potential in the gel, Eq. (6.59), we have taken pure solvent to be the reference in Eq. (6.85). The condition for electroneutrality in the external solution, $\varsigma_0^+ + \varsigma_0^{H+} + \varsigma_0^- = 0$, is also used.

At any deformation state, the equilibrium ion concentrations in the gel, C^+ , C^- , C^{H+} , and C^{A-} can be determined by solving the nonlinear algebraic

systems (Eq. (6.82) and Eq. (6.84)), together with the neutrality condition in the gel.

$$C^+ + C^{H+} - C^- - C^{A-} = 0. \quad (6.86)$$

The resulting ion concentrations can be expressed in terms of J , ζ_0^+ , and ζ_0^{H+} . Consequently, \hat{W} can be expressed as a function of the following independent variables:

$$\hat{W} = \hat{W}(\mathbf{F}, \zeta_0^+, \zeta_0^{H+}). \quad (6.87)$$

It is assumed that the composition of the external solution, ζ_0^+ , and ζ_0^{H+} , remains unchanged when the mechanical forces do work, so that the variation in the free energy \hat{W} is due entirely to the variation of the deformation gradient. The concentrations of counterions and hydrogen ions serve as known parameters to the problem.

This procedure is coded into a user-defined subroutine for hyperelastic materials (UHYPER) in Abaqus^[43], and then used to calculate the example of a composite gel beam. As shown in Fig. 6.6 a, two strips of pH-sensitive gels with different molar fractions of dissociable ionic groups are bounded, forming a composite beam. The beam is assembled under an environment with $pH = -\log_{10}(\zeta_0^{H+}/v^s) = 5$, and counterion fraction $\zeta_0^+ = 1 \times 10^{-4}$. The external pH value is then varied while the counterion concentration is kept constant. Both strips swell when pH value of the solution increases. Due to

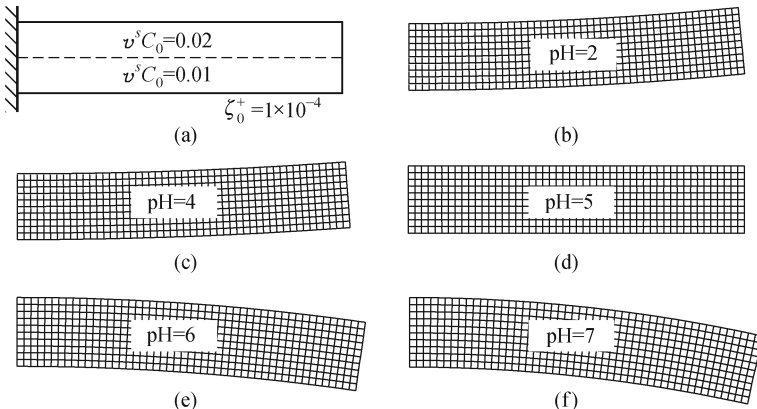


Fig. 6.6 (a) Sketch of the numerical model – a composite beam of two pH-sensitive gels. The two gel strips have different fractions of dissociable acidic groups on polymer networks, and are bonded together at a reference of pH = 5. (b) and (c) When the pH value of the external solution is lower than the reference, both strips shrink, but the top strip shrinks more significantly, causing the composite beam to bend upwards. (d) When pH = 5 at the external solution, the composite beam retracts and recovers the reference state. (e) and (f) When the external solution is less acidic than the reference, both strips swell, but the top strip expands more so that the beam bends downwards.

the difference in the availability of acidic groups, the top strip contains more fixed charge after dissociation. As a result, the composite beam bends back and forth depending on the acidity of the external solution. The deformed meshes under various pH values are plotted in Fig. 6.6 b—f.

In the numerical calculations, we take the dimensionless combinations of parameters. Since the design of the structure does not require very large deformation, we select a relatively stiff polymer network with dimensionless stiffness $Nv^s = 0.01$. If we assume the volume per solvent molecule to be $v^s = 10^{-28} \text{ m}^3$, this dimensionless value corresponds to a modulus of $\sim 0.4 \text{ MPa}$. The material parameter χ is taken to be 0.1. The equilibrium constant of acidic dissociation, K_c , has the same dimension as the concentration. We set $pK_c = -\log_{10}(K_c) = 4.3$, a commonly used value for the dissociation of carboxylic acids.

This example is used for demonstrative purpose, instead of a functional design of an active device. For higher pH sensitivity, one may construct a composite beam from one gel with dissociable acidic groups and the other with dissociable basic groups, so that the two strips will act in different directions and thus enhance the bending motion. Similar devices, consisting of an integrated structure of stimuli-sensitive gels and rigid parts or gels of different types as constraints, can be used as multifunctional actuators or sensors. The theoretical framework presented in this chapter may help qualitative understanding of the mechanisms, as well as serving as the basis of numerical tools for quantitative predictions.

6.9 Summary

This chapter reviews the recent development of continuum models for stimuli-responsive gels. The theoretical framework is derived from thermodynamic principals and is applicable to a wide range of similar materials that have large deformation, mass transportation and multi-physics coupling behavior. Several examples of specific material models are presented, including those for neutral polymeric gels, polyelectrolyte gels, and pH-sensitive gels. The procedure of constructing the phenomenological material models may be extended and applied to the modeling of active gels that are responsive to other types of stimuli, such as heat, magnetic field, and light. The theory and models outlined in this chapter have successfully described many of the qualitative trends and phenomena observed in experiments^[43–47]. However, a quantitative comparison between the theoretical prediction and experimental results is difficult at the current stage for several reasons: the free-energy functions we select to highlight the essence of the theory may be over-simplified while

actual experiments use more complex systems such as copolymers and multi-ingredient solutions; existing experiments often report insufficient details and leave more parameters to fit. With the difficulties in mind, we only focus on illustrating the fundamentals of theories in this chapter and leave extensive comparisons to future work.

References

- [1] Li Y, Tanaka T. Phase transitions of gels. *Annu Rev Mater Sci*, 22: 243-277, 1992.
- [2] Osada Y, Gong J P. Soft and wet materials: polymer gels. *Adv Mater*, 10: 827-837, 1998.
- [3] Melody A S, Mark E F. Interstitial flow and its effects in soft tissues. *Annu Rev Biomed Eng*, 9: 229-256, 2007.
- [4] Zwieniecki M A, Melcher P J, Holbrook N M. Hydrogel control of xylem hydraulic resistance in plants. *Science*, 291: 1059-1062, 2001.
- [5] Hodge W A, Fijian R S, Carlson K L, et al. Contact pressures in the human hip joint measured in vivo. *Proc Natl Acad Sci USA*, 83: 2879-2883, 1986.
- [6] Lee K Y, Mooney D J. Hydrogels for tissue engineering. *Chem Rev*, 101: 1869-1879, 2001.
- [7] Duncan R. The dawning era of polymer therapeutics. *Nat Rev Drug Discov*, 2: 347-360, 2003.
- [8] Lee Y J, Braun P V. Tunable inverse opal hydrogel pH sensors. *Adv Mater*, 15: 563-566, 2003.
- [9] Richter A, Paschew G, Klatt S, et al. Review on hydrogel-based pH sensors and microsensors. *Sensors*, 8: 561-581, 2008.
- [10] Beebe D J, Moore J S, Bauer J M, et al. Functional hydrogel structures for autonomous flow control inside microfluidic channels. *Nature*, 404: 588-590, 2000.
- [11] Dong L, Agarwal A K, Beebe D J, et al. Adaptive liquid microlenses activated by stimuli-responsive hydrogels. *Nature*, 442: 551-554, 2006.
- [12] Carpi F, Smela E. Biomedical Applications of Electroactive Polymer Actuators. Wiley, UK, 2009.
- [13] Gibbs J W. On the equilibrium of heterogeneous substances. In: The Scientific Papers of J. Willard Gibbs. Longmans, Green, and Co., London, 1878.
- [14] Flory P J, Rehner J. Statistical mechanics of cross-linked polymer networks II: Swelling. *J Chem Phys*, 11: 521-526, 1943.
- [15] Biot M A. General theory of three-dimensional consolidation. *J Appl Phys*, 12: 155-164, 1941.
- [16] Hong W, Zhao X, Zhou J, et al. A theory of coupled diffusion and large deformation in polymeric gels. *J. Mech. Phy. Solids*, 56: 1779-1793, 2008.
- [17] Hong W, Liu Z, Suo Z. Inhomogeneous swelling of a gel in equilibrium with a solvent and mechanical load. *I J Solids Struct*, 46: 3282-3289, 2009.
- [18] Hong W, Zhao X, Suo Z. Large deformation and electrochemistry of polyelectrolyte gels. *J. Mech. Phys. Solids*, 58: 558-577, 2010.
- [19] Reese S, Govindjee S. A theory of finite viscoelasticity and numerical aspects. *Int J Solids Struct*, 35: 3455-3482, 1998.

- [20] Tanaka T, Hocker L, Benedek G B. Spectrum of light scattered from a viscoelastic gel. *J Chern Phys*, 59: 5151-5159, 1973.
- [21] Flory P J. Principles of Polymer Chemistry. Cornell University Press, Ithaca, NY, 467-470, 1953.
- [22] Boyce M C, Arruda E M. Constitutive models of rubber elasticity: A review. *Rubber Chem Technol*, 73: 504-523, 2000.
- [23] Marckmann G, Verron E. Comparison of hyperelastic models for rubberlike materials. *Rubber Chem Technol*, 79: 835-858, 2006.
- [24] Horkay F, McKenna, G B. Polymer networks and gels. In: Mark, J.E. ed. Physical Properties of Polymers Handbook. Springer, New York, 497-523, 2007.
- [25] Dorfmann A, Ogden R W. Nonlinear electroelasticity. *Acta Mechanica*, 174: 167-183, 2005.
- [26] Ricka J, Tanaka T. Swelling of ionic gels: Quantitative performance of the Donnan theory. *Macromolecules*, 17: 2916-2921, 1984.
- [27] Hooper H H, Baker J P, Blanch H W, et al. Swelling equilibria for positively ionized polyacrylamide hydrogels. *Macromolecules*, 23: 1096-1104, 1990.
- [28] Brannon-Peppas L, Peppas N A. Equilibrium swelling behavior of pH-sensitive hydrogels. *Chem Eng Sci*, 46: 715-722, 1991.
- [29] Baek S, Srinivasa A R. Modeling of the pH-sensitive behavior of an ionic gel in the presence of diffusion. *I J Non-linear Mech*, 39: 1301-1318, 2004.
- [30] Zhao X H, Hong W, Suo Z G. Electromechanical hysteresis and coexistent states in dielectric elastomers. *Phys Rev B*, 76: 134113, 2007.
- [31] Suo Z G, Zhao X H, Greene W H. A nonlinear field theory of deformable dielectrics. *J Mech Phys Solids*, 56: 467-486, 2008.
- [32] Lai W M, Hou J S, Mow V C. A triphasic theory for the swelling and deformation behaviors of articular-cartilage. *J Biomech Eng — Trans ASME*, 113: 245-258, 1991.
- [33] De S K, Aluru N R, Johnson B, et al. Equilibrium swelling and kinetics of pH-responsive hydrogels: Models, experiments, and simulations. *J Microelectromech Sys*, 11: 544-555, 2002.
- [34] Li H, Luo R, Lam K Y. Modeling and simulation of deformation of hydrogels responding to electric stimulus. *J Biomech*, 40: 1091-1098, 2007.
- [35] Nemat-Nasser S, Li J Y. Electromechanical response of ionic polymer-metal composites. *J Appl Phys*, 87: 3321-3331, 2000.
- [36] Dolbow J, Fried E, Ji H. A numerical strategy for investigating the kinetic response of stimulus-responsive hydrogels. *Comp Meth Appl Mech Eng*, 194: 42-44, 2005.
- [37] Swaminathan N, Qu J, Sun Y. An electrochemomechanical theory of defects in ionic solids, I: Theory. *Philos Mag*, 87: 1705-1721, 2007.
- [38] Hu Z B, Zhang X M, Li Y. Synthesis and application of modulated polymer gels. *Science*, 269: 525-527, 1995.
- [39] Klein Y, Efrati E, Sharon E. Shaping of elastic sheets by prescription of non-Euclidean metrices. *Science*, 315: 1116-1120, 2007.
- [40] Ladet S, David L, Domard A. Multi-membrane hydrogels. *Nature*, 452: 76-79, 2008.
- [41] Treloar L R G. The swelling of cross-linked amorphous polymers under strain. *Trans Faraday Soc*, 46: 783-789, 1950.
- [42] Kim S J, Spinks G M, Prosser S, et al. Surprising shrinkage of expanding gels under external load. *Nature Mater*, 5: 48-51, 2006.

- [43] Marcombe R, Cai S, Hong W, et al. A theory of constrained swelling of a pH-sensitive hydrogel. *Soft Matter*, 6: 784-793, 2010.
- [44] Hong W, Zhao X, Suo Z. Drying-induced bifurcation in a hydrogel-actuated nanostructure. *J Appl Phys*, 104: 084905, 2008.
- [45] Wang X, Hong W. Surface interactions between two like-charged polyelectrolyte gels. *Phys Rev E*, 81: 041803, 2010.
- [46] Hu Y, Zhao X, Vlassak J, et al. Using indentation to characterize the poroelasticity of gels. *Appl Phys Lett*, 96: 121904, 2010.
- [47] Cai S, Bertoldi K, Wang H, et al. Osmotic collapse of a void in an elastomer: Breathing, buckling and creasing. *Soft Matter*, doi: 10.1039/c0sm00451k, 2010.
- [48] Sidorenko A, Krupenkin T, Taylor A, et al. Reversible switching of hydrogel-actuated nanostructures into complex micropatterns. *Science*, 315:487-490.

Chapter 7 Micromechanics of 3D Crystallized Protein Structures

Amir Reza Zamiri and Suvranu De*

Advanced Computational Research Laboratory, Department of Mechanical, Aerospace and Nuclear Engineering, Rensselaer Polytechnic Institute, 110 8th St., Troy, NY 12180, United States

Abstract: In this chapter we develop micromechanics-based models of three-dimensional crystallized protein molecules with tetragonal lysozyme as an example system. While certain crystallographic directions exhibit purely elastic behavior, others exhibit elastoplastic response. The yield stress and critical resolved shear stress are observed to be sensitive to temperature and the amount of intracrystalline water. An increase in temperature and the amount of intracrystalline water molecules leads to a decrease in the critical resolved shear stress of the slip systems and makes the crystal softer. The analysis presented here may be applied to other protein crystal systems as well.

Keywords: 3D protein crystal, bionanoporous, micromechanics, crystal plasticity, model

7.1 Introduction

Advances in technology necessitate the development of new materials and systems with novel mechanical, physical and chemical properties. The bottom-up self-assembly strategy^[1] provides an excellent route to deliver such new materials. Self-assembly allows building matter up from individual atoms, molecules and molecular building blocks through hierachal organization and provides control of the material properties right at the molecular scale.

Nature provides perfect examples of self-assembled materials based on molecular building blocks such as nucleic acids, polysaccharides and lipids which are organized into efficient multifunctional structures and systems ranging from the nanoscopic to the macroscopic scales. Therefore, one of the main efforts in the area of biologically inspired technology is to understand the mechanisms that nature uses to construct structures with inter-

esting properties. Such knowledge will help to develop biomimetic materials and devices for a range of engineering and medical applications including regenerative medicine, electronic materials, biotechnology, nanotechnology and drug delivery. Among all biomolecular units, nucleic acids and peptides have been the subjects of most intense research.

Nucleic acid units, especially DNA, have attracted a significant attention in self-assembly of nanostructures for a range of applications including nanoelectronics, biosensing, and computation which relies only on the base-pairing properties of the DNA duplex. A surprisingly large number of structures ranging from tetrahedron, octahedron, cube, buckyball, dodecahedron to astonishing two-dimensional lattices may be obtained through DNA self-assembly^[2-4].

However, in nature, proteins are used as the primary building units of biological structures as they are composed of 20 different amino acids in comparison to 4 nucleotides in DNA. This variety in the amino acids leads to a range of different properties in charge, hydrophobicity, interactions, chemical reactivity and functionality. Peptides and proteins have not hitherto been considered as useful building blocks in materials technology. However, recent advances in genetic and protein engineering have changed this view. Currently, research is underway that focuses on better understanding and developing approaches to construct 1D, 2D and 3D protein structures and systems such as collagen, keratin, elastin, tubulin, fibroin, enzyme and biomembranes for a range of applications including regenerative medicine, drug delivery and surface engineering^[5-24].

It is now well known that a combination of mechanical, chemical and biological factors is responsible for molecular self-assembly^[25]. Besides, novel applications of such assembled materials and structures require physical, chemical and biological design parameters to be multiplexed to ensure optimal physico-chemical performance. Therefore, substantial work is necessary to map the dependence of such biological, chemical, and mechanical factors to develop self-assembled structures with optimal properties. In this chapter we will focus on the mechanics of 3D crystallized proteins as a class of such self-assembled materials.

7.2 3D crystallized protein structures

3D crystallized protein structures are obtained as a result of molecular self-assembly of protein molecules into highly ordered 3D structures. In the past, the main goal of protein crystallization was to explore the structure of protein molecules using X-ray and electron microscopy^[26]. Recently, protein crys-

tals have emerged as promising bionanoporous materials for different applications including highly selective biocatalysis, biosensing, bioseparation, vaccine formulation, and drug delivery^[26-28]. Over the past decade, significant research and development efforts have been focused on engineering protein crystals, efficacy testing, model development, and production and characterization^[29-32]. These advances have led to new therapeutic applications of protein crystals, which now include treatments in acute conditions such as cancer, cardiovascular disease, viral disease and chronic conditions such as diabetes, growth hormone deficiency, haemophilia, arthritis, psoriasis and Crohn's disease. As proteins are relatively large molecules, the 3D crystal is a mesoporous material and if the protein molecules in the lattice are enzymes, they can be also used as catalysts for bio-sensing and separation.

Despite these successes, many challenges remain such as the characterization of protein crystals including stability. The functionality and stability of protein molecules are largely dependent on the environmental working conditions such as temperature, pH and the surrounding fluid. Several studies have been undertaken on thermal and chemical stability of protein crystals^[33-35] to understand such effects. However, the mechanical stability of protein crystals under different conditions has not been extensively studied. Therefore, to explore the fundamental design principles for development of such materials with optimal functionality and stability, further research is needed.

7.3 Thermomechanical properties of protein crystals

Based upon indentation analysis, protein crystals are relatively fragile and soft materials and their mechanical properties are highly sensitive to both environmental conditions and the type of the protein molecule^[36]. Indentation and compression analysis of 3D crystallized form of the tetragonal lysozyme protein have revealed that its mechanical properties are size-dependent^[36-37]. Compression testing of crystal leads to nonlinear elastic deformation leading to fracture whereas during microindentation, the microcrystals exhibit elastic-plastic deformation. The temperature and amount of intracrystalline water have significant effects on the elastic and plastic properties of the crystals. At lower temperature and water content, the crystal is more brittle while it is more ductile at higher temperature and humidity^[37]. The plastic deformation at the microscale has been established due to crystalline slip.

7.4 A micromechanical model for protein crystals

Based on the knowledge that crystalline slip is a major cause of the plastic deformation in protein crystals, a micromechanical model has been developed to predict the mechanical behavior of such materials^[38]. In this model the effects of the temperature and water molecules on the mechanical behavior of the protein crystals are expressed by their effects on the slip resistance. To explain the model, let us consider Fig. 7.1 which shows the 3D assembled structure of a tetragonal lysozyme protein crystal. In such crystals there are specific molecular planes such as (110) which have the greatest separation and therefore, may glide to each other under external loads.

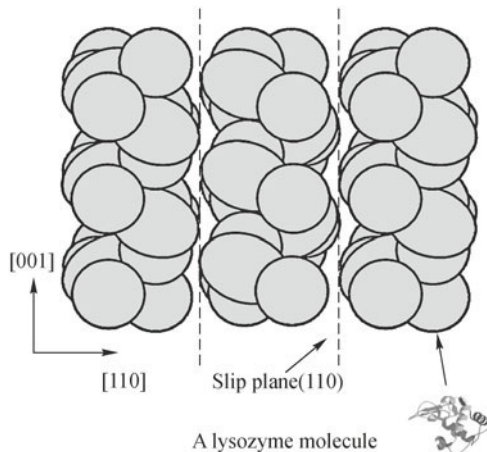


Fig. 7.1 A 3D crystallized structure of a tetragonal lysozyme crystal (protein molecule is from PDB code: 133L)^[45]. (color plot at the end of the book)

The average velocities of dislocations on a slip system α may be expressed generally as^[39]:

$$\bar{v}^\alpha = v_0^\alpha f_p(\tau^\alpha, \chi) \quad (7.1)$$

where v_0^α is the limiting velocity, f_p a probability function, τ^α the resolved shear stress on slip system α , and χ a vector containing state variables such as temperature. It has been shown that for most materials the probability function satisfies a power law expression:

$$f_p(\tau^\alpha, \chi) = K \operatorname{sgn}(\tau^\alpha) \left(\frac{\tau^\alpha}{\tau_y^\alpha} \right)^{2n-1} \quad (7.2)$$

where K and n are material constants and τ_y^α is the critical resolved shear stress of the slip system α . The rate of shear strain on a slip system α is:

$$\dot{\gamma}^\alpha = \phi^\alpha \rho^\alpha b^\alpha \bar{v}^\alpha \quad (7.3)$$

where ϕ^α is a material parameter, ρ^α is the dislocation density, and b^α is the Burgers vector. Combining Eqs. (7.1)–(7.3) one obtains:

$$\dot{\gamma}^\alpha = \kappa \operatorname{sgn}(\tau^\alpha) \left(\frac{\tau^\alpha}{\tau_y^\alpha} \right)^{2n-1} \quad (7.4)$$

where κ is a parameter which is a function of K , ϕ^α , ρ^α , and b^α .

Let \mathbf{m} be a unit vector normal to the slip plane and \mathbf{s} a unit vector in the slip direction in the crystal coordinate system. Then, any slip system can be defined by an orientation matrix

$$\mathbf{I}^\alpha = \mathbf{s}^\alpha \otimes \mathbf{m}^\alpha \quad (7.5)$$

with symmetric and antisymmetric parts

$$\mathbf{P}^\alpha = \frac{1}{2}(\mathbf{I}^\alpha + \mathbf{I}^{\alpha T}), \quad (7.6)$$

$$\mathbf{w}^\alpha = \frac{1}{2}(\mathbf{I}^\alpha - \mathbf{I}^{\alpha T}) \quad (7.7)$$

which define the plastic rate of deformation \mathbf{D}^p and spin rate $\boldsymbol{\Omega}^p$ as:

$$\mathbf{D}^p = \sum_{\alpha=1}^N \dot{\gamma}^\alpha \cdot \mathbf{P}^\alpha, \quad (7.8)$$

$$\boldsymbol{\Omega}^p = \sum_{\alpha=1}^N \dot{\gamma}^\alpha \cdot \mathbf{w}^\alpha \quad (7.9)$$

where N is the number of slip systems in the crystal.

According to the normality rule in plasticity, a yield function $F(\sigma, \chi)$ could be defined so that

$$\mathbf{D}^p = \lambda \frac{\partial F(\sigma, \chi)}{\partial \sigma} \quad (7.10)$$

where λ is a positive parameter which depends on the type of dislocation barriers and needs to be computed numerically. Replacing $\dot{\gamma}^\alpha$ in Eq. (7.8) from Eq. (7.9) and solving the differential equation (7.10), a yield surface for protein crystals can be defined as:

$$F(\sigma, \chi) = \frac{1}{2n} \left(\sum_{\alpha=1}^N \left| \frac{\sigma : \mathbf{P}^\alpha}{\tau_y^\alpha} \right|^{2n} - 1 \right) \quad (7.11)$$

where $\tau^\alpha = \sigma : \mathbf{P}^\alpha$.

Equations (7.8)–(7.11) lead to the following expressions for plastic rates of the deformation and spin:

$$\mathbf{D}^p = \lambda \sum_{\alpha=1}^N \frac{\operatorname{sgn}(\tau^\alpha)}{\tau_y^\alpha} \left| \frac{\tau^\alpha}{\tau_y^\alpha} \right|^{2n-1} \cdot \mathbf{P}^\alpha, \quad (7.12)$$

$$\boldsymbol{\Omega}^p = \lambda \sum_{\alpha=1}^N \frac{\text{sgn}(\tau^\alpha)}{\tau_y^\alpha} \left| \frac{\tau^\alpha}{\tau_y^\alpha} \right|^{2n-1} \cdot \mathbf{w}^\alpha. \quad (7.13)$$

The effects of the temperature, water molecules, and other environmental effects on the deformation behavior of protein crystals are considered through their influences on the critical resolved shear stress τ_y^α .

7.5 Application to tetragonal lysozyme as a protein crystal model

A well studied protein is lysozyme which is an enzyme found in egg white, tear, saliva, mucus and other body fluids. As an enzyme, its main role is to lyse cell walls of gram positive bacteria. Since lysozyme can be easily crystallized, it is usually used as a good protein model in different studies. Lysozyme can be self-assembled into different crystal structures including orthorhombic, tetragonal, and monoclinic ones Fig. 7.2 shows a tetragonal lysozyme crystal obtained by self-assembly. The tetragonal lysozyme crystal (Fig. 7.1) belongs to the $P4_32_12$ space group with lattice constants of $a=b=7.91$ nm, $c=3.79$ nm, and $Z=8$ ^[37].

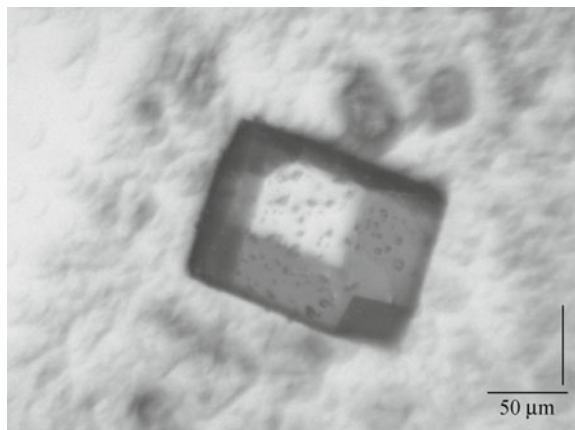


Fig. 7.2 A tetragonal lysozyme single crystal. (color plot at the end of the book)

7.5.1 Elastic deformation in lysozyme crystals

The elastic constants of tetragonal lysozyme crystal are highly sensitive to both temperature and humidity^[40-43]. The Young's modulus of lysozyme

crystal decreases with increasing temperature according to the following relationship^[40].

$$\Delta E = -C_T E_0 \Delta T \quad (7.14)$$

where ΔE and ΔT are increments in the Young's modulus and temperature, respectively, E_0 is the Young's modulus at 300 K and C_T is a constant equal to $2 \times 10^{-3} \text{ K}^{-1}$ for lysozyme crystals. The Young's modulus increases with the increasing amount of the intracrystalline water molecules^[38,41] as follows:

$$\Delta E = C_w E_0 \Delta t \quad (7.15)$$

where Δt is the evaporation time and C_w is a constant whose value depends on environmental parameters such as temperature. For natural evaporation of water from lysozyme crystal surface at room temperature, C_w was calculated to be 0.039 6 min⁻¹^[31].

7.5.2 Plastic deformation in lysozyme crystals

The tetragonal lysozyme crystal has two sets of slip systems^[40]; a primary $\{110\}\langle 001 \rangle$ systems and a secondary $\{110\}\langle 110 \rangle$ systems. Depending on the crystal orientation and environmental conditions, during the deformation the $\{110\}\langle 001 \rangle$ slip systems get activated first followed by the secondary slip systems at higher stresses. Using extensive simulations of microindentation to duplicate the indentation experimental data, the critical resolved shear stresses for these slip systems as a function of temperature and intracrystalline water molecule have been identified^[38]. In such simulations, a 3D cylindrical finite element model of the lysozyme crystal was used, which was fixed at the bottom surface. At any integration point of the finite element model, a lysozyme crystal whose (110) molecular plane is perpendicular to the axes of the cylindrical model was chosen. This model was then used to simulate the micro Vickers hardness tests along $[110]$ crystallographic direction to obtain the force and tip displacement curves at different temperatures and amounts of intracrystalline water. These simulations were used following an optimization procedure to determine the CRSS values for the different slip sets so that the Vickers hardnesses obtained from the simulations matched published experimental values.

Figure 7.3 shows the temperature dependency of the critical resolved shear stresses (CRSS) of tetragonal lysozyme crystals. Similar to other crystalline materials, plastic flow in lysozyme crystals occurs due to creation and motion of dislocations^[37]. At normal rates of deformation, thermal fluctuations provide the energy to carry the dislocations over the lattice potential barriers. Since the dislocations at higher temperatures have a higher probability

of overcoming lattice potential barriers due to higher thermal fluctuations, the CRSS for activation of the slip systems is lower. This explains why the CRSS decreases with increasing temperature for both slip systems, as shown in Fig. 7.3. At lower temperatures, the CRSS of the $\{110\}\langle 001 \rangle$ slip system is much less than the CRSS of the $\{110\}\langle 110 \rangle$ slip system, therefore, it can be more easily activated. At higher temperatures the CRSS of both slip sets is small and both can easily get activated. At temperatures below room temperature, the deformation in lysozyme crystal is primarily elastic while at higher temperatures it is elastic-plastic^[37]. Therefore, at lower temperatures the temperature variation of the CRSS is primarily due to the temperature dependence of the elastic constant. However, at higher temperatures, both the elastic constant and dislocation mechanisms are affected by temperature which results in a higher drop in CRSS with increasing temperature.

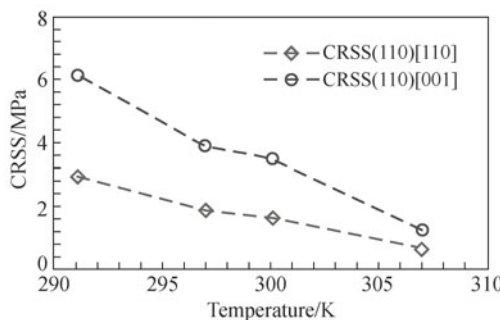


Fig. 7.3 The effect of temperature on critical resolved shear stresses of the tetragonal lysozyme crystal.

Due to their applications, protein crystals are usually in a fluid environment and therefore, have a significant amount of intercrystalline water. As shown in Fig. 7.4, the CRSS for both slip systems increases with evaporation time (decreasing the amount of intracrystalline water). A change in intracrystalline water changes both the lattice and elastic constants of protein crystals. A decrease in the amount of the intracrystalline water leads to an increase in elastic constants and a decrease in lattice parameters^[44]. This increases the self energy of the dislocations significantly and hinders their nucleation and activation, thereby increasing the CRSS of the slip systems.

The decrease in CRSS with increasing temperature (Fig. 7.3) may also be related to the water molecules. Two types of intracrystalline water may be present in the lattice: mobile water, which can easily traverse through the crystal and bounded water, which is more strongly bound to the molecules^[41,43]. Mobile water has a high diffusion coefficient at higher temperatures and therefore has little interaction with dislocations. However, at

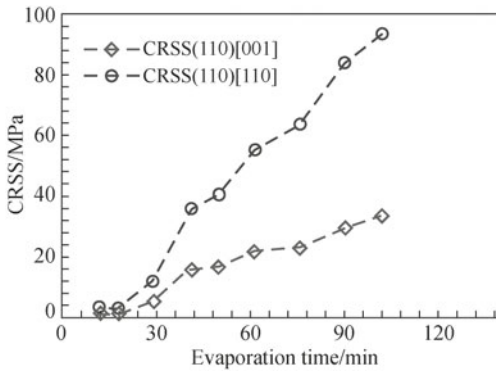
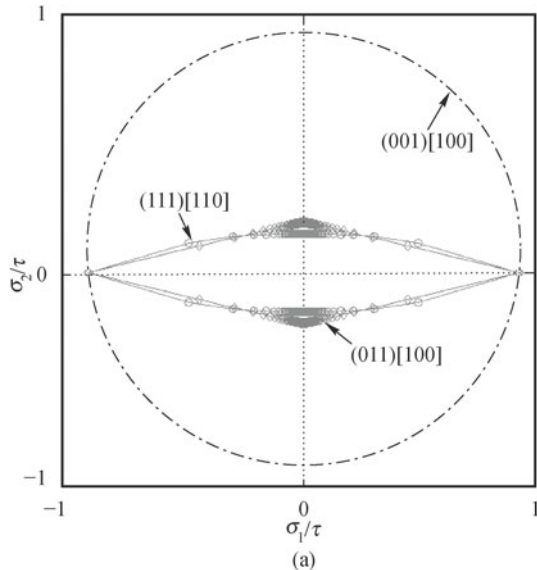


Fig. 7.4 The effect of the amount of intracrystalline water molecules on critical resolved shear stresses of slip systems in tetragonal lysozyme crystal.

lower temperatures it may interact with dislocations and thereby affect dislocation creation and motion in the lattice^[40].

7.5.3 Anisotropic plastic yielding of lysozyme crystals

Figure 7.5 shows the 2D plots of Eq. (7.11) for three different crystal orientations of tetragonal lysozyme at 285 K and 307 K. It is clear that the tetragonal lysozyme crystal is highly anisotropic and the shape of its yield surface changes with both temperature and crystal orientation. As discussed



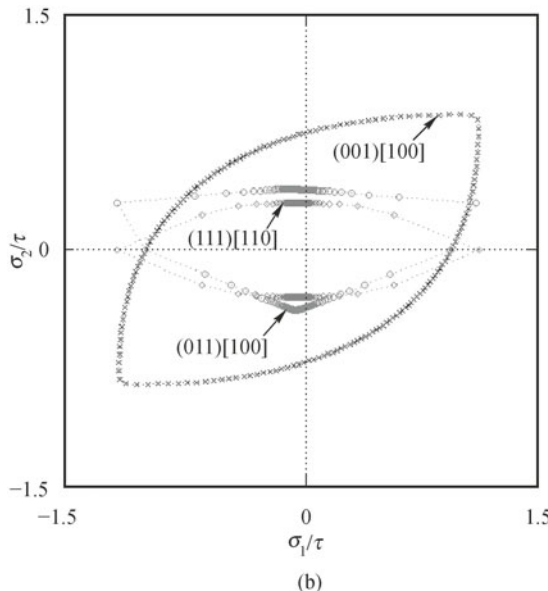


Fig. 7.5 The yield surface of the tetragonal lysozyme crystals for three different crystallographic orientations of (001)[100], (011)[100], and (111)[110] at two temperatures of (a) 285 K and (b) 307 K. (color plot at the end of the book)

before, at higher temperatures both $\{110\}\langle 110 \rangle$ and $\{110\}\langle 001 \rangle$ slip systems are activated during the deformation, therefore the materials are softer while at low temperature only the $\{110\}\langle 001 \rangle$ slip system can get activated and materials are more rigid. At room temperature, for lysozyme crystals that have a large amount of intracrystalline water both $\{110\}\langle 110 \rangle$ and $\{110\}\langle 001 \rangle$ slip systems are activated while at a smaller amount of intracrystalline water only the $\{110\}\langle 001 \rangle$ slip system can get activated.

7.5.4 Orientation effect on mechanical behavior of lysozyme crystals

The mechanical response of tetragonal lysozyme crystals is anisotropic, hence orientation dependent. Crystalline slip activity, damage initiation and propagation, and elastic properties of a crystal are functions of both the orientation of the crystal and external loads. The model developed here can be used to explore the mechanical response of the crystal under variations of both. For this purpose a uniaxial compression of the lysozyme crystals was carried out on a single brick element with sides of 1 mm and a load of 8 N applied along different crystallographic directions at a rate of 0.05 s^{-1} to explore the

anisotropic mechanical properties. Using Eq. (7.4), the overall accumulated slip $\bar{\gamma}$ in a crystal can be obtained by

$$\bar{\gamma} = \sum_{\alpha=1}^N \int_0^t |\dot{\gamma}^\alpha| dt \quad (7.16)$$

The accumulated slip $\bar{\gamma}$ can be used as a good measure for evaluation of the deformation propensity of a crystal having specific orientation with respect to the external loads. We will now transform to the fixed (or lab) coordinate system defined by three Euler angles based on the Bunge system in which the orientation of a crystal is defined by three angles as $\{\varphi_1, \phi, \varphi_2\}$ (φ_1 is the rotation about Z , ϕ is the rotation about X' , and φ_2 is the rotation about Z') (Fig. 7.6). The results of the simulation of the uniaxial compression responses of the tetragonal lysozyme crystal along different crystallographic directions at two different temperatures of 307 K and 285 K are shown in Fig. 7.7. The accumulated slip $\bar{\gamma}$, which is a measure of the ductility, is observed to be orientation and temperature dependent. There are some orientations in which the crystal shows maximum ductility while in some orientations it remains completely rigid. At lower temperatures, the crystal is less ductile.

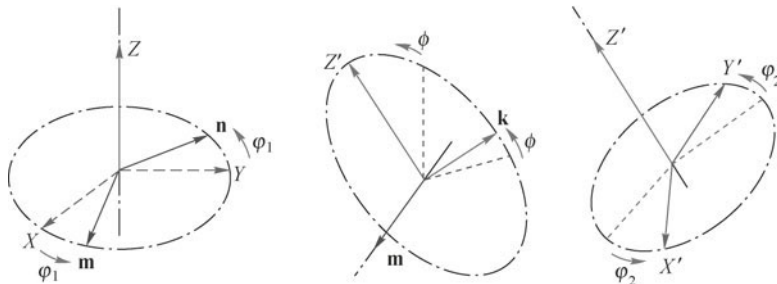


Fig. 7.6 Orientation of a crystal (X', Y', Z') with respect to the fixed coordinate system (X, Y, Z) based on Bunge Euler angles^[21].

Although such analyses provide important information about the ductility of the crystal, calculation of the accumulated slip $\bar{\gamma}$ for all possible orientations is computationally expensive. Therefore, for 3D assembled protein crystals, which have a relatively small plastic regime, for a given stress/strain tensor, Eq. (7.11) may be used directly to predict the nature of responses (elastic/plastic) for a particular crystal orientation. For a 3D protein crystal, a large positive value of f (Eq. 7.11) indicates a higher tendency of the crystal for crystalline slip and early fracture whereas a large negative value of f denotes greater mechanical structural integrity and propensity for elastic deformation. Using the value of f for different crystal orientations, the so-called deformation distribution maps (DDMs) for tetragonal lysozyme crystal

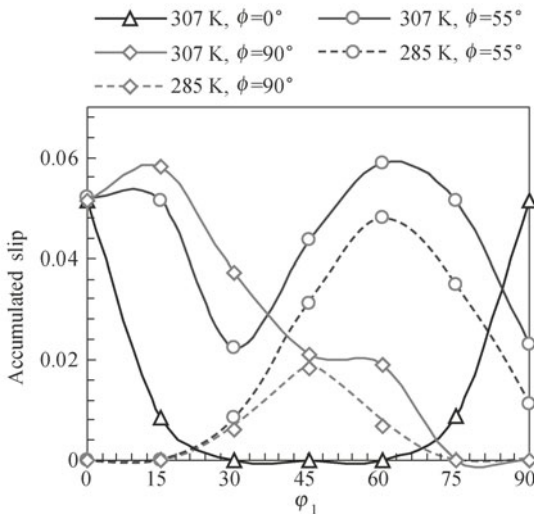


Fig. 7.7 The orientation dependent accumulated slip $\bar{\gamma}$ obtained for 3D lysozyme crystals loaded up to 0.01 strain at two different temperatures of 285 K and 307 K and Euler angles of $\phi = 0^\circ$, 55° , and 90° . In all these analyses, Euler angle $\varphi_2 = 0^\circ$. (color plot at the end of the book)

may be plotted. DDMs show the contours of f for different orientations corresponding to specific values of φ_2 . Figure 7.8 shows a plot of DDMs for all possible crystal orientations corresponding to $\varphi_2 = 0^\circ$, $\varphi_2 = 22.5^\circ$, and $\varphi_2 = 45^\circ$ when the crystal is compressed along X-axis of the lab coordinate system up to 0.01 strain at two different temperatures of 307 K and 285 K. Several local minima and maxima are observed in Fig. 7.8. Therefore, under uniaxial compression there are some orientations which are the softest and some others which are the hardest in terms of plastic deformability.

Crystal symmetry is also evident from the Figure. Because of this symmetry, it is sufficient to consider values of Euler angles that lie between $[0^\circ, 90^\circ]$. At temperatures close to 307 K there are more maxima on the DDMs. As the temperature decreases to 285 K the number of maxima also decreases. Further study of the DDMs reveals that at higher temperatures (Fig. 7.8a) all orientations that have their [100] or [010] crystallographic directions along the compression direction are rather soft. If the X-axis of the lab coordinate system is considered as the compression axis, then all such crystal orientations are placed on the so-called two “orientation fibers”: $[100]/X$ and $[010]/X$ corresponding to $\{\varphi_1 = 0, \phi, \varphi_2 = 0\}$ and $\{\varphi_1, \phi = 0, \varphi_2 = 90^\circ - \varphi_1\}$, respectively. There is another fiber which starts from $\{\varphi_1 = 60^\circ, \phi = 55^\circ, \varphi_2 = 0^\circ\}$ and passes through $\{\varphi_1 = 45^\circ, \phi = 90^\circ, \varphi_2 = 45^\circ\}$. There are two other fibers: $[110]/X$ corresponding to $\{\varphi_1 = 0^\circ, \phi, \varphi_2 = 45^\circ\}$ and $[001]/X$ cor-

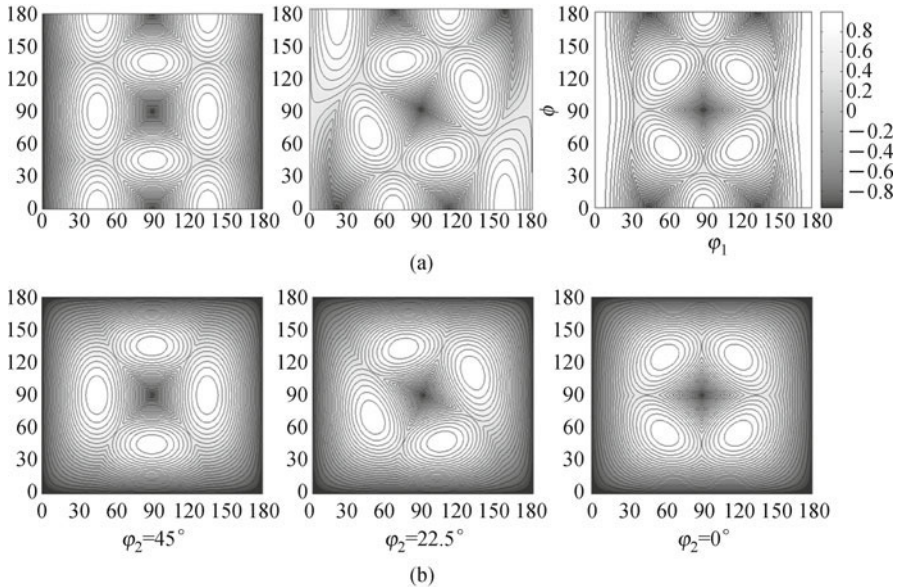


Fig. 7.8 The deformation distribution maps of the 3D assembled lysozyme crystal at two different temperatures of (a) 307 K and (b) 285 K and different values of φ_2 . For all orientations the uniaxial compression is along the X -axis of the lab coordinate system with compression up 0.01 strain. At any φ_2 section, the maps show the crystal orientations that have the highest and the lowest values of f (Eq. (7.11)) and therefore, the greatest tendency for plastic deformation and elastic deformation, respectively.

responding to $\{\varphi_1 = 90^\circ, \phi = 90^\circ, \varphi_2\}$ along which the crystal is rather hard.

At lower temperatures (Fig. 7.8b), there is only one orientation fiber, which starts from $\{\varphi_1 = 60^\circ, \phi = 55^\circ, \varphi_2 = 0^\circ\}$ and passes through $\{\varphi_1 = 45^\circ, \phi = 90^\circ, \varphi_2 = 45^\circ\}$, along which the crystal is soft. The crystal is rather hard along most other orientations. There are two orientation planes: $\{\varphi_1 = 0^\circ, \phi, \varphi_2\}$ and $\{\varphi_1, \phi = 0^\circ, \varphi_2\}$ on which the crystal is the hardest.

To summarize, the mechanical properties of 3D crystallized proteins such as tetragonal lysozyme crystal are highly anisotropic and the degree of anisotropy is a function of temperature and intracrystalline fluid molecules. At higher temperatures the crystals are very ductile while they are more rigid at lower temperatures. These observations provide valuable information regarding design of the structures, devices and systems using 3D crystallized protein materials. For example, if a catalyst made of lysozyme crystals is required to maintain structural integrity over a range of temperatures under compression, then the orientation of the crystal should be along the $\{\varphi_1 = 90^\circ, \phi = 90^\circ, \varphi_2\}$ fiber corresponding to which the crystal is rather hard at both lower and higher temperatures. The analysis presented here

could be easily used to explore the mechanical behavior of any 3D assembled protein crystal under different loading conditions. Multiscale modeling may be used to include effects of molecular flexibility at the lattice points.

References

- [1] Whitesides G M, Boncheva M. Beyond molecules: Self-assembly of mesoscopic and macroscopic components. *Proc Natl Acad Sci USA*, 99: 4769-4774, 2002.
- [2] He Y, Ye T, Su M, et al. Hierarchical self-assembly of DNA into symmetric supramolecular polyhedra. *Nature*, 452: 198-202, 2008.
- [3] Rothemund P W K. Folding DNA to create nanoscale shapes and patterns. *Nature*, 440: 2006.
- [4] Haney L, Carter J D, LaBean T H. Nanofabrication by DNA self-assembly. *Materialstoday*, 12: 24-32, 2009.
- [5] Petka W A, Harden J L, McGrath K P, et al. Reversible hydrogels from self-assembling artificial proteins. *Science*, 281: 389-392, 1998.
- [6] Holmes T C, Delacalle S, Su X, Rich A, et al. Extensive neurite outgrowth and active neuronal synapses on peptide scaffolds. *Proc Natl Acad Sci USA*, 97: 6728-6733, 2000.
- [7] Ghadiri M R, Tirrell D A. Chemistry at the crossroads. *Curr Opin Chem Biol*, 4: 661-662, 2000.
- [8] Fernandez-Lopez S, Kim H S, Choi E C, et al. Antibacterial agents based on the cyclic D, L-alphapeptide architecture. *Nature*, 412: 452-455, 2001.
- [9] Aggeli A, Nyrkova I A, Bell M, et al. Hierarchical self-assembly of chiral rodlike molecules as a model for peptide beta-sheet tapes, ribbons, fibrils, and fibers. *Proc Natl Acad Sci USA*, 98: 11857-11862, 2001.
- [10] Marini D M, Hwang W, Lauffenburger D A, et al. Left handed helical ribbon intermediates in the self-assembly of a beta-sheet peptide. *Nano Letters*, 2: 295-299, 2002.
- [11] Caplan M R, Moore P N, Zhang S, et al. Self-assembly of a beta-sheet protein governed by relief of electrostatic repulsion relative to van der Waals attraction. *Biomacromolecules*, 1: 627-631, 2000.
- [12] Vauthey S, Santoso S, Gong H, et al. Molecular self assembly of surfactant-like peptides to form nanotubes and nanovesicles. *Proc Natl Acad Sci USA*, 99: 5355-5360, 2002.
- [13] Santoso S, Hwang W, Hartman H, et al. Self-assembly of surfactant-like peptides with variable glycine tails to form nanotubes and nanovesicles. *Nano Letters*, 2: 687-691, 2002.
- [14] Marsh E N, DeGrado W F. Noncovalent self-assembly of a heterotetrameric diiron protein. *Proc Natl Acad Sci USA*, 99: 5150-5154, 2002.
- [15] Moffet D A, Case M A, House J C, et al. Carbon monoxide binding by *de novo* heme proteins derived from designed combinatorial libraries. *J Am Chem Soc*, 123: 2109-2115, 2001.
- [16] Nowak A P, Breedveld V, Pakstis L, et al. Rapidly recovering hydrogel scaffolds from selfassembling diblock copolyptide amphiphiles. *Nature*, 417: 424-428, 2002.
- [17] Whaley S R, English D S, Hu E L, et al. Selection of peptides with semiconductor binding specificity for directed nanocrystal assembly. *Nature*, 405: 665-668, 2000.

- [18] Lee S W, Mao C, Flynn C E, et al. Ordering of quantum dots using genetically engineered viruses. *Science*, 296: 892-895, 2002.
- [19] Hartgerink J D, Beniash E, Stupp S I. Self-assembly and mineralization of peptide-amphiphile nanofibers. *Science*, 294: 1684-1687, 2001.
- [20] Hartgerink J D, Beniash E, Stupp S I. Peptide-amphiphile nanofibers: a versatile scaffold for the preparation of self-assembling materials. *Proc Natl Acad Sci USA*, 99: 5133-5138, 2002.
- [21] Szela S, Avtges P, Valluzzi R, et al. Reduction-oxidation control of beta-sheet assembly in genetically engineered silk. *Biomacromolecules*, 1: 534-542, 2000.
- [22] Zhou Y, Wu S, Conticello V P. Genetically directed synthesis and spectroscopic analysis of a protein polymer derived from a flagelliform silk sequence. *Biomacromolecules*, 2: 111-125, 2001.
- [23] Zhou C Z, Confalonieri F, Jacquet M, et al. Silk fibroin: Structural implications of a remarkable amino acid sequence. *Proteins*, 44: 119-122, 2001.
- [24] Zhang S, Marini D M, Hwang W, et al. Design of nanostructured biological materials through self-assembly of peptides and proteins. *Current Opinion in Chemical Biology*, 6: 865-871, 2002.
- [25] Sarikaya M, tamerler C, Jen A Y, et al. Molecular biomimetics: Nanotechnology through biology. *Nature*, 2: 577-585, 2003.
- [26] Malek K. Solute transport in orthorhombic lysozyme crystals: A molecular simulation study. *Biotechnol. Lett.*, 29: 1865-1873, 2007.
- [27] Eddaoudi M, Kim J, Rosi N, et al. Systematic design of pore size and functionality in isoreticular MOFs and their application in methane storage. *Science*, 295: 469, 2002.
- [28] St Clair N, Shenoy B, Jacob J D, et al. Cross-linked proteins for vaccine delivery. *Proc. Natl. Acad. Sci. USA*, 96: 9469-9474, 1999.
- [29] Blundell T L, Jhoti H, Abell C. High-throughput crystallography for lead discovery in drug design. *Nat Rev Drug Discov*, 1: 45-54, 2003.
- [30] Vilenchik L Z, Griffith J P, St Clair N L, et al. Protein crystals as novel microporous materials. *J. Am. Chem. Soc.*, 120: 4290-4294, 1998.
- [31] Margolin A L, Navia M A. Protein crystals as novel catalytic materials. *Angew Chem Int Ed*, 40: 2204-2222, 2001.
- [32] Cvetkovic A, Picioreanu C, Straathof A J J, et al. Quantification of binary diffusion in protein crystals. *J. Phys. Chem. B*, 109: 10561-10566, 2005.
- [33] Daniel R M. The upper limits of enzyme thermal stability. *Enzyme and Microbial Technology*, 19: 74-79, 1996.
- [34] Pechenov S, Shenoy B, Yang M X, et al. Injectable controlled release formulations incorporating protein crystals. *Control Release*, 96: 149-158, 2004.
- [35] Margolin A L, Navia M A. Protein crystals as novel catalytic materials. *Angew. Chem., Int. Ed. Engl.*, 40: 2204-2222, 2001.
- [36] Tait S, White E T, Litster J D. Mechanical characterization of protein crystals. *Part. Part. Syst. Charact.*, 25: 266, 2008.
- [37] Tachibana M, Kobayashi Y, Shimazu T, et al. Growth and mechanical properties of lysozyme crystals. *Journal of Crystal Growth*, 198/199: 661-664, 1999.
- [38] Zamiri A, De S. Modeling the mechanical response of tetragonal lysozyme crystals. *Langmuir*, 26: 4251-4257, 2001.
- [39] Gilman J J. Micromechanics of Flow in Solids. McGraw-Hill, New York, 195, 1962.
- [40] Koizumi H, Tachibana M, Kawamoto H, et al. Temperature dependence of microhardness of tetragonal hen-egg-white lysozyme single crystals. *Philosophical Magazine*, 84: 2961-2968, 2004.

- [41] Koizumi H, Tachibana M, Kojima K. Elastic constants in tetragonal hen egg-white lysozyme crystals containing large amount of water. *Phys. Rev E*, 79: 061917, 2009.
- [42] Speziale S, Jiang F, Caylor C L, et al. Sound velocity and elasticity of tetragonal lysozyme crystals by Brillouin spectroscopy. *Biophys. J.*, 85: 3202, 2003.
- [43] Koizumi, H, Kawamoto, H, Tachibana M, et al. Effect of intracrystalline water on micro-Vickers hardness in tetragonal hen egg-white lysozyme single crystals. *J. Phys. D: Appl. Phys.*, 41: 074019, 2008.
- [44] Tachibana M, Koizumi H, Kojima K. Effect of intracrystalline water on longitudinal sound velocity in tetragonal hen-egg-white lysozyme crystals. *Phys. Rev. E*, 69: 051921, 2004.
- [45] Harata K, Muraki M, Jigami Y. Role of Arg115 in the catalytic action of human lysozyme: X-ray structure of His115 and Glu115 mutants. *J. Mol. Biol.*, 233: 524, 1993.

Chapter 8 Micromechanical Modeling of Three-dimensional Open-cell Foams

Ke Li^{1,*} and Xin-Lin Gao^{2,*}

¹*Department of Mechanical and Industrial Engineering, Southern Illinois University, Edwardsville, IL 62026-1805*

²*Department of Mechanical Engineering, Texas A&M University, College Station, TX 77843-3123*

Abstract: Two micromechanics models for three-dimensional (3-D) open-cell foams are presented. In the first model, an energy method based on Castigliano's second theorem is utilized. The analysis is performed on a tetrakaidecahedral unit cell, which is subjected to compression on its two opposite square faces. The thirty-six struts of the unit cell are treated as uniform slender beams undergoing linearly elastic deformations, and the twenty-four vertices as rigid joints. All three deformation mechanisms of the cell struts (i.e., stretching, shearing and bending) possible under the specified loading are incorporated, and four different strut cross section shapes (i.e., circle, square, equilateral triangle and Plateau border) are treated in a unified manner, unlike in earlier models. Two closed-form formulas for determining the effective Young's modulus and Poisson's ratio of open-cell foams are provided. These two formulas are derived by using the composite homogenization theory and contain more parameters than those included in existing models. The new formulas explicitly show that the elastic properties of the foam depend on the relative foam density, the shape and size of the strut cross section, and the Young's modulus and Poisson's ratio of the strut material. The predicted values of the effective Young's modulus and Poisson's ratio for carbon foams compare favorably with those based on existing models and experimental data.

In the second model, the Voronoi tessellation technique and the finite element method are used to investigate the microstructure-property relations of 3-D open-cell foams that have irregular cell shapes and non-uniform strut cross-sectional areas (SCSAs). Perturbations are introduced to a regular packing of seeds to generate a spatially periodic Voronoi diagram with different degrees of cell shape irregularity (amplitude a), and to the constant SCSA to generate a uniform distribution of SCSAs with different degrees of SCSA non-uniformity (amplitude b). Twenty finite element (FE) models are constructed, based on the Voronoi diagrams for twenty foam samples (specimens)

*Corresponding authors, E-mails: KLi2@slb.com, xlgaot@tamu.edu.

having the same pair of a and b , to obtain the mean values and standard deviations of the elastic properties. Spatially periodic boundary conditions are applied to each specimen. The simulation results indicate that for low-density imperfect foams the elastic moduli increase as cell shapes become more irregular, but decrease as SCSAs get less uniform. When the relative density (R) increases, the elastic moduli of imperfect foams increase substantially, while the Poisson's ratios decrease moderately. The effect of the interaction between the two types of imperfections on foam elastic properties appears to be weak. In addition, it is found that the strut cross-sectional shape has a significant effect on the foam properties. Also, the elastic response of foams with the cell shape and SCSA imperfections appears to be isotropic regardless of changes in a , b and R and the strut cross-sectional shape.

Keywords: open-cell foams, tetrakaidecahedral cell, microstructure, castigliano's second theorem, composite homogenization, elastic properties, irregular cell shapes, non-uniform strut cross-sectional areas, Voronoi tessellation, structure-property relations

8.1 Introduction

Manufactured low-density open-cell foams are finding increasing applications in ultra-light sandwich structures (as core materials) and in functional devices for heat dissipation, vibration control or energy absorption. Polymeric foams (often called cellular plastics) have been studied for a long time^[1,2], and metallic (mostly aluminum) foams have also been extensively investigated^[3]. Microcellular carbon foams, which were developed in 1990s^[4], are emerging as a new class of ultra-light cellular materials for structural and thermal management applications because of their excellent mechanical and thermal properties^[5].

Reliable structural applications of open-cell foams hinge on accurate understanding of their mechanical behavior. These foams are topology-sensitive and, as a result, their mechanical performance depends on the cell micro-architecture, the relative foam density and the properties of the strut material. This requires that mechanical models incorporate microstructural features of cells. To this end, two types of micromechanics models, namely, unit cell-based models and random cell-based models have been developed, which are summarized below.

8.1.1 Unit cell models

Many models, analytical or experimental, have been developed, based on idealized unit cells, for predicting mechanical properties of cellular solids. Such a unit cell (also called repeating unit), when properly identified, can capture the essential microstructural features of a real cellular material. For 3-D open-cell foams, cubic, tetrahedral, dodecahedral and tetrakaidecahedral cells have been used as repeating units. With the simplified geometry of a unit cell, closed-form structure-property relations can often be derived^[2].

Figure 8.1 shows a micrograph of an AFRL carbon foam. It can be seen that the microstructure of such a foam has a three-dimensional (3-D) open-cell topology and may be represented by a tetrahedral repeating unit containing four struts, as shown in Fig. 8.2. A detailed finite element analysis based on this unit cell has been provided by Sihn and Roy^[6].

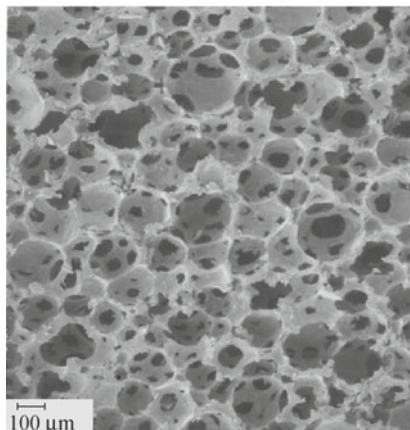


Fig. 8.1 Micrograph of an AFRL carbon foam^[5].

By using a similar repeating unit, Warren and Kraynik^[7] developed a micromechanical model for estimating effective elastic properties of 3-D open-cell solid foams. Their analysis, based on the assumption that the displacements of strut midpoints are affine, considered the equilibrium of the mechanically isolated joint (rather than the connected struts)^[8].

AFRL graphitic carbon foams are blown from anisotropic pitch through a bubble forming process^[9], and, consequently, microstructures of the solidified carbon foams are controlled by the principle of minimum surface energy. On the cell level, the repeating unit shown in Fig. 8.2 corresponds to a regular tetrakaidecahedron (Fig. 8.3), with all of its vertices being connected by slender struts and each vertex shared by four struts. Such a fourteen-sided polyhedron can be generated by uniformly truncating the six corners of an octahedron and contains eight regular hexagonal faces and six square faces.

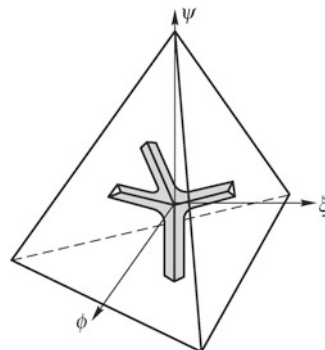


Fig. 8.2 Repeating unit of a carbon foam^[6].

The tetrakaidecahedral cell is known to be the only polyhedron that can pack with identical units to fill space and nearly minimize the surface energy^[10].

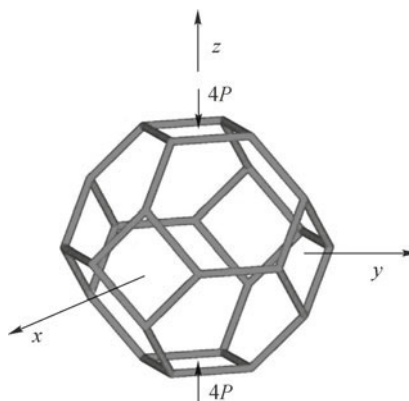


Fig. 8.3 Tetrakaidecahedral cell under compression in the z -direction.

Tetrakaidecahedral cells were first used by Dement'ev and Tarakanov^[11] to model open-cell foams. They applied compressive forces along a $\langle 100 \rangle$ axis of an isolated tetrakaidecahedral cell (i.e., pushing on two square faces) and found the effective Young's modulus to be directly proportional to the relative foam density. This model is inaccurate because strut bending is neglected. In their subsequent analysis^[12], bending of cell struts was included and Young's modulus was more accurately predicted. However, they considered only square strut cross sections and did not express Young's modulus in terms of the relative foam density. The model of Choi and Lakes^[13] utilizes a regular tetrakaidecahedron and an energy method, but it is pseudo three-dimensional and incorporates only bending deformations. Their prediction of Young's modulus differs from that of Dement'ev and Tarakanov^[12].

Warren and Kraynik's^[8] micromechanics model is based on a flat-faced, 14-sided Kelvin cell and considers arbitrary homogeneous deformations of a perfectly packed foam. Equilibrium analyses are performed for isolated joints, and forces, moments and displacements at strut midpoints are analytically derived. This more comprehensive analysis complements their early model based on a tetrahedral unit cell^[7]. Warren and Kraynik's model gives a good estimate of the effective Young's modulus, but it predicts the effective Poisson's ratio to be approximately 0.5 for low-density foams, which is higher than 1/3, the value suggested by experiments^[2].

A common feature of the afore-mentioned micromechanics models is that a single tetrakaidecahedral cell isolated from the foam material is used as a representative volume element (RVE), which is of idealized nature. Nevertheless, such an idealized RVE approach is typical of micromechanical analysis of periodic structures^[14], including cellular solids^[2]. Furthermore, it should be noticed that none of these existing tetrakaidecahedron-based analyses attempts to provide and utilize complete stress/deformation data for all thirty-six full-length struts. In addition, the effect of transverse shearing has been ignored in all of the models mentioned above. Therefore, more comprehensive models that can account for contributions from all structural members, incorporate all possible deformation mechanisms and lead to accurate predictions of both Young's modulus and Poisson's ratio are needed. The first micromechanics model developed by the present authors and described in Section 8.2 are in response to this need.

8.1.2 Random cell models

Although unit cell-based models can provide important results, they are significantly limited by their inability to account for microstructural imperfections inherent in most actual cellular materials, whose cell structures are typically non-periodic, non-uniform and disordered. Thus, more complex, statistical models are necessitated to obtain improved predictions. To this end, suitable numerical methods are often required because of the stochastic nature of the problem.

Efforts have been made to explore the effects of imperfections, such as irregular cell shapes and sizes^[15-18], thickness variations between cell walls^[19], non-uniform solid distribution in cell walls^[20], curved/corrugated cell walls^[21], and wavy cell walls^[22], on mechanical properties of 3-D open-cell and closed-cell foams. However, in each of these existing studies only one type of imperfections was included at a time. In general, two or more types of imperfections are simultaneously involved in the microstructure of a cellular material. Therefore, models incorporating two or more types of imperfections are in need. This motivated the development of the second model to be presented in Section 8.3.

8.2 Micromechanics model using a tetrakaidecahedral unit cell

In this section, a unit-cell-based micromechanical model is presented for 3-D open-cell foams, which can account for contributions from all structural members, incorporate all possible deformation mechanisms and lead to accurate predictions of both Young's modulus and Poisson's ratio. The tetrakaidecahedral unit cell shown in Fig. 8.3 is adopted, and an energy method based on Castigliano's second theorem is employed in the formulation. Energy methods are known to work best for systems with complicated geometry^[23-26].

In Subsection 8.2.1, equilibrium analysis is first carried out to obtain the resultant forces in each of the thirty-six struts of the unit cell, which differs from what was done in existing models. Castigliano's second theorem is then applied to determining the displacements of the unit cell in the loading and lateral directions. These, together with the use of the composite homogenization theory, lead to closed-form formulas for calculating the effective Young's modulus and Poisson's ratio of open-cell foams. As a direct application of the new model, a parametric study on sample cases involving four different strut cross section shapes and various values of the relative foam density is conducted for carbon foams in Subsection 8.2.2, where the current model is also compared to and verified by existing models and experimental results. A summary is given in the third and last subsection.

8.2.1 Formulation

Consider the tetrakaidecahedral unit cell illustrated in Fig. 8.3, which is representative of the open-cell foam structure perfectly packed by regular tetrakaidecahedra sitting on a body-centered cubic (BCC) lattice^[8] and subjected to uniaxial compression (Fig. 8.4). The center of this cell is located at one lattice point. As shown in Fig. 8.3, a pair of concentrated compressive forces is applied on the two opposite square faces perpendicular to the z -direction. This symmetric loading mode of pushing on two square faces results in no twisting in any strut. In fact, the geometric and loading symmetry enables one to further identify that the struts lying in the xy -plane and the two surface planes parallel to it experience only stretching and bending, while the remaining struts undergo bending, shearing and stretching deformations, with the bending moments vanishing at the strut midpoints^[8].

It is assumed that the strut material is linearly elastic and isotropic. Also, all of the thirty-six struts are taken to be uniform slender beams having the same geometric and material properties, which are linked to each other at rigid vertices. Each strut, having the length L and the cross sectional area A , is assumed to satisfy the classical beam theory, as was done in previous studies.

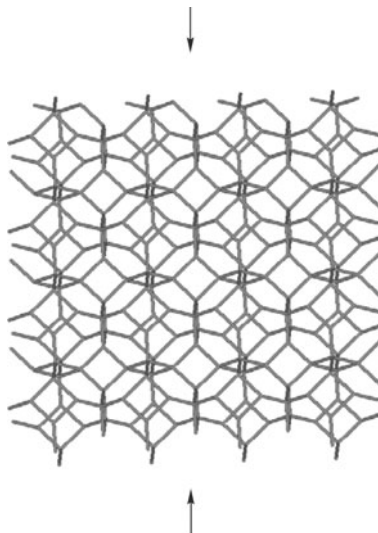


Fig. 8.4 Open-cell foam structure.

8.2.1.1 Young's modulus

The unit cell shown in Fig. 8.3 is a statically indeterminate frame structure. Energy principles in structural mechanics can be applied to determine the resultant forces in each strut. Owing to the geometric and loading symmetry, only one quarter of the tetrakaidecahedral cell, as shown in Fig. 8.5, needs to be analyzed. This isolated quarter cell contains twelve structural members (S_1 — S_{12}) and six joints (J_1 — J_6). Members S_1 , S_2 , S_8 , S_9 , S_{11} and S_{12} have the length $L/2$, while the rest, as full-length struts, have the length L . Applied (statically equivalent) forces acting on the quarter cell are the pair of compressive forces P passing through J_1 and J_6 .

With the struts undergoing no twisting under the applied forces shown in Fig. 8.3, there is no resisting torque present in any strut. Consequently, only three types of (generalized) resultant forces (i.e., axial force, transverse shear forces and bending moments) need to be included in the analysis of any structural member. Let the resultant forces in the n th structural member be represented by N_n , $V_{n\alpha}$ and $M_{n\alpha}$, where N , V and M denote, respectively, axial force, transverse shear force and bending moment, and α stands for the direction of the bending moment or the transverse shear force, which coincides with one of the two local coordinate axes η and ζ perpendicular to the strut axis direction that is aligned with the local coordinate ξ .

Due to symmetry, transverse shear forces in S_1 , S_2 , S_8 , S_9 , S_{11} and S_{12} vanish, and there is only one constant-valued bending moment present in each of these members, as shown in Fig. 8.5. Here, the local coordinate η is perpendicular to the strut, and is normal to the applied force P for struts S_1 , S_2 , S_{11} and S_{12} but parallel to the direction of the force P for struts S_8

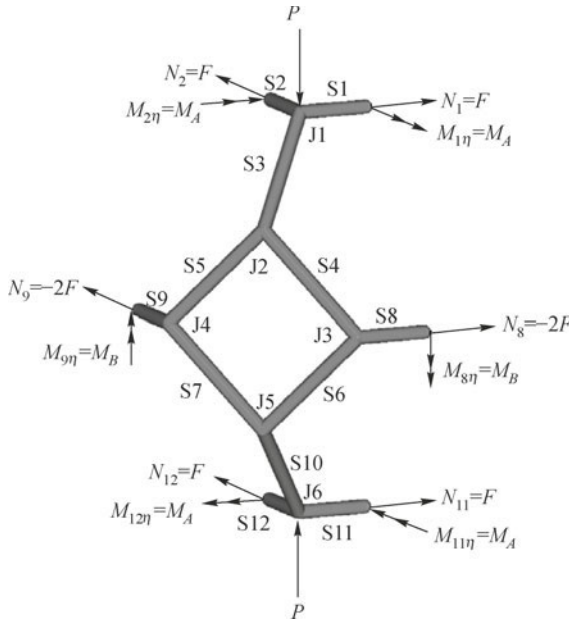


Fig. 8.5 Free body diagram of a quarter of the tetrakaidecahedral cell. (color plot at the end of the book)

and S9. Furthermore, symmetry requires that, at equal distances from the respective joint(s),

$$\begin{aligned}
 N_1 &= N_2 = N_{11} = N_{12}, & M_{1\eta} &= M_{2\eta} = M_{11\eta} = M_{12\eta}, \\
 N_8 &= N_9, & M_{8\eta} &= M_{9\eta}, \\
 N_3 &= N_{10}, & V_{3\alpha} &= V_{10\alpha}, & M_{3\alpha} &= M_{10\alpha}, \\
 N_4 &= N_5 = N_6 = N_7, & V_{4\alpha} &= V_{5\alpha} = V_{6\alpha} = V_{7\alpha}, \\
 M_{4\alpha} &= M_{5\alpha} = M_{6\alpha} = M_{7\alpha}.
 \end{aligned} \tag{8.1}$$

The global equilibrium of the quarter cell gives, noting that S1 and S2, S8 and S9, and S11 and S12 are, respectively, orthogonal,

$$N_8 = -(N_1 + N_{11}), \quad N_9 = -(N_2 + N_{12}). \tag{8.2}$$

Let $N_1 \equiv F$, $M_{1\eta} \equiv M_A$ and $M_{8\eta} \equiv M_B$, with F , M_A and M_B being three (yet-unknown) convenient constants. Then, it follows from Eqs. (8.1) and (8.2) that

$$\begin{aligned}
 N_1 &= N_2 = N_{11} = N_{12} = F, & N_8 &= N_9 = -2F, \\
 M_{1\eta} &= M_{2\eta} = M_{11\eta} = M_{12\eta} = M_A, & M_{8\eta} &= M_{9\eta} = M_B.
 \end{aligned} \tag{8.3}$$

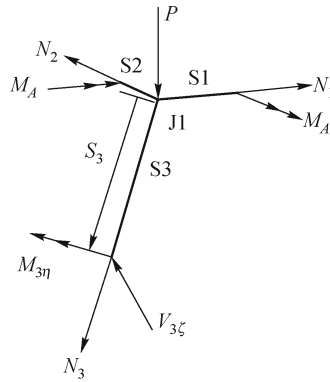


Fig. 8.6 Free body diagram of the S1, S2 and S3 assemblage.

The equilibrium of Joint J1 (Fig. 8.6) requires that

$$\begin{aligned} N_3 + \frac{\sqrt{2}}{2}P - \frac{\sqrt{2}}{2} \left(\frac{\sqrt{2}}{2}N_1 + \frac{\sqrt{2}}{2}N_2 \right) &= 0, \\ V_{3\zeta} - \frac{\sqrt{2}}{2}P - \frac{\sqrt{2}}{2} \left(\frac{\sqrt{2}}{2}N_1 + \frac{\sqrt{2}}{2}N_2 \right) &= 0, \\ \sqrt{2}M_A - M_{3\eta} - \frac{\sqrt{2}}{2}Ps_3 - \frac{\sqrt{2}}{2} \left(\frac{\sqrt{2}}{2}N_1 + \frac{\sqrt{2}}{2}N_2 \right) s_3 &= 0, \end{aligned} \quad (8.4a, b, c)$$

which gives, together with Eq. (8.3),

$$N_3 = F - \frac{\sqrt{2}}{2}P, \quad V_{3\zeta} = F + \frac{\sqrt{2}}{2}P, \quad M_{3\eta} = \sqrt{2}M_A - \left(F + \frac{\sqrt{2}}{2}P \right) s_3, \quad (8.5a, b, c)$$

where s_3 is the (local) distance along S3 measured from J1. In Fig. 8.6, $M_{3\eta}$ is parallel to the segment that connects the middle points of S1 and S2 (and is therefore normal to S3), and $V_{3\zeta}$ is perpendicular to both $M_{3\eta}$ and the strut and points outward. Since $M_{3\eta}$ vanishes at the midpoint of S3, it follows from Eq. (8.5c), with $s_3 = L/2$, that

$$M_A = \frac{\sqrt{2}}{4} \left(F + \frac{\sqrt{2}}{2}P \right) L. \quad (8.6)$$

Note that $V_{3\eta} \equiv 0$ and $M_{3\zeta} \equiv 0$ due to symmetry.

When viewed in plane, the square frame composed of S4–S7 is a statically indeterminate planar frame loaded by two pairs of concentrated forces at its four joints. This frame problem can be decomposed into two simpler problems (I) and (II), as shown in Fig. 8.7. Since the resultant forces in each member

of the frame are the same (Eq. (8.1)), only one of the four members, e.g., S5, needs to be analyzed in each problem. Problem (I) is considered first. A free body diagram of S5 is illustrated in Fig. 8.8. The two ends C and D stand for J2 and J4 of S5, respectively.

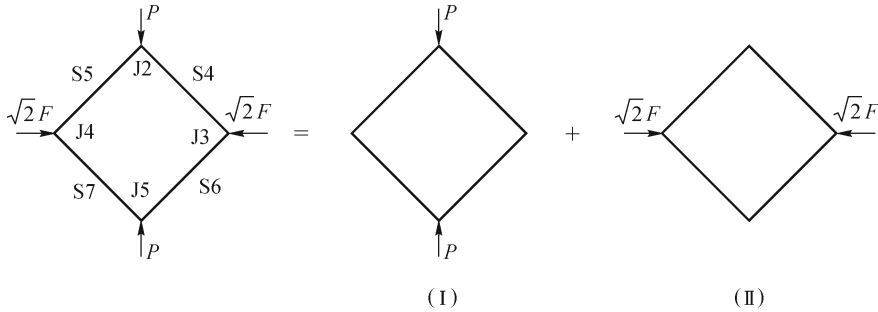


Fig. 8.7 Square frame.

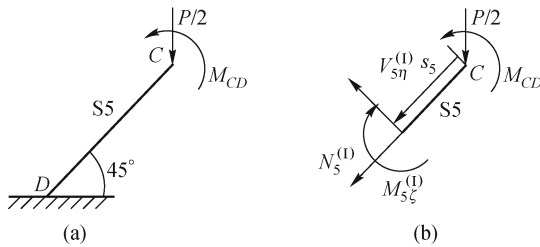


Fig. 8.8 Free body diagram of S5 in Problem (I): (a) isolated S5; (b) FBD.

The equilibrium of S5 (Fig. 8.8b) gives

$$N_5^{(I)} = -\frac{\sqrt{2}}{4}P, \quad V_{5\eta}^{(I)} = \frac{\sqrt{2}}{4}P, \quad M_{5\zeta}^{(I)} = M_{CD} - \frac{\sqrt{2}}{4}Ps_5, \quad (8.7a, b, c)$$

where s_5 is the (local) distance along S5 measured from Joint 2 (at point C), and the superscript “(I)” denotes Problem (I).

The internal moment M_{CD} needs to be determined using a compatibility condition. This is provided by the rigidity of Joint 2, which gives, using Castigliano’s second theorem^[27],

$$\theta_C = \int_0^L \left(\frac{N_5^{(I)}}{EA} \frac{\partial N_5^{(I)}}{\partial M_{CD}} + \frac{k_1 V_{5\eta}^{(I)}}{GA} \frac{\partial V_{5\eta}^{(I)}}{\partial M_{CD}} + \frac{M_{5\zeta}^{(I)}}{EI} \frac{\partial M_{5\zeta}^{(I)}}{\partial M_{CD}} \right) ds_5 = 0, \quad (8.8)$$

where θ_C is the (relative) rotation at point C, E and G are, respectively, the Young’s modulus and the shear modulus of the strut material, and I and k_1 are, respectively, the second moment of area of the cross section and

the transverse shear factor. Inserting Eqs. (8.7a,b,c) into Eq. (8.8) results in, noting that only the third term in the integrand remains after differentiation,

$$M_{CD} = \frac{\sqrt{2}}{8} PL. \quad (8.9)$$

Using Eq. (8.9) in Eq. (8.7c) leads to

$$M_{5\zeta}^{(I)} = \frac{\sqrt{2}}{4} P \left(\frac{L}{2} - s_5 \right). \quad (8.10)$$

For Problem (II), the in-plane resultant forces in S5 can be obtained by following the procedures similar to those used above for determining the solution of Problem (I). The results give

$$N_5^{(II)} = -\frac{1}{2}F, \quad V_{5\eta}^{(II)} = -\frac{1}{2}F, \quad M_{5\zeta}^{(II)} = -\frac{1}{2}F \left(\frac{L}{2} - s_5 \right). \quad (8.11a, b, c)$$

The principle of superposition then yields, using Eqs. (8.7a,b), (8.10) and (8.11a,b,c), the total in-plane resultant forces in S5 (and thus in the entire square frame) as

$$N_5 = - \left(\frac{\sqrt{2}}{4} P + \frac{1}{2}F \right), \quad V_{5\eta} = \frac{\sqrt{2}}{4} P - \frac{1}{2}F, \quad (8.12a, b)$$

$$M_{5\zeta} = \left(\frac{\sqrt{2}}{4} P - \frac{1}{2}F \right) \left(\frac{L}{2} - s_5 \right). \quad (8.12c)$$

Note from Eq. (8.12c) that $M_{5\zeta}$ is indeed equal to zero at the midpoint of S5, where $s_5 = L/2$.

To determine the remaining two out-of-plane resultant forces $V_{5\zeta}$ and $M_{5\eta}$, consider an assemblage of S5, S7 and S9, as shown in Fig. 8.9a, where s_7 , the (local) distance along S7 measured from Joint 5, is taken to be equal to s_5 to make use of the symmetry conditions. Here, the local coordinate η is perpendicular to the strut and lies in the plane of the square frame for both S5 and S7, and the coordinate ζ is normal to the plane of the square frame. The force balance in the direction normal to the planar square frame results in, with $V_{5\zeta} = V_{7\zeta}$ (due to symmetry),

$$V_{5\zeta} = -\frac{\sqrt{2}}{2} F. \quad (8.13)$$

The moment balance of J4 gives, with $M_{5\eta} = M_{7\eta}$ (due to symmetry),

$$M_{5\eta} = -\frac{\sqrt{2}}{2} M_B - \frac{\sqrt{2}}{2} F(L - s_5). \quad (8.14)$$

The requirement of $M_{5\eta} = 0$ at the midpoint of S5 then yields, from Eq. (8.14),

$$M_B = -\frac{FL}{2}. \quad (8.15)$$

Next, the moment balance about J2 can be established with the help of Fig. 8.9b, where $M_{4\eta}$ and $M_{5\eta}$ are perpendicular to S4 and S5, respectively, and lie in the plane formed by the two struts, and $M_{3\eta}$ is parallel to the segment that connects the middle points of S4 and S5 (and is therefore normal to S3). It requires that

$$M_{3\eta}|_{s_3=L} + \frac{\sqrt{2}}{2}(M_{4\eta}|_{s_4=0} + M_{5\eta}|_{s_5=0}) = 0, \quad (8.16)$$

where s_4 is the (local) distance along S4 measured from Joint 2. Equation (8.16) leads to, using Eqs. (8.5c) and (8.14) and $M_{4\eta}|_{s_4=0} = M_{5\eta}|_{s_5=0}$ (see Eq. (8.1)),

$$F = -\frac{\sqrt{2}}{4}P. \quad (8.17)$$

Finally, the substitution of Eq. (8.17) into Eqs. (8.6) and (8.15) gives

$$M_A = \frac{1}{8}PL, \quad M_B = \frac{\sqrt{2}}{8}PL. \quad (8.18a, b)$$

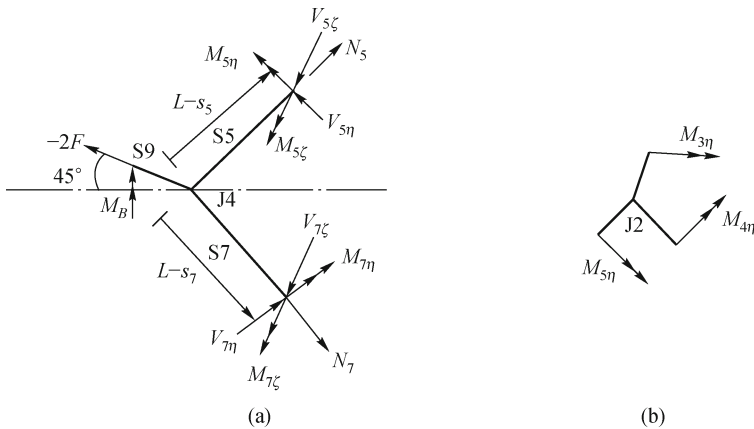


Fig. 8.9 Free body diagrams of (a) the assemblage of S5, S7 and S9; (b) joint 2 (moments only).

With the constants F , M_A and M_B determined, the resultant forces in S1, S3, S5 and S8 can be readily calculated using Eqs. (8.3), (8.5a,b,c) and (8.12a,b,c)–(8.14). The resultant forces in the remaining members can then be obtained from Eq. (8.1).

As a summary, the resultant forces in each of the twelve members of the quarter cell shown in Fig. 8.5 are listed in Table 8.1, where s_6 is the (local) distance along S6 measured from Joint 5, and s_{10} is that along S10 measured from Joint 6.

The effective Young's modulus can be derived from the stress-strain relation of the unit cell. Equivalently, the symmetry and linearity also enable one to determine the Young's modulus using the load-displacement relation obtained for the uniaxially loaded quarter cell shown in Fig. 8.5. This can be accomplished by applying Castigliano's second theorem, as what was done by Gao et al.^[26]. As an energy principle, this theorem allows one to work with scalars and to use local coordinates.

Table 8.1 Resultant forces in S1—S12

n	N_n	$V_{n\eta}$	$V_{n\zeta}$	$M_{n\eta}$	$M_{n\zeta}$
1	$-\frac{\sqrt{2}}{4}P$	0	0	$\frac{1}{8}PL$	0
2	$-\frac{\sqrt{2}}{4}P$	0	0	$\frac{1}{8}PL$	0
3	$-\frac{3\sqrt{2}}{4}P$	0	$\frac{\sqrt{2}}{4}P$	$\frac{\sqrt{2}}{4}P\left(\frac{L}{2}-s_3\right)$	0
4	$-\frac{\sqrt{2}}{8}P$	$\frac{3\sqrt{2}}{8}P$	$\frac{1}{4}P$	$\frac{1}{4}P\left(\frac{L}{2}-s_4\right)$	$\frac{3\sqrt{2}}{8}P\left(\frac{L}{2}-s_4\right)$
5	$-\frac{\sqrt{2}}{8}P$	$\frac{3\sqrt{2}}{8}P$	$\frac{1}{4}P$	$\frac{1}{4}P\left(\frac{L}{2}-s_5\right)$	$\frac{3\sqrt{2}}{8}P\left(\frac{L}{2}-s_5\right)$
6	$-\frac{\sqrt{2}}{8}P$	$\frac{3\sqrt{2}}{8}P$	$\frac{1}{4}P$	$\frac{1}{4}P\left(\frac{L}{2}-s_6\right)$	$\frac{3\sqrt{2}}{8}P\left(\frac{L}{2}-s_6\right)$
7	$-\frac{\sqrt{2}}{8}P$	$\frac{3\sqrt{2}}{8}P$	$\frac{1}{4}P$	$\frac{1}{4}P\left(\frac{L}{2}-s_7\right)$	$\frac{3\sqrt{2}}{8}P\left(\frac{L}{2}-s_7\right)$
8	$\frac{\sqrt{2}}{2}P$	0	0	$\frac{\sqrt{2}}{8}PL$	0
9	$\frac{\sqrt{2}}{2}P$	0	0	$\frac{\sqrt{2}}{8}PL$	0
10	$-\frac{3\sqrt{2}}{4}P$	0	$\frac{\sqrt{2}}{4}P$	$\frac{\sqrt{2}}{4}P\left(\frac{L}{2}-s_{10}\right)$	0
11	$-\frac{\sqrt{2}}{4}P$	0	0	$\frac{1}{8}PL$	0
12	$-\frac{\sqrt{2}}{4}P$	0	0	$\frac{1}{8}PL$	0

Note that the total complementary energy of the quarter cell is given by

$$\Pi_c = \sum_{n=1}^{12} \Pi_n, \quad (8.19)$$

where Π_n is the complementary energy in the n th member. For S1, S2, S8,

S9, S11 and S12,

$$\Pi_n = \int_0^{\frac{L}{2}} \frac{N_n^2}{2EA} ds_n + \int_0^{\frac{L}{2}} \frac{k_1 V_{n\eta}^2}{2GA} ds_n + \int_0^{\frac{L}{2}} \frac{k_1 V_{n\zeta}^2}{2GA} ds_n + \int_0^{\frac{L}{2}} \frac{M_{n\eta}^2}{2EI} ds_n + \int_0^{\frac{L}{2}} \frac{M_{n\zeta}^2}{2EI} ds_n. \quad (8.20)$$

For S3—S7 and S10,

$$\Pi_n = \int_0^L \frac{N_n^2}{2EA} ds_n + \int_0^L \frac{k_1 V_{n\eta}^2}{2GA} ds_n + \int_0^L \frac{k_1 V_{n\zeta}^2}{2GA} ds_n + \int_0^L \frac{M_{n\eta}^2}{2EI} ds_n + \int_0^L \frac{M_{n\zeta}^2}{2EI} ds_n. \quad (8.21)$$

The results of the integral terms for each member are listed in Table 8.2, where use has been made of Table 8.1. Applying Castigliano's second theorem then gives, from Eq. (8.19),

$$\Delta_z = \frac{\partial \Pi_c}{\partial P} = \sum_{n=1}^{12} \frac{\partial \Pi_n}{\partial P}, \quad (8.22)$$

where Δ_z is the displacement of the quarter cell in the loading direction, which is also equal to the displacement of the tetrakaidecahedral unit cell in the same direction.

By substituting Eqs. (8.20) and (8.21) and the results in Table 8.2 into Eq. (8.22), the load-displacement relation is finally obtained as

$$\Delta_z = \frac{25PL}{8EA} + \frac{13k_1 PL}{8GA} + \frac{19PL^3}{96EI}. \quad (8.23)$$

Clearly, Eq. (8.23) shows that the contribution from transverse shear forces (i.e., the second term) is on the same order of magnitude as that from axial forces (i.e., the first term), although the contribution due to bending moments (i.e., the third term) is dominant for foams having slender struts (i.e., with large L/\sqrt{A}). This differs from the existing analyses reviewed earlier, where the transverse shearing effect was not explicitly included.

The effective Young's modulus of the tetrakaidecahedral unit cell, and thus of the foam, can be determined by using the average strain theorem in the homogenization theory of composite materials^[26,28]. According to this theorem,

$$\bar{\varepsilon}_z \equiv \frac{\Delta_z}{L^*}, \quad (8.24)$$

where $\bar{\varepsilon}_z$ is the uniform (constant) strain applied in the z -direction on the homogenized body and $L^* = 2\sqrt{2}L$ is the initial height of the unit cell. Then, the effective Young's modulus is given by

$$E_z^* = \frac{\bar{\sigma}_z}{\bar{\varepsilon}_z} = \frac{L^* P^*}{A^* \Delta_z}, \quad (8.25)$$

where $\bar{\sigma}_z$ is the effective stress applied in the z -direction, $P^* \equiv 4P$ is the total force applied in the z -direction, and $A^* = V_c/L^*$ is the effective cross-

sectional area of the unit cell, with V_c being the cell volume. For the tetrakaidecahedral unit cell, $V_c = 8\sqrt{2}L^3$. It then follows from Eq. (8.25) that

$$E_z^* = \frac{2\sqrt{2}P}{L\Delta_z}. \quad (8.26)$$

Table 8.2 Complementary energies in S1—S12

n	$\int \frac{N_n^2}{2EA} ds_n$	$\int \frac{k_1 V_{n\eta}^2}{2GA} ds_n$	$\int \frac{k_1 V_{n\zeta}^2}{2GA} ds_n$	$\int \frac{M_{n\eta}^2}{2EI} ds_n$	$\int \frac{N_{n\zeta}^2}{2EI} ds_n$
1	$\frac{P^2 L}{32EA}$	0	0	$\frac{P^2 L^3}{256EI}$	0
2	$\frac{P^2 L}{32EA}$	0	0	$\frac{P^2 L^3}{256EI}$	0
3	$\frac{9P^2 L}{16EA}$	0	$\frac{k_1 P^2 L}{16GA}$	$\frac{P^2 L^3}{192EI}$	0
4	$\frac{P^2 L}{64EA}$	$\frac{9k_1 P^2 L}{64GA}$	$\frac{k_1 P^2 L}{32GA}$	$\frac{P^2 L^3}{384EI}$	$\frac{3P^2 L^3}{256EI}$
5	$\frac{P^2 L}{64EA}$	$\frac{9k_1 P^2 L}{64GA}$	$\frac{k_1 P^2 L}{32GA}$	$\frac{P^2 L^3}{384EI}$	$\frac{3P^2 L^3}{256EI}$
6	$\frac{P^2 L}{64EA}$	$\frac{9k_1 P^2 L}{64GA}$	$\frac{k_1 P^2 L}{32GA}$	$\frac{P^2 L^3}{384EI}$	$\frac{3P^2 L^3}{256EI}$
7	$\frac{P^2 L}{64EA}$	$\frac{9k_1 P^2 L}{64GA}$	$\frac{k_1 P^2 L}{32GA}$	$\frac{P^2 L^3}{384EI}$	$\frac{3P^2 L^3}{256EI}$
8	$\frac{P^2 L}{8EA}$	0	0	$\frac{P^2 L^3}{128EI}$	0
9	$\frac{P^2 L}{8EA}$	0	0	$\frac{P^2 L^3}{128EI}$	0
10	$\frac{9P^2 L}{16EA}$	0	$\frac{k_1 P^2 L}{16GA}$	$\frac{P^2 L^3}{192EI}$	0
11	$\frac{P^2 L}{32EA}$	0	0	$\frac{P^2 L^3}{256EI}$	0
12	$\frac{P^2 L}{32EA}$	0	0	$\frac{P^2 L^3}{256EI}$	0

The relative density of such an open-cell foam with negligible vertex volume is given by^[8]

$$R = \frac{3}{2\sqrt{2}} \frac{A}{L^2}. \quad (8.27)$$

Inserting Eqs. (8.23) and (8.27) into Eq. (8.26) then yields

$$E_z^* = \frac{EcR^2}{0.07872 + [1.171875 + 1.218750k_1(1+\nu)]cR}, \quad (8.28)$$

where use has been made of the relation $G = E/[2(1+\nu)]$, with ν being Poisson's ratio of the strut material, and c is the radius of gyration defined

by

$$c \equiv \sqrt{\frac{I}{A}}, \quad (8.29)$$

whose value for a given strut cross section can be readily determined. The radius of gyration represents the bending stiffness of a section with a given cross sectional area. The values of the geometric parameters c and k_1 for four types of strut cross sections are listed in Table 8.3. It can be seen that with the same cross sectional area the Plateau border cross section provides the largest bending stiffness, followed by the equilateral triangle, square and circular cross sections. The values of the transverse shear factor k_1 for circular and square cross sections are, respectively, 1.1 and 1.2^[27]. By using the same method as that discussed by Cook and Young^[27], the value of k_1 is found to be 1.2 for equilateral triangle cross sections. The value of k_1 for a Plateau border cross section, which occupies the area enclosed by three identical, mutually tangent circles, is taken to be the same as that for an equilateral triangle cross section because of the geometric similarity between them.

Table 8.3 Geometric constants

Strut cross section	c	k_1
Circle	0.079 58	1.1
Square	0.083 33	1.2
Equilateral triangle	0.096 23	1.2
Plateau border	0.133 80	1.2

Equation (8.28) provides a closed-form formula for calculating the effective Young's modulus of open-cell foams. This formula explicitly shows that E_z^* depends on the relative foam density (R), the size and shape of the strut cross section (c and k_1), and the elastic properties of the strut material (E and ν). The expression for E_z^* given by Eq. (28) contains more parameters than those obtained in the previous studies and can be readily reduced to special cases by specifying the parameters ν , c or k_1 .

8.2.1.2 Poisson's ratio

The effective Poisson's ratio can be obtained from^[25,29]

$$\nu_{zx}^* = -\frac{\bar{\varepsilon}_x}{\bar{\varepsilon}_z}, \quad (8.30)$$

where $\bar{\varepsilon}_x$ is the average lateral strain caused by the uniaxial loading in the z -direction. Since the dimensions of the unit cell in the x -and z -directions are the same, Eq. (8.30) is equivalent to

$$\nu_{zx}^* = -\frac{\Delta_x}{\Delta_z}. \quad (8.31)$$

The displacement in the z -direction, Δ_z , has been determined in the preceding subsection. The lateral displacement along the x -direction, Δ_x , can also be calculated using Castiglione's second theorem. To accomplish this, a fictitious pair of concentrated compressive forces $P_I^* \equiv 4P_I$, in addition to

the compressive loading in the z -direction, is applied on the two opposite square faces in the x -direction, as shown in Fig. 8.10. Due to symmetry, only one hexagonal frame formed by the struts S1, S3, S4, S8, S18 and S19 needs to be analyzed (Fig. 8.10). For the case with loading in the z -direction only, the resultant forces in S1, S3, S4 and S8 have been listed in Table 8.1. The resultant forces in S18 and S19 are, respectively, the same as those in S3 and S4 because of symmetry.

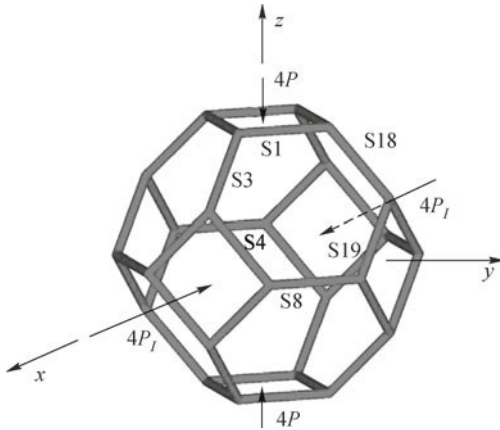


Fig. 8.10 Tetrakaidecahedral cell under compression in the x - and z -directions. (color plot at the end of the book)

When the unit cell is loaded only in the x -direction, the resultant forces in these struts can be readily determined by following the same procedures as those used for the z -direction loading case. The results are given in Table 8.4, in which use has been made of

$$F_I = -\frac{\sqrt{2}}{4} P_I, \quad (8.32)$$

which is a result parallel to that given in Eq. (8.17). In Table 8.4, s_8 is the (local) distance along S8 measured from its right end, and s_{19} the (local) distance along S19 measured from its upper end. By superposing the corresponding results in Tables 8.1 and 8.4, the resultant forces in the six struts of the cell subjected to simultaneous compression in the x - and z -directions can be readily determined. The results are given in Table 8.5, where s_{18} is the (local) distance along S18 measured from its upper end.

Table 8.4 Resultant forces in the six struts caused by loading in the x -direction

n	N_n	$V_{n\eta}$	$V_{n\zeta}$	$M_{n\eta}$	$M_{n\zeta}$
1	$-\frac{\sqrt{2}}{8} P_I$	$-\frac{3\sqrt{2}}{8} P_I$	$-\frac{1}{4} P_I$	$-\frac{1}{4} P_I \left(\frac{L}{2} - s_1 \right)$	$-\frac{3\sqrt{2}}{8} P_I \left(\frac{L}{2} - s_1 \right)$

Continued

n	N_n	$V_{n\eta}$	$V_{n\zeta}$	$M_{n\eta}$	$M_{n\zeta}$
3	$-\frac{3\sqrt{2}}{4}P_I$	0	$-\frac{\sqrt{2}}{4}P_I$	$-\frac{\sqrt{2}}{4}P_I \left(\frac{L}{2} - s_3\right)$	0
4	$-\frac{\sqrt{2}}{4}P_I$	0	0	$\frac{P_I L}{8}$	0
8	$-\frac{3\sqrt{2}}{4}P_I$	0	$-\frac{\sqrt{2}}{4}P_I$	$-\frac{\sqrt{2}}{4}P_I \left(\frac{L}{2} - s_8\right)$	0
18	$\frac{\sqrt{2}}{2}P_I$	0	0	$\frac{\sqrt{2}}{8}P_I L$	0
19	$-\frac{\sqrt{2}}{8}P_I$	$-\frac{3\sqrt{2}}{8}P_I$	$-\frac{1}{4}P_I$	$-\frac{1}{4}P_I \left(\frac{L}{2} - s_{19}\right)$	$-\frac{3\sqrt{2}}{8}P_I \left(\frac{L}{2} - s_{19}\right)$

The total complementary energy of the tetrakaidecahedral unit cell under compression in both the x -and z -directions is given by

$$\Pi_c = \sum_{n=1}^{36} \Pi_n, \quad (8.33)$$

where Π_n is the complementary energy in the n th strut. Based on the geometric and loading symmetry, the general expression given in Eq. (8.33) can be further simplified to obtain

$$\Pi_c = 8\Pi_1 + 4\Pi_3 + 8\Pi_4 + 4\Pi_8 + 4\Pi_{18} + 8\Pi_{19}. \quad (8.34)$$

Using Eq. (8.21) gives the complementary energy for each of the six struts, as summarized in Table 8.6. Applying Castigliano's second theorem then yields, from Eq. (8.34),

$$\Delta_x = \frac{\partial \Pi_c}{\partial P_I^*} = 8\frac{\partial \Pi_1}{\partial P_I^*} + 4\frac{\partial \Pi_3}{\partial P_I^*} + 8\frac{\partial \Pi_4}{\partial P_I^*} + 4\frac{\partial \Pi_8}{\partial P_I^*} + 4\frac{\partial \Pi_{18}}{\partial P_I^*} + 8\frac{\partial \Pi_{19}}{\partial P_I^*}, \quad (8.35)$$

where Δ_x is the displacement of the tetrakaidecahedral unit cell in the x -direction. By setting P_I^* equal to zero in evaluating Eq. (8.35), Δ_x , as the displacement caused solely by the applied force $4P$ in the z -direction, will be determined. The substitution of Eqs. (8.21) and (8.34) and the results given in Table 8.6 into Eq. (8.35) leads to, after letting $P_I^* \equiv 4P_I = 0$,

$$\Delta_x = - \left(\frac{PL}{16EA} + \frac{3k_1 PL}{16GA} + \frac{6.5PL^3}{96EI} \right), \quad (8.36)$$

where the negative sign means that the lateral displacement is in the opposite direction to the fictitious force $4P_I$. Again, it is seen from Eq. (8.36) that the contribution from transverse shear forces (i.e., the second term) is comparable to that due to axial forces (i.e., the first term). Hence, neglecting

Table 8.5 Resultant forces in the six struts when compressed in both the x - and z -directions

n	N_n	$V_{n\eta}$	$V_{n\zeta}$	$M_{n\eta}$	$M_{n\zeta}$
1	$-\frac{\sqrt{2}}{8}(2P + P_I)$	$-\frac{3\sqrt{2}}{8}P_I$	$-\frac{1}{4}P_I$	$\frac{1}{8}PL - \frac{1}{4}P_I\left(\frac{L}{2} - s_1\right)$	$-\frac{3\sqrt{2}}{8}P_I\left(\frac{L}{2} - s_1\right)$
3	$-\frac{3\sqrt{2}}{4}(P + P_I)$	0	$\frac{\sqrt{2}}{4}(P - P_I)$	$\frac{\sqrt{2}}{4}(P - P_I)\left(\frac{L}{2} - s_3\right)$	0
4	$-\frac{\sqrt{2}}{8}(P + 2P_I)$	$\frac{3\sqrt{2}}{8}P$	$\frac{1}{4}P$	$\frac{1}{4}P\left(\frac{L}{2} - s_4\right) + \frac{1}{8}P_I L$	$\frac{3\sqrt{2}}{8}P\left(\frac{L}{2} - s_4\right)$
8	$\frac{\sqrt{2}}{4}(2P - 3P_I)$	0	$-\frac{\sqrt{2}}{4}P_I$	$\frac{\sqrt{2}}{8}PL - \frac{\sqrt{2}}{4}P_I\left(\frac{L}{2} - s_8\right)$	0
18	$-\frac{\sqrt{2}}{4}(3P - 2P_I)$	0	$\frac{\sqrt{2}}{4}P$	$\frac{\sqrt{2}}{4}P\left(\frac{L}{2} - s_{18}\right) + \frac{\sqrt{2}}{8}P_I$	0
19	$-\frac{\sqrt{2}}{8}(P + P_I)$	$\frac{3\sqrt{2}}{8}(P - P_I)$	$\frac{1}{4}(P - P_I)$	$\frac{1}{4}(P - P_I)\left(\frac{L}{2} - s_{19}\right)$	$\frac{3\sqrt{2}}{8}(P - P_I)\left(\frac{L}{2} - s_{19}\right)$

this contribution, as what was done in the previous models, may result in less accurate predictions.

Finally, inserting Eqs. (8.23) and (8.36) into Eq. (8.31) gives

$$\nu_{zx}^* = \frac{0.342\ 105 + 0.297\ 729[1 + 6(1 + \nu)k_1]cR}{1 + 0.595\ 458[25 + 26(1 + \nu)k_1]cR}, \quad (8.37)$$

where use has been made of Eqs. (8.27) and (8.29).

Table 8.6 Complementary energy in the six struts

n	$\int_0^L \frac{N_n^2}{2EA} ds_n$	$\int_0^L \frac{k_1 V_{n\eta}^2}{2GA} ds_n$	$\int_0^L \frac{k_1 V_{n\zeta}^2}{2GA} ds_n$	$\int_0^L \frac{M_{n\eta}^2}{2EI} ds_n$	$\int_0^L \frac{M_{n\zeta}^2}{2EI} ds_n$
1	$\frac{(2P + P_I)^2 L}{64EA}$	$\frac{9k_1 P_I^2 L}{64GA}$	$\frac{k_1 P_I^2 L}{32GA}$	$\frac{(3P^2 + P_I^2)L^3}{384EI}$	$\frac{3P_I^2 L^3}{256EI}$
3	$\frac{9(P + P_I)^2 L}{16EA}$	0	$\frac{k_1(P - P_I)^2 L}{16GA}$	$\frac{(P - P_I)^2 L^3}{192EI}$	0
4	$\frac{(P + 2P_I)^2 L}{64EA}$	$\frac{9k_1 P^2 L}{64GA}$	$\frac{k_1 P^2 L}{32GA}$	$\frac{(P^2 + 3P_I^2)L^3}{384EI}$	$\frac{3P^2 L^3}{256EI}$
8	$\frac{(2P - 3P_I)^2 L}{16EA}$	0	$\frac{k_1 P_I^2 L}{16GA}$	$\frac{(3P^2 + P_I^2)L^3}{192EI}$	0
18	$\frac{(-3P + 2P_I)^2 L}{16EA}$	0	$\frac{k_1 P^2 L}{16GA}$	$\frac{(P^2 + 3P_I^2)L^3}{192EI}$	0
19	$\frac{(P + P_I)^2 L}{64EA}$	$\frac{9k_1(P - P_I)^2 L}{64GA}$	$\frac{k_1(P - P_I)^2 L}{32GA}$	$\frac{(P - P_I)^2 L^3}{384EI}$	$\frac{3(P - P_I)^2 L^3}{256EI}$

The closed-form formula given in Eq. (8.37) for calculating the effective Poisson's ratio of open-cell foams shows that ν_{zx}^* is explicitly dependent on the relative foam density (R), the size and shape of the strut cross section (c and k_1), and Poisson's ratio of the strut material (ν). Compared with the corresponding formulas provided in the existing models, the expression for ν_{zx}^* given by Eq. (8.37) incorporates more parameters and can be readily reduced to specific cases.

8.2.2 Numerical results

To illustrate the application of the new model developed in the preceding subsection, a parametric study of sample cases has been conducted for 3-D open-cell carbon foams, whose modeling motivated the work presented in this chapter. Following Sihm and Roy^[6], Young's modulus (E) and Poisson's ratio (ν) of the carbon strut material are, respectively, taken to be 15.61 GPa and 0.33. The shapes used for the strut cross section here include circle, square, equilateral triangle and Plateau border, among which the last one is believed to be closest to real struts.

For carbon foams with Plateau border strut cross sections, the effective

Young's modulus (E_z^*) and Poisson's ratio (ν_{zx}^*) varying with the relative foam density (R) predicted by the current model are graphically illustrated in Figs. 8.11 and 8.12, where they are also compared to the predictions of four existing models.

Gibson and Ashby^[2] used a micromechanics model of staggered cubic cells for an open-cell foam and showed that

$$\frac{E_z^*}{E} = KR^2, \quad (8.38)$$

where the constant K was found to be close to unity after curve fitting the available experimental data (mostly on polymer foams). Warren and Kraynik^[8] found that for incompressible (i.e., $\nu = 0.5$) struts with Plateau border cross sections, $K = 0.979$, which is very close to $K = 1$ proposed by Gibson and Ashby^[2]. This explains the good agreement between the predictions of these two models, as illustrated in Fig. 8.11.

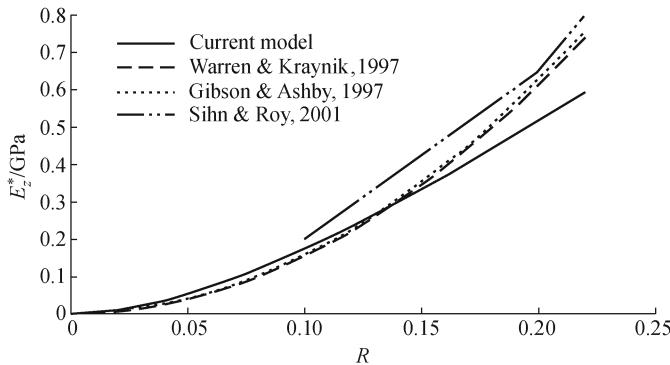


Fig. 8.11 Young's modulus vs. relative foam density.

Figure 8.11 shows that the values of E_z^* predicted by the current model and those by the two afore-mentioned models are very close for low-density foams (with $R < 0.15$). For high-density foams (with $R > 0.15$), however, this is no longer the case; discrepancies between the predictions of the current model and those of the two existing models increase with R , as shown in Fig. 8.11. This indicates that the transverse shearing effect, which is incorporated in the current model but excluded in the two earlier models, does not play a significant role in deformations of low-density foams, where the dominant mechanism is strut bending. The shearing effect is related to the strut slenderness ratio L/c , where c is the radius of gyration and L is the strut length. When L/c is large (and the relative density of the foam is small), the strut can be simplified to a Bernoulli–Euler beam so that the shear effect can be neglected. However, for high-density foams strut shearing becomes a very important factor and needs to be accounted for in order to obtain accurate predictions^[20].

The finite element (FE) method offers an alternative approach to deformation analyses of structural foams. An FE model was developed by Sihm and Roy^[6] to calculate Young's modulus and Poisson's ratio of carbon foams with R ranging from 0.1 to 0.35. As shown in Fig. 8.11, the FE model predicts higher values of E_z^* than those by the current analytical model. The reason for this is that according to the composite homogenization theory^[28], the FE model of Sihm and Roy^[6], developed using a displacement formulation, is expected to provide an upper bound estimate of actual value of the effective Young's modulus, while the current model, based on the principle of minimum complementary energy, should furnish the best lower bound solution^[23,25].

The predicted values of the effective Poisson's ratio (ν_{zx}^*) varying with R are illustrated in Fig. 8.12. According to our new model, ν_{zx}^* is 0.342 at $R = 0$ and decreases gradually as R increases. Gibson and Ashby^[2] quoted some scattered experimental data on ν_{zx}^* , ranging from 0.15 to 0.4, of open-cell foams with $R < 0.1$ and proposed 1/3 to be a reasonable value for ν_{zx}^* . Fig. 8.12 shows that ν_{zx}^* predicted by the current model is very close to 1/3 for $R < 0.1$. Comparisons are also made with the results given by Warren and Kraynik^[7], as illustrated in Fig. 8.12. Clearly, their predicted values of ν_{zx}^* are higher, as noted in Section 8.2.1. In addition, Fig. 8.12 reveals that the values of ν_{zx}^* predicted by the FE model of Sihm and Roy^[6] agree well with those obtained by the current model for $R > 0.04$.

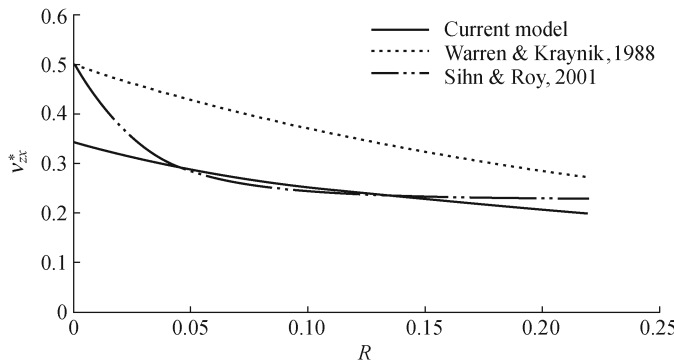


Fig. 8.12 Poisson's ratio vs. relative foam density.

The effects of strut cross section shapes on E_z^* and ν_{zx}^* at various values of R are graphically illustrated in Figs. 8.13 and 8.14. It is seen from Fig. 8.13 that E_z^* is the highest for the Plateau border strut cross section, followed by the equilateral triangle, square and circular strut cross sections. This descending order conforms to what was observed by Warren and Kraynik^[8]. The order of influence of the strut cross section shape on ν_{zx}^* is opposite to that on E_z^* , as shown in Fig. 8.14. This agrees with that stated by Warren and Kraynik^[7]. At $R = 0.05$, the maximum relative differences in E_z^* and ν_{zx}^* ,

resulting from the use of different shapes of strut cross sections, are 34.5% and 7.2%, respectively. This implies that the Young's modulus (E_z^*) is much more sensitive to the strut cross section shape than the Poisson's ratio (ν_{zx}^*).

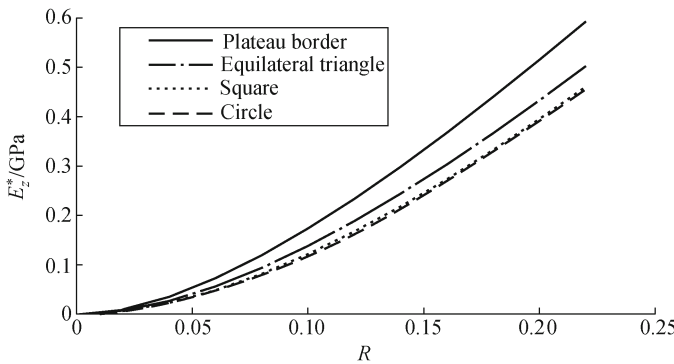


Fig. 8.13 Effects of strut cross section shapes on Young's modulus.

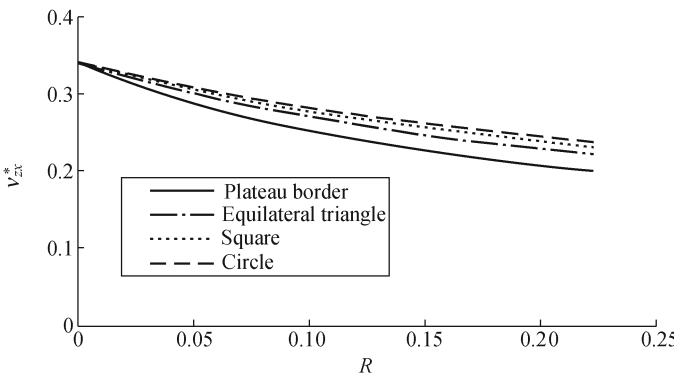


Fig. 8.14 Effects of strut cross section shapes on Poisson's ratio.

8.2.3 Summary

A micromechanics model is developed for 3-D open-cell foams using a tetrakaidecahedral unit cell sitting on a BCC lattice and subjected to compression on its two opposite square faces. This model is based on Castiglione's second theorem and is of the mechanics-of-materials type. All three deformation mechanisms (i.e., stretching, shearing and bending) of the cell struts possible under the specified loading are incorporated, and four different strut cross section shapes (i.e., circle, square, equilateral triangle and Plateau border) are dealt with in a unified manner in this model, unlike in earlier models.

Two closed-form formulas for calculating the effective Young's modulus and Poisson's ratio of open-cell foams are derived using the composite homogenization theory. These formulas contain more parameters than those included in existing models, which ignore the transverse shearing effect. The two formulas explicitly show that the effective elastic properties of open-cell foams depend on the relative foam density, the shape and size of the strut cross section, and the elastic properties of the strut material.

As a direct application of the new model, a parametric study of sample cases involving the four strut cross section shapes and various values of the relative foam density is conducted for carbon foams. The predicted values of the effective Young's modulus agree well with those obtained using two existing analytical models for low-density foams, and the values of the effective Poisson's ratio predicted by the current model are in good agreement with those results based on the available experimental data and finite element analyses.

8.3 Random cell model incorporating cell shape and strut cross-sectional area irregularities

In this section, a random cell model is presented for open-cell foams that contain two types of co-existing imperfections – irregular cell shapes and non-uniform strut cross-sectional areas (SCSAs). In Subsection 8.3.1, foams with different degrees of cell shape irregularity and SCSA non-uniformity are first constructed using the Voronoi tessellation technique. Twenty finite element (FE) models are then developed using the constructed Voronoi diagrams to calculate the effective Young's moduli, Poisson's ratios and shear moduli of the foams. Each of these diagrams (specimens) contains 125 tetrakaidecahedral cells. In Subsection 8.3.2, a mesh sensitivity study is first performed to determine the appropriate number of cells to be included in each specimen and the suitable number of specimens to be used in statistical analysis. This is followed by an investigation into the elastic behavior (isotropic or anisotropic) of the foams based on the Voronoi diagrams and the FE models. Finally, a parametric study for sample cases involving various cell shape and cross-sectional area irregularities is conducted, with the simulation results presented and discussed. A summary is provided in the last subsection.

8.3.1 Analysis

3-D open-cell foams (e.g., graphitic carbon foams) are often produced through a bubble forming process. As a result, microstructures of such foams are controlled by the principle of minimum surface energy. This indicates that the morphology of such a 3-D open-cell foam may be best represented by

packed tetrakaidecahedral cells, since tetrakaidecahedron is known to be the only polyhedron that can pack with identical units to fill space (Fig. 8.15) and nearly minimize the surface energy^[10].

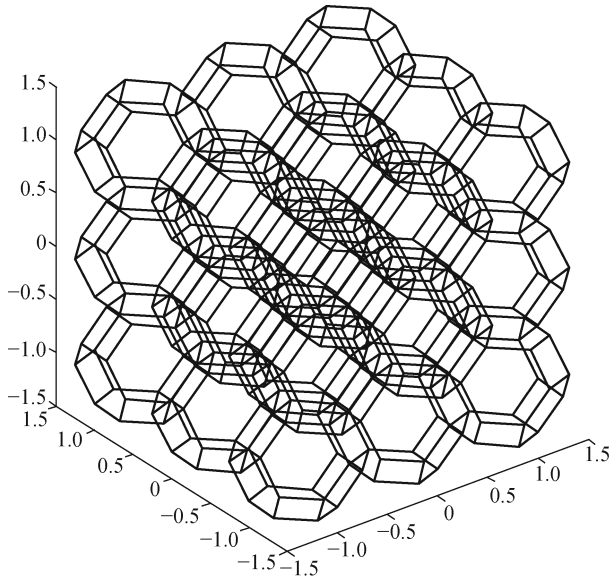


Fig. 8.15 A regular foam sample with 27 complete cells.

Due to the similarity between the mathematical procedure of the Voronoi tessellation and the physics of foam production, the Voronoi tessellation technique is a natural choice for describing the microstructure of a foam resulting from a bubble forming process. The Voronoi tessellation of space is fully determined by the initial locations of generating seeds^[30]. Using regularly positioned seeds produces regular Voronoi diagrams. The current analysis starts with a reference model, which is of a tetrakaidecahedral foam structure with cells of regular shapes and struts of uniform cross-sectional areas. This reference model is constructed from a set of regularly packed seeds sitting on a body-centered cubic (BCC) lattice using the Voronoi tessellation technique, as shown in Fig. 8.15. Perturbations are then introduced to the reference model to generate Voronoi diagrams with irregular cell shapes and non-uniform SCSAs^[16,19]. The non-uniformity here and in the sequel means that the cross-sectional area of each strut may differ from that of any other strut, although each strut is regarded as having a constant cross-sectional area along its length and the cross-sectional shape remains the same for all the struts.

8.3.1.1 Spatially periodic random foams with cell shape and SCSA variations

There are two methods to construct 3-D random foam models using the Voronoi tessellation technique. One is to first build a Voronoi tessellation that is larger than the foam specimen of interest from a set of randomly placed seeds. Then, a bounding parallelepiped with dimensions same as those of the foam specimen is imposed to trim off the extraneous layer of the tessellation^[15]. This layer contains Voronoi cells that do not resemble (irregular) cells of a foam. It should be noted that the model so obtained is not periodic and many cells must be included in the specimen to avoid the edge effect. In addition, only displacement boundary conditions can be applied in this case. The second method is to use a set of seeds of periodic symmetry^[31]. At the beginning, a pre-set number of seeds are generated within a parallelepiped having the desired dimensions. Then, the position of each seed within the parallelepiped is copied to 26 identical parallelepipeds adjacent to or sitting at the corners of the original parallelepiped. Finally, the Voronoi tessellation technique is applied to all of the seeds within the 27 parallelepipeds. Part of the resulting Voronoi tessellation inscribed by the center (original) parallelepiped can then be taken out as the periodic specimen of the specified size. In the current study, the second method is adopted to generate seeds of periodic symmetry, and the needed Voronoi diagrams are subsequently constructed using the program Qhull developed at the Geometry Center, the University of Minnesota – Twin Cities (now available at <http://www.geom.uiuc.edu/software/qhull/>).

The irregularity of cell shapes is determined by the irregular distribution of the seeds. By perturbing the locations of the seeds sitting on a BCC lattice, the coordinates of a perturbed seed k can be obtained as^[16]

$$x_i^k = \bar{x}_i^k + aL\varphi_i^k, \quad (8.39)$$

where $\bar{x}_i^k (i \in \{1, 2, 3\})$ are the coordinates of the same seed k in the initially regular lattice, L is the height of a regular tetrakaidecahedron, $\varphi_i^k (\in [-1, 1])$ is a random variable with a uniform distribution, and $a (\in [0, 1])$ is the amplitude used to quantify the degree of cell shape irregularity. The smaller a is, the more regular the Voronoi diagram will be, as illustrated in Fig. 8.16. Regular 3-D foams are obtained when $a = 0$, and completely irregular foams are defined when $a = 1.0$. Fig. 8.16 shows foam samples with different degrees of cell shape irregularity. Each sample includes 125 complete tetrakaidecahedral cells. It is noted from Fig. 8.16 that the two foam specimens with $a = 0.5$ and $a = 1.0$ respectively have very similar cell shapes. This is because when a is greater than 0.5, the cubic space reachable by a seed, whose coordinates are defined by Eq. (8.39), overlaps with those spaces reachable by its adjacent seeds, thereby leading to highly irregular cells in the resulting Voronoi diagram before a reaches 1.0.

As indicated in Eq. (8.39), for given relative density and amplitude of cell shape irregularity, the predicted properties of a foam having uniform SCSAs

depend on the set of stochastic variables $\varphi_i^k (i \in \{1, 2, 3\}; k \in \{1, \dots, M\}, M = \text{the total number of seeds})$. These variables are produced using a generator of uniform random numbers. To obtain the expectation values of the foam properties, a significant number of simulations with various sets of $\varphi_i^k (\in [-1, 1])$ are needed. In the current work, twenty samples are analyzed for each value of a . The choice of twenty specimens (samples) will be discussed further in Subsection 8.3.2.

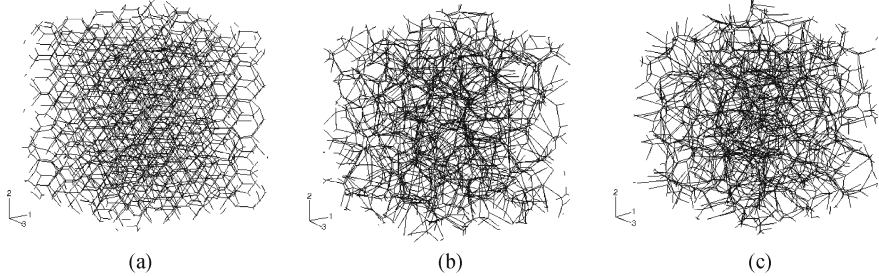


Fig. 8.16 Foam samples with varying a : (a) $a = 0.1$, (b) $a = 0.5$, (c) $a = 1.0$.

After the cell shapes are determined, statistical variations of SCSAs can be introduced to the uniform SCSA, A_0 , given by

$$A_0 = \frac{RL_1L_2L_3}{\sum_{j=1}^N l_j}, \quad (8.40)$$

where R is the relative foam density, L_1, L_2 and L_3 are the dimensions of the foam sample (specimen), l_j is the length of strut j , and N is the total number of struts. To this end, each strut is assigned a random area given by^[19]

$$A_j = wA_0(1 + b\psi_j), \quad (8.41)$$

where $b (\in [0, 1])$ is the amplitude used to quantify the degree of non-uniformity of SCSAs, $\psi_j (\in [-1, 1])$ is a random variable with a uniform distribution, and w , called the normalizing factor, is defined by

$$w = \frac{\sum_{j=1}^N l_j}{\sum_{j=1}^N (1 + b\psi_j)l_j} \quad (8.42)$$

to ensure that the relative density remains unchanged with the variation of SCSAs. Given R , a , b and the set of random variables $\varphi_i^k (i \in \{1, 2, 3\}; k \in \{1, \dots, M\})$, the predicted foam properties depend on the set of random

variables $\psi_j (j \in \{1, 2, \dots, N\})$, which are generated independently of φ_i^k . Statistically, it is required to run sufficient simulations with different sets of ψ_j to get the expectation values of the foam properties. In the current study, twenty foam samples, with a remaining fixed for each sample, will be analyzed for each given value of b . Similarly, twenty samples are considered for each value of a when b is held constant, as indicated earlier. The reason for choosing twenty specimens will be provided in Subsection 8.3.2.

8.3.1.2 Finite element analysis

A finite element study is performed to obtain the elastic properties of foams with cell shape and SCSA irregularities using the commercial software package ABAQUS 6.3^[32]. Graphitic carbon foams are considered here. The Young's modulus E_s and Poisson's ratio ν_s of the carbon strut material are, respectively, taken to be 15.61 GPa and 0.33^[33,34]. Each strut is represented using a three-node beam element (element type B32 in ABAQUS), which involves bending, stretching, twisting and shearing deformation mechanisms. Struts are rigidly connected at the joints by node sharing. A preliminary study has shown that using such a beam element to model each strut is sufficient for convergence. It is noted that exceptionally short struts do exist in foam specimens having highly irregular cell shapes. Typical beam elements cannot well represent these short struts. However, since short struts only account for a small fraction (a few percent) of the total number of struts, the effect incurred from using inappropriate element types is negligible^[15].

Uniaxial compressive tests on foam specimens along three orthogonal directions, x_1 , x_2 and x_3 , are considered in three separate analyses to obtain the effective Young's moduli and Poisson's ratios of the foam relative to the three directions. In each analysis, a small effective compressive strain (e.g., -0.001) is applied to the foam specimen in the loading direction through controlling displacements. This constrains the lateral deflections of slender struts in a random foam model so that no local buckling of struts will take place. The effective Young's moduli E_1 , E_2 and E_3 of the foam are given by

$$E_1 = \frac{-F_1}{\varepsilon_1 L_2 L_3}, \quad (8.43)$$

$$E_2 = \frac{-F_2}{\varepsilon_2 L_1 L_3}, \quad (8.44)$$

$$E_3 = \frac{-F_3}{\varepsilon_3 L_1 L_2}, \quad (8.45)$$

where ε_1 , ε_2 and ε_3 , all being -0.001 , are the applied compressive strains, and F_1 , F_2 and F_3 are, respectively, the total reaction forces along x_1 , x_2 and x_3 directions on the prescribed boundary, which are to be obtained from the finite element analysis. The effective Poisson's ratios are determined as

$$\nu_{12} = -\frac{u_2^1}{\varepsilon_1 L_2}, \quad \nu_{13} = -\frac{u_3^1}{\varepsilon_1 L_3}, \quad (8.46a, b)$$

$$\nu_{21} = -\frac{u_1^2}{\varepsilon_2 L_1}, \quad \nu_{23} = -\frac{u_3^2}{\varepsilon_2 L_3}, \quad (8.47a, b)$$

$$\nu_{31} = -\frac{u_1^3}{\varepsilon_3 L_1}, \quad \nu_{32} = -\frac{u_2^3}{\varepsilon_3 L_2}, \quad (8.48a, b)$$

where $u_j^i (i, j \in \{1, 2, 3\})$ is the lateral displacement (extension) in the x_j direction perpendicular to the loading direction x_i . Note that u_j^i are the effective displacements of a foam model (a parallelepiped) along the three directions.

To determine the effective shear modulus G_{12} , a biaxial loading test is simulated. A tensile strain $\varepsilon_1 = 0.001$ in the x_1 direction and a compressive strain $\varepsilon_2 = -0.001$ in the x_2 direction are applied simultaneously. Then, the effective shear modulus G_{12} , defined by $G_{12} = \tau_{12}/\gamma_{12}$, is given by

$$G_{12} = \frac{F_1/L_2 - F_2/L_1}{2L_3(\varepsilon_1 - \varepsilon_2)}. \quad (8.49)$$

Similarly, the other two shear moduli G_{23} and G_{31} are obtained as

$$G_{23} = \frac{F_2/L_3 - F_3/L_2}{2L_1(\varepsilon_2 - \varepsilon_3)}, \quad (8.50)$$

$$G_{31} = \frac{F_3/L_1 - F_1/L_3}{2L_2(\varepsilon_3 - \varepsilon_1)}. \quad (8.51)$$

In modeling uniaxial or biaxial loading tests, displacement boundary conditions are typically used^[15,20,21,35,36]. However, displacement boundary conditions that only restrain normal displacements may underestimate foam properties^[37]. Since the specimen is cut out of an infinite structure that can be regarded as being periodic, spatially periodic boundary conditions should be applied to ensure that the predicted properties of the specimen are representative of those of the foam material^[18,37,38]. The specimen obtained by following the procedure described in Subsection 8.3.1.1 is periodic, i.e., each node on one face (e.g., v^-) has a matched node on the opposite face of the specimen (e.g., v^+), as shown in Fig. 8.17. For a uniaxially deformed specimen subjected to prescribed strain ε_i , the periodic boundary conditions may be represented by

$$u_i^{k^+} - u_i^{k^-} = \varepsilon_i(x_i^{k^+} - x_i^{k^-}), \quad \omega_i^{k^+} - \omega_i^{k^-} = 0, \quad i \in \{1, 2, 3\}, \quad (8.52)$$

where $x_i^{k^+}$ and $x_i^{k^-}$ are, respectively, the positions of the matched nodes k^+ and k^- on the specimen boundary faces with outward unit normal vectors e_i and $-e_i$, $u_i^{k^+}$ and $u_i^{k^-}$ are, respectively, the normal displacement components of k^+ and k^- , and ω_i^+ and ω_i^- are, respectively, the rotations of k^+ and k^- .

The periodic boundary conditions given in Eq. (8.52) can be implemented by using the option EQUATION in ABAQUS and by introducing four reference nodes N0, N1, N2 and N3, which define three two-node AXIAL connector

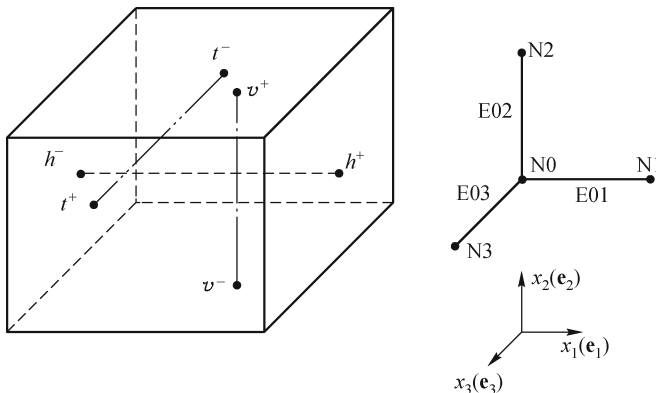


Fig. 8.17 Matched nodes for implementing spatially periodic boundary conditions.

elements E01, E02 and E03 (Fig. 8.17). The three connector elements intersect at reference node N0 and are located along the e_1 , e_2 and e_3 directions, respectively. Nodes N1, N2 and N3 are allowed to move axially only along their associated connector elements. The degrees of freedom of the matched nodes may be coupled with those of the reference nodes by

$$u_i^{k^+} - u_i^{k^-} - \frac{x_i^{k^+} - x_i^{k^-}}{X_i^{K^+} - X_i^{K^-}}(U_i^{K^+} - U_i^{K^-}) = 0, \quad \omega_i^{k^+} - \omega_i^{k^-} - (\Omega_i^{K^+} - \Omega_i^{K^-}) = 0, \quad (8.53)$$

where X_i , U_i and Ω_i are, respectively, the positions, displacements and rotations of the reference nodes, the superscript “ K^+ ” denotes reference nodes N1, N2 and N3, and the superscript “ K^- ” means reference node N0. For uniaxial compression along $-e_2$, say, node N0 is fixed and a displacement corresponding to $\varepsilon_2 = -0.001$ is applied at node N2. The reaction force induced in element E02, called ETF1 in ABAQUS, can be substituted into Eq. (8.44) for F_2 , and the axial displacements of elements E01 and E03, called EU1 in ABAQUS, can be inserted into Eqs. (8.47a,b) for u_1^2 and u_3^2 , respectively.

8.3.2 Results and discussion

8.3.2.1 Mesh sensitivity

Before proceeding to model 3-D foams having irregular cell shapes and non-uniform SCSAs, an important issue that needs to be resolved is to determine the appropriate number of cells to be included in a specimen and the appropriate number of specimens (S) to be analyzed for each type of foams. Based on a finite element analysis of random heterogeneous materials using representative volume elements (RVEs) of various sizes, Kanit et al.^[39] found that

for a given precision the effective elastic properties of the materials can be obtained through using either a large RVE accompanied by a small number of specimens or a small RVE accompanied by a large number of specimens. This indicates that the number of specimens needs to be carefully chosen for accurate predictions. As mentioned earlier, in the current study the number of specimens is initially taken to be 20 (i.e., $S = 20$), which is the same as that used by Li, Gao and Subhash^[37]. Four families of specimens, with each containing a same number of cells C ($C \in \{8, 27, 64, 125, 216\}$), are considered to determine the appropriate C . For each family, twenty specimens are modeled to obtain the mean values m and standard deviations δ of the effective properties. The shape irregularity amplitude a and the relative density R remain to be 0.5 and 0.01, respectively, for all of the four families of specimens. The obtained numerical results of E_1 , G_{12} and ν_{12} are graphically shown in Figs. 8.18–8.20. The results for the other elastic properties, including E_2 , E_3 , G_{23} , G_{31} , ν_{23} and ν_{31} , have similar trends of variation, as displayed in Figs. 8.18–8.20.

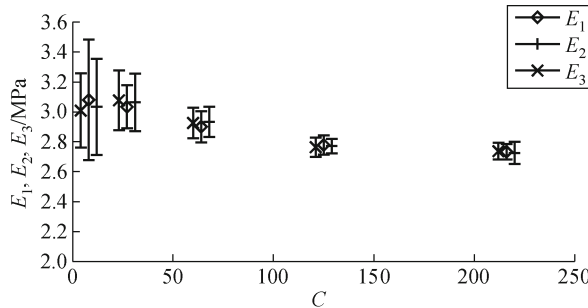


Fig. 8.18 Young's modulus (E_1) vs. the number of cells.

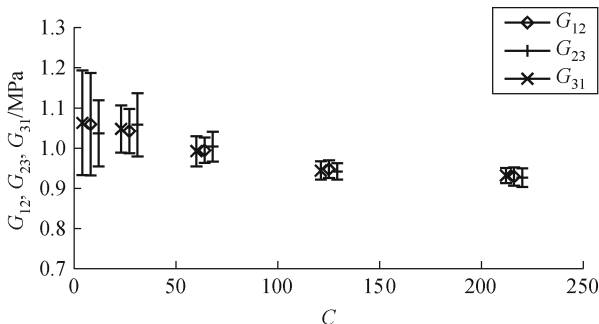


Fig. 8.19 Shear modulus (G_{12}) vs. the number of cells.

From Figs. 8.18–8.20 it is seen that as the number of cells (C) increases, the mean values of the effective Young's modulus E_1 and the effective shear

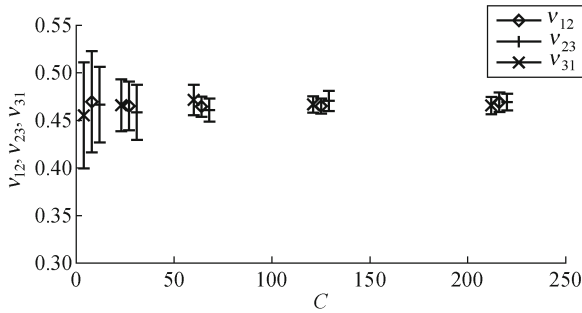


Fig. 8.20 Poisson's ratio (ν_{12}) vs. the number of cells.

modulus G_{12} decrease slightly, while those of the effective Poisson's ratio ν_{12} remain almost the same. The standard deviations (δ) of all the three properties are reduced with the increase of C for $C \leq 125$. When $C = 125$, δ is small (no more than 4% of the mean value) for all the three properties. Further increase of C does not considerably lower the value of δ for E_1 , but leads to increased δ values for G_{12} and ν_{12} . Therefore, $C = 125$ is chosen as the number of cells to be included in each specimen.

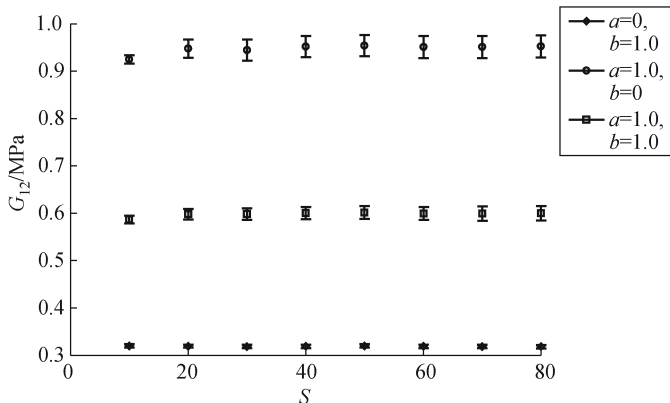


Fig. 8.21 The shear modulus varying with the number of specimens.

In order to evaluate whether the initially chosen number of specimens ($S = 20$) is an appropriate one, finite element analyses are conducted on three types of foams: the completely irregular foams with a uniform SCSA ($a = 1.0$, $b = 0$), the regular foams with completely non-uniform SCSAs ($a = 0$, $b = 1.0$), and the completely irregular foams with completely non-uniform SCSAs ($a = 1.0$, $b = 1.0$). Each specimen contains 125 cells and has a relative density $R = 0.01$. The mean values (m) and standard deviations (δ) of the effective shear modulus G_{12} are obtained for the three types of foams using various values of S ($S \in \{10, 20, 30, 40, 50, 60, 70, 80\}$), which are

shown in Fig. 8.21. It is seen from Fig. 8.21 that there is a slight increase in the mean values of G_{12} as S increases from 10 to 20, and further increase of S does not lead to any significant change in the values of m and δ . Hence, the initial choice of $S = 20$ as the number of specimens is appropriate.

8.3.2.2 Isotropy of the effective properties

A total of 38 cases, which can be classified into four groups, as listed in Table 8.7, are analyzed in this study. Controlling parameters include the degree of cell shape irregularity (amplitude a), the degree of SCSA non-uniformity (amplitude b), the relative density (R) and the strut cross-sectional shape. The shapes for the strut cross section examined here include circle, square, equilateral triangle and Plateau border, among which the last one is believed to be closest to real strut cross-sectional shapes^[33]. Hence, most of the simulations to be presented below are conducted for foams with Plateau border strut cross sections, as indicated in Table 8.7. Except for the cases with $a = 0$ and $b = 0$ (totaling 5), the mean values and standard deviations of the elastic properties for each case listed in Table 8.7 are obtained from the results of the finite element analyses performed on twenty specimens. For the former (i.e., perfect foams with different values of R), only one specimen is needed in each case. The maximum and minimum mean values (m_{\max} and m_{\min}) and the maximum standard deviations (δ_{\max}) of E_1/E_2 , E_2/E_3 , E_3/E_1 , ν_{12}/ν_{21} , ν_{23}/ν_{32} and ν_{31}/ν_{13} are given in Table 8.8. In addition, to examine whether the shear relation $G = E/[2(1 + \nu)]$ is satisfied, which is required for material isotropy, the results for m_{\max} , m_{\min} and δ_{\max} of G_{12}/G_{12}^T , G_{23}/G_{23}^T and G_{31}/G_{31}^T are also listed in Table 8.8, where the values of G_{12}^T , G_{23}^T and G_{31}^T are, respectively, obtained using $G_{12}^T = E_1/[2(1 + \nu_{12})]$, $G_{23}^T = E_2/[2(1 + \nu_{23})]$ and $G_{31}^T = E_3/[2(1 + \nu_{31})]$. An inspection of Table 8.8 indicates that the extreme mean values of each of the nine ratios are very close to unity, and the maximum standard deviations are all small (less than 7% of the corresponding mean values). Therefore, it can be concluded that the elastic response of

Table 8.7 Modeling cases

Group number	Cross-sectional shape	R	a	b	Remarks
1	Plateau border	0.01	0,0.1,0.2, 0.3,0.4, 0.5,0.8,1.0	0	Effects of cell shape irregularity
2	Plateau border	0.01	0,1.0	0,0.2,0.5, 0.8,1.0	Effects of SCSA non-uniformity
3	Plateau border	0.01,0.06, 0.11,0.16, 0.22	0,1.0		Effects of the relative density
4	Plateau border, equilateral triangle, square, circle	0.01,0.11	1.0	1.0	Effects of the strut cross-sectional shape

the foams studied is isotropic regardless of changes in cell shape irregularity, SCSA non-uniformity, relative density and strut cross-sectional shape. Accordingly, only three properties, namely, E_1 , G_{12} and ν_{12} , will be discussed in the sequel. Similar trends can be observed for other effective elastic properties.

Table 8.8 Isotropy of elastic properties

Ratio of elastic properties	m_{\max}	m_{\min}	δ_{\max}
E_1/E_2	1.023 677	0.991 939	0.065 771
E_2/E_3	1.014 180	0.986 012	0.055 143
E_3/E_1	1.010 613	0.981 335	0.066 920
ν_{12}/ν_{21}	1.023 682	0.993 173	0.065 750
ν_{23}/ν_{32}	1.014 122	0.981 473	0.055 130
ν_{31}/ν_{13}	1.010 553	0.981 386	0.067 005
G_{12}/G_{12}^T	1.003 098	0.993 218	0.022 807
G_{23}/G_{23}^T	1.007 912	0.996 438	0.019 437
G_{31}/G_{31}^T	1.008 779	0.996 548	0.023 663

8.3.2.3 Effects of cell shape irregularity

The effects of irregular cell shapes on elastic properties are analyzed for low-density foams having the same relative density (e.g., $R = 0.01$). For each value of a , twenty independent lists of random variables $\varphi_i^k (i \in \{1, 2, 3\}; k \in \{1, \dots, M\})$ are used to generate twenty foam samples, each of which has a unique arrangement of struts. Finite element analyses are then conducted on the twenty samples, and the mean values and standard deviations of the effective properties, i.e., the Young's moduli, Poisson's ratios and shear moduli, are obtained.

Figures 8.22–8.24 graphically show the predicted values of the Young's modulus E_1 , shear modulus G_{12} and Poisson's ratio ν_{12} at different values of a . From Figs. 8.22 and 8.23 it is observed that on average, both E_1 and G_{12} increase considerably with increasing a (up to $a = 0.5$) and then stay, respectively, around 2.8 MPa and 0.95 MPa with small variations as a in-

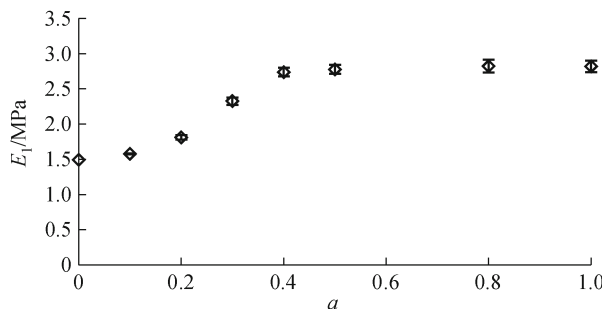


Fig. 8.22 Effects of cell shape irregularity on the Young's modulus E_1 (with $R = 0.01$)

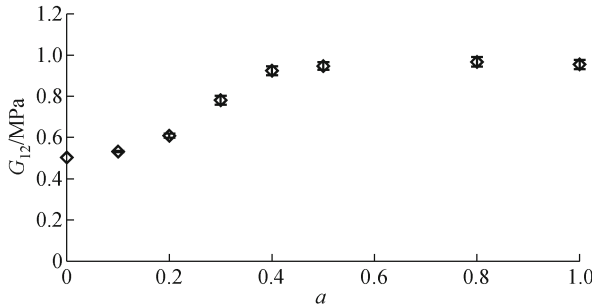


Fig. 8.23 Effects of cell shape irregularity on the shear modulus G_{12} (with $R = 0.01$).

creases further. This implies that foams with $a = 0.5$ may be regarded as being highly irregular. Further increase of a can no longer significantly lower the regularity of cell shapes, as noted in Subsection 8.3.1.1. The mean values of E_1 and G_{12} at $a = 1.0$ are, respectively, 86.4% and 88.6% higher than their corresponding values at $a = 0$. The regular foam (with $a = 0$) is the weakest in terms of the elastic moduli. This conforms to what was observed by Van der Burg et al.^[15]. As a increases, the mean values of the Poisson's ratio ν_{12} , however, decrease slightly, as shown in Fig. 8.24. Figure 8.25 indicates the reduction of normalized SCSA, A_i/A_r , with the increase of a (up to $a = 0.5$), which undermines the moduli. Here A_r and A_i are, respectively, the SCSAs of regular and irregular foams. For the same reason as that for the effects of a on the moduli, the mean values of A_i/A_r change insignificantly when $a > 0.5$. These observations are similar to what was found by Li et al.^[37] for 2-D imperfect cellular solids. To explore the reason for strong dependence of the moduli on cell shape irregularity, Van der Burg et al.^[15] visualized the stress distributions in the struts of a foam specimen loaded by uniaxial tension. They found that as the foam becomes less regular, stretching deformations in the struts are fostered, which is similarly observed for imperfect

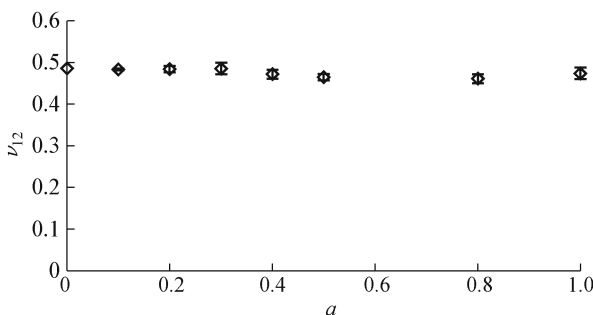


Fig. 8.24 Effects of cell shape irregularity on the Poisson's ratio ν_{12} (with $R = 0.01$).

honeycombs by Li et al.^[37]. Van der Burg et al.^[15] further attributed the enhancement in the foam moduli to the appearance of chains of struts with strong axial stresses along the loading direction when the cells in the foam get irregular. These chains were believed to transmit the applied load from one cell face to another in the specimen. This stiffening effect substantially outweighs the loss in stiffness caused by the slight decrease in the SCSA, thereby leading to a significant increase of the elastic moduli.

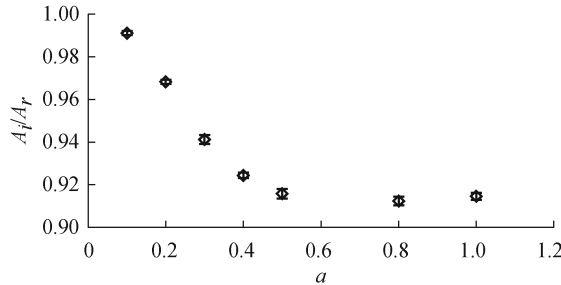


Fig. 8.25 Effects of cell shape irregularity on the non-dimensional SCSA (with $R = 0.01$).

Roberts and Garboczi^[18] analyzed random, isotropic open-cell foams with a roughly uniform cell size. They also used the Voronoi tessellation technique to generate foam models, each containing approximately 125 cells, and applied periodic boundary conditions to each foam specimen in their finite element analyses. Their foam models have shapes similar to the ones generated here with $a = 0.1$ (Fig. 8.16a). Based on five specimens, they obtained the mean values of the elastic properties as $E = 2.062\ 44$ MPa, $G = 0.705\ 01$ MPa and $\nu = 0.44$. The Young's modulus and Poisson's ratio of the solid strut material used in their study are, respectively, $E_s = 1$ GPa and $\nu_s = 0.2$. To compare with their results, finite element simulations of five specimens having the same R , E_s and ν_s as theirs are conducted in this study. Each specimen contains 125 cells, as shown in Fig. 8.16a, and has a relative density of 0.05. The mean values of the Young's modulus E_1 , the shear modulus G_{12} and the Poisson's ratio ν_{12} predicted in the current study are, respectively, 2.051 36 MPa, 0.713 36 MPa and 0.437 11, which are very close to the predictions of Roberts and Garboczi^[18] mentioned above.

8.3.2.4 Effects of SCSA non-uniformity

For three-dimensional open-cell foams, the influence of SCSA variations on the elastic properties is still unclear. The regular foams with $a = 0$, the irregular foams with $a = 0.3$, and the completely random foams with $a = 1.0$, all having non-uniform SCSAs, are therefore analyzed here. Four values of the SCSA non-uniformity amplitude, namely, $b = 0.2, 0.5, 0.8$ and 1.0 , are used for each of the three values of a . When $b = 1.0$, SCSA variations are completely random. For each pair of a and b , twenty foam samples are

modeled using independent lists of random variables $\varphi_i^k (i \in \{1, 2, 3\}; k \in \{1, \dots, M\})$ and $\psi_j (j \in \{1, \dots, N\})$. The relative density remains to be 0.01 for the samples analyzed here, and more samples with different values of R will be discussed in Subsection 8.3.2.5.

The predicted values of the effective Young's modulus E_1 , shear modulus G_{12} and Poisson's ratio ν_{12} at various values of b are shown in Figs. 8.26–8.28. Figures 8.26 and 8.27 indicate that for all the three values of a considered the elastic moduli E_1 and G_{12} significantly decrease, in a monotonic manner, as b increases. For the regular foams ($a = 0$), both E_1 and G_{12} are reduced by 36% as b changes from 0 to 1.0, while the relative reduction is 37% for fully irregular foams with $a = 1.0$ and 36% for the irregular foams with $a = 0.3$. The Poisson's ratio ν_{12} , however, is negligibly influenced in each case by the values of b , as shown in Fig. 8.28. An inspection of Figs. 8.26–8.28 also reveals that for each value of b the elastic moduli are the highest for the completely irregular foam with $a = 1.0$, the second highest for the irregular foam with $a = 0.3$, and the lowest for the regular foam with $a = 0$, while the Poisson's ratio is slightly lower for the irregular foam with $a = 1.0$ than that for the irregular foam with $a = 0.3$ and that for the regular foam with $a = 0$. This agrees with what has been observed from Figs. 8.22–8.24.

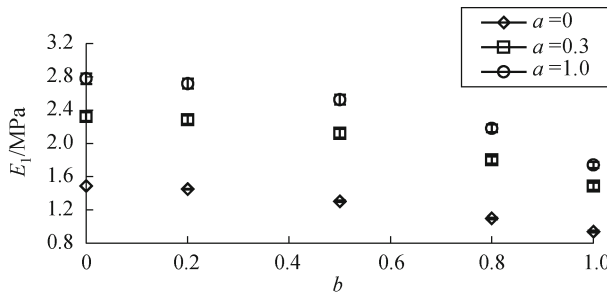


Fig. 8.26 Effects of SCSA variations on the Young's modulus E_1 (with $R = 0.01$).

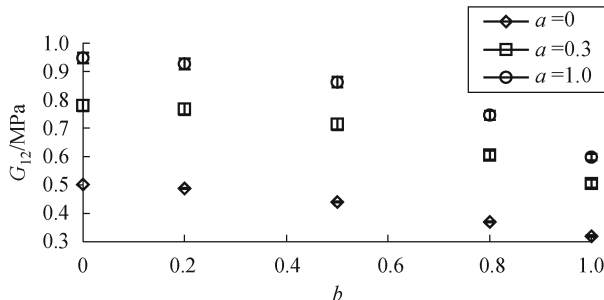


Fig. 8.27 Effects of SCSA variations on the shear modulus G_{12} (with $R = 0.01$).

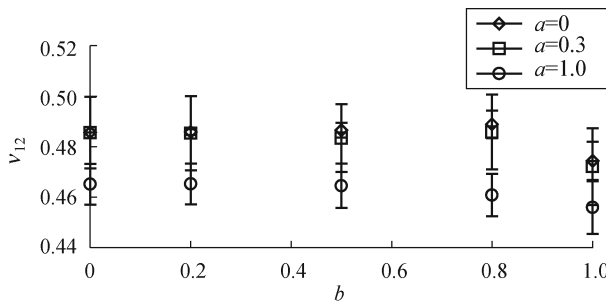


Fig. 8.28 Effects of SCSA variations on the Poisson's ratio ν_{12} (with $R = 0.01$).

Moreover, it can be noticed from Figs. 8.26–8.28 that the differences between the mean values of the elastic moduli for any two of the three types of foams with $a = 1.0$, $a = 0.3$ and $a = 0$ are insignificantly affected by varying b . This implies that the effect of the interaction between the cell shape and SCSA variations on the elastic moduli of each foam is weak. When these two variations are very small (i.e., $a \ll 1$, $b \ll 1$), the weak interaction observed here can be analytically shown to be true for any such imperfect foam with a given value of R .

A further examination of Figs. 8.26 and 8.27 shows that the elastic moduli are affected more by the cell shape irregularity than by the SCSA non-uniformity. This follows from the fact that the elastic moduli for the case with $a = 1.0$, $b = 1.0$ and $a = 0.3$, $b = 0.3$ are larger than the corresponding ones for the case with $a = 0$, $b = 0$ (i.e., foams without imperfections), even though the two elastic moduli are both found to increase as a increases (for fixed values of b) and to decrease with the increase of b (for fixed values of a), as discussed earlier. The trend observed above is based on low-density foams (with $R = 0.01$ here) and differs from that exhibited by foams with high values of R , which will be discussed next.

8.3.2.5 Effects of the relative density

Figures 8.29–8.31 graphically show the results of the effective Young's modulus E_1 , shear modulus G_{12} and Poisson's ratio ν_{12} as a function of the relative density for four types of foams: the regular foams with a uniform SCSA ($a = 0$, $b = 0$), the completely irregular foams with a uniform SCSA ($a = 1.0$, $b = 0$), the regular foams with completely non-uniform SCSAs ($a = 0$, $b = 1.0$), and the completely irregular foams with completely non-uniform SCSAs ($a = 1.0$, $b = 1.0$). The variation of the effective Young's modulus (E_1) with the relative density (R) predicted using the unit cell model developed by Li et al.^[33] is also illustrated in Fig. 8.29 for comparison. In calculating E_1 using the formulas derived by Li et al.^[33] [see Eqs. (25) and (28) there], the effective cross-sectional area of the unit cell (A^*) is taken to be $7L^2$, which is the area projected by the tetrakaidecahedral

unit cell onto the xy -plane (Fig. 3 in [33]). For the foams with a uniform SCSA (i.e., $b = 0$), the relative density (R) depends on the SCSA, as dictated by Eq. (8.40). The relative density of the irregular foams with $b \neq 0$ depends not only on the SCSAs but also on cell shapes, as governed by Eqs. (8.40)–(8.42). Five relative densities, i.e., 0.01, 0.06, 0.11, 0.16 and 0.22, are used for each type of the foams listed above. For the perfect foams (i.e., $a = 0$, $b = 0$) only one model is needed for each density. For the remaining three types of foams with cell shape and/or SCSA imperfections, twenty models are constructed for each density except for the case with $R = 0.01$, which has been dealt with in the previous simulations. The statistical distributions of φ_i^k ($i \in \{1, 2, 3\}$; $k \in \{1, \dots, M\}$) and ψ_j ($j \in \{1, \dots, N\}$) for the models with $R = 0.06, 0.11, 0.16$ and 0.22 remain the same as those for the models with $R = 0.01$.

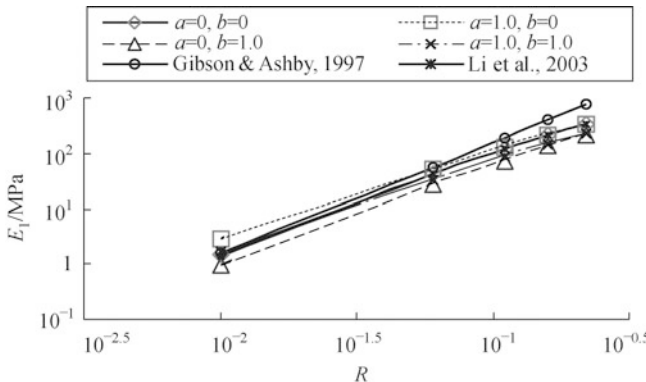


Fig. 8.29 Effects of the relative density on the Young's modulus E_1 (in logarithmic scales).

As shown in Figs. 8.29 and 8.30, E_1 and G_{12} for each of the four types of foams increase monotonically with the relative density. For the perfect foams ($a = 0$, $b = 0$) with the Plateau border strut cross section, Fig. 8.29 shows that the values of the effective Young's modulus (E_1) predicted by the unit cell model developed by Li et al.^[33] are in very good agreement with the finite element results. For a given value of R , the fact that the values of E_1 and G_{12} for the perfect foam are less than those for the foams with $a = 1.0$ and $b = 0$ and greater than those for the foams with $a = 0$ and $b = 1.0$ indicates that the elastic moduli (E_1 and G_{12}) are enhanced by the cell shape irregularity but undermined by the SCSA non-uniformity. This agrees with the observation made earlier based on Figs. 8.22, 8.23, 8.26 and 8.27 for foams with $R = 0.01$. Smaller values of E_1 and G_{12} for the foams with $a = 1.0$ and $b = 1.0$ than those for the perfect foams imply that the stiffness-strengthening effect caused by the cell shape irregularity is less pronounced than the stiffness-weakening effect due to the SCSA non-uniformity. This is the same as that for 2-D imperfect honeycombs found by Li et al.^[37].

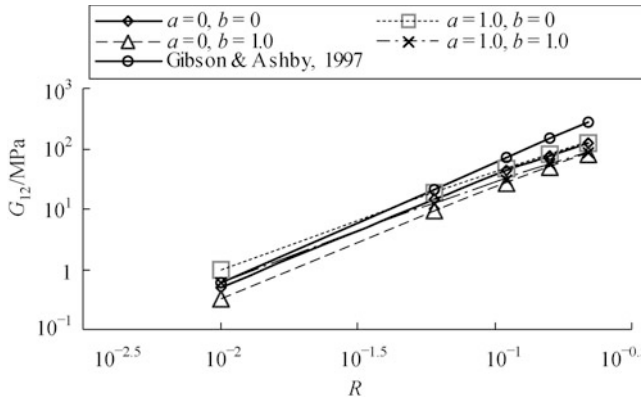


Fig. 8.30 Effects of the relative density on the shear modulus G_{12} (in logarithmic scales).

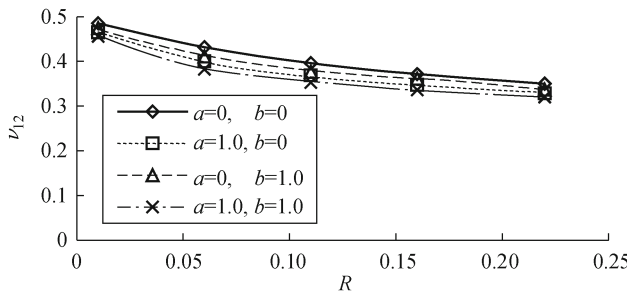


Fig. 8.31 Effects of the relative density on the Poisson's ratio ν_{12} .

Figure 8.31 illustrates the relations between the Poisson's ratio ν_{12} and the relative density R . For all of the four types of foams, ν_{12} decreases moderately with the increase of R in a monotonic manner. It is seen that for various values of R considered, both types of imperfections slightly reduce ν_{12} , and the influence of a is stronger than that of b when $a = b$.

In order to further explore the effects of the relative density (R) on the behavior of foams having the two co-existing imperfections, the differences between the elastic properties of the imperfect foams and those of the perfect foams (with $a = 0$, $b = 0$) are calculated and examined. Let

$$e_Q = Q^r - Q^p, \quad (8.54)$$

where e_Q is the difference, Q denotes the elastic property (E_1 or G_{12}), and the superscripts r and p stand for, respectively, the random and perfect foams. The numerical results for e_Q as a function of R are illustrated in Figs. 8.32 and 8.33.

It is observed from Figs. 8.32 and 8.33 that when R increases the differences in the two elastic moduli induced solely by the presence of irregular cell

shapes (i.e., $a = 1.0, b = 0$) initially increase and then decrease, while those purely caused by the presence of non-uniform SCSAs (i.e., $a = 0, b = 1.0$) decrease in a monotonic manner. A further examination of Figs. 8.32 and 8.33 reveals that when R is small the increase in the moduli due to the appearance of irregular cell shapes (i.e., $a = 0.3, 0.5, 1.0$) is slightly larger than the decrease in the moduli caused by the presence of non-uniform SCSAs (i.e., $b = 0.3, 0.5$). When R becomes large, however, the effects of the SCSA non-uniformity on the elastic moduli are more significant than those of the cell shape irregularity. As a result, the elastic moduli of the foams with the two co-existing imperfections (i.e., $a = b = 0.3, 0.5, 1.0$ here) are lower than those of the perfect foams (i.e., $a = 0$ and $b = 0$) when R is large, and the differences between them increase with R , as illustrated in Figs. 8.32 and 8.33. These observations support and enhance those made earlier based on Figs. 8.26 and 8.27 for foams with $R = 0.01$ and on Figs. 8.29 and 8.30 for foams with various values of R .

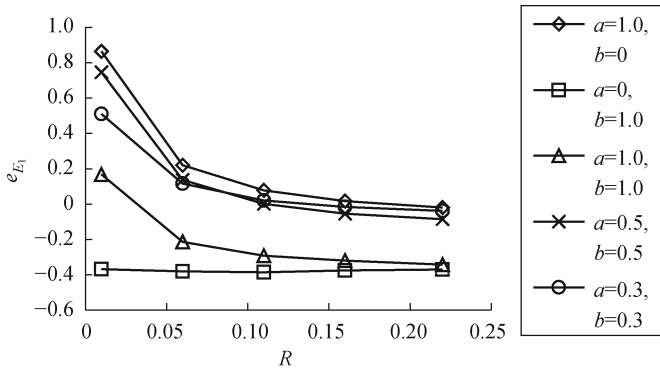


Fig. 8.32 Differences in the Young's modulus varying with the relative density.

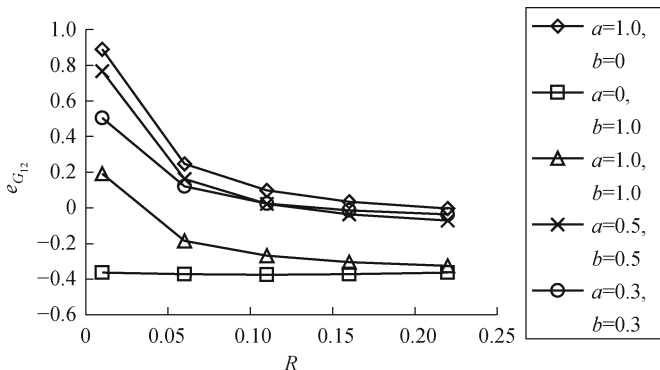


Fig. 8.33 Differences in the shear modulus varying with the relative density.

8.3.2.6 Effects of strut cross-sectional shapes

The effects of strut cross-sectional shapes are studied using completely irregular foams with completely non-uniform SCSAs ($a = 1.0$, $b = 1.0$). Four cross sectional shapes, namely, Plateau border (PB), equilateral triangle (ET), square (SQ) and circle (CR), and two relative densities, namely, 0.01 and 0.11, are used. The predicted mean values of normalized elastic properties Q^{cs}/Q^{PB} , where the superscript “ cs ” refers to ET, SQ or CR, at various values of R are graphically illustrated in Fig. 8.34. It is seen from Fig. 8.34 that for a given value of R , E_1 and G_{12} are the highest for the Plateau border strut cross section, followed by the equilateral triangle, square and circular strut cross sections. The order of influence of the strut cross-sectional shape on ν_{12} is opposite to that on the moduli. These conform to what was found by Li et al.^[33] using a unit cell-based model. An inspection of Fig. 8.34 also indicates that the values of Q^{cs}/Q^{PB} are greater for a higher value of R . This implies that as R increases, the differences in the elastic moduli (E_1 and G_{12}) resulting from the use of different strut cross sections are reduced, while those in the Poisson’s ratio (ν_{12}) increase. In addition, a further examination of Fig. 8.34 shows that for both values of R considered, the elastic moduli are more sensitive to the strut cross-sectional shape than the Poisson’s ratio. This is reflected by the fact that the maximum relative difference in E_1 and G_{12} caused by utilizing different strut cross sections (approximately 20%) is larger than that in ν_{12} (8%) for $R = 0.11$. The disparity is even larger for lower values of R : the maximum relative differences in the elastic moduli and the Poisson’s ratio are, respectively, 21% and 6% when $R = 0.01$.

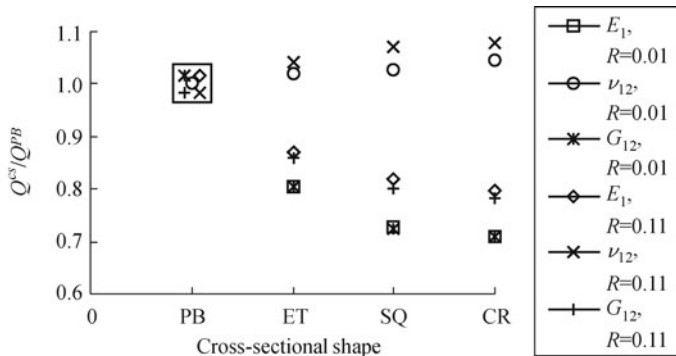


Fig. 8.34 Effects of strut cross-sectional shapes on normalized elastic properties.

8.3.3 Summary

The effects of cell shape and strut cross-sectional area (SCSA) imperfections on the elastic properties of 3-D open-cell foams are studied using the Voronoi

tessellation technique and the finite element method. Voronoi diagrams with different degrees of cell shape irregularity (amplitude a) are produced by perturbing regularly packed seeds. Perturbations are then introduced to the uniform cross-sectional area of the struts to generate a uniform distribution of SCSAs with different degrees of non-uniformity (amplitude b). Twenty finite element (FE) models are constructed, based on the Voronoi diagrams for twenty foam samples having the same pair of a and b , to obtain the mean values and standard deviations of the elastic properties.

Based on the simulation results and analyses presented, the following conclusions can be drawn:

(1) The elastic response of foams with cell shape and SCSA imperfections appears to be isotropic regardless of changes in the cell shape irregularity (amplitude a), the SCSA non-uniformity (amplitude b), the relative density (R) and the strut cross-sectional shape.

(2) For low-density random foams with struts of a uniform cross-sectional area, as the cell shapes become more irregular, on average, the elastic moduli increase considerably, while the Poisson's ratios decrease slightly.

(3) For regular foams, the increase in the SCSA non-uniformity substantially reduces the elastic moduli but has little influence on the Poisson's ratios.

(4) When irregular cell shapes and non-uniform SCSAs co-exist in a foam, the effect of the interaction between the two types of imperfections on the elastic properties appears to be weak. For low-density foams, when the degree of irregularity and the degree of non-uniformity are equal, the stiffness gain resulting from the appearance of irregular cells is more than the stiffness loss due to the perturbation to the uniform SCSA. As the relative density (R) increases, however, this order of influence is reversed. Consequently, the elastic moduli of the foams with the two co-existing imperfections are lower than those of the perfect foams when R becomes large, and the differences increase with R .

(5) When the relative density increases, the elastic moduli of imperfect foams increase remarkably, while the Poisson's ratios decrease moderately.

(6) The strut cross-sectional shape has a significant effect on the elastic properties of imperfect foams. At a given relative density, the highest moduli and lowest Poisson's ratios are obtained for the Plateau border cross section, followed by the equilateral triangle, square and circular strut cross sections. Also, elastic moduli appear to be more sensitive to the strut cross-sectional shape than Poisson's ratios.

Acknowledgements

The work reported here was funded by a grant from the AFOSR and by a contract from L & L Products. These supports are gratefully acknowledged. The authors also thank Drs. G. Subhash and A. K. Roy for their contributions. In addition, the public access to

the Qhull program initially made available by the Geometry Center at the University of Minnesota—Twin Cities is greatly appreciated.

References

- [1] Hilyard N C. Mechanics of Cellular Plastics. Applied Science, London, 1982.
- [2] Gibson L J, Ashby M F. Cellular Solids: Structures and Properties. 2nd ed. Cambridge University Press, Cambridge, 1997.
- [3] Ashby M F, Evans A, Fleck N A, et al. Metal Foams: A Design Guide. Butterworth-Heinemann, Woburn (MA), 2000.
- [4] Hall R B, Hager J W. Performance limits for stiffness-critical graphitic foam structures, part I: Comparisons with high-modulus foams, refractory alloys and graphite-epoxy composites. *J Compos Mater*, 30: 1922-1937, 1996.
- [5] Roy A K, Pullman D, Kearns K M. Experimental methods for measuring tensile and shear stiffness and strength of graphitic foam. Proceedings of the 43rd International SAMPE Symposium and Exhibition, Anaheim, California, USA, May 31—June 4, 1998.
- [6] Sih S, Roy A K. Modeling and stress analysis of open-cell carbon foam. Proceedings of the 46th International SAMPE Symposium and Exhibition, Long Beach, CA, USA, May 6-10, 2001.
- [7] Warren W E, Kraynik A M. The linear elastic properties of open-cell foams. *ASME J Appl Mech*, 55: 341-346, 1988.
- [8] Warren W E, Kraynik A M. The linear elastic behavior of a low-density Kelvin foam with open cells. *ASME J Appl Mech*, 64: 787-795, 1997.
- [9] Anderson D P, Kearns K M, Klett J W, et al. Microcellular graphite carbon foams for next generation structures and thermal management. Proceedings of the 2000 IEEE Aerospace Conference, Vol. 4, Big Sky, Montana, USA, March 18-25, 2000.
- [10] Weaire D, Fortes M A. Stress and strain in liquid and solid foams. *Adv Phys*, 43: 685-738, 1994.
- [11] Dement'ev A G, Tarakanov O G. Effect of cellular structure on the mechanical properties of plastic foams. *Polymer Mechanics*, 6: 519-525, 1970.
- [12] Dement'ev A G, Tarakanov O G. Model analysis of the cellular structure of plastic foams of the polyurethane type. *Polymer Mechanics*, 6: 744-749, 1970.
- [13] Choi J B, Lakes R S. Analysis of elastic modulus of conventional foams and of re-entrant foam materials with a negative Poisson's ratio. *Int J Mech Sci*, 37: 51-59, 1995.
- [14] Chou T W. Microstructural Design of Fiber Composites. Cambridge University Press, Cambridge, 1992.
- [15] Van der Burg M W D, Shulmeister V, Van der Geissen E, et al. On the linear elastic properties of regular and random open-cell foam models. *J Cell Plastics*, 33: 31-54, 1997.
- [16] Grenestedt J L, Tanaka K. Influence of cell shape variations on elastic stiffness of closed cell cellular solids. *Script Mater*, 40: 71-77, 1999.
- [17] Roberts A P, Garboczi E J. Elastic moduli of model random three-dimensional closed-cell cellular solids. *Acta Mater*, 49: 189-197, 2001.
- [18] Roberts A P, Garboczi E J. Elastic properties of model random three-dimensional open-cell solids. *J Mech Phys Solids*, 50: 33-55, 2002.

- [19] Grenestedt J L, Bassinet F. Influence of cell wall thickness variations on elastic stiffness of closed-cell cellular solids. *Int J Mech Sci*, 42: 1327-1338, 2000.
- [20] Simone A E, Gibson L J. Effects of solid distribution on the stiffness and strength of metallic foams. *Acta Mater*, 46: 2139-2150, 1998.
- [21] Simone A E, Gibson L J. The effects of cell face curvature and corrugations on the stiffness and strength of metallic foams. *Acta Mater*, 46: 3929-3935, 1998.
- [22] Grenestedt J L. Influence of wavy imperfections in cell walls on elastic stiffness of cellular solids. *J Mech Phys Solids*, 46: 29-50, 1998.
- [23] Gao X L, Mall S. Variational solution for a cracked mosaic model of woven fabric composites. *Int J Solids Struct*, 38: 855-874, 2001.
- [24] Roy A K, Sihl S. Development of a three-dimensional mixed variational model for woven composites I: mathematical formulation. *Int J Solids Struct*, 38: 5935-5947, 2001.
- [25] Gao X L, Li K. Damaged mosaic laminate model of woven fabric composites with transverse yarn cracking and interface debonding. *Compos Sci Tech*, 62: 1821-1834, 2002.
- [26] Gao X L, Li K, Mall S. A mechanics-of-materials model for predicting Young's modulus of damaged woven fabric composites involving three damage modes. *Int J Solids Struct*, 40: 981-999, 2003.
- [27] Cook R D, Young W C. Advanced Mechanics of Materials. 2nd ed. Prentice Hall, Upper Saddle River (NJ), 1999.
- [28] Hashin Z. Analysis of composite materials-a survey. *ASME J Appl Mech*, 50: 481-505, 1983.
- [29] Hashin Z. Analysis of orthogonally cracked laminates under tension. *ASME J Appl Mech*, 54: 872-879, 1987.
- [30] Glaessgen E H, Phillips D R, Iesulauro E, et al. A multiscale approach to modeling fracture in metallic materials containing nonmetallic inclusions. AIAA-2003-1616, American Institute of Aeronautics and Astronautics, Reston, VA, 2003.
- [31] Nygards M, Gudmundson P. Three-dimensional periodic Voronoi grain models and micromechanical FE-simulations of a two-phase steel. *Comp Mater Sci*, 24: 513-519, 2002.
- [32] Hibbit, Karlson, Sorenson, Inc. ABAQUS Theory and User's Manuals. Version 6.3. Hibbit, Karlson and Sorenson, Inc., Pawtucket, RI, 2002.
- [33] Li K, Gao X L, Roy A K. Micromechanics model for three-dimensional open-cell foams using a tetrakaidecahedral unit cell and Castiglione's second theorem. *Compos Sci Tech*, 63: 1769-1781, 2003.
- [34] Li K, Gao X L, Roy A K. Micromechanical analysis of three-dimensional open-cell foams using the matrix method for spatial frames. *Composites: Part B*, 36: 249-262, 2005.
- [35] Silva M J, Hayes W C, Gibson L J. The effects of non-periodic microstructure on the elastic properties of two-dimensional cellular solids. *Int J Mech Sci*, 37: 1161-1177, 1995.
- [36] Silva M J, Gibson L J. The effects of non-periodic microstructure and defects on the compressive strength of two-dimensional cellular solids. *Int J Mech Sci*, 39: 549-563, 1997.
- [37] Li K, Gao X L, Subhash G. Effects of cell shape and cell wall thickness variations on the elastic properties of two-dimensional cellular solids. *Int J Solids Struc*, 42: 1777-1795, 2005.

- [38] Laroussi M, Sab K, Alaoui A. Foam mechanics: nonlinear response of an elastic 3D-periodic microstructure. *Int J Solids Struc*, 39: 3599-3623, 2002.
- [39] Kanit T, Forest S, Galliet I, et al. Determination of the size of the representative volume element for random composites: Statistical and numerical approach. *Int J Solids Struc*, 40: 3647-3679, 2003.

Chapter 9 Capillary Adhesion of Micro-beams and Plates: A Review

Jianlin Liu^{1,*} and Re Xia^{2,*}

¹*Department of Engineering Mechanics, China University of Petroleum,
Qingdao 266555, China*

²*Schoool of Power and Mechanical Engineering, Wuhan University,
Wuhan 430072, China*

Abstract: A review is presented for the capillary adhesion of micro-beams and plates, and this phenomenon exists widely in MEMS, animal hairs, carbon nanotubes or nanowires. Although the capillary force is usually negligible at the macroscopic scale of human buildings, bridges or vehicles, it becomes dominant at small scales since the surface/volume ratio increases as smaller objects are considered. In this review, we show the fundamental theory and analysis method for general problems of capillary adhesion. Firstly, for the adhesion of micro-beam or micro-plate, the existing investigation deals with the cases of both infinitesimal and finite deformation. In use of the principle of minimum total potential energy, the critical adhered length and deflection of the micro-structure can be derived. Furthermore, the mechanism of the hierarchical structure in adhesion can be elucidated by means of energy theory. The method adopted in this chapter can also be developed to solve other adhesion problems associated with van der Waals force or electrostatic force. These findings may provide inspirations for the design of micro-devices, MEMS, micro-sensor and non-wetting materials from different aspects (e.g., geometric shape, characteristic size, surface microstructure and elasticity).

Keywords: capillary adhesion, infinitesimal deformation, finite deformation, hierarchical structure, critical parameters

9.1 Introduction

Capillary action of liquid exists widely in nature, which causes a lot of interesting phenomena in industry and our daily life. For example, water can be transported by capillary tubes in plants, the lotus and lady's mantle have the strong capability of self-cleaning, i.e. "lotus effect"^[1-3], water striders or

*Corresponding authors, E-mails: liujianlin@upc.edu.cn, xiare@whu.edu.cn.

spiders can walk or jump freely on water surface^[4,5], Texas horned lizard draws water by capillary action through thin channels that extend from its feet to mouth^[6], some millimeter-scale water-walking insects can arrive at the land with the help of a lateral capillary force originating from the meniscus surface^[7], shore birds can remove a liquid drop with its beak opening and closing in a tweezing motion^[8], and the solid components floating at liquid interfaces can self-assemble automatically by their interacting forces^[9]. Additionally, capillary force or surface tension is closely related to various applications in industry, e.g., porous media, micro-fluidic devices, self-cleaning paints, and glass windows^[10,11].

Another important issue about surface tension is the capillary adhesion of micro-structures or devices. In the past decades, wide attention has been attracted on the adhesion of materials and devices at micro- and nano-scales, which may be caused by van der Waals force, Casimir force, capillary force or some other interaction forces^[12-15]. On one hand, adhesion may cause the failure or collapse of micro-electromechanical systems (MEMS)^[12]. In micro-contact printing technology, for instance, adhesion associated with van der Waals force leads to stamp deformation and limits the application of this technology^[16,17]. Three kinds of stamp deformation, i.e., roof collapse, buckling and lateral sticking of the fibrillar structures, have been observed in the process. Besides, van der Waals force may also cause the stiction of high aspect ratio SU-8 resist when preparing the photonic crystals. On the other hand, adhesion mechanisms may be useful in the manipulation and operation of some micro-devices, which are also beneficial for various biological processes of creatures, such as adhesion of biological macromolecules, cells or vesicles on a substrate^[18-20]. Among others, an interesting example is the striking adhesion ability of gecko, which is attributed primarily to the van der Waals force between their feet and the contact surfaces^[21,22].

In the process of adhesion, hierarchical structure may often appear compared with some other morphologies. In fact, structural hierarchy plays a significant role in the physical properties and biological behavior of various kinds of man-made and natural materials and systems (e.g., the branches and roots of trees, and the hierarchical macro/meso/micro/nano structure of bones, silks and other biomaterials). As a representative example, the hierarchical structures of the specialized adhesive feet of geckos attracted great interest in the past few years. Gao et al.^[23,24] used the fractal concept to characterize the self-similar fibrillar structures of gecko feet at multiple levels, and elucidated the importance of the nanometer length scale and structural hierarchy on the superior adhesion strength.

In this review, we focus on the adhesion of micro-structures induced mainly by capillary force of liquid films/bridges. In the areas of biology surface, carbon nanotube (CNT) array, MEMS, micro-sensor and micro-fluidics, surface tension or capillary force becomes a predominant factor with the ratio of surface and volume increasing. Capillary adhesion may often happen in the fast developing MEMS techniques, in which typical surface separations

are in the range of 500–2 000 nm. Henceforth, water can be trapping in the gaps of the high surface tension micromachining structures and then produce strong capillary forces^[12,25]. The capillary force may even drive the CNT arrays to reorganize into cellular structure upon drying and produce different nano-patterns of CNT arrays on thin films^[26,27]. The process of self-assembly of ZnO nanowire arrays into hierarchical patterns is also driven by the capillary force^[28]. What is more, the adhesion of animal hairs, carbon nanotubes or nanowires of a periodically or randomly distributed array always leads to hierarchical structures^[29]. As yet, however, there is a lack of theoretical investigation on why and how hierarchical structures form due to adhesion.

Therefore, the outline of this chapter is planned as follows: First, we will mention the capillary adhesion models of micro-beams of infinitesimal deformation. Then the finite deformation of micro-beams induced by surface tension will be introduced. Next, the mechanism of the hierarchical structure of two bundles of beams will be presented. Finally, some other capillary adhesion phenomena about plates will be reviewed.

9.2 Capillary adhesion of micro-beams of infinitesimal deformation

For the characteristic size of MEMS has been reduced to micro or nano-meter, capillary force is considered as a dominant factor in design and fabricate. To avoid the collapse of capillary adhesion of MEMS structures, a lot of experimental and analytical models have been analyzed and constructed. For example, Mastrangelo et al.^[14,15] analyzed the deflection, mechanical stability and adhesion of thin micromechanical structures under capillary forces. They got an approximate condition to avoid adhesion contact of a structure to the substrate. Zhu et al.^[30] also investigated the adhesion of microcantilevers driven by the capillary force and calculated the critical values of surface energy for initial and full adhesion of two opposing cantilevers. De Bohr^[31] calculated the characteristic parameters of a beam adhered by liquid on a rough substrate, and compared them with the experimental results. By using the fracture mechanics theory, they pointed out that the work of adhesion is equal to the surface energy difference in the separated versus the joined materials minus an interfacial energy term. Their analysis includes the evaporation of liquid at the interface between two solid materials.

Li et al.^[32] also carried out an experiment to study the deflection of a cantilever adhered by a liquid bridge using electronic speckle pattern interferometry (ESPI). They measured the transient deformation of a microcantilever caused by the capillary force, and then constructed the energy function of the adhesion system based on the independent parameters of adhesion length and volume fraction of the adhesion medium. The experimental result of the cantilever in equilibrium is consistent with the analytical solution. Moreover,

Kwon et al.^[33] analyzed the spontaneous spreading of a liquid drop confined between an elastic plate and a rigid substrate due to the effects of interfacial forces. The eventual equilibrium shape of the droplet is determined by the balance between elastic and capillary effects. They provided an analytical theory for the static shape of the sheet and the extent of liquid spreading, and the result shows that the experiments are quantitatively consistent with the theory. The theory is relevant to the first step of painting when a brush is brought down onto canvas. More mundanely, the result allows us to understand the stiction of microcantilevers to wafer substrates occurring in microelectromechanical fabrication processes.

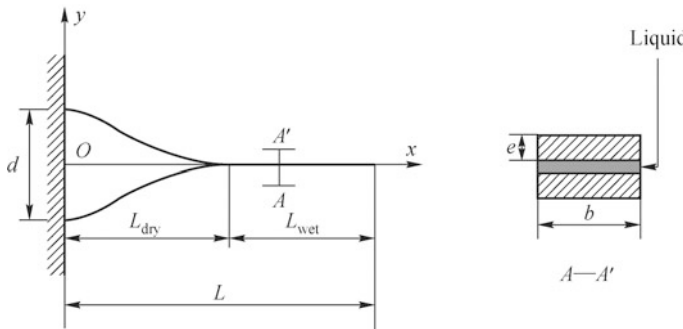


Fig. 9.1 Capillary adhesion of two micro-beams of infinitesimal deformation. (color plot at the end of the book)

Recently, Bico et al., Kim, Mahadevan and Liu et al.^[29,34,35] calculated the critical dry length of two or two bundles of adhered hairs by considering capillary force and elastic deformation. Refer to a Cartesian coordinate system ($O-xy$). For two micro-beams adhered by a thin liquid film, as shown in Fig. 9.1, the hairs are assumed to have an identical size of length L , width b , and thickness e . The distance between the two hairs at the clamped ends is d . The lengths of the dry (unadhered) and the wet (adhered) segments are denoted as L_{dry} and L_{wet} , respectively. The deflections of the two beams are symmetric with respect to x -axis. The deflection of the upper beam can be written as

$$w = \frac{d}{L_{\text{dry}}^3} x^3 - \frac{3d}{2L_{\text{dry}}^2} x^2 + \frac{d}{2} \quad (9.1)$$

according to the boundary conditions: $w(0) = d/2$, $w'(0) = 0$, $w(L_{\text{dry}}) = 0$, and $w'(L_{\text{dry}}) = 0$. The total potential energy includes two parts, namely, the strain energy and the surface energy, which can be expressed as

$$\begin{aligned} \Pi &= \frac{EI}{2} \int_0^{L_{\text{dry}}} (w'')^2 dx + 2(\gamma_{\text{SL}} - \gamma_{\text{SV}}) L_{\text{wet}} b \\ &= \frac{3EI d^2}{L_{\text{dry}}^3} - 2\gamma \cos \theta_Y (L - L_{\text{dry}}) b, \end{aligned} \quad (9.2)$$

where E is the Young's modulus, $I = be^3/12$ the inertia moment of the beam, and w the deflection. The symbols γ_{SL} and γ_{SV} denote the surface tension of solid/liquid and solid/vapor interfaces, respectively, which satisfy the Young's equation, $\gamma_{SV} - \gamma_{SL} = \gamma \cos \theta_Y$, with γ being the surface tension of liquid/vapor interface and θ_Y being the Young's contact angle of the beam.

In use of the principle of minimum total potential energy, one can obtain the critical length in equilibrium state according to the condition of $d\Pi/dL_{\text{dry}} = 0$:

$$L_{\text{dry}} = \sqrt[4]{\frac{3Ee^3d^2}{8\gamma \cos \theta_Y}}. \quad (9.3)$$

The analytical result of Eq. (9.3) is compared with Liu's experimental result in Fig. 9.2, which indicates that this solution is in good agreement with the actual case. Furthermore, we can see that if the total length $L < L_{\text{dry}}$, the adhesion energy induced by the introduction of a liquid film between the two beams is insufficient to provide the strain energy of deformation, and therefore, the two beams will not adhere together. On the contrary, if $L > L_{\text{dry}}$, the surface energy is higher than the strain energy, and then the adhesion of the two beams becomes possible. The calculated result requires that the contact angle θ_Y must satisfy $0 \leq \theta_Y < \pi/2$, that is, the hairs must be hydrophilic. In other words, capillary adhesion can not happen between two hydrophobic hairs.

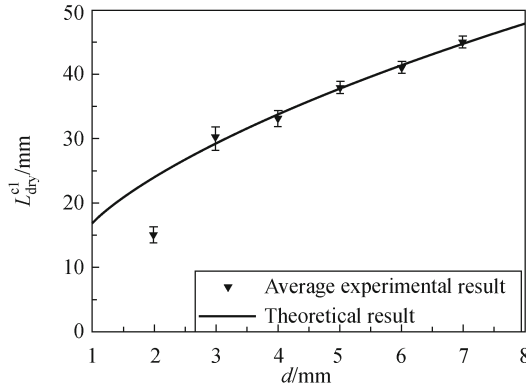


Fig. 9.2 Critical adhesion length as a function of the spacing of two micro-beams.

Based upon the similar analysis, Liu et al.^[35] investigated the capillary adhesion of three beams and two bundles of beams, and got the similar results. Also, this method applies to the capillary adhesion of a beam stuck on a solid substrate.

9.3 Capillary adhesion of micro-beams of finite deformation

The above analyses of capillary adhesion in Section 9.2 are mainly based on the elastic theory of a beam in small deformation. However, the deformation of the adhered CNTs and micro-beams is often large because of their very small bending stiffness. The infinitesimal deformation approximation may cause a significant error in the solutions. Therefore, based upon the experimental phenomenon of Journet et al.^[36], Liu et al.^[37] constructed the adhesion models of two beams which were adhered by the capillary force in finite deformation, as shown in Fig. 9.3a. The beams are modeled as two parallel cantilevers of length L , whose right ends are clamped with a distance d in between. Without loss of generality, the beams are assumed to have an identical circular cross-section of radius R and that their left segments of length l are adhered by water or other liquids. Refer to the Cartesian coordinate system ($O-xy$). Besides the Euler coordinate x , the arc length s , which is a Lagrange coordinate, is also used in the analysis. Because of the configurational symmetry, only the upper beam will be considered. For simplicity, the constraints at its right end are released and, instead, a force P and a moment M as yet to be determined are applied there, as shown in Fig. 9.3b. The slope angle of the beam at point s is denoted by a function $\phi(s)$, with $\phi(l_0) = \phi_0$ at the midpoint $s = l_0 = (L + l)/2$ of the dry segment. Assuming that the beam is inextensible, the boundary conditions are $\phi(l) = 0, y(l) = 0, \dot{\phi}(L) = 0$ and $y(L) = d/2$. In addition, the configurational symmetry requires that $\dot{\phi}(l_0) = 0$ and $y(l_0) = d/4 = y(L)/2$ at the midpoint $s = l_0$ of the dry segment, where the dot symbol stands for the derivation

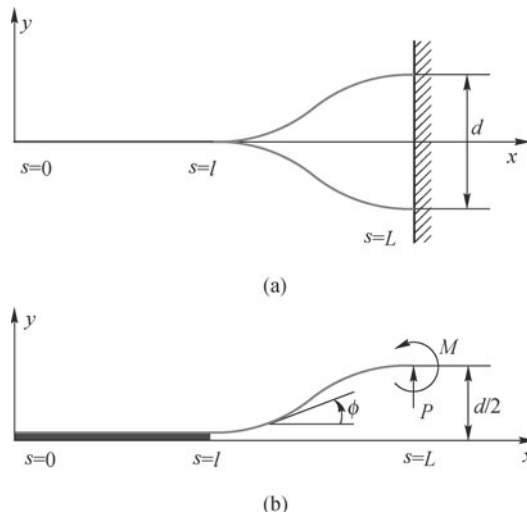


Fig. 9.3 Capillary adhesion of two micro-beams of finite deformation.

with respect to s .

The total potential energy of the system contains the elastic strain energy, the surface/interface energy and the potential energy of the external forces. Considering the geometrical relation $\dot{y} = \sin \phi$, the energy functional with respect to the deflection of the beam is expressed as

$$\Pi = \int_l^{l_0} EI\dot{\phi}^2 ds + (\gamma_{SL} - \gamma_{SV})bl - 2Py(l_0) + \int_l^{l_0} \lambda(\dot{y} - \sin \phi)ds, \quad (9.4)$$

where $\lambda(s)$ is a Lagrange multiplier, and $I = \pi R^4/4$ the inertial moment of the beam of a solid cylindrical cross-section. The width of the liquid film between the two beams is assumed to be $b = \pi R$. In the above analysis, the strain of the linearly elastic beam is still assumed to be infinitesimal though large displacement and nonlinear force-deflection relationship are considered. This assumption is usually reasonable for slender beams.

The variation of the functional in Eq. (9.4) about the real deflection curve of the beam should equal zero, that is, $\delta\Pi = 0$. Then, one may derive the governing equation named as Euler-Lagrange equation

$$\ddot{\phi} + \alpha^2 \cos \phi = 0, \quad (9.5)$$

where $\alpha^2 = P/(EI)$. The transversality boundary condition at $s = l$ can also be derived as $\phi(l)^2 = \gamma \cos \theta_Y b/(EI)$, corresponding to the balance between surface/interface energy and elastic strain energy.

Using the inextensible condition of the beam, the deflection at $s = l_0$ is derived as

$$\frac{d}{4} = (l_0 - l) \left[1 - 2 \frac{E(k) - E(k, \theta_1)}{F(k) - F(k, \theta_1)} \right], \quad (9.6)$$

where $\sin \theta_1 = \frac{1}{\sqrt{2k}}$, $F(k)$ and $F(k, \theta_1)$ are the complete and the incomplete elliptic integrals of the first kinds, and $E(k)$ and $E(k, \theta_1)$ the second kinds, respectively. From Eq. 9.6 in conjunction with the transversality condition $\alpha = \sqrt{\frac{\gamma \cos \theta_Y b}{2EI \sin \phi_0}}$, the values of k and l can be determined for a given d .

Thereby, the other parameters ϕ_0, l_0, α, P and M can also be solved.

Then from Eq. (9.6), the deflection of the beam can be calculated from the finite deformation analysis. The Cartesian coordinates of an arbitrary point of the deformed beam can be given by

$$\begin{cases} \alpha x = \alpha l + 2k(\cos \theta_1 - \cos \theta) \\ \alpha y = \int_{\theta_1}^{\theta} \frac{2k^2 \sin^2 \theta - 1}{\sqrt{1 - k^2 \sin^2 \theta}} d\theta. \end{cases} \quad (9.7)$$

According to the above equations, the deflection curves of the two adhered CNTs predicted by the two methods are plotted in Fig. 9.4 for a representative distance $d=500$ nm. For a beam with large displacement, the deformation

predicted by finite deformation theory seems to be more “stiffer” than that predicted by infinitesimal deformation analysis. The considerable difference between the results of the two methods clearly evidences the necessity of adopting the finite deformation elasticity theory to analyze microsized and nanosized beams.

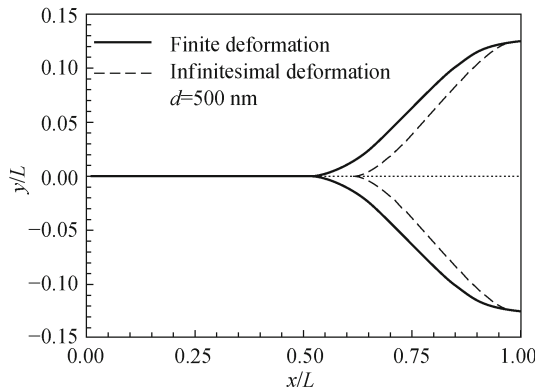


Fig. 9.4 The deflections of two micro-beams adhered by a liquid film in infinitesimal or finite deformation.

Seeing the elliptical integration solution of Eq. (9.7), Liu^[38] found that there is an interesting analogy between a liquid bridge and a cantilever of finite deformation, as shown in Figs. 9.5 and 9.6. It indicates that the two governing equations take the same style after coordinate translation and scale transformation. The stiffness, generalized force, curvature, energy origination and some other parameters are compared for the two physical phenomena (Table 9.1). The present analyses can make us grasp the nature of this phys-

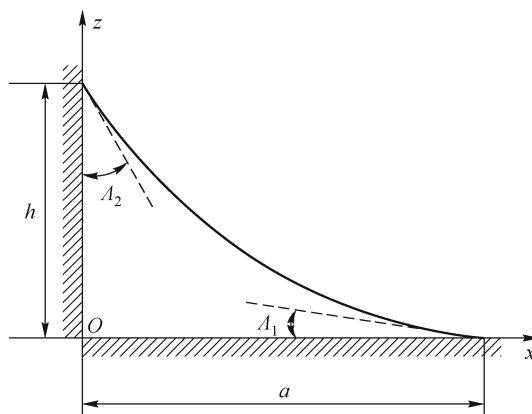


Fig. 9.5 A liquid bridge between a vertical wall and a substrate, where Λ_1 and Λ_2 are the Young's contact angles of the substrate and the side wall, respectively.

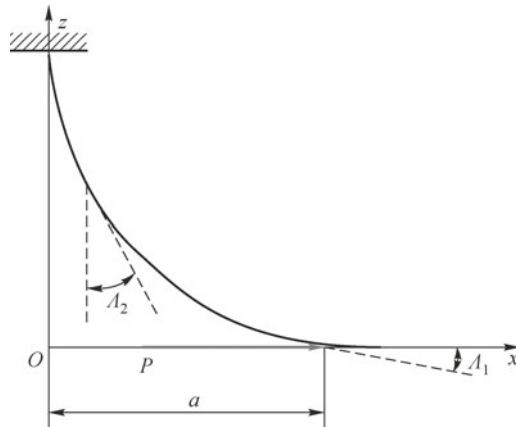


Fig. 9.6 A cantilever under a concentrated force at the free end, where Λ_1 is the slope angle at the free end, and Λ_2 is the angle between the tangent line and the vertical line at an arbitrary point.

ical phenomenon deeply and widely, and give us some inspirations to design certain analogy experiments between a meniscus and an elastica. Moreover, the calculated results are beneficial to engineering applications, such as design and fabrication of MEMS and some micro-manipulations in micro/nano-technology.

Table 9.1 Analogies between a meniscus and a cantilever

Items	Liquid bridge or bubble	Cantilever
Governing equation	$z''(1+z'^2)^{-3/2} = c_0 + \alpha^2 z$	$z''(1+z'^2)^{-3/2} = \beta^2 z$
Stiffness	Surface tension (γ)	Bending stiffness (EI)
Generalized force	ρg or Δp	P or M
Curvature	$\Delta p/\gamma$	$M/(EI)$
Reduced parameter	$\alpha = \sqrt{\rho g / \gamma}$	$\beta = \sqrt{P/(EI)}$
Angle (Λ_1)	Young's contact angle on the substrate	Slope angle at free end
Angle (Λ_2)	Young's contact angle on the wall	Angle between the beam and the vertical line
Parameter (a)	Maximum width	Maximum deflection
Internal potential energy	Surface energy $\left(\gamma \int_0^a \sqrt{1+z'^2} dx \right)$	Strain energy $\left(\frac{EI}{2} \int_0^l \varphi'^2 ds \right)$
External potential energy	$- \int_0^a (\Delta p_0 + \rho g z) x z' dx$	$-Pa$
Conservative parameter	Area of the meniscus S	Length of the beam l

9.4 Hierarchical structure of micro-beams induced by capillary force

In reality, the arrays of hairs, nanotubes and nanowires often form hierarchical structures as a result of capillary adhesion. The level number of structural hierarchy is dependent on the number, spacing and elasticity of hairs. Bico et al.^[29] found the bundle aggregation of two bundles of hairs withdrawn from water. Based upon this investigation, Py et al.^[39] found wet fibrous structures tend to self-assemble into bundles while the liquid evaporates. They studied the complex 3D aggregation process of the bundles. Furthermore, they showed that the physical process imposes a maximal size for the aggregates, which appears as the relevant scale for the distribution. Their simple toy model involving the aggregation of nearest neighbors exhibits the same statistics. The mean-field theory accounting for a maximal size is in agreement with both experiments and numerics^[40].

In the real world, we can observe that the level number of structural hierarchy depends on the number, spacing and elasticity of hairs. For simplicity and without loss of generality, Liu et al.^[35] considered the adhesion of $N = 2^n (n = 1, 2, 3, \dots)$ hairs of a periodic array. They may form different structures in the case of adhesion, and the actual structure tends to minimize the total potential energy. Thus, the one-level adhesion morphology in Fig. 9.7 and the hierarchical (multi-level) structures in Fig. 9.8 are compared in

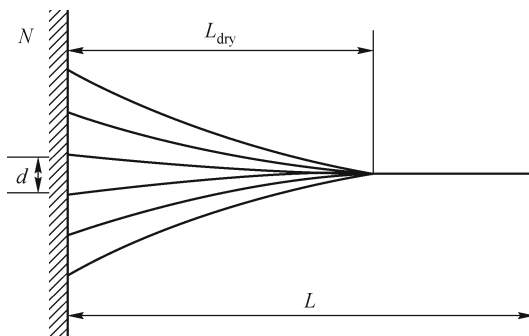


Fig. 9.7 One-level structure of a bundle of beams.

order to find out which one is the most energetically favorable. Figure 9.8a illustrates a two-level adhesion in which any two hairs combine into a larger one and the bundled hairs will adhere further in the second level, Fig. 9.8b delineates another two-level configuration in which any three hairs group in the first level, and Fig. 9.8c gives a hierarchical structure in which each beam of the N level is composed of two smaller beams of the $N - 1$ level. For conciseness, they give in the sequel only the energy expression of the hierarchical system in Fig. 9.8c. Its non-dimensional potential energy at the equilibrium

state is written as

$$\tilde{\Pi}_3 = A_1 B - (2^n - 1), \quad (9.8)$$

where $A_1 = (2^n - 1) \left(\frac{2^{2n} + 2^n}{6} \right)^{1/4}$ and $B = (3^{-3/4} + 3^{1/4})(A)^{1/4}$.

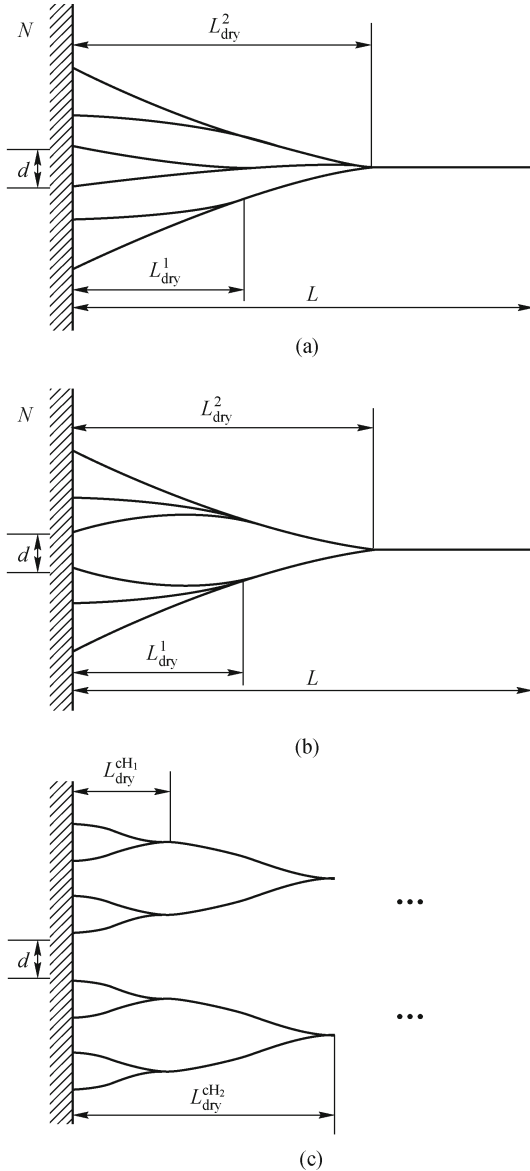


Fig. 9.8 Three possible hierarchical structures of a bundle of beams.

For the hierarchical structure in Fig. 9.8c, the potential energy of the n th

hierarchy is written as

$$\tilde{\Pi}_{H_n} = A_2 B - (2^n - 1), \quad (9.9)$$

$$\text{where } A_2 = 2^{3(n-1)/4} + 2 \frac{1 - 2^{3(n-1)/4}}{1 - 2^{3/4}}.$$

The energy values of the one-level and hierarchical structures are compared in terms of the non-dimensional parameters, A_1 and A_2 . It is seen that for a larger number n of hairs, the relation $A_1 > A_2$ or $\tilde{\Pi}_3 > \tilde{\Pi}_{H_n}$ always holds, or in other words, the energy of the hierarchical structure is lower than that of the one-level structure. Therefore, the hierarchical phenomenon is more energetically favorable. This explains why the hierarchical phenomena can often be observed in reality, such as the hierarchical structure of two bundles of hairs dipped into water^[29], as shown in Liu's experiment of Fig. 9.9. Using the infinitesimal deformation theory of elasticity, the deflection of the adhered hairs in such a hierarchical structure can also be simulated as in Section 9.2 but it is omitted here for simplicity.

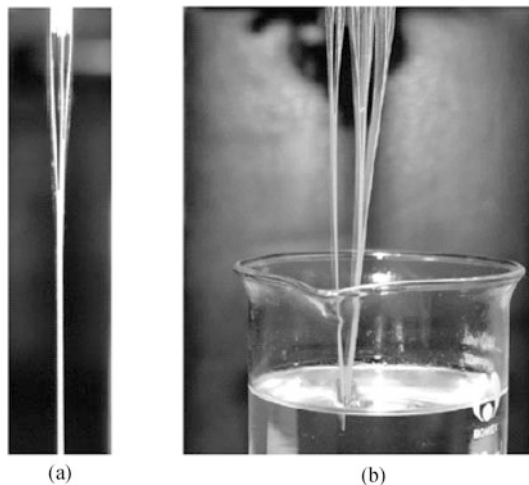


Fig. 9.9 Experimental photos for the hierarchical structures. (color plot at the end of the book)

9.5 Capillary adhesion of a plate

In addition to the beam's stiction, there are some other micro-structures which can be adhered on the substrate due to capillary force. For instance, the stiction of a thin plate induced by the capillary force has attracted much attention to the broad range of applications, such as MEMS industry and

micro/nano-technology. Lin et al.^[41] investigated the adhesion criterion between a center-anchored circular plate and its underlying substrate caused by strong capillary forces. The calculation result gives a critical gap for stiction. Bico's group^[42,43] studied a paper or thin sheet wrapped by a liquid drop, which is of finite deformation state. Moreover, Liu^[44] provided another novel method to calculate the capillary adhesion problem of the plate through analytical method.

The model is a thin plate with an arbitrary geometry, whose bound is clamped on a plane curve Γ_1 . Refer to a Cartesian coordinate system $O - xz$, as shown in Fig. 9.10. The plate is assumed to be adhered on the rigid substrate due to the capillary force induced by a liquid film between the stiction part of the plate and the substrate. Consequently, the plate includes a non-adhered part and an adhered one, denoted by D_1 and D_2 , respectively. The boundary of the adhesion zone is assumed as a plane curve Γ_2 as well. The initial distance between the substrate and the plate is H , and the deflection of the plate is w . The deflection of the plate w is much smaller than the thickness of the plate, i.e. the plate is in the infinitesimal deformation state. As the thickness of the liquid film is quite thin, its total volume can be ignored in calculation, but in some cases its real morphology must be incorporated^[15,33].

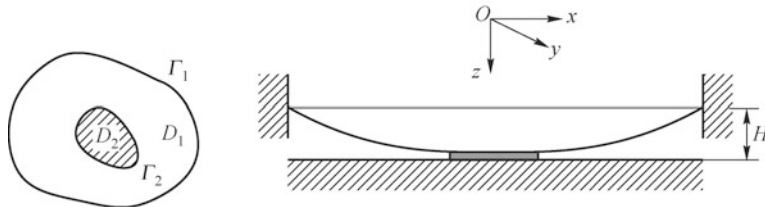


Fig. 9.10 Capillary adhesion of a micro-plate on the substrate. (color plot at the end of the book)

In consideration of the bounds of plate being clamped fixedly on a plane curve Γ_1 , the strain energy may be derived as

$$U = \frac{\kappa}{2} \iint_{D_1} (\nabla^2 w)^2 dx dy, \quad (9.10)$$

where the bending rigidity of the plate is $\kappa = Eh^3/[12(1-\nu^2)]$, h the thickness and ν the Poisson's ratio of the plate. The potential energy functional of the plate-substrate can be expressed as

$$\Pi = \iint_{D_1} F dx dy - 2 \iint_{D_1+D_2} \gamma \cos \theta_Y dx dy, \quad (9.11)$$

where $F = F(w_{xx}, w_{yy}) = \frac{\kappa}{2}(\nabla^2 w)^2 + 2\gamma \cos \theta_Y$.

Considering the moving boundary conditions and taking variation of Eq. (9.11), one can obtain the corresponding Euler–Ostrogradskii equation, that is,

$$\nabla^4 w = 0, \quad (x, y) \in D_1. \quad (9.12)$$

During the variation process, one can get the supplementary boundary condition, i.e. the transversality condition, according to the principle of minimum total potential energy

$$\left[\frac{\kappa}{2} (\nabla^2 w)^2 + 2\gamma \cos \theta_Y + \kappa \frac{\partial}{\partial n_2} (\nabla^2 w) \frac{\partial w}{\partial n_2} - \kappa \nabla^2 w \frac{\partial^2 w}{\partial n_2^2} \right] \Big|_{\Gamma_2} = 0. \quad (9.13)$$

Equation (9.13) represents the equilibrium condition about the surface energy and strain energy on the moving bound.

Especially, the case of a circular plate adhered on the rigid substrate is investigated. For the axi-symmetrical shape of the circular plate, the stiction domain is also a circle. The initial radius of the plate is R_1 , the radius of the adhered circle is R_2 , and the other parameters or constraints are the same as those in Fig. 9.9. In combination with Eqs. (9.12) and (9.13), one has

$$\frac{\mu}{2} = \frac{\lambda^2 - 1 - 2 \ln \lambda}{(\lambda^2 - 1)^2 - 4\lambda^2(\ln \lambda)^2}, \quad (9.14)$$

where the non-dimensional parameter $\mu = \frac{R_1^2}{H} \sqrt{\frac{\gamma \cos \theta_Y}{\kappa}}$. This expression indicates that μ is not a monotonic function of λ , but has a minimum value μ_c with the corresponding value λ_c . When $\lambda < \lambda_c$, μ decreases with the increasing of λ ; but when $\lambda > \lambda_c$, μ should increase with the increasing of λ . As is well known, when the radius of the plate R_1 and the surface tension of the liquid γ increase, or the initial gap between the plate and the substrate H and the bending rigidity of the plate κ decreases, the plate can be more easily adhered on the substrate. Henceforth, the non-dimensional variable μ should increase with increasing λ . The former part of the evolution rule about μ and λ conflicts with the physical phenomenon, which is not reasonable and should be discarded.

To reduce the adhesion of the plate, the initial radius of the plate R_1 and the surface tension of the liquid γ must be decreased, or the initial gap between the plate and the substrate H and the bending rigidity of the plate κ should be increased. Also, the stiction of the plate is related with the Young's contact angles of the plate and the substrate. To satisfy Eq. (9.14), the Young's contact angle must satisfy $\cos \theta_Y \geq 0$, which indicates that only when $\theta_Y \leq 90^\circ$, i.e. the plate and the substrate are both hydrophilic, can the plate be adhered on the substrate. This provides some good advices to the electronic engineers that to avoid the adhesion of the micro-structures in MEMS, the structures and the substrate should be modified to hydrophobicity.

From Eq. (9.14), it can be seen that in order to adhere on the substrate, the radius of the plate must satisfy $R_2 \geq R_c = \lambda_c R_1$. If $R_2 < R_c$, the adhesion phenomenon of the plate will not occur. Minimizing μ with respect to λ yields $d\mu/d\lambda = 0$, i.e.

$$8\lambda^2(\ln \lambda)^3 + 8\lambda^2(\ln \lambda)^2 - 8\lambda^2(\lambda^2 - 1)\ln \lambda + (\lambda^2 + 1)(\lambda^2 - 1)^2 = 0. \quad (9.15)$$

The solution of Eq. (9.15) is $\lambda_c \approx 0.176$, which corresponds to the critical value $\mu_c = 8.868$. This means that the plate can not stick to the substrate at a single contact point, but takes an initial value of adhesion radius. The result of λ_c accords with the approximated result 0.175 and the experimental result 0.15^[15]. The slight difference between these calculated results and the experimental result may be due to the meniscus effect of the liquid film and the nonideal boundary conditions.

Identically, the above analyses are adaptable to the solid-solid contact case, i.e. the surface energy is displaced by $-\iint_{D_1+D_2} \gamma_s dxdy$, where γ_s is the interfacial adhesion energy of per unit contact area. In this case, the boundary conditions are the same as those of the plate-liquid-substrate contact. The dependence relationship between the detachment radius $R_d (=R_1 - R_2)$ and the parameter $H^{\frac{1}{2}}h^{\frac{3}{4}}$ is

$$H^{\frac{1}{4}}h^{\frac{3}{4}} = \frac{R_d [12(1 - \nu^2)\gamma_s/E]^{\frac{1}{4}}}{8^{\frac{1}{4}}(1 - \lambda)F^{\frac{1}{2}}}, \quad (9.16)$$

where $F = F(\lambda) = (\lambda^2 - 1 - 2\ln \lambda)/[(\lambda^2 - 1)^2 - 4\lambda^2(\ln \lambda)^2]$. This calculated result and the experimental result^[15] are compared, indicating that the two results are agreeable in tendency. The reason for the difference between the two results may be that part of the parameters are not listed in the reference, for example, the poisson's ratio of the polysilicon ν is taken as 0.23 for calculation.

9.6 Conclusions

With the development of micro/nano science and technology, it has been a hot topic for the advanced science to design and fabricate new materials and new devices in micro/nano scale. Consequently, the wetting property, deformation and self-assemble effect of micro-structures induced by capillary force must be considered properly. In this chapter, we review the capillary adhesion of micro-beams and micro-plates, which is termed part of the “elasto-capillary phenomena”. Generally, all kinds of elasto-capillary phenomena can be divided into the following aspects, namely, capillary adhesion, capillary assembly, deformation or collapse induced by capillary force, and capillary

buckling or wrinkling. For brevity's sake, only the capillary adhesion is discussed in this review.

We demonstrated the general theory and analysis method of capillary adhesion, dealing with the competition between the strain energy and the surface energy. Firstly, the total potential energy of the system must be constructed. Then according to the principle of minimum total potential energy, the governing equation and the transversality condition associated with the moving boundary condition are derived. The finite deformation and the hierarchical structure are also considered, mainly due to the energy equilibrium.

However, there still remain a lot of unsolved problems about capillary adhesion, such as the adhesion of a single CNT on the substrate, assembly of the CNT forest, and the problem of CNT beaten down for the existing water. Capillary effect of nano-indentation, capillary assembly of the cell and biology setae are also important issues to be investigated.

These analyses may provide some inspirations for the design of micro-devices, CNT forest, MEMS, micro-sensor and non-wetting materials from different aspects (e.g., geometric shape, characteristic size, surface microstructure and elasticity).

Acknowledgements

The project was supported by the National Natural Science Foundation of China (10802099), Doctoral Fund of Ministry of Education of China (200804251520), Natural Science Foundation of Shandong Province (2009ZRA05008), Fundamental Research Funds for the Central Universities (27R0915031A).

References

- [1] Neinhuis C, Barthlott W. Characterization and distribution of water-repellent, self-cleaning plant surfaces. *Ann Bot*, 79: 667-677, 1997.
- [2] Otten A, Herminghaus S. How plants keep dry: A physicist's point of view. *Langmuir*, 20: 2405-2408, 2004.
- [3] Liu J L, Feng X Q, Wang G F, et al. Mechanisms of superhydrophobicity on hydrophilic substrates. *J Phys: Condens Matter*, 19: 356002, 2007.
- [4] Hu D L, Chan B, Bush J W M. The hydrodynamics of water strider locomotion. *Nature*, 424: 663-666, 2004.
- [5] Liu J L, Feng X Q, Wang G F. Buoyant force and sinking conditions of a hydrophobic thin rod floating on water. *Phys Rev E*, 76: 066103, 2007.
- [6] Stewart D. The quest to quench. *Nat Wildlife*, 42: 52-56, 2004.
- [7] Hu D L, Bush J W M. Meniscus-climbing insects. *Nature*, 437: 733-736, 2005.
- [8] Prakash M, Quere D, Bush J W M. Surface tension transport of prey by feeding shorebirds: The capillary ratchet. *Science*, 320: 931-934, 2008.
- [9] Whitesides G M, Grzybowski B. Self-assembly at all scales. *Science*, 295: 2418-2421, 2002.

- [10] Blossey R. Self-cleaning surfaces: Virtual realities. *Nature Mater*, 2: 301-306, 2003.
- [11] Liu J L, Xia R, Li B W, et al. Directional motion of droplets in a conical tube or on a conical fibre. *Chin Phys Lett*, 24: 3210-3213, 2007.
- [12] Zhao Y P, Wang L S, Yu T X. Mechanics of adhesion in MEMS: A review. *J Adhesion Sci Technol*, 17: 519-546, 2003.
- [13] Israelachvili J N. Intermolecular and Surface Forces. 2nd ed. Academic, San Diego, CA, 1992.
- [14] Mastrangelo C H, Hsu C H. Mechanical stability and adhesion of microstructures under capillary forces, part I: Basic theory. *J Microelectromech Syst*, 2: 33-43, 1993.
- [15] Mastrangelo C H, Hsu C H. Mechanical stability and adhesion of microstructures under capillary forces, part II: Experiments. *J Microelectromech Syst*, 2: 44-55, 1993.
- [16] Tang T, Hui C Y, Glassmaker N J. Can a fibrillar interface be stronger and tougher than a non-fibrillar one? *J R Soc Interface*, 2: 505-516, 2005.
- [17] Hui C Y, Jagota A, Lin Y Y, et al. Constraints on microcontact printing imposed by stamp deformation. *Langmuir*, 18: 1394-1407, 2002.
- [18] Capovilla R, Guven J. Geometry of lipid vesicle adhesion. *Phys Rev E*, 66: 041604, 2002.
- [19] Gruhn T, Lipowsky R. Temperature dependence of vesicle adhesion. *Phys Rev E*, 71: 011903, 2005.
- [20] Seifert U. Dynamics of a bound membrane. *Phys. Rev. E*, 49: 3124-3127, 1994.
- [21] Gorb S, Scherge M. Biological microtribology: Anisotropy in frictional forces of orthopteran attachment pads reflects the ultrastructure of a highly deformable material. *Proc R Soc Lond B*, 267: 1239-1244, 2000.
- [22] Geim A K, Dubonos S V, Grigorieva I V, et al. Microfabricated adhesive mimicking gecko foot-hair. *Nature Mater*, 2: 461-463, 2003.
- [23] Gao H J, Wang X, Yao H M, et al. Mechanics of hierarchical adhesion structures of geckos. *Mech Mater*, 37: 275-285, 2005.
- [24] Yao H M, Gao H J. Shape insensitive optimal adhesion of nanoscale fibrillar structures. *P Natl Acad Sci USA*, 101: 7851-7856, 2004.
- [25] Williams J A, Le H R. Tribology and MEMS. *J Phys D: Appl Phys*, 39: R201-R214, 2006.
- [26] Li Q W, DePaula R, Zhang X F, et al. Drying induced upright sliding and reorganization of carbon nanotube arrays. *Nanotechnology*, 17: 4533-4536, 2006.
- [27] Wei B Q, Vajtai R, Jung Y, et al. Microfabrication technology: Organized assembly of carbon nanotubes. *Nature*, 416: 495-496, 2002.
- [28] Lu C H, Qi L M, Yang J H, et al. Hydrothermal growth of large-scale micropatterned arrays of ultralong ZnO nanowires and nanobelts on zinc substrate. *Chem Commun*, 33: 3551-3553, 2006.
- [29] Bico J, Roman B, Moulin L, et al. Adhesion: Elastocapillary coalescence in wet hair. *Nature*, 432: 690, 2004.
- [30] Zhu J, Ru C Q, Mioduchowski A. Surface energy-driven adhesion of two opposing microcantilevers. *Acta Mech*, 184: 33-45, 2006.
- [31] de Boer M P, Michalske T A. Accurate method for determining adhesion of cantilever beams. *J Appl Phys*, 86: 817-827, 1999.
- [32] Li X, Peng Y. Investigation of capillary adhesion between the microcantilever and the substrate with electronic speckle pattern interferometry. *Appl Phys Lett*, 89: 234104, 2006.

- [33] Kwon H M, Kim H Y, Puell J, et al. Equilibrium of an elastically confined liquid drop. *J Appl Phys*, 103: 093519, 2008.
- [34] Kim H Y, Mahadevan L. Capillary rise between elastic sheets. *J Fluid Mech*, 548: 141-150, 2006.
- [35] Liu J L, Feng X Q, Xia R, et al. Hierarchical capillary adhesion of microcantilevers or hairs. *J Phys D: Appl Phys*, 40: 5564-5570, 2007.
- [36] Journet C, Moulinet S, Ybert C, et al. Contact angle measurements on superhydrophobic carbon nanotube forest: Effect of fluid pressure. *Europhys Lett*, 71: 104-109, 2005.
- [37] Liu J L, Feng X Q. Capillary adhesion of micro-beams: Finite deformation analyses. *Chin Phys Lett*, 8: 2349-2352, 2007.
- [38] Liu J L. Analogies between a meniscus and a cantilever. *Chin Phys Lett*, 26: 116803, 2009.
- [39] Py C, Bastien R, Bico J, et al. 3D aggregation of wet fibers. *Europhys Lett*, 77: 44005, 2007.
- [40] Boudaoud A, Bico J, Roman B. Elastocapillary coalescence: Aggregation and fragmentation with a maximal size. *Phys Rev E*, 76: 060102, 2007.
- [41] Lin M J, Chen R. Sticking effect on center-anchored circular plates in microstructures. *IEEE T Compon Pack T*, 24: 645-649, 2001.
- [42] Py C, Reverdy P, Doppler L, et al. Capillarity induced folding of elastic sheets. *Eur Phys J Special Topics*, 166: 67-71, 2009.
- [43] Py C, Reverdy P, Doppler L, et al. Capillary origami: Spontaneous wrapping of a droplet with an elastic sheet. *Phys Rev Lett*, 98: 156103, 2007.
- [44] Liu J L. Theoretical analysis on capillary adhesion of microsized plates with a substrate. *Acta Mechanica Sinica*, 26: 217-223, 2010.

Color Plots

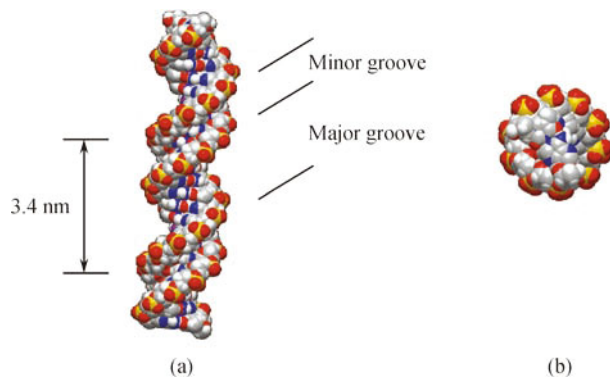


Fig. 1.1 Molecular structure of the double-stranded DNA molecule: (a) side view, (b) top view.

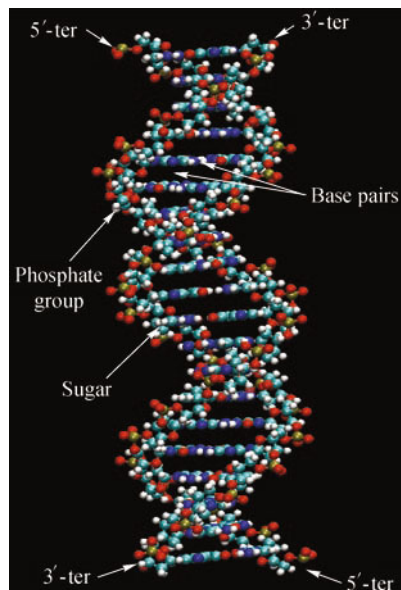


Fig. 1.4 Double helical structure of the dsDNA molecule.

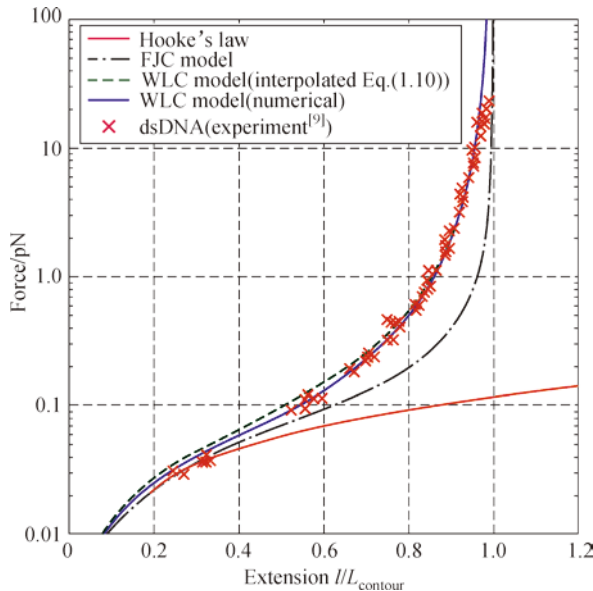


Fig. 1.7 Force versus extension experimental data taken from [1] for λ phage DNA pulled by magnetic beads in 10 mM Na^+ buffer. The data are fit for a WLC model solved numerically (WLC exact, solid line), using Eq. (1.10) (WLC interpolated, dash line), both assuming the persistence length $P = 53 \text{ nm}$. The FJC curve (dotted-dash line) assumes $b = 2P = 106 \text{ nm}$ from Eq. (1.4). The Hooke's law force curve (solid line with circle) for the low-force extension is from Eq. (1.6)^[1].

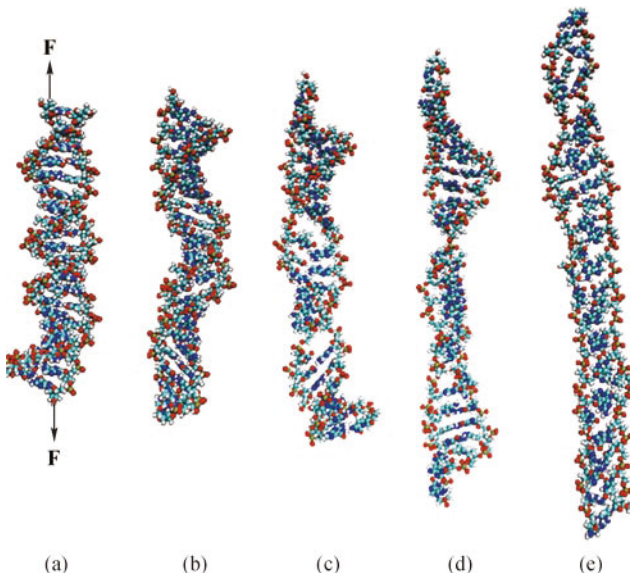


Fig. 1.11 Conformational changes of DNA molecule during the stretching process: (a) initial, (b) 10 ps, (c) 20 ps, (d) 40 ps, (e) 60 ps.

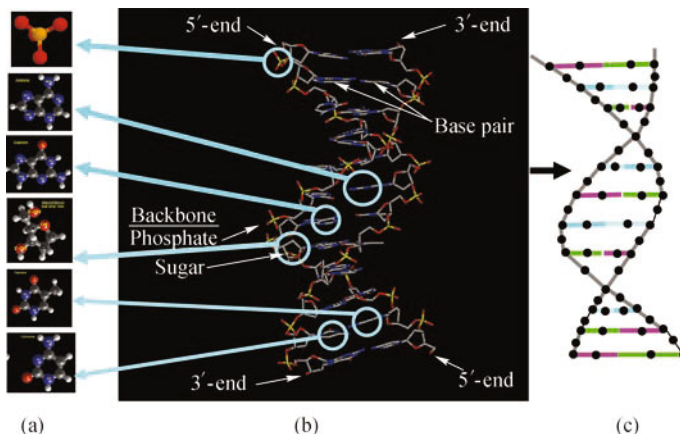


Fig. 1.16 Schematic of mapping full atomistic DNA model to a coarse-grained model: (a) building blocks of DNA molecule, (b) DNA molecular structure, and (c) coarse-grained DNA model.

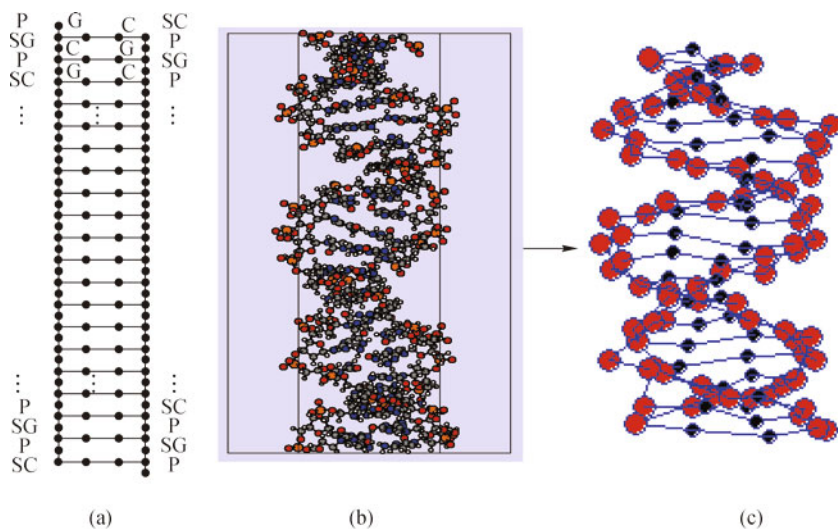


Fig. 1.17 Coarse-graining of DNA molecule: (a) schematic representation of DNA containing pure G–C base pairs, (b) fine-scale atomistic model, and (c) corresponding coarse-grained model.

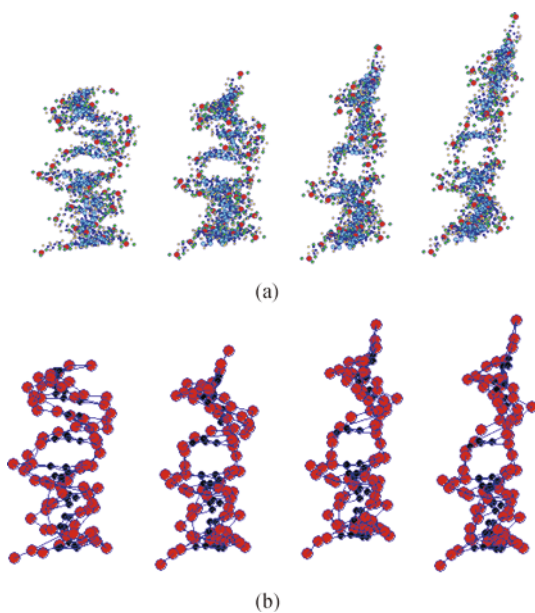


Fig. 1.29 The progressive DNA configurations of (a) full atomistic DNA model, and (b) coarse-grained DNA model.

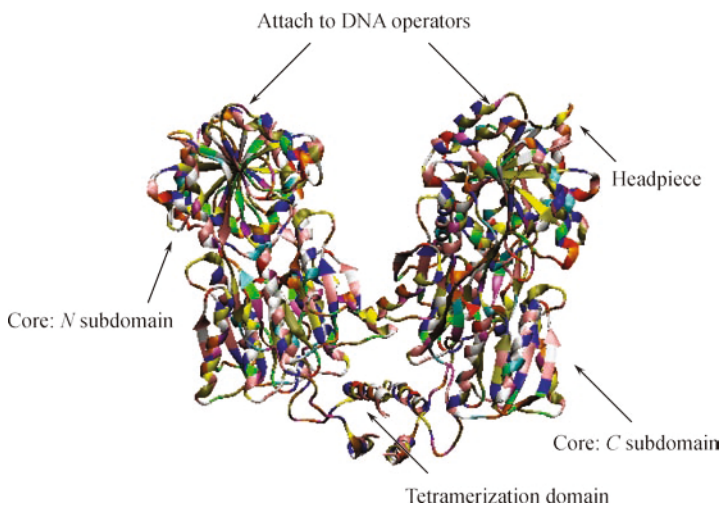


Fig. 1.32 Crystal structure of the *lac* repressor binding DNA.

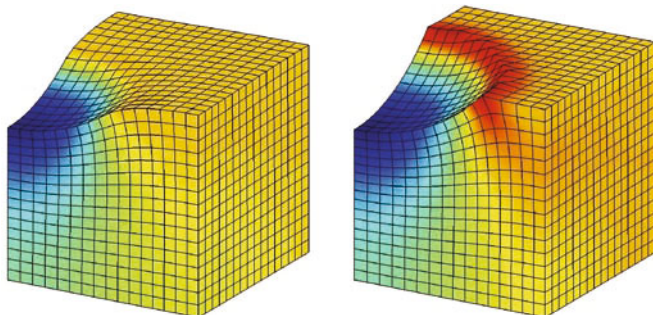


Fig. 2.3 Comparison between weak adhesion ($\gamma_w = 1\,000$, left) and strong adhesion ($\gamma_w = 1$, right)^[33]. Increasing the strength of adhesion has the same relative effect as decreasing the stiffness of the bodies.

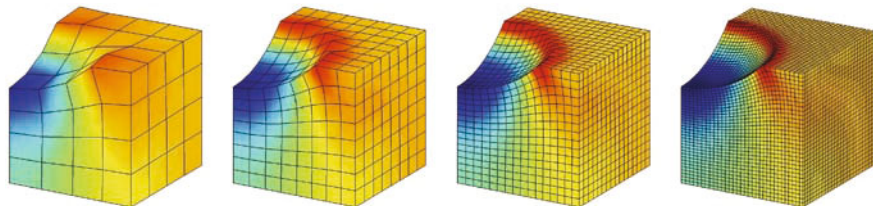


Fig. 2.4 Mesh convergence of the SF formulation (using a mesh with 4^3 , 8^3 , 16^3 and 32^3 finite elements. Contact with a rigid sphere is considered^[33].

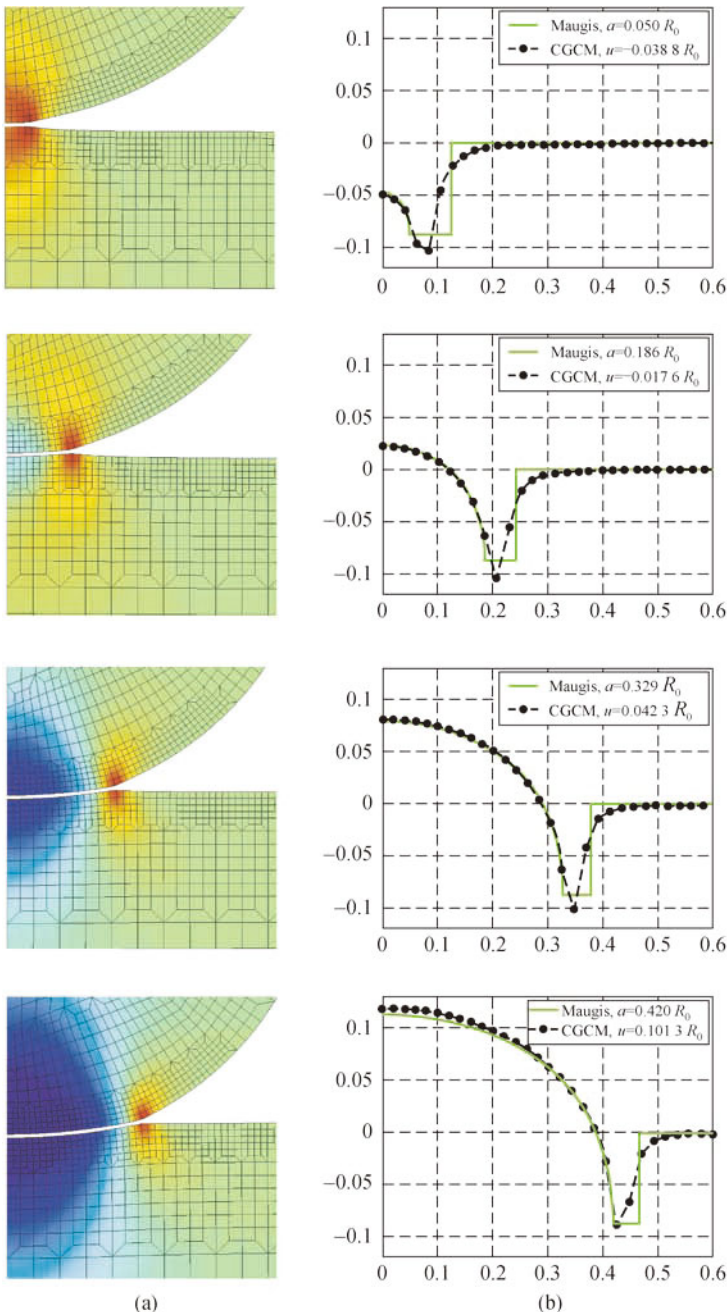


Fig. 2.8 Adhesion of soft spheres: deformation and stress field (a); contact pressure between the two bodies (b)^[44]. The four cases correspond to the four states marked in Fig. 2.7.

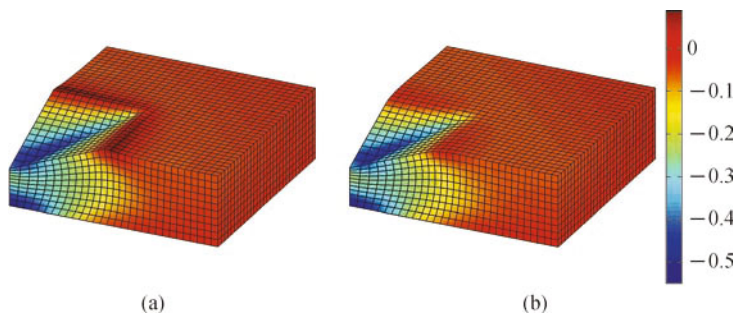


Fig. 2.9 Nanoindentation with strong (a) and weak (b) adhesion^[44].

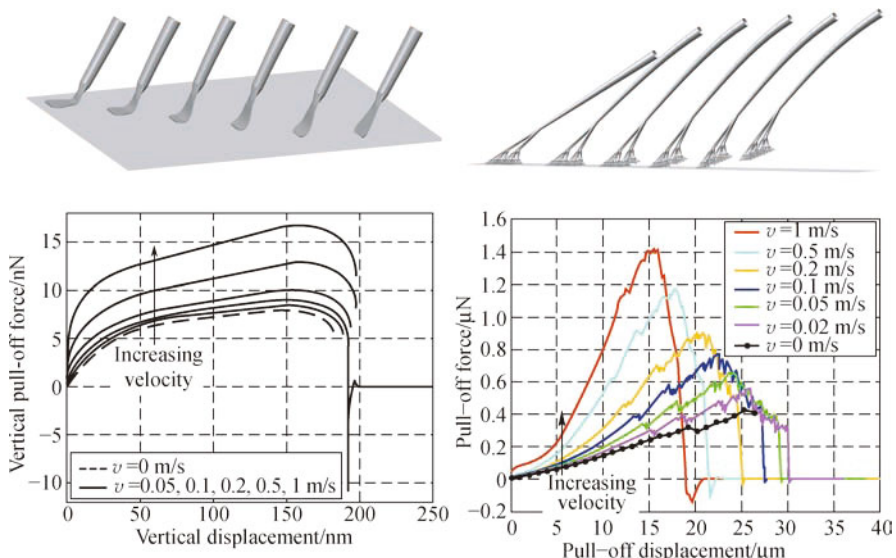


Fig. 2.11 Pull-off computation of a gecko spatula (left) and seta (right); deformation (top) and force-displacement curve (bottom)^[45].

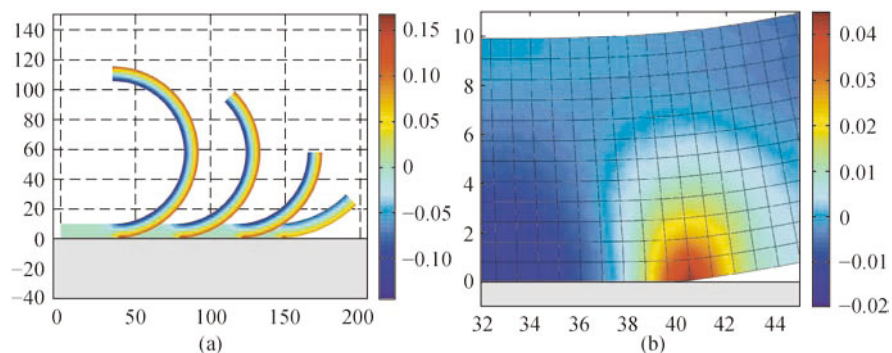


Fig. 2.12 Peeling of an elastic strip by an applied end rotation: deformation of the strip (a); stress at the peeling front (b)^[63].

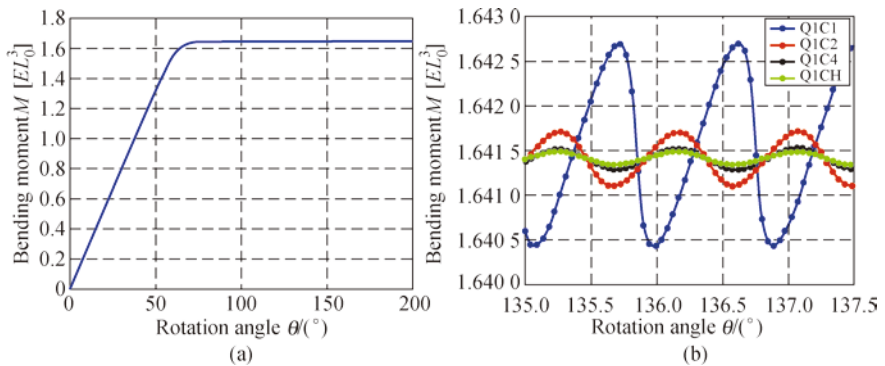


Fig. 2.13 Peeling forces: force-displacement curve (a); oscillation in the force-displacement curve (b)^[63].

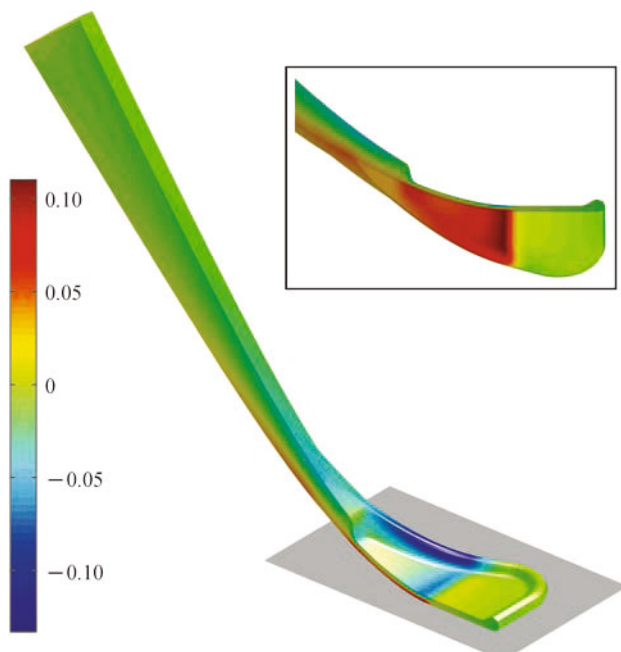


Fig. 2.14 Finite element computation of the peeling of a single gecko spatula^[66].

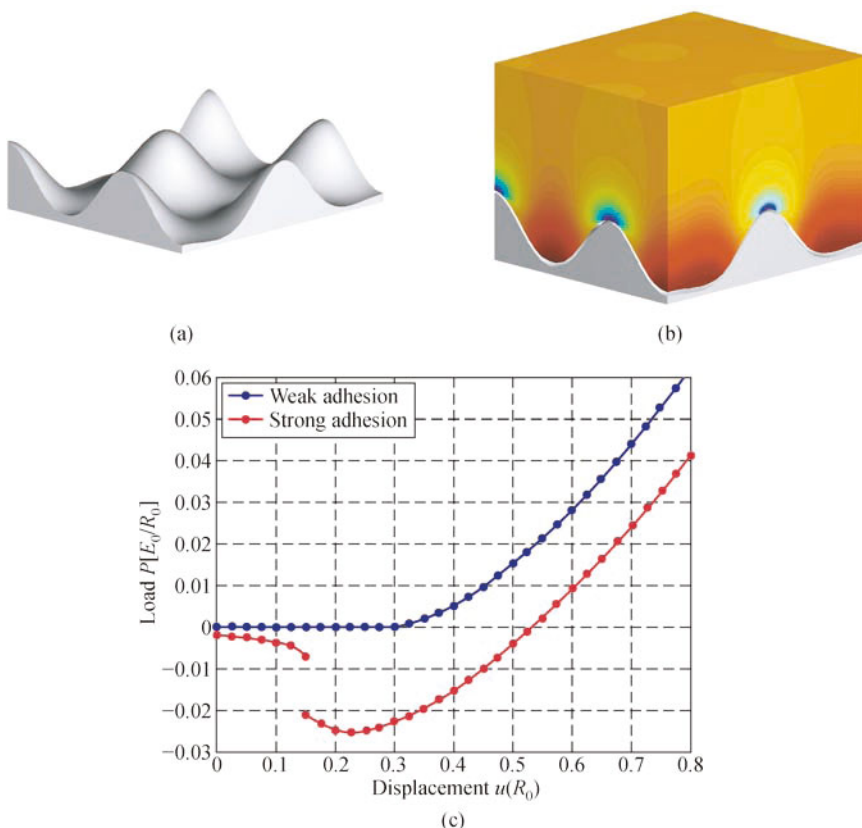


Fig. 2.15 Rough surface contact: surface roughness (a); contact deformation and stress of a soft elastic block pressed onto the surface (b); (c) force-displacement curve considering strong adhesion ($\gamma_W = 2$) in contrast to weak adhesion ($\gamma_W = 1\,000$). Equivalently, this corresponds to comparing a soft block with a stiff block for fixed adhesion strength. The data is normalized by the asperity spacing R_0 and the energy $E_0 = ER_0^2$.

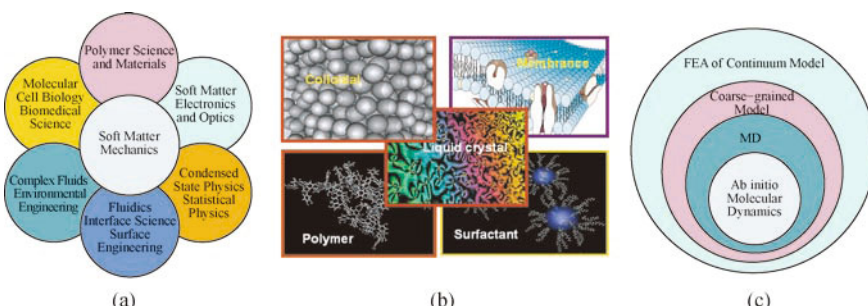


Fig. 3.1 Mechanics of soft matter and its multiscale components.

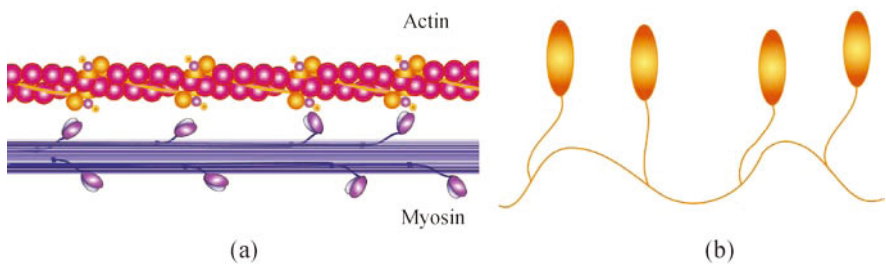


Fig. 3.2 Comparison between (a) myosin-actin in cells and (b) mesogens in liquid crystal elastomers.

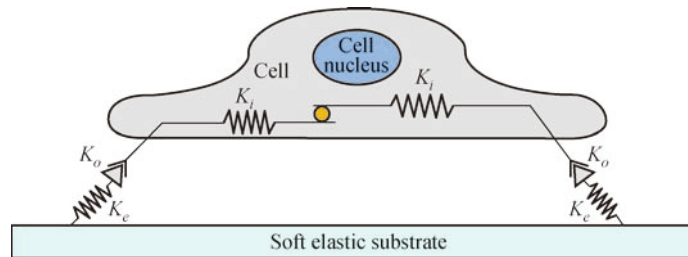


Fig. 3.3 The two-spring rigidity sensing model^[21].

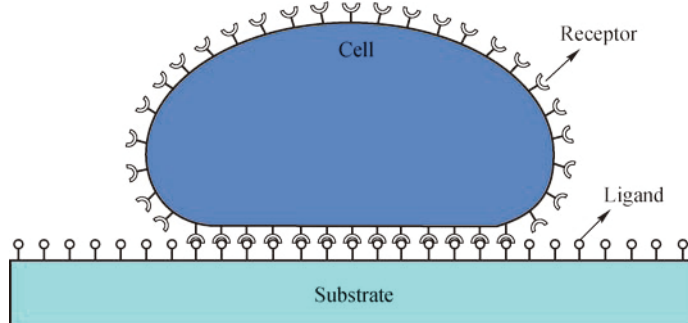


Fig. 3.4 Soft matter cell model and soft adhesive contact model.

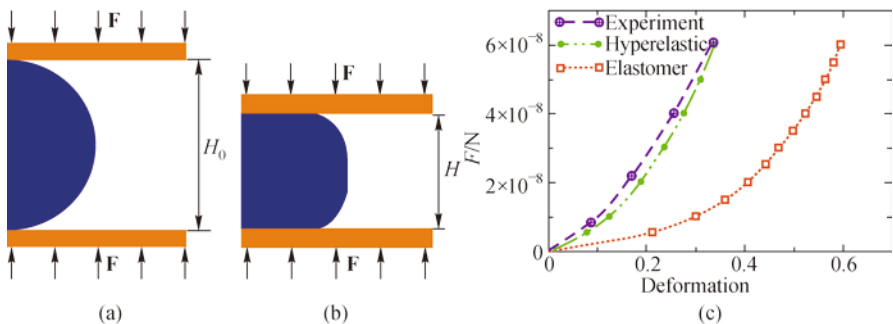


Fig. 3.6 Validation of the cell model: (a) before deformation, (b) after deformation, (c) force-deformation curve.

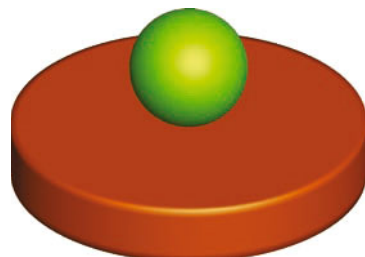


Fig. 3.7 3D Computational model of cell spreading.

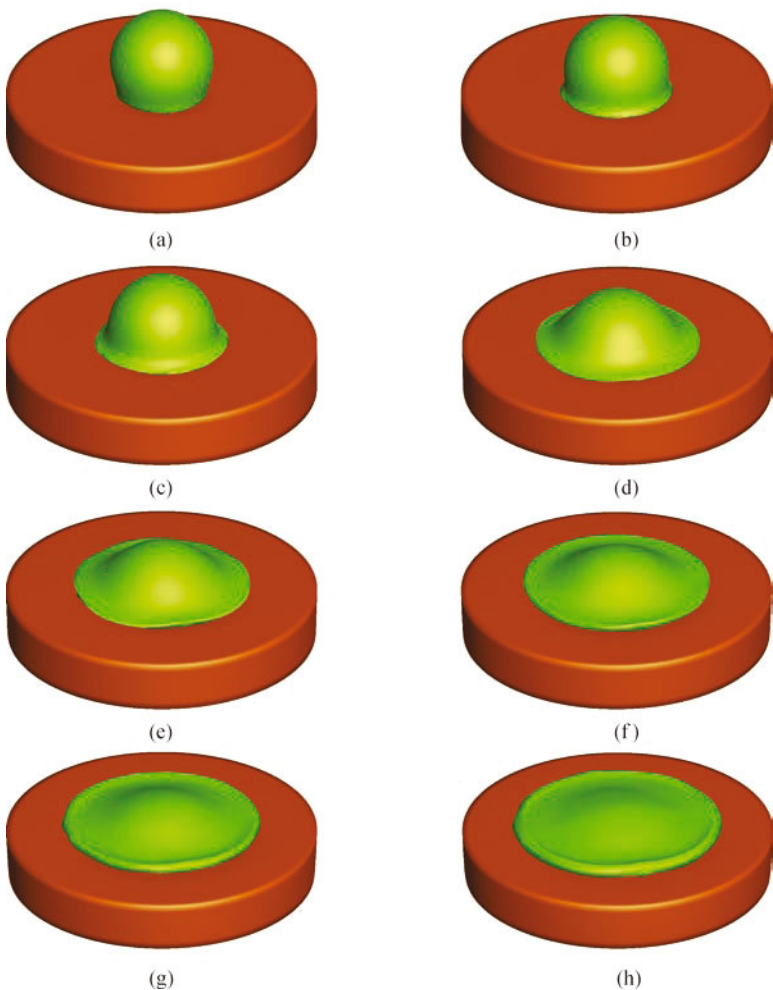


Fig. 3.8 Time sequence of endothelial cell contact with a soft substrate.

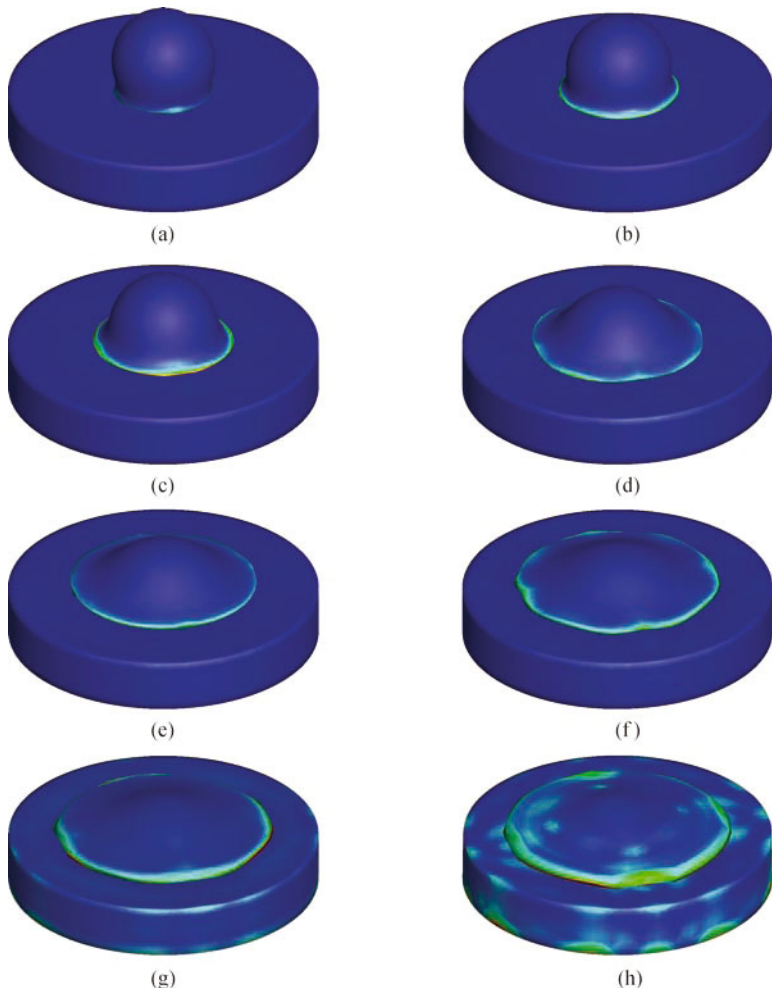


Fig. 3.9 Time sequence of endothelial cell contact with a stiff substrate.

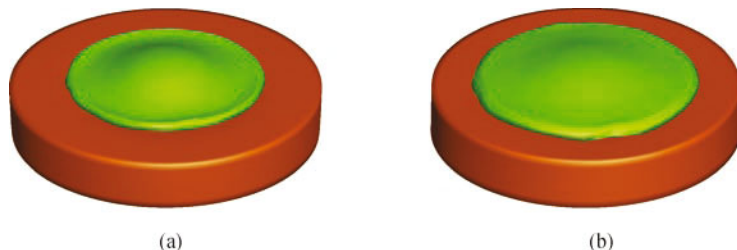


Fig. 3.10 Cell spreading over substrates with different stiffnesses: (a) soft substrate, (b) stiff substrate.

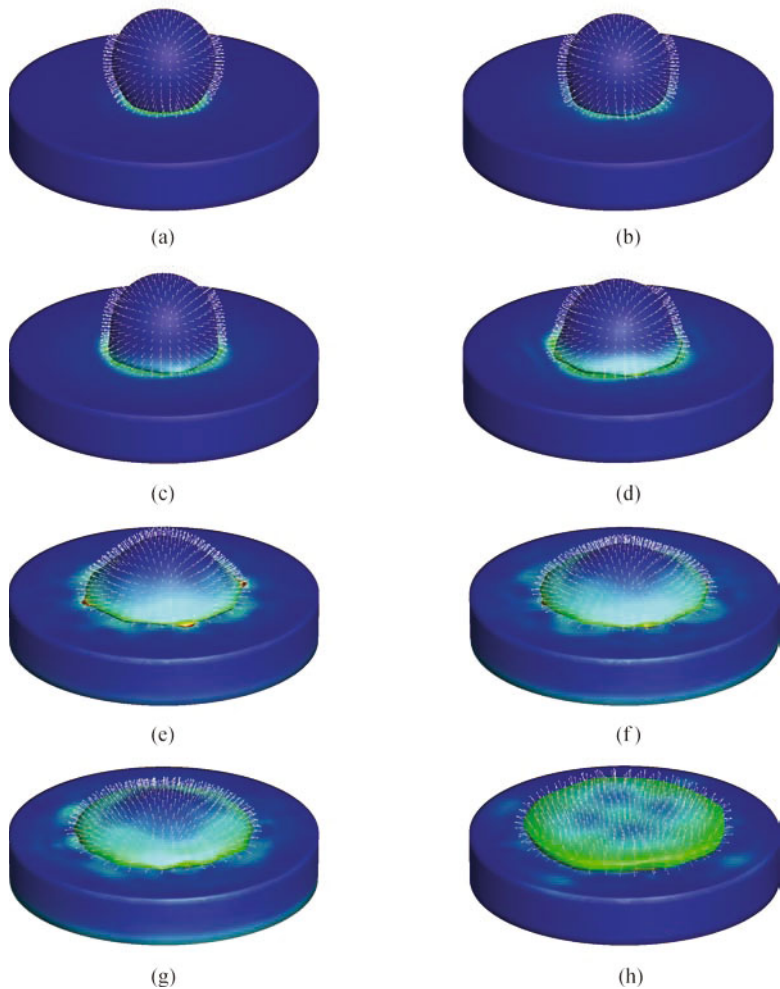


Fig. 3.11 Time sequence of stem cell contact with a soft substrate.

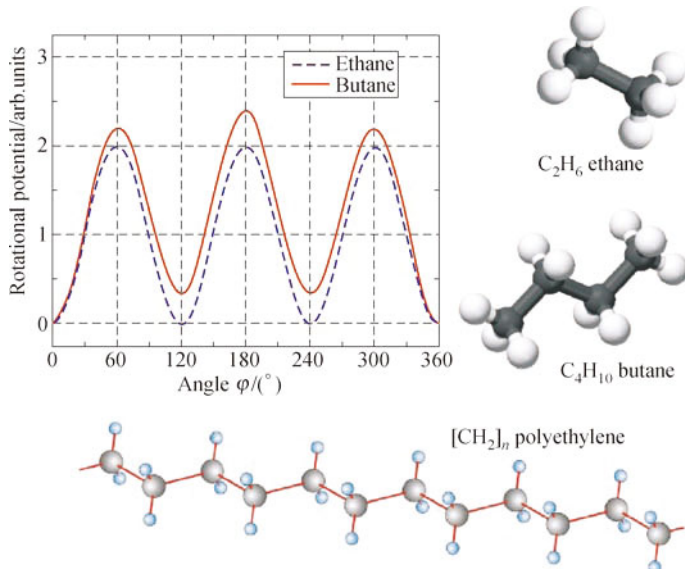


Fig. 5.2 Rotational symmetry of bonding energy potential in hydrocarbon molecules. The plot shows an accurate 3-fold symmetry of the potential for ethane or propane and a quasiperiodicity for butane and higher order molecules, including polyethylene.

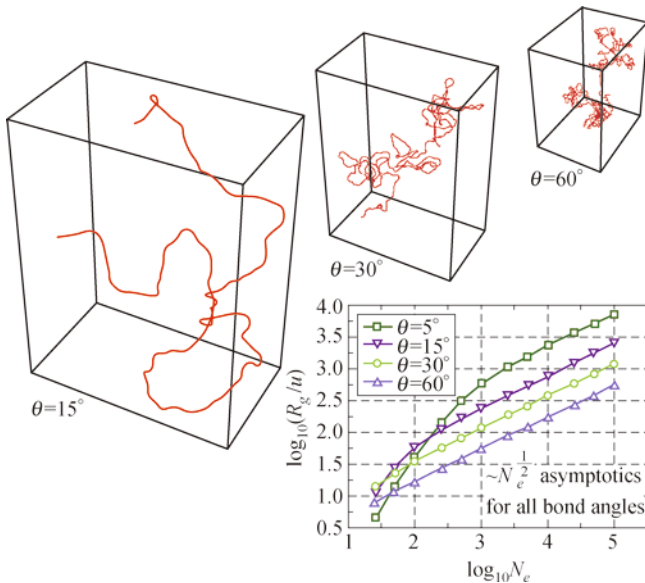


Fig. 5.5 Overall geometry samples for various bond angles θ and constant number N_e of monomers in the molecular chain. The plot shows dependence of the gyration radius of the molecule on N_e .

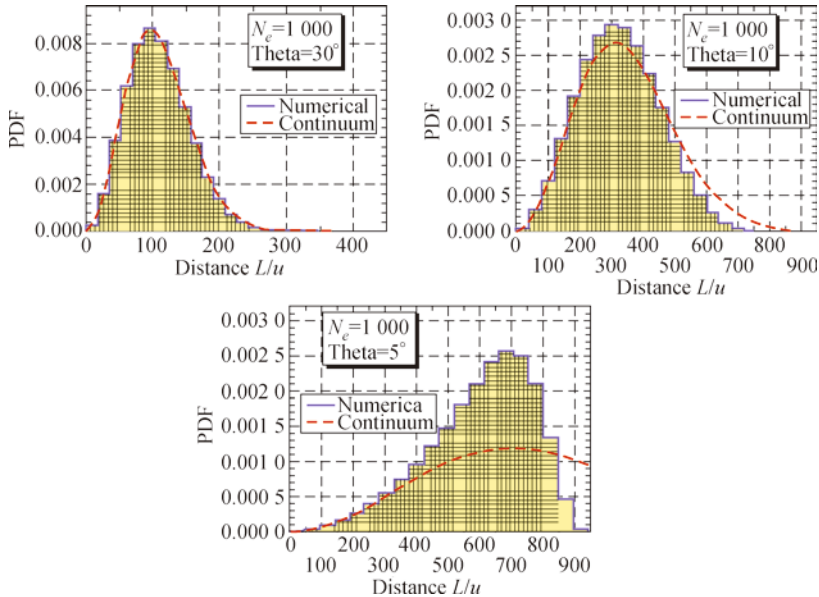


Fig. 5.6 Examples of the numerical distribution (Eq. (5.20)) in comparison with the analytical continuum model distribution (Eq. (5.13)) at various bonding angles θ .

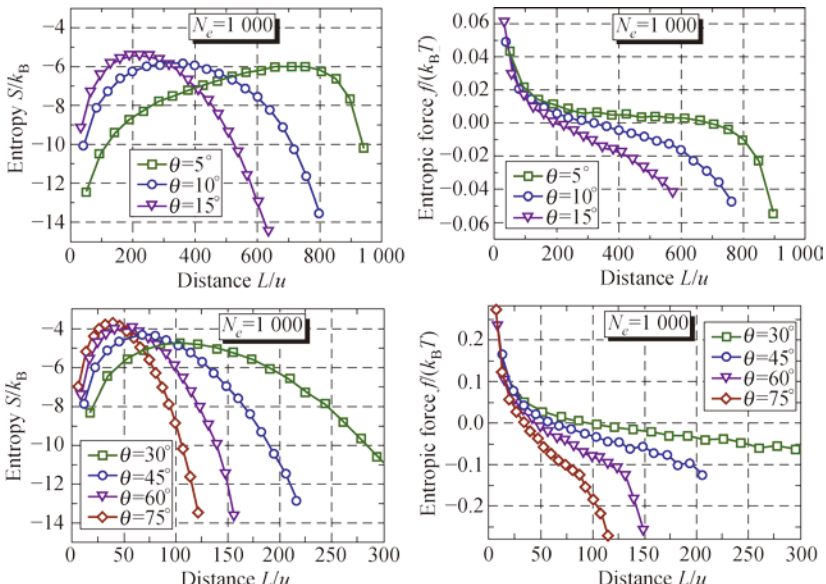


Fig. 5.7 Numerical values of the molecular entropy and entropic elastic force varying with separation distances between two loaded endpoints of the molecule (Fig. 5.1) for small (top) and large (bottom) kink angles θ ; u is the distance between two adjacent monomers or the C–C bond length.

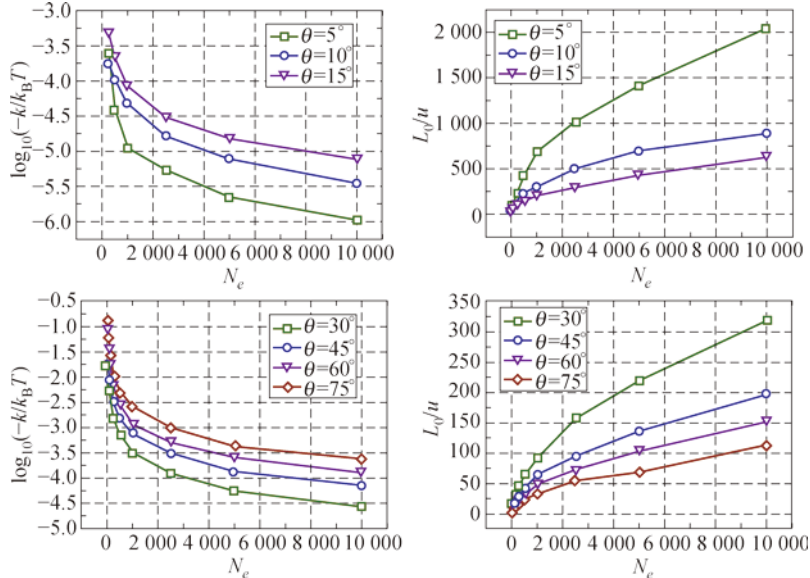


Fig. 5.8 Elastic moduli (left) and relaxed lengths of the endpoint separation (right) for the linear elastic regimes observed in Fig. 5.7.

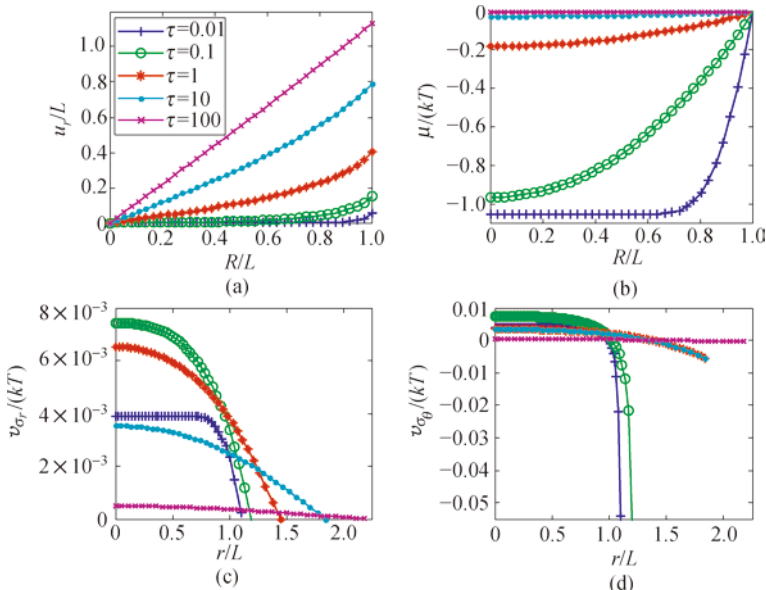


Fig. 6.2 (a) The spatial profiles of normalized radial displacement of a spherical gel at various dimensionless time during swelling, (b) the spatial profiles of normalized chemical potential of solvent, (c) the distribution of normalized true radial stress, plotted in the deformed configuration, (d) the distribution of normalized true hoop stress, plotted in the deformed configuration.

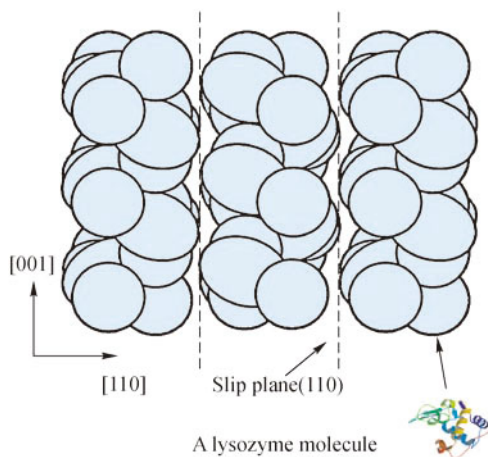


Fig. 7.1 A 3D crystallized structure of a tetragonal lysozyme crystal (protein molecule is from PDB code: 133L)^[45].

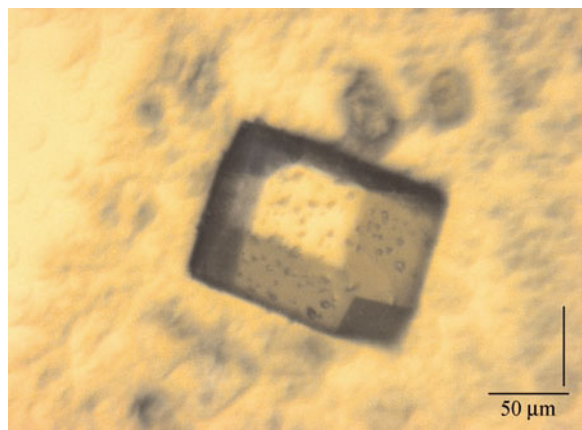


Fig. 7.2 A tetragonal lysozyme single crystal.

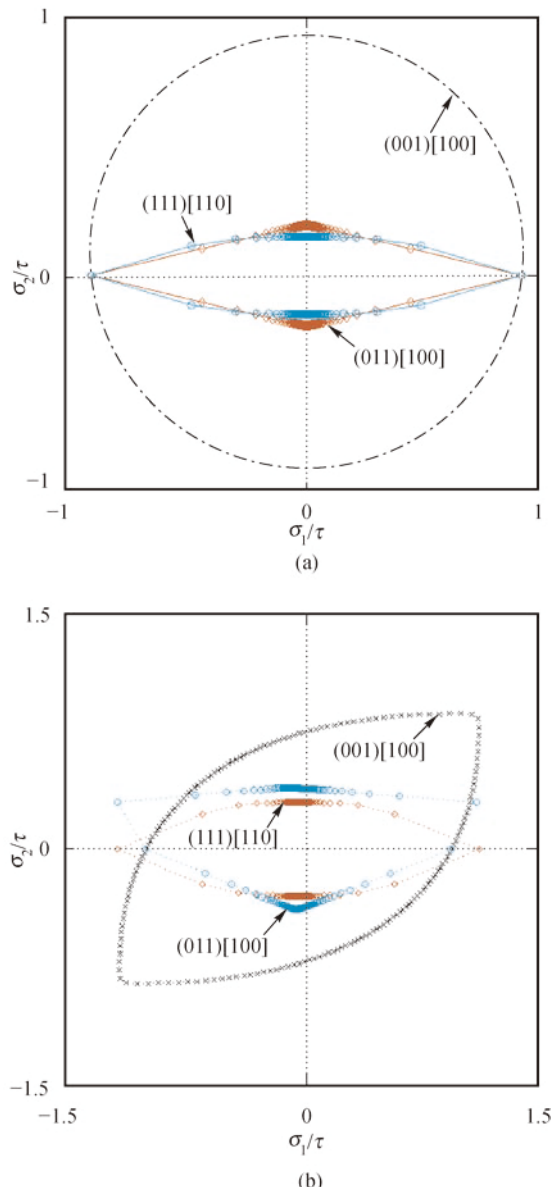


Fig. 7.5 The yield surface of the tetragonal lysozyme crystals for three different crystallographic orientations of $(001)[100]$, $(011)[100]$, and $(111)[110]$ at two temperatures of (a) 285 K and (b) 307 K.

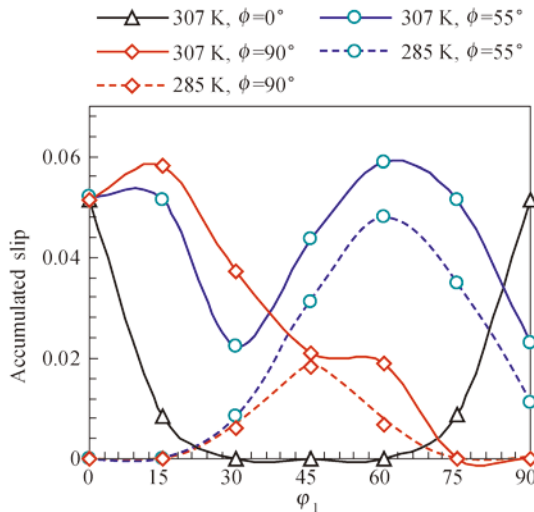


Fig. 7.7 The orientation dependent accumulated slip $\bar{\gamma}$ obtained for 3D lysozyme crystals loaded up to 0.01 strain at two different temperatures of 285 K and 307 K and Euler angles of $\phi = 0^\circ, 55^\circ$, and 90° . In all these analyses, Euler angle $\varphi_2 = 0^\circ$.

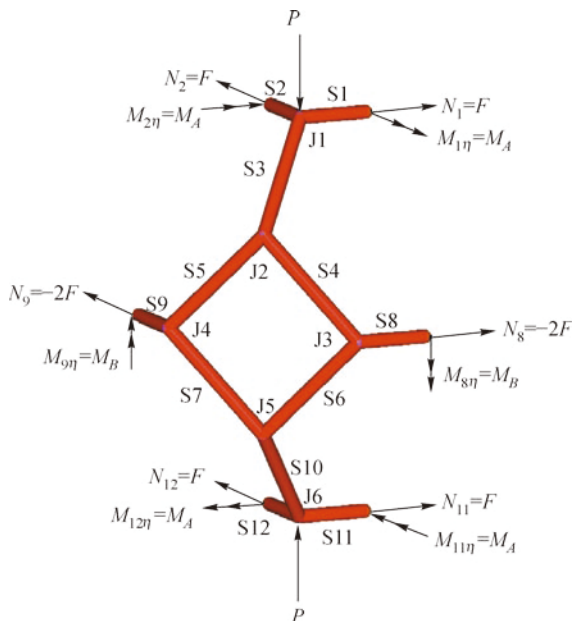


Fig. 8.5 Free body diagram of a quarter of the tetrakaidecahedral cell.

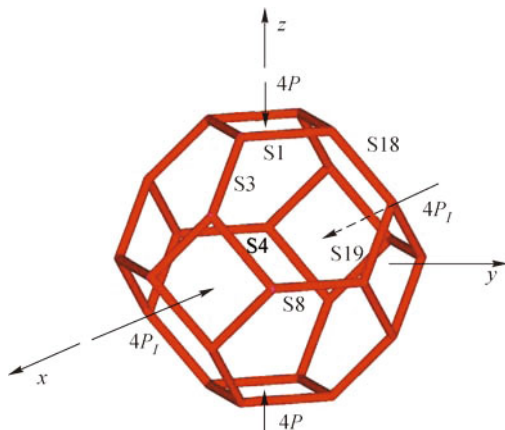


Fig. 8.10 Tetrakaidecahedral cell under compression in the x - and z -directions.

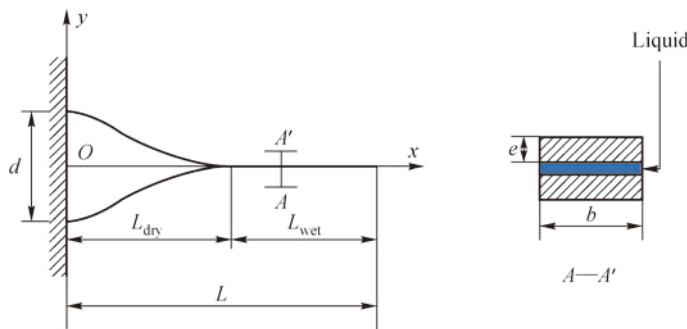


Fig. 9.1 Capillary adhesion of two micro-beams of infinitesimal deformation.

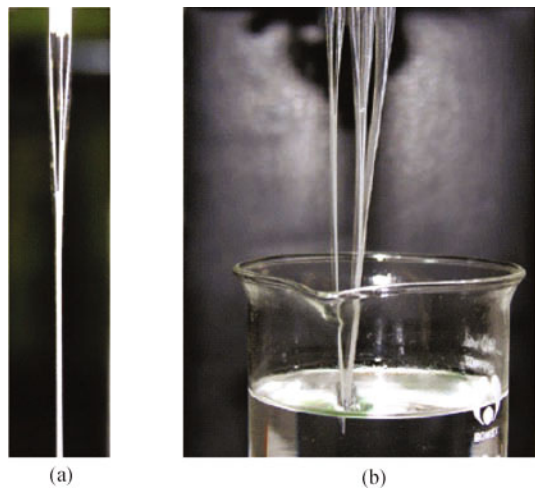


Fig. 9.9 Experimental photos for the hierarchical structures.

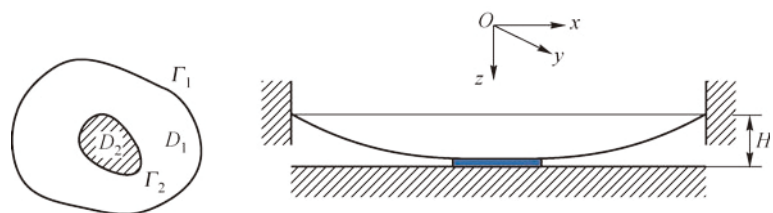


Fig. 9.10 Capillary adhesion of a micro-plate on the substrate.